IRRADIATION ACCELERATED CORROSION OF 316L STAINLESS STEEL IN SIMULATED PRIMARY WATER

by

Stephen S. Raiman

A dissertation submitted in partial fulfillment
of the requirements for the degree of
Doctor of Philosophy
(Nuclear Engineering and Radiological Sciences)
In The University of Michigan
2016

Doctoral Committee:

Professor Gary S. Was, Chair
Professor David M. Bartels, University of Notre Dame
Professor Fei Gao
Professor J. Wayne Jones

ACKNOWLEDGEMENTS

I would like to thank my advisor, Dr. Gary Was, for his guidance, wisdom, and encouragement throughout my time in Michigan.

My colleagues, who have supported me, encouraged me, assisted me, mentored me, made me laugh, and have filled so many roles during my PhD studies: Dr. Pantip Ampornrat, Dr. Janelle Wharry, Dr. Mike McMurtrey, Dr. Cheng Xu, Dr. Anne Campbell, Dr. Tyler Moss, Dr. Gokce Gulsoy, Dr. Kale Stephenson, Dr. Shyam Dwarknath, Dr. Elizabeth Getto, Anthony Monterrossa, Stephen Taller, David Woodley, Justin Hesterberg, Gerit VanCoevering, Drew Johnson, Tai-Ni Yang, Rajan Bhambroo, Rigel Hanbury, Dr. Peng Wang, Dr. Mi Wang, Dr. Miao Song, Dr. Wenjun Kuang, Dr. George Jiao, Dr. Yugo Ashida.

Our HTCL and MIBL staff: Alex Flick, Dr. Fabian Naab, Thomas Kubley, Ethan Uberseder, and especially Dr. Ovidiu Toader.

The staff at EMAL: Dr. Kai Sun, Dr. Haiping Sun, and Dr. John Mansfield.

Dr. Bernie Weinstein and Dr. Yogesh Vohra for their guidance and mentorship in the early stages of my career.

Dr. David Bartels for his advice and guidance.

Dr. Wayne Jones and Dr. Fei Gao for their service on my committee.

My father and mother for their tireless encouragement and support throughout the years.

My fiancée Dr. Maya Aravind, for helping me to be the best version of myself.

This work was supported by the DOE-NEUP, grant number DE-AC07-05ID14517 and EDF, Contract No. 8610-BVW-4300243004

TABLE OF CONTENTS

LIST OF TABLES

LIST OF FIGURES

LIST OF APPENDICES

ABSTRACT

IRRADIATION ACCELERATED CORROSION OF 316L STAINLESS STEEEL IN SIMULATED PRIMARY WATER

by Stephen S. Raiman

Chair: Gary S. Was

The objective of this work is to understand the effects of irradiation on the corrosion of 316L stainless steel in simulated primary water. 316L stainless steel samples were irradiated with a proton beam while simultaneously exposed to simulated PWR primary water to study the effects of radiation on corrosion. A 3.2 MeV proton beam was transmitted through a 37 μm thick sample that served as a "window" into a corrosion cell containing flowing 320˚ C water with 3 wppm H_2. This design permitted radiolysis and displacement damage to occur on the sample surface in contact with the simulated primary water environment. Samples were irradiated for 4, 12, 24, and 72 hrs at dose rates between 400 and 4000 kGy/s, corresponding to damage rates of $7x10^{-7}$ to $7x10^{-6}$ dpa/s respectively. The structure and composition of the oxide films were characterized using Raman spectroscopy, STEM, and SEM.

Sample areas exposed to direct proton irradiation had inner oxide films that were thinner, more porous, and were deficient in chromium when compared to unirradiated oxides. Outer

oxides on irradiated samples exhibited a smaller particle size, and had a significant amount of hematite, which was not found on unirradiated samples. The presence of hematite on irradiated samples indicates an increase in electrochemical potential due to irradiation. Dissolution of chromium-rich spinels due to the elevated potential is identified as a likely mechanism behind the loss of inner oxide chromium. It is suggested that the loss of inner-oxide chromium leads to a less protective inner oxide, and a higher rate of oxide dissolution.

Sample areas that were not irradiated, but were exposed to the flow of radiolyzed water, exhibited most of the same phenomena found on irradiated areas including loss of Cr and thinner more porous oxides, indicating that water radiolysis is the primary mechanism. When a sample with a pre-formed oxide was irradiated in the same conditions, the region exposed to radiolyzed water showed signs of elevated potential (hematite), but was not deficient in chromium, and did not exhibit porosity, suggesting displacement damage may still affect corrosion kinetics in an already formed oxide.

CHAPTER 1 - INTRODUCTION

Nuclear power is an important source of electricity in today's world. Nuclear reactors currently supply 19% of electricity in the United States[1], and 11% of electricity globally[2]. In addition to providing reliable baseload energy, nuclear reactors are free of primary emissions, making them environmentally friendly. As the only source of scalable clean baseload electricity that is currently available, nuclear power can play a valuable role in mitigating climate change. Due to the high cost and political difficulties inherent in new reactor construction, it is important to maintain the current fleet of light water reactors for as long as reasonably possible.

The challenge in extending the life of the LWR fleet is ensuring safe and economical operation despite the various forms of material degradation that take place. The conditions inside reactor pressure vessels are highly aggressive due to high temperatures and the presence of oxidizing species. Among the degradation modes of concern is stress corrosion cracking (SCC), a phenomenon in which stainless steel components crack due to a combination of mechanical stress and a corrosive environment. Further, in reactor cores, radiation can affect the properties of the materials and/or the environment, which may result in irradiation assisted stress corrosion cracking (IASCC). Radiation has also been shown to greatly accelerate corrosion in stainless steel [3]–[5] and Zircaloy [6]–[8].

With these issues in mind, it is important to understand IASCC for several reasons. First, as we seek to extend the life of current light water reactors, an understanding of IASCC will enable material lifetimes to be predicted with greater confidence, so potential safety issues can

be addressed before they become larger problems, and costly shutdowns can be avoided. Second, a fundamental understanding of the mechanisms underlying IASCC in stainless steel can enable new operating procedures, new water chemistries, and advanced material designs to minimize material degradation issues. As we look the future of nuclear power, advanced reactor designs will bring new materials degradation issues, and our understanding of IASCC will enable the safe and reliable operation of the next generation nuclear fleet.

To fully understand IASCC, the individual components must be analyzed. Figure 1.1 shows a matrix of the factors affecting IASCC, each of which must be understood individually if IASCC is to be understood as a whole. This work sits at the intersection of radiation, materials, and the water environment, and seeks to develop a fundamental understanding of the mechanisms behind irradiation accelerated corrosion (IAC).

Protons cause displacement damage in both the metal and the oxide, creating point defects that could potentially accelerate corrosion due to enhanced diffusion[8]–[10]. Corrosion in stainless steel is believed to be highly dependent on both the rate of cation and oxygen diffusion through the oxide[11]–[13]. Experimental data has shown higher diffusion rates along dislocations in stainless steel [14], [15], suggesting that irradiation induced microstructural changes may affect corrosion rates.

In water, radiation is known to create several strong oxidizing species due to water radiolysis. Among the long-lived species, H_2O_2 [16], [17] and dissolved O_2 [18], [19] have been shown to increase the corrosion potential of stainless steel and affect the composition and morphology of the oxide in LWR conditions[20]. In addition to these long-lived species, several

short lived radicals such as $OH^{\bullet}$ and $H^{\bullet}$ are created in the water [21] and may affect the rate of corrosion.

Unfortunately, little mechanistic data on IAC currently exists, in-part due to experimental limitations. The most difficult challenge to overcome is the design of an experiment in which a sample surface can be irradiated while simultaneously exposed to controlled LWR conditions. High energy proton irradiation offers a potential means for studying IAC by virtue of its high dose rates, ease of access, controllable experimental conditions, and flexibility with in-situ diagnostics. A primary limitation of proton beams is their limited penetration depth through solid and liquid media. This is notable, since it is important to study the effects of irradiation both in the solid and in the solution simultaneously.

The objective of this work is to understand the effects of irradiation on the corrosion of 316L stainless steel in simulated primary water. Chapter 2 presents background relevant to this work. Chapter 3 presents an objective and approach. Chapter 4 describes the design and testing of a novel experiment in which samples are irradiated with a proton beam while simultaneously exposed to carefully monitored flowing LWR conditions, allowing studies into the effect of displacement damage and radiolysis on the corrosion process. Experimental results are presented in chapter 5. Chapter 6 contains discussion on the thermodynamic effects of radiation on the corrosion process, and how radiation affects the growth and dissolution of the oxide layers. Concluding remarks are given in chapter 7.

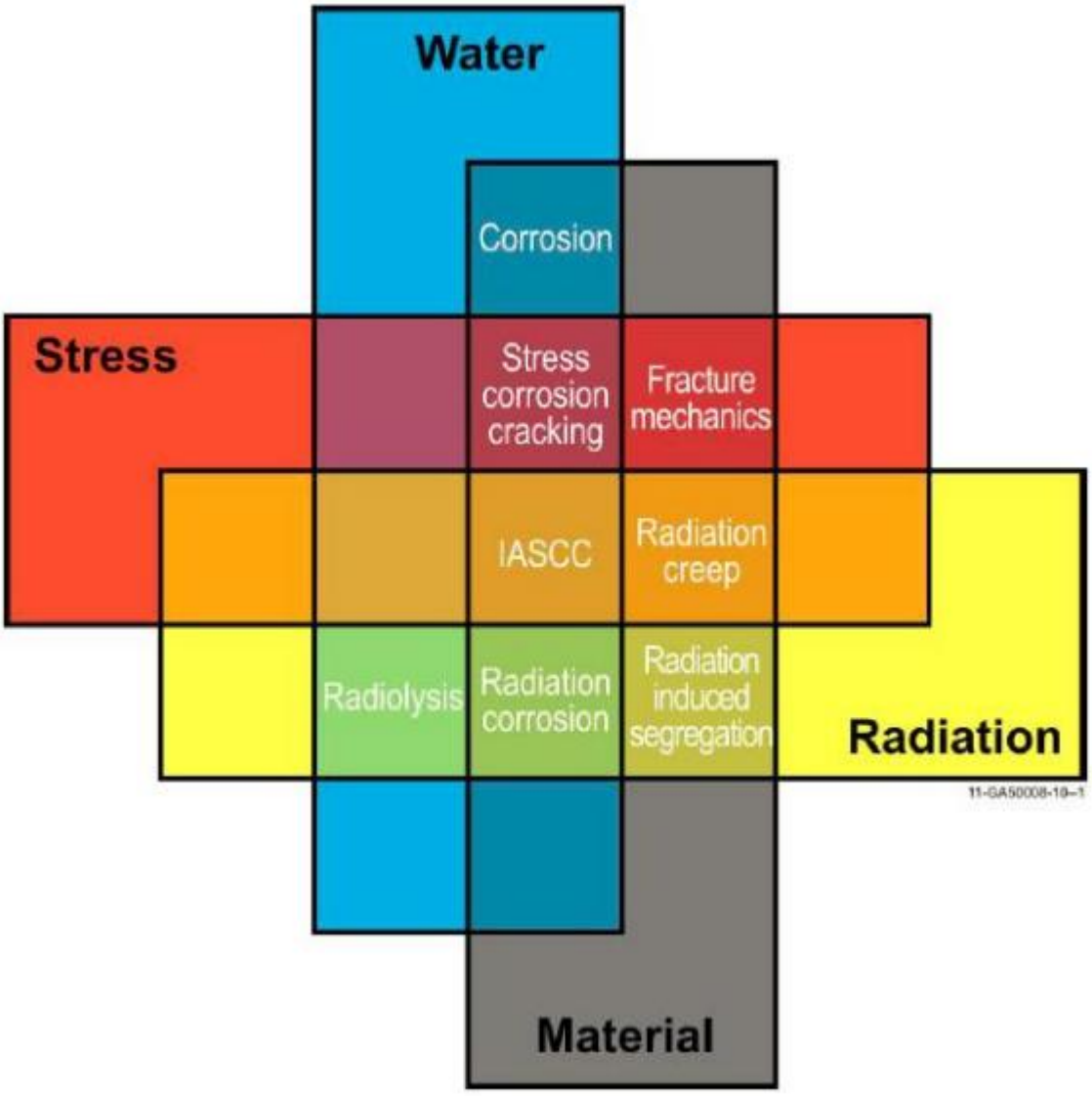

Figure 1.1. Graphic representation of the factors affecting IASCC[22]

CHAPTER 2 - BACKGROUND

2.1 Properties of Stainless Steel

Although the focus of this work is on the intersection of oxidation and radiation, it is proper to begin with a brief discussion of some of the metallurgical and mechanical properties of 316L stainless steel.

Stainless steels are classified by the amount of other elements that are alloyed with the iron. The American Iron and Steel Institute (AISI) classifies alloys with a 3-digit code where austenitic alloys are given a 300-series number, ferritic and martensitic steels are given a 400-series number, and high-manganese steels are in the 200-series. Figure 2.1 shows the stainless steels organized by alloying additions to 304 stainless steel. At the center of the diagram is AISI 304, a very common type of stainless steel in commercial use. Depending on the application, various alloying elements can be added to the base 304 stainless steel to make alloys more suited for specific purposes, such as added strength, easier machinability, or better corrosion resistance. Following the arrow at the bottom, AISI 316L is made by adding Mo for added pitting resistance, and reducing carbon for greater resistance to sensitization. Some of the details of the alloying elements in stainless steel are discussed in the next section.

2.1.1 Composition

The particular heat of 316L stainless steel used in this study has the composition shown in Table 2.1. Other non-specified elements may be present in a given heat of stainless steel. There are no set limits to the amount of non-specified elements, although stainless can be described as high-purity, ultra-high purity, or commercial grade depending on the tolerance of impurities.[23]

By definition, stainless steel is a steel alloy with at least 10.5% chromium content by weight. Since corrosion resistance is a key attribute of stainless steel, it is important to note how chromium is responsible for the favorable corrosion properties of stainless steel.

In water and air, chromium reacts with oxygen to form a layer of chromium-oxide that shields the material from further corrosion. The layer is passive, meaning oxidation is not kinetically favorable, thus oxidation is dramatically slowed. Observations have found that high resistance to corrosion and oxidation is found in alloys with greater than 13% chromium by weight.[24] In addition to chromium, molybdenum is added to improve performance against pitting and crevice corrosion. It has also been shown that silicon improves resistance to crevice corrosion[25].

The austenite phase occurs in iron between approximately 910˚C and 1400˚C. The phase transformation into austenite is marked by a change from a body-centered-cubic structure to a face-centered-cubic structure. To remain in the austenitic phase at room temperature, nickel is added to the alloy to lower the eutectic temperature. Countering the effect of the added nickel, some elements, known as ferrite stabilizers, raise the eutectic temperature. Chromium is the most abundant austenitic destabilizer, with molybdenum, and silicon also present.[26]

Due to the high cost of nickel, some stainless alloys include manganese and nitrogen, which also act as austenite stabilizers. The latter is not part of the AISI classification for 316L

stainless. Manganese does make up 2% of the alloy by weight, but it is included more for its effect on mechanical properties than its cost advantage over nickel.[27]

In general, alloying additions that substitute for iron atoms in the lattice do not increase strength much. Chromium is a good example, since it has minimal effect on the strength of the steel to which it is added. Chromium atoms are of similar size to iron atoms, and therefore fit nicely into the FCC structure with little distortion.[28]

All steels, stainless or not, contain carbon as a strengthener. By occupying interstitial sites, carbon atoms increase the yield strength and decrease ductility of steels. Unlike BCC steels, carbon atoms can easily occupy interstitial sites in the FCC lattice of austenitic steels without the need for heat treatments.[28] However, since carbon greatly detracts from corrosion performance due to the formation of carbides, austenitic steels have very low carbon content. The large difference in yield strength can be noted in comparison to alloys with higher carbon content such as the ferritic martensitic alloys.[29]

2.1.2 Phase Structure

The phase structure of stainless steel can be modeled using the Schaeffler Diagram shown in Figure 2.2. The diagram predicts the phase(s) of the metal after rapid cooling from 1050°C to room temperature. The chart is constructed by grouping austenite stabilizers and ferrite stabilizers into nickel and chromium equivalents according to Equation 2.1 and Equation 2.2[25], and charting the stability of the phases based on the concentration of each group.

$$\%\text{Ni equivalent} = \%\text{Ni} + \%\text{Co} + 30(\%\text{C}) + 25(\%\text{N}) + 0.5(\%\text{Mn}) + 0.3(\%\text{Cu}) \qquad (2.1)$$

$$\%\text{Cr equivalent} = \%\text{Cr} + 2(\%\text{Si}) + 1.5(\%\text{Mo}) + 5(\%\text{V}) + 5.5(\%\text{Al})$$
$$+1.75(\%\text{Nb}) + 1.5(\%\text{Ti}) + 0.75(\%\text{W}) \quad (2.2)$$

Austenitic steels are classified as such due to their high nickel content, which allows the steel to remain in the austenite phase below the eutectic temperature. Greater concentrations of austenite stabilizers such as nickel relative to austenite destabilizers will produce a material with a larger percentage in the austenite phase.

The most prevalent phase aside from austenite is the ferrite phase. This phase tends to form precipitates with greater concentrations of austenite destabilizing elements than the predominant austenite phase. The nature of the σ phase is still largely unsettled. Some work has suggested that the σ phase forms over time from low-temperature ferrite. Other work has suggested that the σ phase formed directly from austenite.[30]

These non-austenite precipitates can be annealed out by heating above the eutectic temperature. The amount of ferrite precipitates that form in the material during cooling is proportional to the length of time over which cooling takes place. Generally, slower cooling will yield a material with fewer non-austenite precipitates.[28]

2.1.3 Mechanical Behavior

While the experiments in this project are not concerned directly with the mechanical properties, they are still relevant to the successful progress of the study, as the samples to be used will be under constant pressure, so the tensile strength of the samples will be tested. This section will briefly cover the mechanical properties of 316L stainless steel.

Due to the fcc structure of austenitic stainless steel, it is generally more ductile and has lower tensile strength than other classifications of steel. Table 2.2 shows some relevant properties of 316L stainless steel in various forms, with different finished conditions.

Other factors that can affect the mechanical behavior of austenitic stainless steel include degree of cold work and temperature, which are shown in Figure 2.4 and Figure 2.5.

The variability of hardness from room temperature to LWR temperatures is small compared to the variability of toughness. The increase in toughness is likely due to the increased ductility of the material as temperature goes up, resulting in lower likelihood of brittle fracture.

2.2 Oxidation Behavior

This section will discuss the oxidation behavior of stainless steel in high temperature water. Section 2.2.1 will cover oxidation kinetics, and section 2.2.2 will discuss oxidation thermodynamics.

2.2.1 Oxide Growth Kinetics

This section will provide background on electronics, diffusion properties, and growth rate laws that govern the oxidation of stainless steel. It will discuss a defect-based treatment of growth kinetics, as well as include oxide growth laws.

In PWR conditions, a duplex oxide forms on stainless steel. An inner oxide is formed by inward migrating oxygen[11], composed primarily of iron-chromium-nickel spinels, (Fe_3O_4, $FeCr_2O_4$, $NiCr_2O_4$, $NiFe_2O_4$). Spinel oxides have a structure consisting of an oxygen lattice with 8 fcc sub-units. Cations occupy 24 of the 96 interstitial octahedral and tetrahedral sites in the unit cell. In a normal spinel structure such as chromite ($FeCr_2O_4$), A^{2+} cations occupy 8 of the 64 tetrahedral sites, and B^{3+} cations occupy 16 of the 32 octahedral sites[31], [32]. In the inverse spinel structure, the B^{3+} cations are evenly split between octahedral and tetrahedral sites, while A^{2+} cations all occupy octahedral sites. A schematic of the spinel unit cell is shown in Figure 2.6.

These oxides are a mixture of n-type and p-type semiconductors[33], but several studies[34]–[36] have found the inner layer on 316L stainless in high temperature water displayed an overall p-type behavior, so the oxide scale will be treated as p-type.

For a p-type oxide, the oxidation reaction at the oxide-metal interface can be expressed in a very general form as shown in Equation 2.3.

$$aM + bO^{2-} + (2b)h^{+} \rightarrow M_aO_b, \tag{2.3}$$

Where *a* and *b* are stoichiometric coefficients, M is a metal atom, O is an oxygen ion, and h is an electron hole. This same reaction can also be described in a more point-defect-centric form, as shown by Kieffer[37], Kofstad[38], and Macdonald[39], who describe a reaction at the metal-oxide interface, given in Equation 2.4.

$$\ddot{V}_M + 2h + M \leftrightarrow M_M \tag{2.4}$$

Where $\ddot{V}_M$ is a cation vacancy, h is an electron hole, M is a metal atom, and M_M is a metal atom in a cation site. Accompanying reduction reactions at the oxide-solution interface have

been described by Kieffer[37], Macdonald[39], and Birks & Meier[40] as shown in Equation 2.5.

$$\frac{1}{2}O_2(g) \leftrightarrow O_O + \ddot{V}_M + 2h \qquad (2.5)$$

Where O_2 is dissolved oxygen, O_O is oxygen in an anion site, $\ddot{V}_M$ is a cation vacancy, and h is an electron hole.

According to Wagner's model for metal oxidation, the inward movement of electron holes must be charge-balanced by the outward motion of cations, which is the limiting factor due to their slower rate of transport[41]. The result of this reaction will be a charge buildup at the interface, and a resulting potential across the oxide layer.

The outer layer is formed by the precipitation of metal cations from solution that have been transported through the inner layer[12], [35], [42]. Cations travel through the spinel lattice along fast diffusion paths and by occupying interstitial sites [32][43]. Iron diffuses much faster through spinel oxides than nickel, which in-turn diffuses much faster than does chromium. In addition, iron has a significantly higher solubility in water, leading to preferential dissolution of iron[12]. Due to these phenomena, the outer oxide is composed primarily of Fe spinels (Fe_3O_4) with some Ni content.

A simplified schematic is shown in Figure 2.7. The growth of the oxide film on stainless steel ideally follows a parabolic rate law, given in Equation 2.6.

$$x^2 = kt \qquad (2.6)$$

Where $x = \text{oxidation depth}, t = \text{time}, \text{and } k = \text{rate law constant}$. Robertson reports a rate constant of ~10^{-16} cm^2/s for 304 stainless steel at 320˚C [11]. Real-world experiments rarely exhibit ideal behavior, so to reflect this reality, Equation 2.6 can be changed to Equation 2.7

$$x^n = kt \tag{2.7}$$

Where n is an empirically-determined rate law exponent.

With the recognition that k is governed by diffusion, the rate law can be linked to the diffusion coefficient, which has an Arrhenius dependence, and is given by Equation 2.8.

$$D = D_0 e^{-\frac{E_A}{kT}} \tag{2.8}$$

Where D_0 is a constant representing the maximum diffusion rate at infinite temperature, and E_A is the activation energy (The k in the exponential is the Boltzmann constant, not to be confused with the rate constant k). Substituting *D* in for *k*, and rearranging the equation yields Equation 2.9.

$$x = (D_0 t)^{1/n} \exp\left(-\frac{E_A}{nkT}\right) \tag{2.9}$$

Which gives the oxidation rate as a function of time, diffusion constant, and activation energy. For diffusion of oxygen in magnetite, Crouch and Robertson[13] report

$$D_0 = 1.2 \text{ x } 10^{-6} \frac{cm^2}{s} \text{ and } E_A = 264 \frac{kJ}{mol}$$

For cation diffusion through the oxides, Smith et al. [44] conducted tracer diffusion experiments on Fe and Cr through the oxides on stainless steel, and the values are reported in Table 2.3. The measured diffusion coefficients and activation energies can also be used with Equation 2.9 to determine the rate of diffusion through the oxides on stainless steel. Diffusion of

cation species through a range of Fe-Cr spinel oxides at different stoichiometries were compiled by Topfer et al., and are shown in Table 2.4

Reliable data on Ni diffusion in spinel oxides is limited (more data exists for Ni transport in NiO, but that is not relevant to this work). Therefore, the discussion of cation transport will be limited to Fe and Cr.

It has been noted in several works that the bulk diffusion coefficients are not sufficient to account for the rate of oxide growth that has been measured experimentally on the poly-crystalline oxides on stainless steel [11], [13], [45]. To account for the discrepancy, it is usually suggested that diffusion is controlled by diffusion along fast diffusion paths such as grain boundaries and dislocations. Sample dislocation density has been shown to affect the rate of corrosion[14], [15], and several experiments have observed via APT and TEM, enhanced oxidation along fast diffusion paths [15], [46], [47].

2.2.2 Oxidation Thermodynamics

This section will discuss oxidation thermodynamics, including oxide phase stability, and cation mixing in the inner oxides.

2.2.2.1 Oxide Stability

Critical to the discussion of stainless steel oxidation is the stability of oxide species that form in high temperature water. Oxide stability is clearly shown with the use of Pourbaix diagrams, which show the stability of species as a function of ECP and pH. While Pourbaix

diagrams disregard the kinetics of oxide formation, they provide valuable information on the thermodynamic stability of species.

Relevant to stainless steel are Pourbaix diagrams of the Fe-Cr-Ni ternary system. Diagrams of iron, chromium, and nickel species in the ternary system at 300˚C by Beverskog and Puigdemenech[48] are shown in Figure 2.8, Figure 2.9, and Figure 2.10 respectively. Cubicciotti has also published Pourbaix diagrams of the Fe-Cr-Ni ternary system[49], which are generally in good agreement with Beverskog and Puigdemenech.

In PWR water, a typical potential for stainless steel is around -500 to -600 mV_{SHE}, with a pH just under 6. Figure 2.8 and Figure 2.9 indicate that in these conditions $FeCr_2O_4$ and $NiFe_2O_4$ are the dominant oxides. This is in good agreement with experimental observations which typically find a solid solution of Fe-Cr-Ni spinel oxides[35], [50]–[53]. NiO, which should be stable in PWR conditions as indicated by Figure 2.10, was not found in any of these studies, which found $NiFe_2O_4$ to be the dominant form of Ni.

It is notable that Cr_2O_3, the oxide responsible for passivity in room-temperature air, is not stable in PWR conditions. This finding is backed up by experimental results, including early work by Robertson [54] and Stellwag[12], as well as computationally by Ziemniak et al.[55]. It is generally believed that the unstable Cr_2O_3 molecules immediately join with a Fe-O group to form $FeCr_2O_4$.

While the ternary system is most useful for considering the inner oxide, this is not the case for examining the outer oxide. It is important to note that iron diffuses much faster through the oxide than does nickel or chromium[32], so it is reasonable to use a Pourbaix diagram for Fe

only. It can be seen in Figure 2.11 that the dominant outer oxide species in PWR water should be Fe_3O_4 which is consistent with observations[11], [12]

2.2.2.2 Thermodynamics of Fe-Cr spinel mixing

The cation content of the solid-solution spinel oxides that make up the inner oxide scale are of great importance to the oxidation of stainless steel in high temperature water, and will be discussed in this section. In particular, the balance of iron and chromium spinels in the B^{3+} sites have important implications for the passivity and growth kinetics of the inner oxide film, which is discussed further in section 2.2.2.3.

Spinel oxides on stainless steel can be expressed generally as $A^{2+}B_2^{3+}O_4$ with Fe and Ni occupying the A sites, and Fe and Cr occupying the B sites. For reasons that will become apparent when discussing passivity, there is great interest in the mixing of Fe and Cr in the B^{3+} sites of the spinel oxides, and less interest in the mixing of Fe and Ni in A^{2+} sites[35], [56], [57]. Therefore, the focus of this discussion will be on the behavior of iron and chromium in B^{3+} sites, while the role of nickel-iron mixing in A^{2+} sites will be largely omitted, and referenced when appropriate. With this in-mind, iron chromium spinels will be expressed more simply as $Fe(Fe_{1-x}Cr_x)_2O_4$.

To find the most stable configuration of iron and chromium in the B^{3+} position, the free energy of mixing as a function of Cr in the B spinel site was calculated by Ziemniak and

Castelli[58], and is shown in Figure 2.12. Their work is in good agreement with Kurepin et al. [57] At 600K, the free energy of mixing is negative above x=0.7, therefore the minimum stable configuration is $Fe(Fe_{0.3}Cr_{0.7})_2O_4 = Fe_{1.6}Cr_{1.4}O_4$. This ratio of iron and chromium cations is in good general agreement with experimental data[17], [34], [46], [47].

2.2.3 Passivity

The protectiveness of the oxide that forms on stainless steel is immensely important for determining its corrosion rate. While the Cr_2O_3 film from which stainless steel derives its passivity in air does not form in high temperature water[11], a protective film still forms, and is discussed in this section.

Xu et al. [59] conducted electrochemical measurements on 304 stainless steel, as shown in Figure 2.13, which shows potentiostatic polarization curves for stainless steel in 250˚C water. The primary passive region extends from approximately -500 mV to 200 mV. Above the main passive region there is a second passive region around 200 mV.

The peak in the polarization curve at approximately -300 mV is attributed to the oxidation of magnetite to hematite, and is in good agreement with the magnetite/hematite phase boundary shown in Figure 2.11. The upper bound on the passive region at around 200 mV_{SHE} is in good agreement with the phase stability boundary between $FeCr_2O_4$ and $HCrO_4^-$ shown in Figure 2.9. The second passive region at approximately 600 mV corresponds roughly with the upper bound of the stability region of trevorite ($NiFe_2O_4$)[48].

Sun et al[19] performed similar polarization experiments on 304 stainless steel in 300˚C water at pH between 6.8 and 9.1, and found results that were also in general agreement with the $FeCr_2O_4$ / $HCrO_4^-$ phase boundary. Their results of polarization experiments conducted at 300˚C at varying pH are shown in Figure 2.14.

Both Xu and Sun asserted that $FeCr_2O_4$ spinels are responsible for passivity in stainless steel in high temperature water. Chromium spinels are known to be protective for a number of reasons. As discussed in section 2.2.1, chromium is known to diffuse much slower through the spinel lattice[32] than iron or nickel. Also, comparing the bandgaps of the oxides[60], chromite has a bandgap of 3 eV[61], compared to 0.2 for magnetite[62], indicating that higher chromium content presents a barrier to charge transport across the oxide film. Finally, solubility of the oxide films is known to decrease as chromium content increases[12].

2.3 Radiation Effects

With a discussion of the oxidation of stainless steel in-place, the effect of radiation will be established. There are two major processes by which radiation can affect the oxidation of stainless steel. The first, radiolysis, is the disruption of chemical bonds in water, and is at the root of all chemical effects of radiation in solution. The second process, displacement damage, describes the creation of point defects in the solid, and is at the root of all relevant radiation effects in the solid.

2.3.1 Radiolysis

Radiolysis of water occurs when radiation interacts with water molecules, and disrupts the ionic bonds between the hydrogen and oxygen atoms. This occurs first when incoming radiation ionizes a water molecule to form excited water and an aqueous electron, as shown in Equation 2.10.

$$H_2O \rightarrow H_2O^+ + e^-(aq) \tag{2.10}$$

Once the water molecule is excited, a number of reactions can occur, producing both short-lived and long-lived chemical species. The number of possible reactions is extensive, with some models accounting for over 100 reactions. A summary of the most important reactions with their rate constants at 300˚C compiled by Kanjana et al.[63] using values from Bartels and Elliot[21] is given in Table 2.5. The rate constant k is empirically determined using Equation 2.11.

$$\text{reaction rate} = k * [A]^a[B]^b \tag{2.11}$$

where *A* and *B* are concentrations of reactants, and *a* and *b* are the order of each reactant.

These reactions, which occur in radiolysis tracks, result in several short and long-lived species. Short lived species are defined as species that generally do not escape the radiolysis track, and have lifetimes of less than a tenth of a second. Long lived species are stable in water, but may react with ionic species in water or with solid surfaces. The yields of the most important oxidizing radiolysis products are given in Table 2.6 by Sanguanmith et al. [64]. A more extensive treatment is beyond the scope of this work, but a complete treatment of all the reactions that occur in radiolyzed water with G-values of long and short-lived species is available

in review form from Bartels and Elliot [21]. Table 2.6 does not include O_2, which is another long-lived oxidizing product of radiolysis, because it is produced in small amounts. This assertion agrees with Kanajana and Bartels, who simulated the yields of $H_2, O_2,$ and H_2O_2, and the results are shown in Figure 2.15. The most important observation is that H_2O_2 production exceeds O_2 production by more than an order of magnitude.

The yield of radiolysis products is dependent on a number of factors, including dose, temperature, particle type, and linear energy transfer (LET). Unfortunately, no data exists on the yield of radiolysis products by light ions at high temperature, but some insight can be gained by analyzing modeling data along with experimental results of low LET radiation at high temperature, and high LET radiation at low temperature.

The yield of hydrogen peroxide under proton irradiation was modeled with Monte-Carlo simulations by Meesungnoen et al[65] in 25˚ and 300˚C water, and the results are shown in Figure 2.16. The black solid curve represents the results of the simulation at 25˚C, while the data points represent experimental results taken from other sources to compare to simulated data. Experimental and simulation data at 300˚C is overlaid onto the graph, and is shown in red, as a line and dots for the simulation and experimental results respectively.

Since the H_2O_2 molecules are stable, yield only increases with increased LET. This can be compared to the yield of an unstable particle, like H radicals (uncharged, unstable monatomic hydrogen). Meesungnoen also simulated the yield of H radical, and the results are shown in Figure 2.17 with experimental results from other works for comparison.

The most striking difference in this graph when compared to the graph of H_2O_2 yield is the drop-off in yield at around 10 keV/μm. Meesungnoen asserts that at lower LET, the areas

where H radicals along with other radiolysis products are created (spurs) are distributed inhomogeneously in the target water, determined by the paths of the incoming protons. As LET reaches the critical value, the spurs become close enough that recombination of short lived radiolysis products begins to dominate.

In addition to LET dependence, the yield of radiolysis products is also highly dependent on temperature. Experimental and simulated data from Sanguanmith[64] in Figure 2.18 shows how the yields of the important radiolysis products vary with temperature. While the yields of $OH^{\cdot}, H_2,$ and $H^{\cdot}$ increase with temperature, the yield of solvated electrons and H_2O_2 decrease with temperature.

2.3.2 Displacement Damage

At their root, the effects of radiation on a solid come from the collision of incoming particles with lattice atoms, creating two kinds of point defects: vacancies and interstitials. Enhanced diffusion due to the presence of radiation-created point defects may result in an increase in the corrosion rate[8], [10], [66], since corrosion in stainless steel is highly dependent on both the rate of cation and oxygen diffusion through the oxide[11]–[13].

To examine the effect of radiation on diffusion of species, Equation 2.8 be modified to include a point defect concentration term, shown in Equation 2.12.

$$D_{rad} = D_{0_{rad}} e^{-\frac{Q}{kT}} * C \tag{2.12}$$

Where $D_{0_{rad}}$ is the radiation-adjusted pre-factor, and C is the concentration of point defects. C is given as the dimensionless fraction $\frac{defects}{atom}$.

To show how radiation affects diffusion, the point defect concentration under the dose rate used in this work will be calculated and compared to the thermal point defect concentration to see the large effect of radiation on diffusion.

C is dependent upon dose rate. Assuming low temperature and low sink density, the steady-state defect concentration can be written as shown in Equations 2.13[67].

$$C_v = \left(\frac{K_0 K_{is}}{K_{iv} K_{vs}}\right)^{\frac{1}{2}} \tag{2.13a}$$

$$C_i = \left(\frac{K_0 K_{vs}}{K_{iv} K_{is}}\right)^{\frac{1}{2}} \tag{2.13b}$$

K_0 = defect production rate
K_{iv} = recombination rate coefficient
K_{vs} = vacancy-sink reaction rate coefficient
K_{is} = interstitial-sink reaction rate coefficient

$K_{iv,}$ $K_{vs,\ and,}$ K_{is} are solved with Equations 2.14

$$K_{iv} = 4\pi r_{iv} D_i \tag{2.14a}$$

$$K_{is} = 4\pi r_{is} D_i \tag{2.14b}$$

$$K_{vs} = 4\pi r_{vs} D_v \tag{2.14c}$$

The interstitial self-diffusion coefficients are given by Equations 2.15

$$D_i = \alpha a^2 \upsilon \exp(\frac{-E_f^i}{kT}) \quad (2.15a)$$

$$D_v = \alpha a^2 \upsilon \exp(\frac{-E_f^v}{kT}) \quad (2.15b)$$

For stainless steel, use

$$\alpha = \frac{1}{2}$$

$$a = 0.35 \text{ nm}$$

$$E_m^v = -0.8$$

$$E_m^i = -0.12$$

$$r = 0.4\text{nm}$$

(Values are from Ref. [67], except *a* which is the lattice parameter)

Producing

$$D_v = 6.125 \text{ x } 10^{13} \frac{\text{nm}^2}{\text{s}} * \exp\left(\frac{-0.8 \text{ eV}}{8.617 * 10^{-5} \frac{\text{eV}}{\text{K}} * 593 \text{ K}}\right) = 9.7 \text{ x } 10^6 \frac{\text{nm}^2}{\text{s}}$$

$$D_i = 6.125 \text{ x } 10^{13} \frac{\text{nm}^2}{\text{s}} * \exp\left(\frac{-0.12 \text{ eV}}{8.617 * 10^{-5} \frac{\text{eV}}{\text{K}} * 593 \text{ K}}\right) = 1.505 \text{ x } 10^{12} \frac{\text{nm}^2}{\text{s}}$$

$$K_{iv} = 2.9\,x10^{-7}\ \frac{cm^3}{s}$$

$$K_{is} = 2.9\,x10^{-7}\ \frac{cm^3}{s}$$

$$K_{is} = 4.9\,x10^{-13}\ \frac{cm^3}{s}$$

Now, with a damage rate $K_0 = 7\,x\,10^{-6}\frac{dpa}{s} * 8.5 * 10^{22}\frac{atoms}{cm^3}$

Equations 2.13 produce

$$C_v^{rad} = 1.1 * 10^{15}\ \text{vacancies per cm}^3 = 1.3\,x\,10^{-8}\ \text{vacancies per atom}$$

$$C_i^{rad} = 1.8 * 10^{9}\ \text{interstitials per cm}^3 = 2.2\,x\,10^{-14}\ \text{interstitials per atom}$$

This is the irradiation-produced point defect concentration.

Now, the concentration of thermal defects can be found with Equations 2.16[67]

$$C_v = \exp\left(\frac{S_f^v}{k}\right)\exp\left(-\frac{E_f^v}{kT}\right) \quad (2.16a)$$

$$C_i = \exp\left(\frac{S_f^i}{k}\right)\exp\left(-\frac{E_f^i}{kT}\right) \quad (2.16b)$$

For stainless steel, these values can be calculated roughly using values taken from modeling work by Dogo[68].

$$E_f^v = 2\ eV$$

$$E_f^i = 4\ eV$$

$$S_f^v = 2\ k$$

$$S_f^i = 0$$

$$C_v = \exp\left(\frac{S_f^v}{k}\right)\exp\left(-\frac{E_f^v}{kT}\right) = 1.4 \times 10^{-18}\ per\ atom$$

$$C_i = \exp\left(\frac{S_f^i}{k}\right)\exp\left(-\frac{E_f^i}{kT}\right) = 1.0 \times 10^{-34}\ per\ atom$$

So, the point defect concentration under irradiation is about ten orders of magnitude higher than the thermal point defect concentration. This translates to a ten order of magnitude increase in the diffusion coefficient under irradiation.

The effect of radiation enhanced diffusion was demonstrated in iron by Lapuerta et al.[4]. Iron samples were irradiated in moist air, and exposed to proton irradiation at currents of 5 nA, 10 nA, and 20 nA, corresponding to damage rates of 1.6×10^{-8}, 3.2×10^{-8}, and 6.4×10^{-8} dpa/s respectively. The results are shown in Figure 2.19. The greater oxygen penetration at higher currents shows that increased proton current results in a greater rate of oxidation.

2.3.3 Electronic effects

The electronic effects of radiation are often overlooked. Their effect on corrosion has only been theorized, as no experiment has successfully isolated electronic effects from radiation from the other factors that play a role in corrosion. The production of excitons and the effect of photoluminescence will be discussed in this section.

2.3.3.1 Exciton Production

A proper discussion should begin with some background on the nature of excitons. An exciton is not a "particle" as much as it is a "state". An exciton is a state that occurs when an atom absorbs a photon, causing one of its valence electrons to move to its conduction band. This excitation leaves a hole on the valence band formerly occupied by the electron. There is no net change in charge, and only a small change in energy, related to the exciton binding energy. Since excitons require a bandgap, it's clear that they do not exist in metals like stainless steel. The oxide films that form on stainless steel, however, are semiconductors that can produce excitons. For simplicity, this section will discuss simple, single-cation oxides (Fe_2O_3, Cr_2O_3, NiO) instead of the more complex spinel oxides that make up the oxide scale on stainless steel. This approach is still valid, as the bandgaps in the more complex oxides are similar to their simpler constituents.

Chromia has a bandgap of 3.4 eV [69]. This is nicely observed using electron energy loss spectroscopy, as shown by Fukuda et al[70] in Figure 2.20. The bandgap is indicated by E_b, and there is another energy loss peak at 1.6 eV below the conduction band.

The extra peak represents electron energy loss due to core excitons. The binding energy represents a decrease in the electron energy due to the extra coulombic attraction between the excited electron and the vacated hole in the valence band. Excitons that occur on the surface of materials (surface excitons) also behave differently than excitons in the bulk material. Most notably, the absorption energy of surface excitons is lower than those in the bulk[71]. EELS measurements of MgO have confirmed this, showing an absorption peak attributable to excitons at 7.7eV in the bulk, while the peak shifts to 6.15 eV when examining surface sites [72].

With an understanding of how excitons are formed, a discussion of how they may affect corrosion can begin. The use of the term "may" is deliberate, as there is no direct evidence that excitons contribute to corrosion at all. LaVerne et al.[73]–[75] have conducted radiolysis studies in which hydrogen production was greater than the amount that would be produced by disassociation alone. Exciton production was the hypothesized cause of the excess.

For exciton production and its effect on H_2 production, LaVerne suggested the reactions given in Equations 2.17.[75]

$$\text{exciton} + 2\text{Zr} - \text{OH} \rightarrow \text{H}_2 + 2\text{Zr} - \text{O}^* \quad (2.17a)$$

$$\text{exciton} + 2\text{Zr} - \text{OH} - \text{Zr} \rightarrow \text{H}_2 + 2\text{Zr} - \text{O}^* - \text{Zr} \quad (2.17b)$$

$$\text{exciton} + \text{Zr} - \text{H}_2\text{O} \rightarrow \text{H}_2 + \text{Zr} - \text{O}^* \quad (2.17c)$$

The first two reactions show excitons interacting with chemisorbed OH groups. The first is a free OH group, while the second shows a bridged group. The third reaction shows an exciton interacting with an adsorbed water molecule.

Equation 2.17 occur on the surface of zirconium oxide in water. While excitons can occur on all semi-conducting oxides, not all have shown a tendency to contribute to hydrogen production. Petrik et al.[76] conducted experiments on several oxides in which hydrogen yield due to excitons and radiolysis was compared to the yield from radiolysis alone. The oxides were classified into three groups: Oxides in which electronic excitation reduced the amount of H_2 produced (group1), oxides in which there was little effect (group 2), and oxides in which the H_2 yield increased significantly (group3).

Figure 2.21 shows the measured H_2 yield of various oxides in water as a function of bandgap energy. The three groups are shown with different symbols. Samples were irradiated at 315 K with 1.25 MeV gamma rays at a dose rate of 1.8 Gy/s. Total dose ranged from 0.1 to 1.5 MGy.

The most obvious feature is the peak between 4 eV and 6 eV. All of the group 3 oxides, which showed significant increases in hydrogen production due to electronic excitement, reside in this range. The group 1 oxides all reside near the left of the graph, and the group 2 oxides are scattered across the range.

The maximum around 5 eV corresponds to the H-OH bond energy in the water molecule which is 5.1 eV. This correspondence suggests a resonant mechanism in which the energy spectrum of the exciton in the oxide overlaps the bond energy of the adsorbed molecule, enabling a transfer to the conduction band of the acceptor molecule. ZrO_2 is noted because it received special focus in this study. Other literature shows a distinct focus on ZrO_2 in exciton studies, which is natural since it is a material that is found in nuclear reactors that displays the effect strongly.

2.3.3.2 Photoluminescence

Photon illumination has been shown to affect corrosion of some metals. Breslin et al. observed the effect in stainless steel[77], but it is illustrative to first discuss results on the copper alloy CA-715 (70% copper, 30% nickel)[78]. The values are unimportant in the study of stainless steel, but Breslin's results are much clearer in his work on CA-715.

Figure 2.22 depicts polarization plots for CA-715 in buffered NaCl solution. A polarization curve of the non-illuminated surface is shown with curves illuminated at three different wavelengths.

Current is greatly reduced under illumination. Increasing the energy of the incident photons further reduced the current. Also notable is the increase in breakdown potential under illumination. A sharp rise in current indicating breakdown occurs at higher potentials in the illuminated cases compared to the non-illuminated case, and this breakdown potential increases with increasing frequency. Similar results with stainless steel are shown in Figure 2.23. A significant shift up in the breakdown potential is observed in the illuminated case, resulting in higher breakdown potential and a lower corrosion current.

Illumination has also been shown to affect pitting of stainless steel. Figure 2.24 shows pitting cumulative probability plotted against pitting potential. A noticeable decrease in the pitting probability for a given potential is observed in the illuminated case. Breslin suggests that the corrosion-lowering effect is seen when incident photons exceed the bandgap of the target material.

Figure 2.25 shows the change in breakdown potential as a function of photon wavelength in 304 and 316 stainless. The decrease in ΔE_b is not clear-cut, possibly due to the mixed-oxide surface of the materials. The range over which they decrease, between 330 and 440 nm (3.8-2.8 eV), encompasses the bandgaps of chromium-oxide and nickel-oxide. It seems possible that as more photons are absorbed and used to create electron-hole pairs, they do not contribute to the photo-inhibition of corrosion.

Although these findings are interesting, there is no experimental evidence linking photoillumination to enhanced corrosion in LWR conditions. Further, the effect has only been shown using photons, and gamma irradiation is not being used in this study. For these reasons, photoillumination will not be considered in the present work.

2.4 Irradiation-Corrosion

Now that corrosion and radiation have been discussed separately, it is appropriate to provide background on the topic of this thesis, the intersection of irradiation and corrosion. Since Zircaloy cladding receives a relatively high radiation dose, it is unsurprising that more early work has been done on IAC of Zircaloy rather than on stainless steel. For this reason, this section will begin by presenting work on irradiation accelerated corrosion of Zircaloy, with the concession that it is limited in applicability to this work. Following the discussion of Zircaloy, IAC of stainless steel will be discussed.

2.4.1 Irradiation-Corrosion of Zircaloy

Early work by Asher et al. studied the effect of radiation on the corrosion and hydrogen pickup of zirconium alloys[6]. Zircaloy-2 and Zr - 2.5 wt% Nb were corroded in an air and CO_2 mixture, and the results are shown in Figure 2.26.

There is a very noticeable effect on Zircaloy-2. The in-reactor weight-gains at 300˚C are much higher than the out-of-reactor experiments. The addition of radiation pushes the weight gain rate to around what one would expect at 340˚C out-of-reactor. The effect on Zr-2.5wt% Nb seems to vary depending on the metallurgical condition of the sample, with the most dramatic change shown by alloy ZNC.

Bradhurst et al. [8] performed experiments on Zircaloy-2 both in-reactor and out with varying oxygen overpressures. While it is logical to assume that increasing dissolved oxygen in water would increase its oxidizing potential, and Bradhurst found this, radiation also affected the oxidation of Zircaloy. As shown in Figure 2.27, out-of-reactor weight gain increase with increasing hydrogen overpressure, but in-reactor weight gain increases by much more.

To explore this result further, Bradhurst et al. pre-oxidized samples of zirconium alloys under irradiation at both low oxygen overpressure and high oxygen overpressure, and then further oxidized both samples in-reactor at high oxygen overpressure. The results are shown in Figure 2.28.

There is a large difference in weight gain between the samples pre-oxidized at .0004 atm and the samples pre-oxidized at 27 atm. Bradhurst et al. explained this difference by examining the oxide layers formed under the different conditions. They found that the oxide produced in-reactor with high amounts of dissolved oxygen was more porous than the oxide formed under de-oxygenated conditions.

Lanning et al. [79] also examined the effect of radiation on zirconium, this time in graphite-moderated reactor pressure tubes. Lanning found an increase in the oxidation rate under irradiation, at different temperatures. The results are shown in Figure 2.29.

An interesting aspect of the Lanning data is the noticeable difference between the thick-film growth rate and the thin-film grown rate, which Lanning attributes to the penetration of hydrogen from radiolysis. He postulates that the reducing hydrogen radicals no longer penetrate the oxide at the transition depth, thus less oxidizing species are scavenged and are free to form oxide with the bulk metal at a greater rate.

In 1991, Almarshad and Klein attempted to model the oxidation of zirconium in a PWR environment[7]. To account for accelerated oxidation due to neutron irradiation, they used an enhancement factor developed by Pyecha, given in Equation 2.18.

$$\frac{x'}{x} = 1 + 3.2214(7.46 * 10^{15} * \phi)^{0.23} \quad (2.18)$$

Equation 2.18 is an empirical relation that shows the ratio of in-reactor oxidation to out-of-reactor oxidation as a function of flux. Figure 2.30 shows the results of the enhancement factor on the model.

Almarshad and Klein make little attempt to explain the reasons for the enhancement aside from a short mention of possible modification of the oxide structure due to radiation damage and radiolysis of the primary water. An interesting note, though, in their section on the effect of lithiated water, was their discussion of a report by Hillner and Chirigos[80] which found that lithiated water increased corrosion of zirconium. The proposed mechanism was an increase in anion vacancies caused by the substitution of lithium for zirconium in the oxide causing a decrease in local charge. The increase in oxygen mobility caused by this effect is consistent with earlier work showing inward oxygen diffusion is the primary driver of aqueous corrosion of zirconium[81]. This was the only mention of the effect of point defect creation on the oxidation

rate in the paper. The possibility of increased oxide porosity as proposed by Billot et al. was also mentioned[82], which was also observed by Wang et al. much later [83].

2.4.2 Irradiation-Corrosion of Stainless Steel

While the experiments on Zircaloy provide valuable background, experiments on stainless steel, while more limited in number, provide more relevant information. This section will discuss some important work on the effects of irradiation on corrosion on stainless steel.

Early work on the effect of radiolyzed water on stainless steel corrosion was performed at the University of Tokyo in the early 1980s using a flowing water system and a Co-60 source. Kawaguchi et al. [5] found a significant increase in oxide thickness under gamma irradiation, as shown in Table 2.7. Since a Co-60 source was used for the experiment, displacement damage is not a factor in the measurements.

The most compelling data is at the 100 mL/min flow rate, where irradiated and unirradiated samples were exposed for similar lengths of time, and the irradiated samples show an oxide layer 2-6 times as thick as the unirradiated samples.

Later work by Ishigure et al.[84] explored the release of crud from 304 stainless steel under irradiation from a Co-60 source. Crud is the term for metallic oxide particles that tend to form in nuclear reactor coolant water, and deposit on core internals, especially on fuel rods. Crud typically takes the form of M_2O_3 or M_3O_4 oxides, with Fe, Ni, and Co commonly occupying

cation sites. Crud tends to precipitate from solution, and does not form on surfaces, so it is highly dependent on the solubility of metallic species in water. Despite differences, the study of crud formation does provide compelling insights into oxide stability, and thus into the processes that govern corrosion under irradiation.

Ishigure found that irradiation caused a large increase in crud throughout the experiment, and a decrease in aqueous Fe ions, as shown in Figure 2.31. This work and a review paper also by Ishigure [85] explored the reason for the lower concentration of aqueous metallic ions. Ishigure proposed the following set of reactions (Equations 2.19) which describe crud formation under irradiation.

$$\mathrm{Fe(s)} + \tfrac{1}{2}\mathrm{O_2(g)} + 2\mathrm{H^+(aq)} \rightarrow \mathrm{Fe^{2+}(aq)} + \mathrm{H_2O(l)} \quad (2.19a)$$

$$2\mathrm{Fe^{2+}} + 2\mathrm{H^+} + \tfrac{1}{2}\mathrm{O_2} \rightarrow 2\mathrm{Fe^{3+}} + \mathrm{H_2O} \quad (2.19b)$$

$$\mathrm{Fe^{2+}} + \mathrm{OH} \rightarrow \mathrm{Fe^{3+}} + \mathrm{OH^-} \quad (2.19c)$$

$$\mathrm{Fe^{3+}} + \mathrm{OH(l)} \rightarrow \mathrm{Fe(OH)_3(s)} + 3\mathrm{H^+(aq)} \quad (2.19d)$$

$$2\mathrm{Fe(OH)_3(s)} \rightarrow \mathrm{Fe_2O_3(s)} + 3\mathrm{H_2O} \quad (2.19e)$$

Since radiolysis increases the concentration of oxidizing species such as OH, O_2 and H_2O_2, Ishigure proposed that aqueous Fe ions more readily form ferric hydroxides and hematite, which are insoluble, and thus tend to precipitate as crud, accounting for the decrease in aqueous ions and the increase in crud under irradiation.

Moving on to later work, Lewis and Hunn [3] investigated the effect of proton irradiation on the aqueous corrosion of stainless steel in 1998. Their experimental setup is shown in Figure 2.32 and the irradiation conditions are described in Table 2.8. They used a 10-12 μm thick

stainless steel foil sample, through which protons passed into standing water. An RGA system was employed to collect gasses produced by water radiolysis. The temperature was measured to be 80˚C at the water-steel interface. The collected data from the RGA is shown in Figure 2.33

The figure shows the experiment that used D_2O produced D_2 and the experiment containing $H_2{}^{18}O$ produced heavy O_2. Gas bubbles at the water-foil interface were observed during the experiment, which grew to as large as a few millimeters in diameter after 2 minutes. The production of bubbles continued though the length of the experiment. The oxide layer produced under irradiation was observed to be 100 atomic layers (estimated to be ~40 nm in Table 2.8). An oxide grown under similar conditions with no irradiation was found to be 20 atomic layers, while a room temperature oxide with no irradiation was approximately 5 atomic layers.

The Lewis and Hunn experiment was intended to be a proof-of-concept experiment, and it certainly succeeded at its goal. Their core idea of irradiating through a thin sample with protons stopping in water on the other side has been used in several later experiments, and has become somewhat of a standard in studying the effect of irradiation on corrosion. That said, their experiment is short on data, and only brief attempts are made to show quantitative results.

2.4.2.1 Radiolysis and ECP

The effect of radiolysis on corrosion potential was explored by Andresen [86], who found increases in corrosion potential under proton and gamma irradiation. Figure 2.34 shows corrosion potential measurements taken on 304 SS and Pt in 288˚C water, with varied DO

content and different types of irradiation. Data points that were taken in the same conditions both with and without irradiation are connected by vertical lines.

The data on proton irradiation is most relevant. Unlike the Lewis and Hunn experiment, protons were not transmitted through the sample, and instead were stopped in water very near the sample. At the far left of the graph where DO is suppressed by hydrogen addition (DO < 1 ppb), the effect of proton irradiation on the corrosion potential is small. At a slightly elevated DO level (~1.2 ppb) in deaerated water without hydrogen addition, proton irradiation was observed to increase ECP by ~250 mV. The dose rate for this experiment was 4.7 kGy/s (1700 Mrad/hr), which was chosen to reflect the peak neutron dose in a BWR core. Proton irradiation measurements taken at higher DO levels between 30 and 300 ppb show smaller ECP increases under irradiation, while a measurement at 2000 ppb DO shows a very small increase in in ECP.

The very small increase in ECP in hydrogenated water is likely due to the rapid reduction of radiolysis products by the hydrogen in the water. When the hydrogen is removed, but DO is still relatively low, the oxidizing radiolysis products are instead reduced on the stainless steel (or oxide) surface, causing an increase in corrosion potential, and oxidizing the metal. At higher DO concentrations, the stoichiometric significance of radiolysis-produced oxidizing species becomes smaller compared to the concentration of oxidizers already in the water, so the effect of radiolysis becomes smaller. At very high DO levels, it is likely that the surface sites on the stainless steel and platinum become saturated, so the addition on radiolysis products does not affect the ECP.

The effect of gamma irradiation is less pronounced, and less clear. The gamma irradiation under different conditions produces both increases and decreases in ECP with no clear trends.

The gamma and proton irradiation data from Figure 2.34 is more easily shown on Figure 2.35. While the trend in the proton data is clear, gamma irradiation data produces a less clear trend. ECP tends to increase under gamma irradiation at very low DO, tends to decrease under irradiation at ~20 ppb, and then increases again above 200 ppb. The addition of 200 ppb of hydrogen peroxide seems to suppress the effect of gamma irradiation.

The reasons for these trends are unclear. It is notable that gamma doses are several orders of magnitude lower than proton doses (0.3-200 MRad/h gamma dose compared to 1700 Mrad/h used for BWR peak proton irradiations). In addition, the LET of gamma irradiation is several orders of magnitude lower than neutron and proton irradiation, so it is possible that at very low LET, the effect of radiolysis-produced reducing species is more pronounced at some DO levels, although this amounts to speculation. Despite the ambiguity of gamma irradiation data, the findings presented on proton irradiation present a compelling case for the effect of neutron and proton irradiation on ECP.

A major challenge in determining the effect of radiolysis products on corrosion is determining their tendency to adsorb on, and react with metal and oxide surfaces vs. their tendency to react with other species in solution. The oxidizing effects of oxygen and hydrogen peroxide are well studied[16], [18]–[20], [87] in LWR conditions. Since LWRs are mildly acidic environments, oxygen and hydrogen peroxide are reduced at metal sites according to the reaction given in Equation 2.20[88] (note the use of electrons instead of holes, since these reactions involve aqueous species).

$$O_2 + 4H^+ + 4e^- \rightleftarrows 2H_2O \quad (2.20a)$$

$$H_2O_2 + 2H^+ + 2e^- \rightleftarrows 2H_2O \quad (2.20b)$$

with the accompanying oxidation reactions

$$Fe \rightleftarrows Fe^{2+} + 2e^{-} \quad (2.20c)$$

$$Fe^{2+} \rightleftarrows Fe^{3+} + e^{-} \quad (2.20d)$$

To emulate the effect of a potential increase due to radiolysis, Y. J. Kim[20][89] studied the effect of added H_2O_2, O_2 and H_2 on the oxidation of 304 stainless steel in 288˚C water. Figure 2.36 shows the effect of added H_2O_2 and O_2 on the corrosion potential of stainless steel.

This change in ECP can have a profound effect on oxide composition, since it is believed [12] that the abundance of chromium-rich spinels on the inner oxide layer of stainless steel in LWR environments is due in-part to the preferential dissolution of iron over chromium.

Kim points out that at high ECP, solid chromium tends to go into solution as chromate ($2CrO_4^{2-}$), according to Equation 2.21.

$$(Ni, Fe)Cr_2O_4 + \frac{3}{2}O_2 + H_2O \rightarrow (Fe^{2+}, Ni^{2+}) + 2CrO_4^{2-} + 2H^{+} \quad (2.21)$$

This suggests that oxygen or hydrogen peroxide addition lessen the effect of preferential dissolution, and result in a more iron-rich inner oxide layer, which is what Kim observed. Figure 2.37 shows AES profiles for oxidized stainless steel samples in H_2O_2, O_2 and H_2. There is a notable decrease in oxide chromium content in the sample oxidized with hydrogen peroxide compared to the sample oxidized in hydrogen. The sample in oxygen shows a less dramatic drop in oxide Cr content. Also of note, the sample in hydrogen peroxide showed nickel enrichment in the oxide.

The different water chemistries also produced different oxide thicknesses, as shown in Figure 2.38. Although the difference is not dramatic, the oxide grown in low potential conditions (H_2) is thinner than the oxides grown in high potential water.

Table 2.1. Composition of 316L stainless steel, heat 13364044, used in this study

Element	**C**	**Si**	**Mn**	**S**	**P**	**Cr**	**Ni**	**Mo**	**Cu**	**N**	**Co**	**Fe**
Wt %	0.020	0.520	1.34	0.0010	0.0270	16.40	10.11	2.04	0.420	0.020	0.230	bal

Table 2.2. Tensile strength, yield strength, and hardness of 316L stainless steel in various forms[29]

Form	**Condition**	**Tensile Strength (MPa)**	**0.2% Yield Strength (MPa)**	**Hardness (HRB)**
Forging	Annealed	450	170	95
Bar	Hot finished and annealed	480	170	95
Bar	Cold finished and annealed	620	310	95
Bar	Cold finished and annealed	480	170	95
Wire	Annealed	480	170	95
Wire	Cold finished	620	310	95
Plate, Sheet, Strip	Annealed	485	170	95

Table 2.3. Tracer diffusion coefficients of Fe and Cr through the inner and outer oxides of stainless steel measured from 655 to 1000˚C.[44]

Species	Medium	D_0 (cm^2/s)	E_A (kJ/mol)
Fe	Fe_3O_4 (outer oxide)	9 x 10^{-6}	146
Fe	$(Cr, Ni, Fe)_3O_4$ (inner oxide)	8 x 10^{-5}	151
Cr	Fe_3O_4 (outer oxide)	2 x 10^{-7}	121
Cr	$(Cr, Ni, Fe)_3O_4$ (inner oxide)	1.6 x 10^{-6}	130

Table 2.4. Normalized defect formation constants and partial tracer diffusion coefficients for $(Cr_xFe_{1-x})_3O_4$ at 1200˚C[90]

	$x = 0$	$x = 0.1$	$x = 0.2$	$x = 0.33$	$x = 0.4$	$x = 0.5$
$\log [V]^0$	0.699 [5]	0.644	0.649	0.544	0.467	0.487
		±0.003	±0.003	±0.004	±0.005	±0.008
$\log [I]^0$	−8.495 [5]	−9.38	−9.65	−10.50	−10.65	−10.49
		±0.04	±0.02	±0.05	±0.05	±0.05
$\log D^0_{Fe[V]}$	−5.44	−4.94	−5.67	−5.77	−5.31	
	±0.04 [5]	±0.05	±0.03	±0.03	±0.05	
$\log D^0_{Co[V]}$	−5.53	−5.00	−5.81	−5.83	−5.37	
	±0.03 [5]	±0.05	±0.04	±0.06	±0.10	
$\log D^0_{Mn[V]}$	−5.49	−4.68	−5.69	−5.61	−5.18	
	±0.03 [5]	±0.03	±0.03	±0.04	±0.05	
$\log D^0_{Cr[V]}$	−8.06 [4]	−7.71	−8.14	−8.38	−8.41	
		±0.07	±0.10	±0.07	±0.05	
$\log D^0_{Fe[I]}$	−14.00	−14.19	−14.58	−15.56	−15.65	
	±0.03 [5]	±0.04	±0.02	±0.03	±0.01	
$\log D^0_{Co[I]}$	−13.76	−14.05	−14.51	−15.45	−15.68	
	±0.02 [5]	±0.06	±0.04	±0.04	±0.02	
$\log D^0_{Mn[I]}$	−14.03	−14.15	−14.54	−15.57	−15.66	
	±0.03 [5]	±0.04	±0.02	±0.03	±0.02	
$\log D^0_{Cr[I]}$	−16.90 [4]	−17.16	−17.76	−18.50	−18.78	
		±0.06	±0.09	±0.04	±0.07	

Table 2.5. Rate constants 300˚C of important reactions that occur in radiolyzed water. Values are from Bartels and Elliot[21], compiled by Kanjana et al.[63]

Reaction	Rate Constant at 300˚C (L/mol/s for 2nd order, s^{-1} for 1st order)
Non-Reversible Reactions	
$e_{aq}^- + e_{aq}^- + (2H_2O) \rightarrow H_2 + 2OH^-$	6.06E+06
$H + H \rightarrow H_2$	1.04E+11
$OH + OH \rightarrow H_2O_2$	9.87e+09
$e_{aq}^- + H(+H_2O) \rightarrow H_2 + OH^-$	4.97E+11
$e_{aq}^- + OH \rightarrow OH^-$	3.73E+11
$H + OH \rightarrow H_2O$	6.34E+10
$e_{aq}^- + H_2O_2 \rightarrow OH + OH^-$	2.85E+11
$e_{aq}^- + O_2 \rightarrow O_2^-$	2.18E+11
$e_{aq}^- + O_2^-(+H_2O) \rightarrow H_2O_2 + 2OH^-$	1.61E+11
$e_{aq}^- + HO_2 \rightarrow HO_2^-$	1.61E+11
$H + H_2O_2 \rightarrow OH + H_2O$	2.15E+09
$H + O_2 \rightarrow HO_2$	6.06E+10
$H + HO_2 \rightarrow 2OH$	2.14E+11
$H + O_2^- \rightarrow HO_2^-$	2.14E+11
$OH + H_2O_2 \rightarrow HO_2 + H_2O$	4.23E+08
$OH + O_2^- \rightarrow (HO_3^-) \rightarrow O_2 + OH^-$	8.98E+10
$OH + HO_2 \rightarrow (H_2O_3) \rightarrow O_2 + H_2O$	3.20E+10
$HO_2 + HO_2 \rightarrow H_2O_2 + O_2$	4.10E+07
Reversible Reactions	
$H_2O \rightleftharpoons H^+ + OH^-$	Forward: 6.52E-02 Back: 1.13E+12
$H_2O_2 \rightleftharpoons H^+ + HO_2^-$	Forward: 2.52E+01 Back: 5.69E+11
$H_2O_2 + OH^- \rightleftharpoons HO_2^- + H_2O$	Forward: 1.36E+11 Back: 1.76E+08
$OH \rightleftharpoons H^+ + O^-$	Forward: 2.52E+01 Back:5.69E+11
$OH + OH^- \rightleftharpoons O^- + H_2O$	Forward:1.36E+11 Back: 1.76E+08
$HO_2 \rightleftharpoons H^+ + O_2^-$	Forward: 1.55E+05 Back: 5.69E+11
$HO_2 + OH^- \rightleftharpoons H_2O + O_2^-$	Forward: 2.87E+04 Back: 1.36E+11
$H \rightleftharpoons H^+ + e_{aq}^-$	Forward: 1.65E+05 Back: 7.16E+11
$H + OH^- \rightleftharpoons e_{aq}^- + H_2O$	Forward: 8.03E+09 Back: 2.01E+03
$H + H_2O \rightleftharpoons H_2 + OH$	Forward: 2.10E+03 Back:7.80E+08

Table 2.6. Yield of common radiolysis products at 320˚C for low LET radiation [64].

Species	Type	G-Value (# / 100eV)
$OH^{\cdot}$	Radical	4.5
H_2O_2	Stable	0.3
e^-_{aq}	Radical	2.5
$H^{\cdot}$	Radical	1.5
H_2	Stable	0.7

Table 2.7. Oxide layer thickness on 304 stainless steel under Co-60 irradiation in 250˚C water with 20 ppb DO.[5]

Flow rate ml/min	T-Ray irradiation	Testing Time Hr	Thickness of oxide films μm
100	Absent	234	0.03
	"	959	0 20
	"	989	0.09
	Present	939	0 43
		939	0 59
50	Absent	494	0 27
	Present	1491	0 50
21	Absent	245	0 20
	Present	374	0 30
	"	652	0 36
9	Absent	200	0
	Present	660	0 40

Table 2.8. Lewis and Hunn experimental conditions

Temperature (˚C)	Time (h)	Damage (dpa)	Damage Rate (dpa/hr)	Oxide Thickness (nm)	LET in water (MeV)
80	4	0.02-0.04	0.005-0.01	40	1

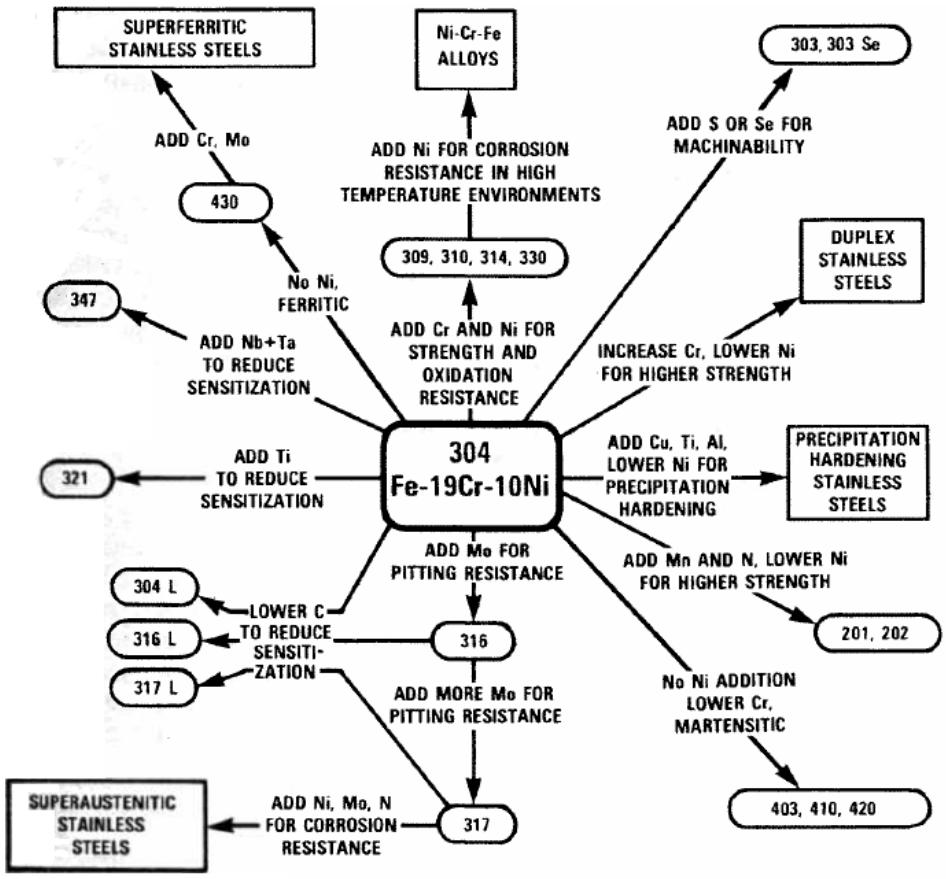

Figure 2.1. Diagram of stainless steels, organized by additions to 304. [25]

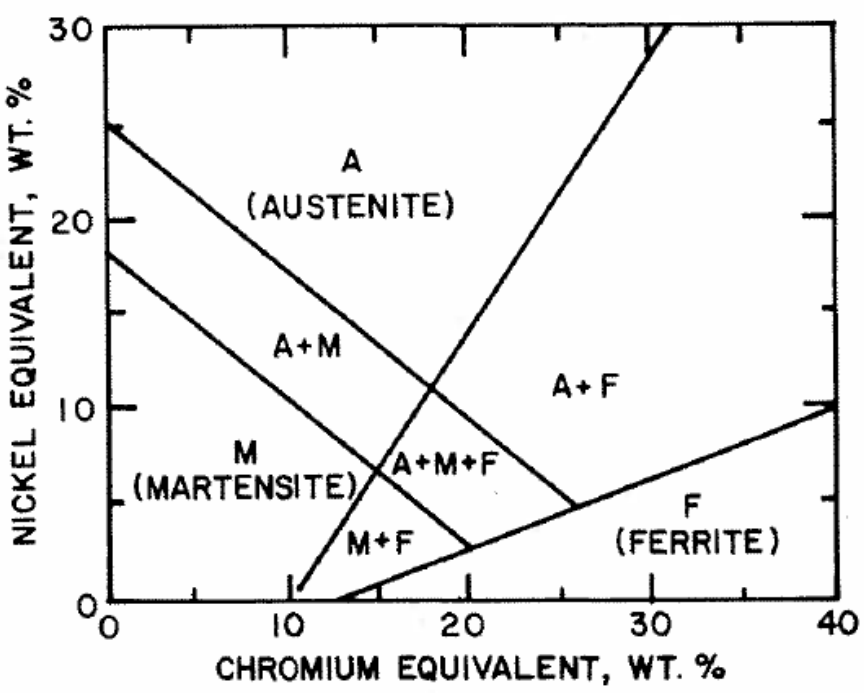

Figure 2.2. Shaeffler Diagram of austenitic stainless steel[25]

Figure 2.3 shows some typical stress-strain curves for 316 stainless. It is apparent that as strain rate is increased from .002 in/min to 2 in/min, the UTS of the alloy increases.

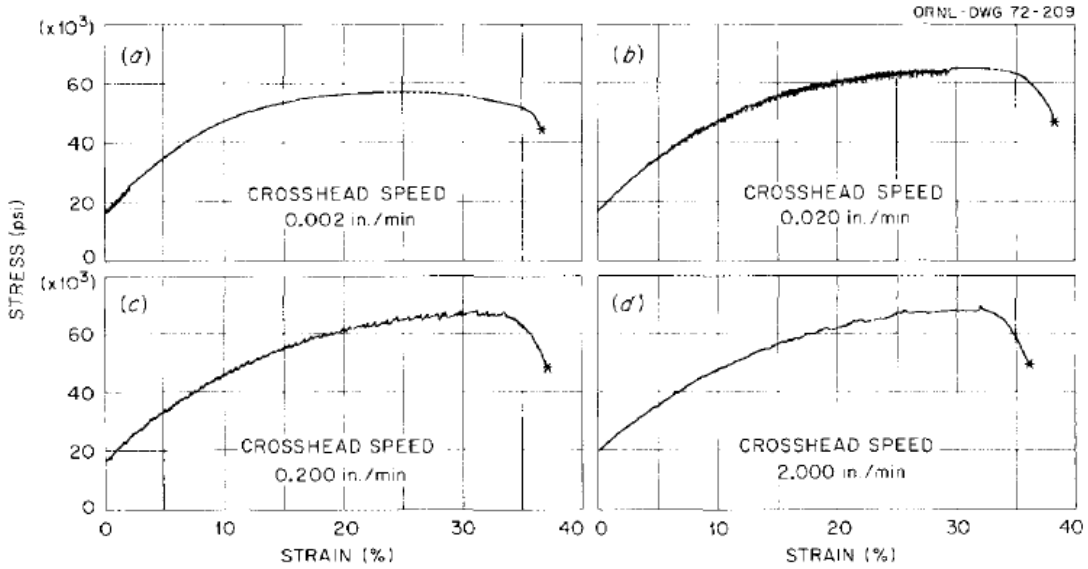

Figure 2.3. Stress-strain curves for 316 stainless at different strain rates[9]

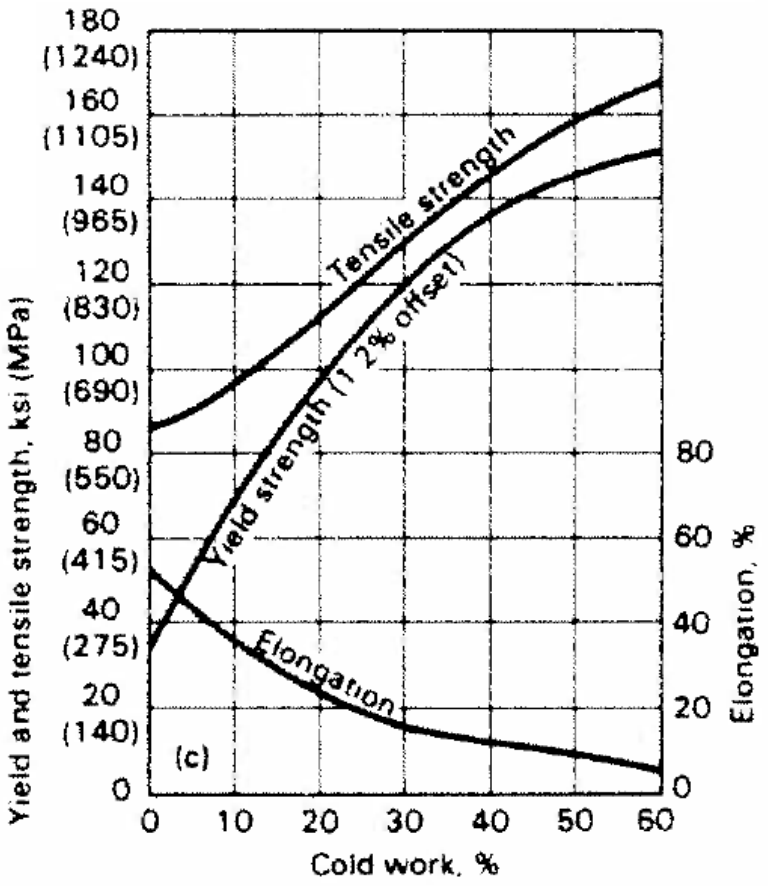

Figure 2.4 Effect of cold work on tensile strength, yield strength, and elongation in 304 stainless steel[29].

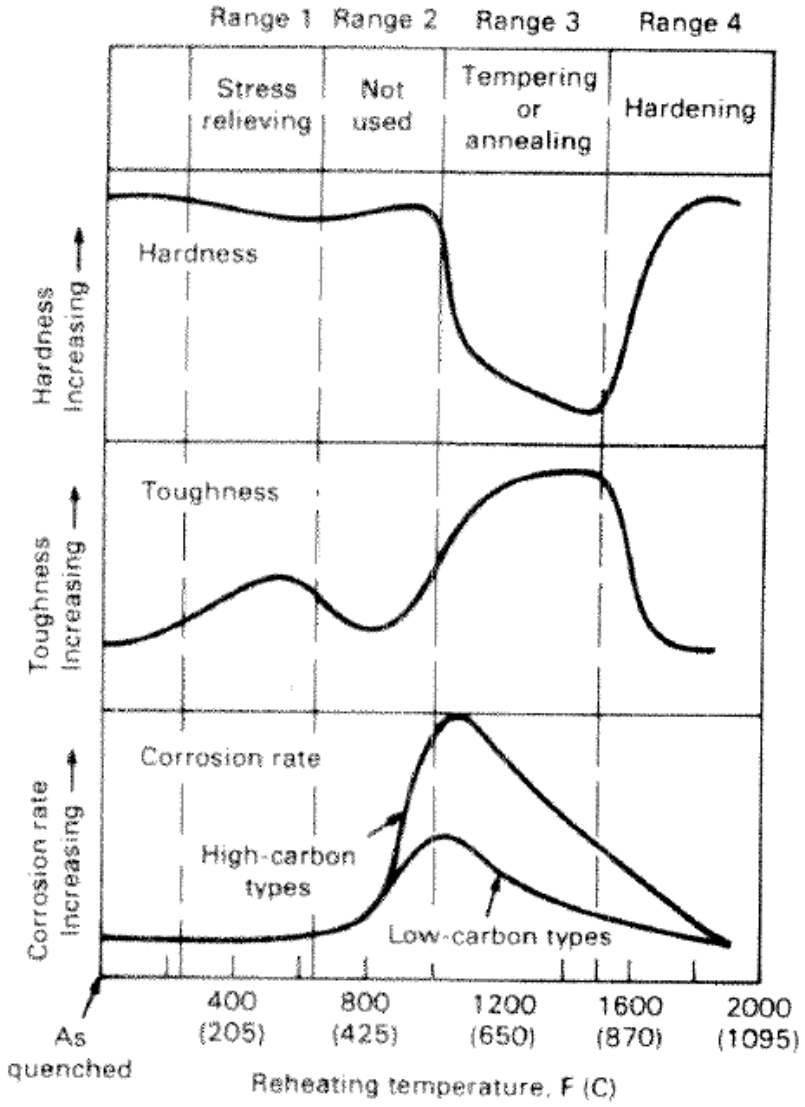

Figure 2.5. Generalized effect of temperature on hardening, toughness, and corrosion of austenitic stainless steel[29].

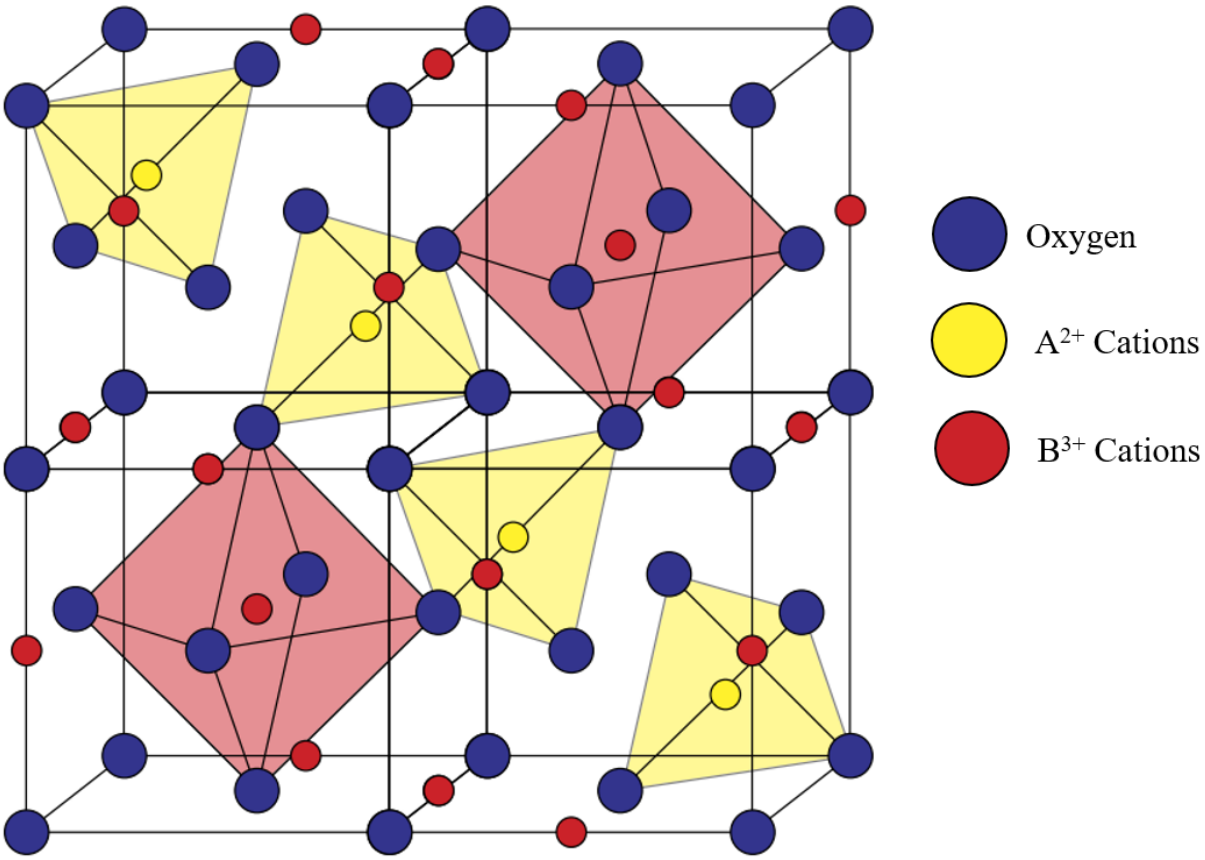

Figure 2.6. Schematic of the spinel unit cell.[91]

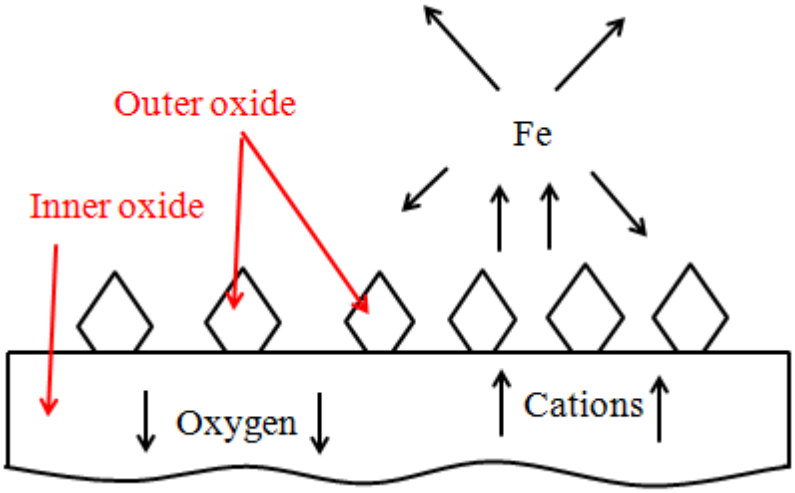

Figure 2.7. Schematic of the oxides on stainless steel

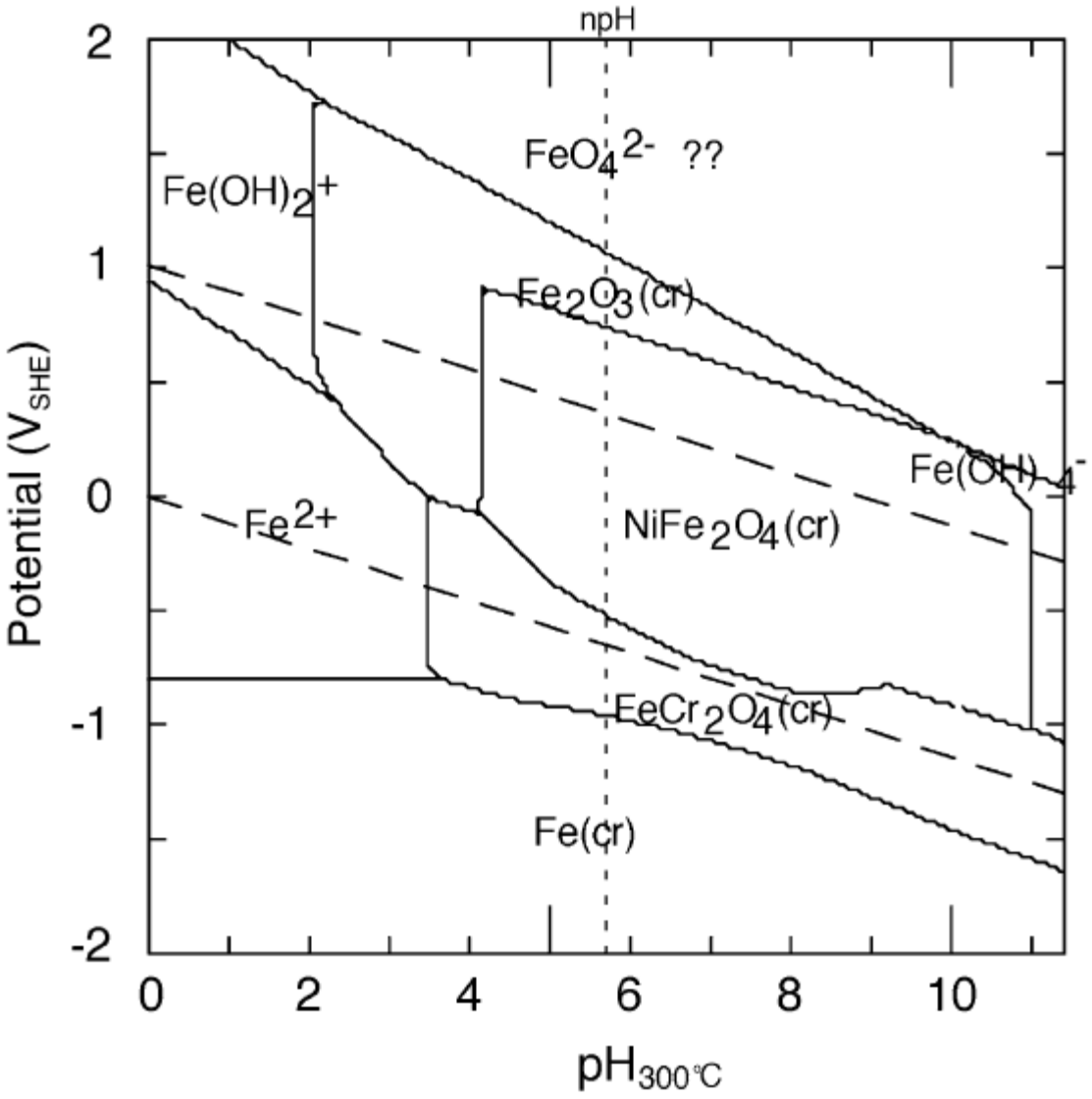

Figure 2.8. Pourbaix diagram of iron species in the Fe-Ni-Cr ternary system at 300˚C with all aqueous species set to an activity of 10^{-6} mol/kg [48]

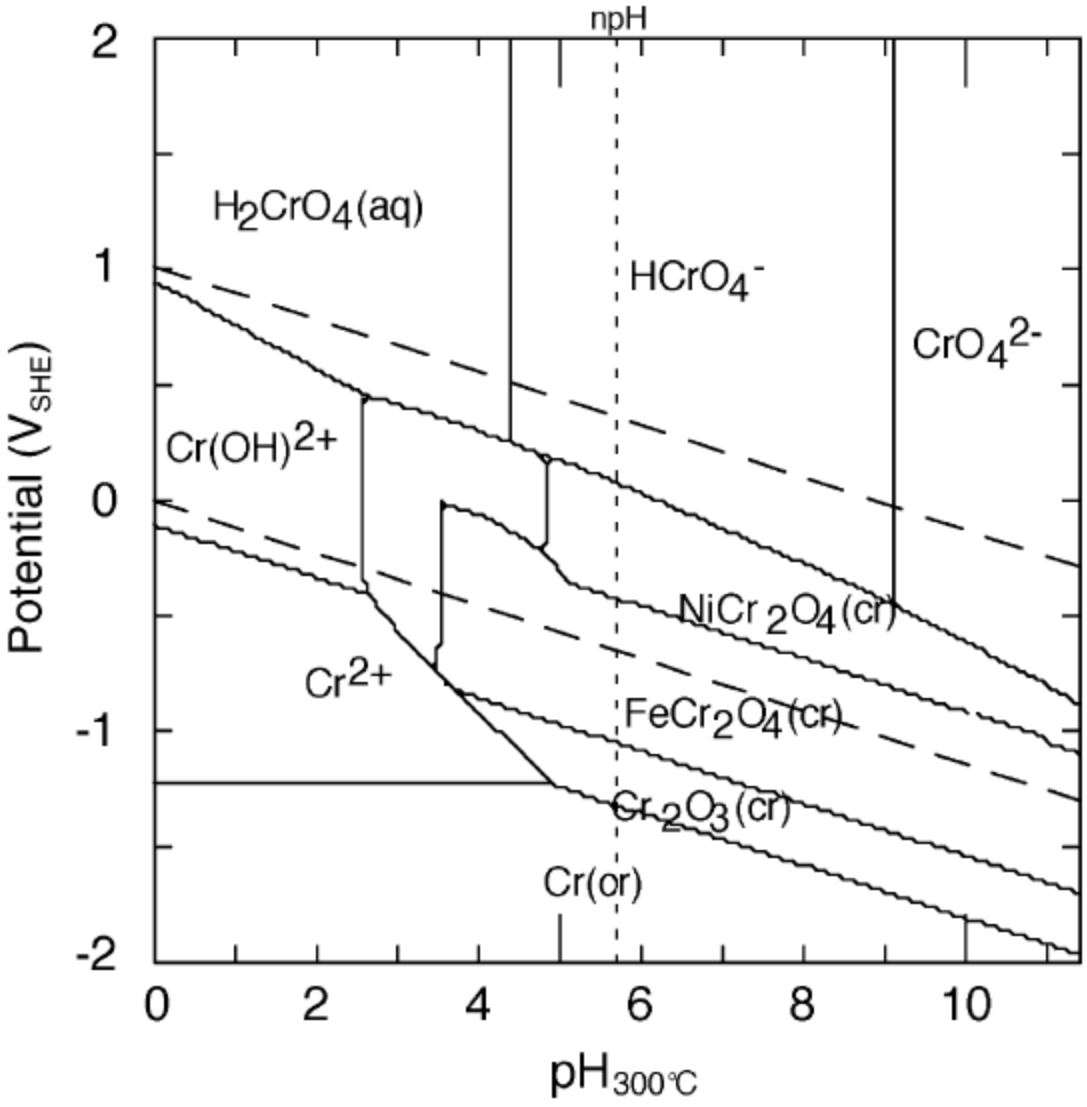

Figure 2.9. Pourbaix diagram of chromium species in the Fe-Ni-Cr ternary system at 300˚C with all aqueous species set to an activity of 10^{-6} mol/kg [48]

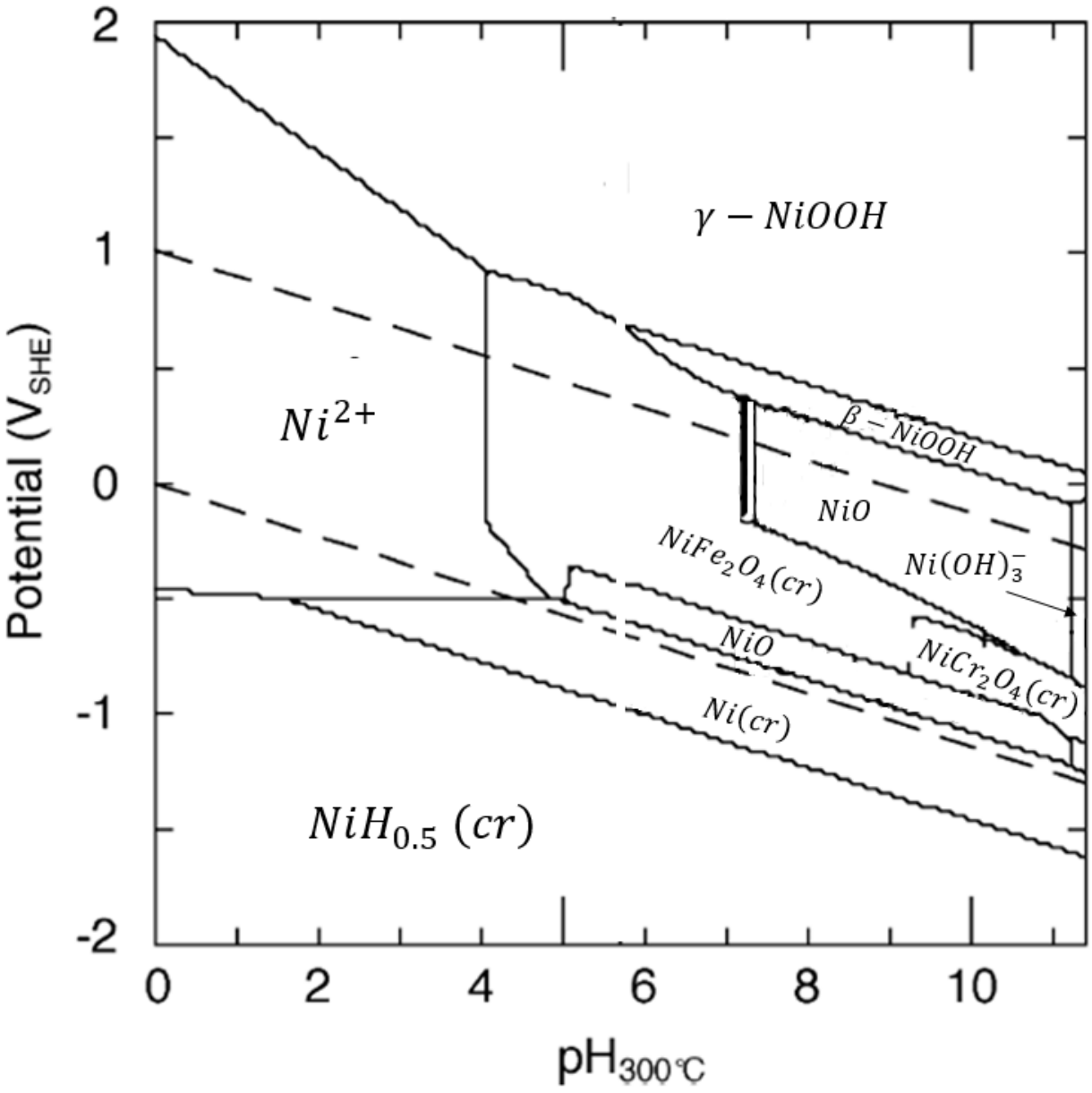

Figure 2.10. Pourbaix diagram of nickel species in the Fe-Ni-Cr ternary system at 300˚C with all aqueous species set to an activity of 10^{-6} mol/kg. [48]

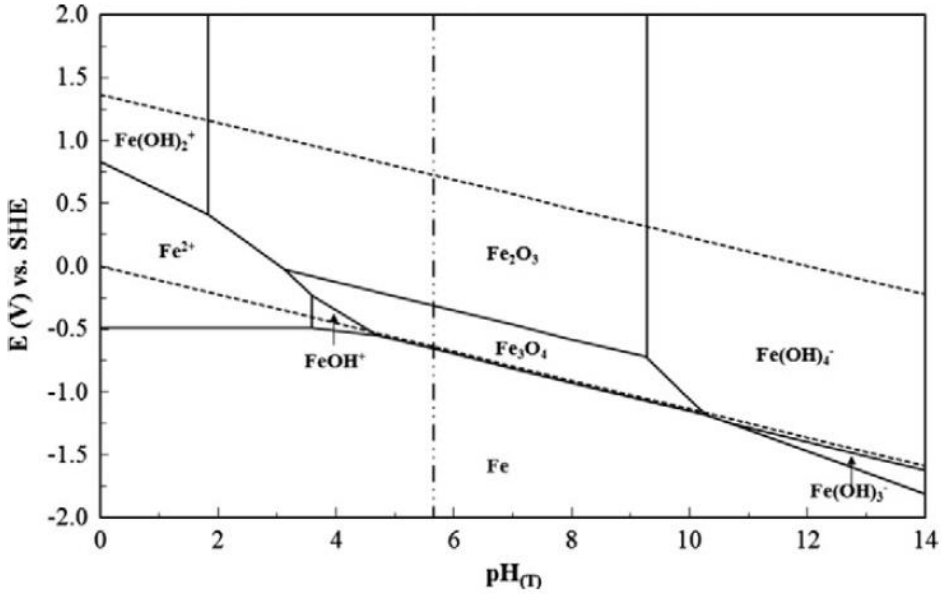

Figure 2.11. Pourbaix diagram of Iron at 300˚C with all aqueous species set to an activity of 10^{-6} mol/kg [92].

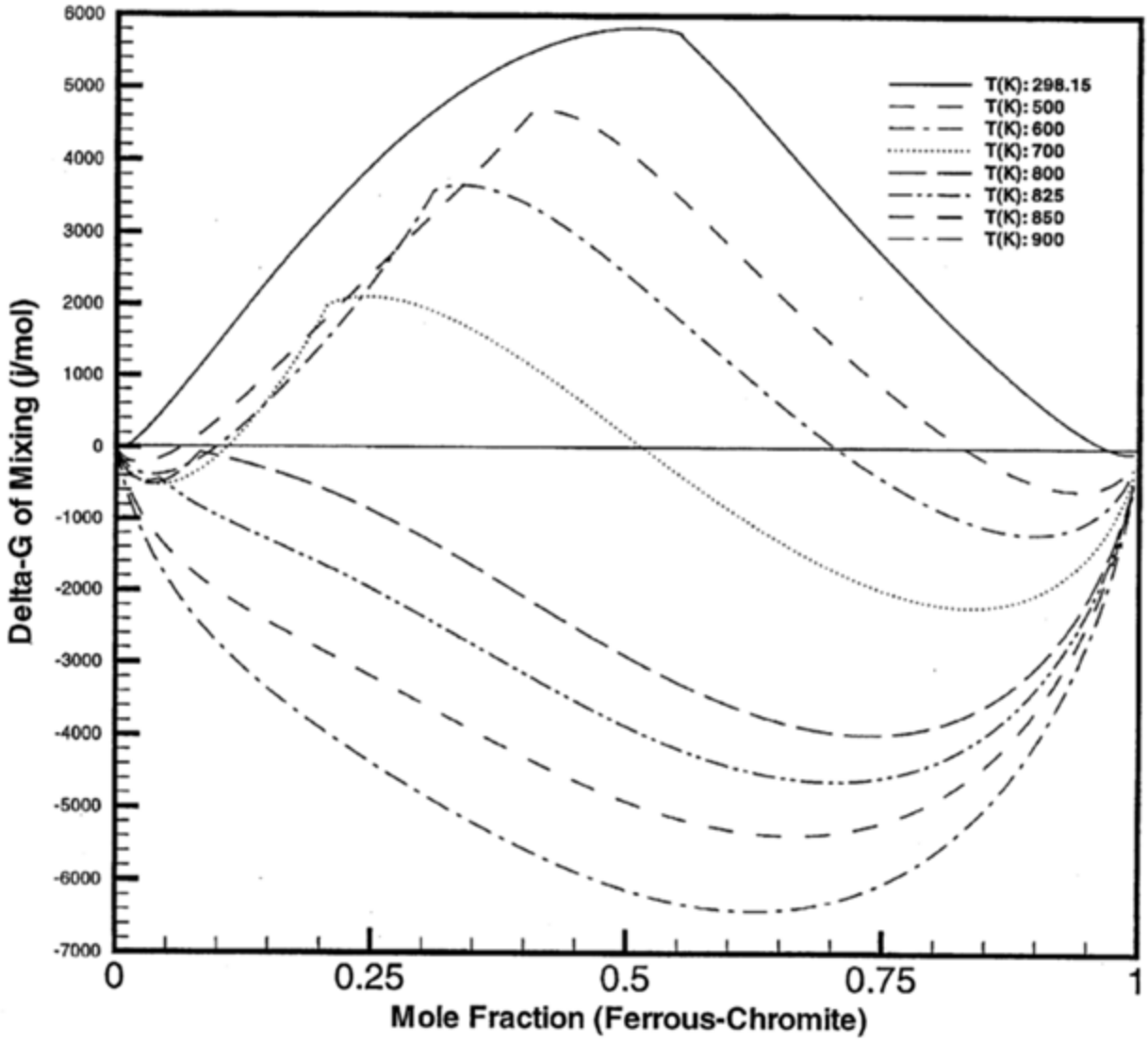

Figure 2.12. Calculated free energy of mixing in $Fe(Fe_{1-x}Cr_x)_2O_4$ spinel oxides at different temperatures.[58]

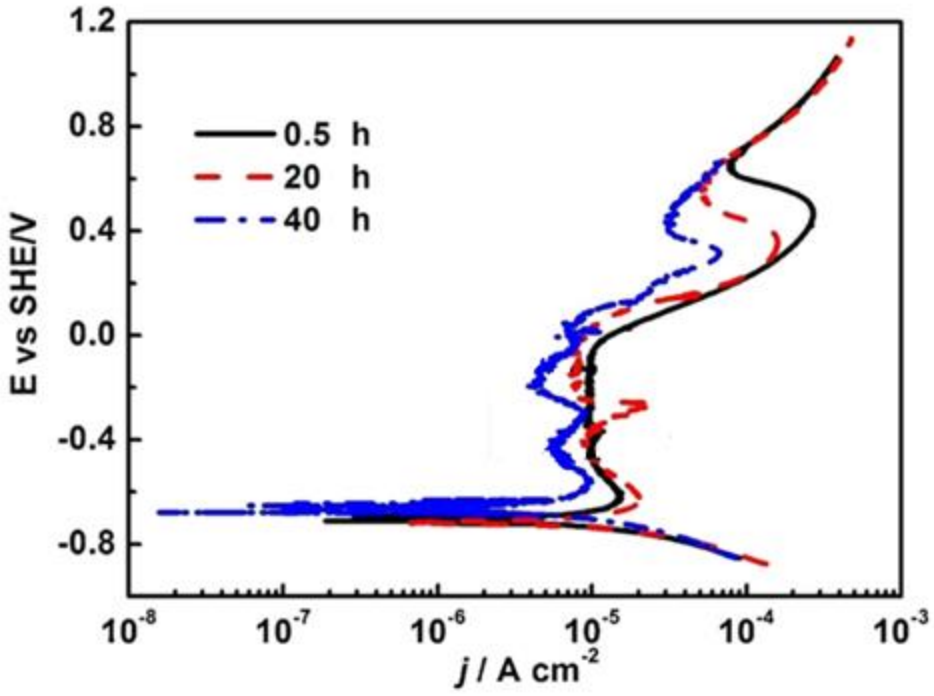

Figure 2.13. Potentiostatic polarization curve of 304 stainless steel in 250˚C water after 0.5, 20, and 40 hrs.[59]

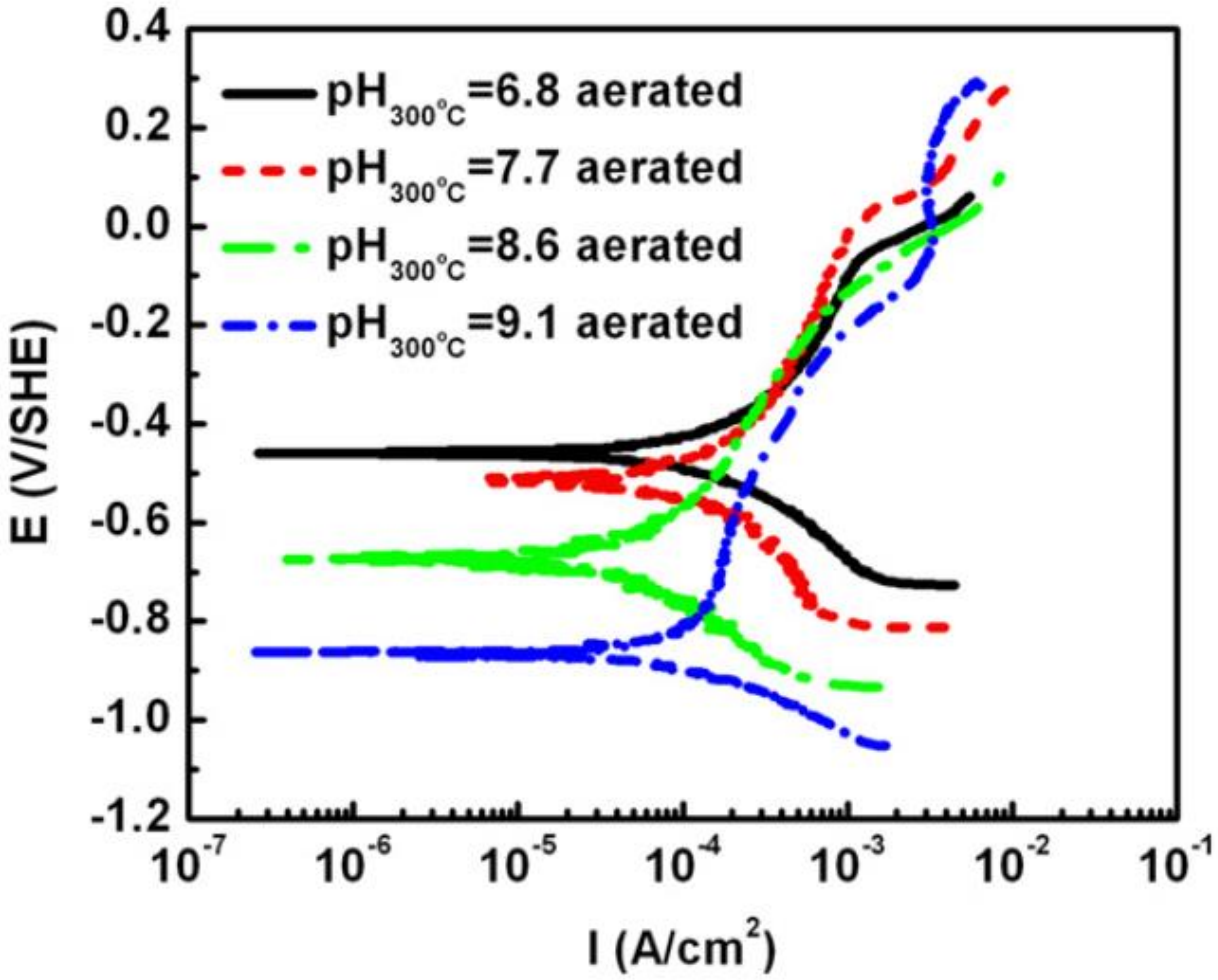

Figure 2.14 Potentiostatic polarization curve of 304 stainless steel in 300˚C water after with 1500 wppm B at different Li concentrations. [93]

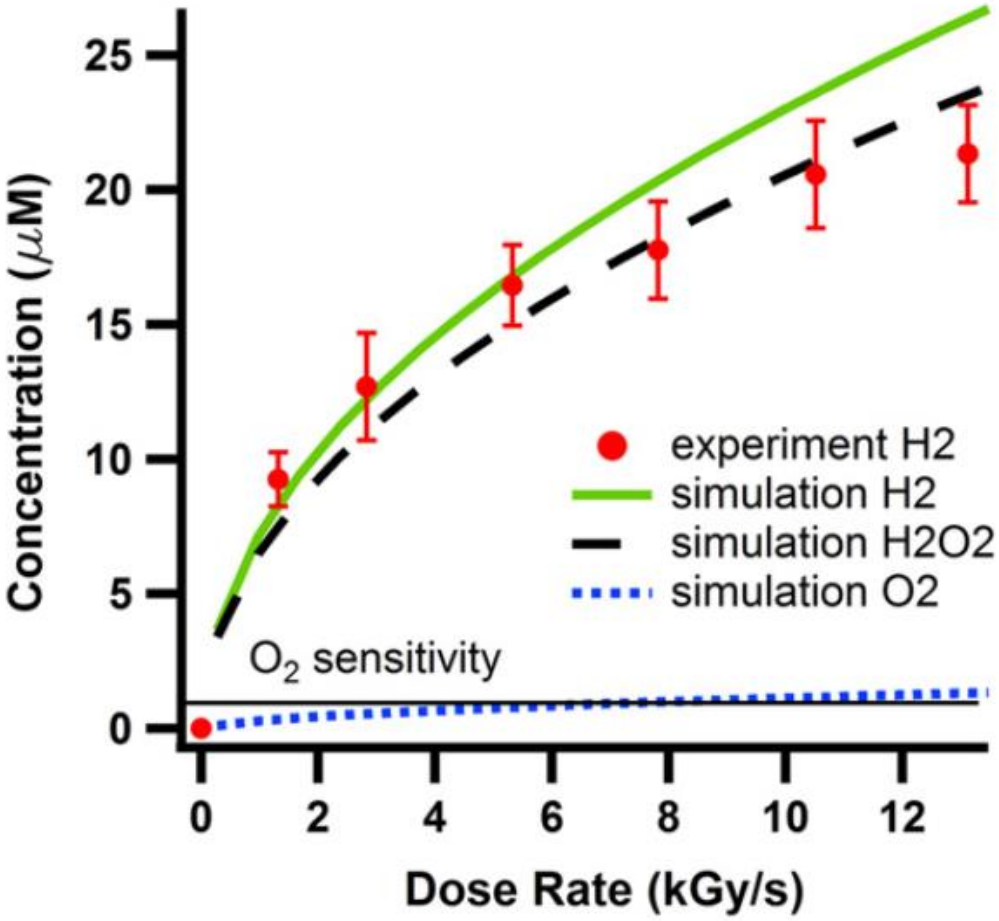

Figure 2.15. Simulated yield of the long-lived radiolysis products during electron irradiation at 20˚C, with experimental H_2 measurements[63].

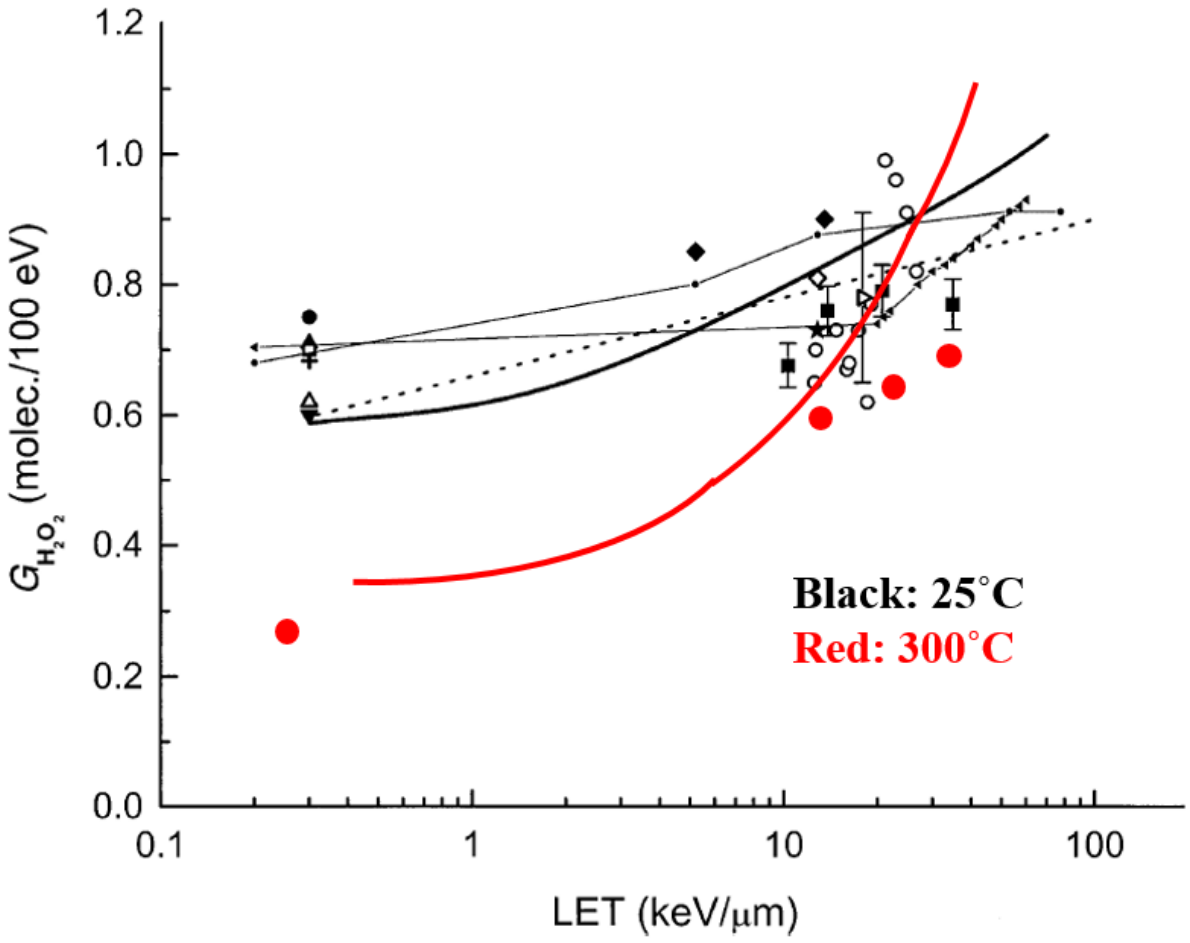

Figure 2.16. Monte-Carlo simulated H_2O_2 yield under proton irradiation at 25ºC and 300˚C. Solid curves represent simulation data, and points represent experimental results for comparison [65].

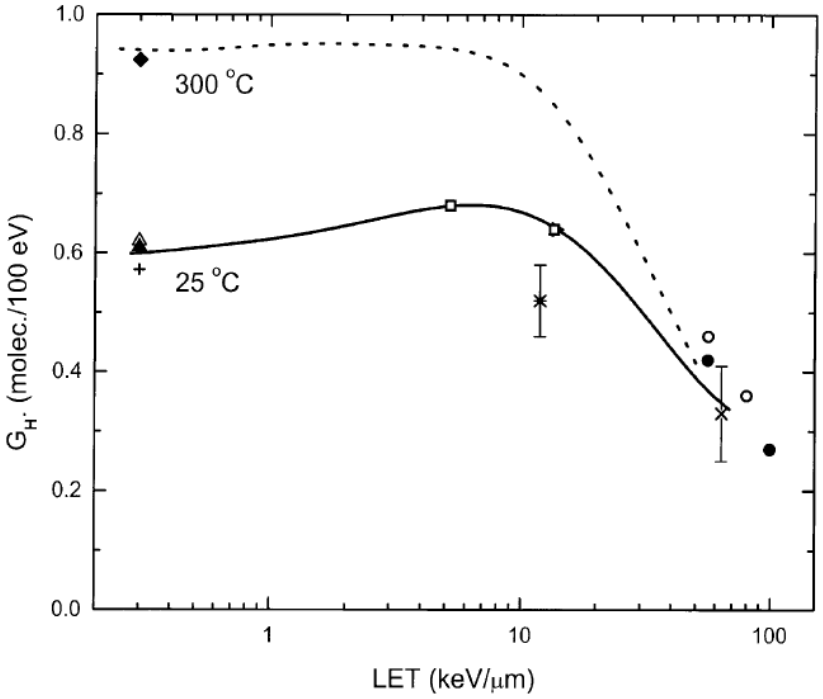

Figure 2.17. Monte-Carlo simulated H* radical yield under proton irradiation at 25ºC and 280ºC, with experimental results for comparison. All data points were taken at 25˚C except the diamond in the upper left.[94]

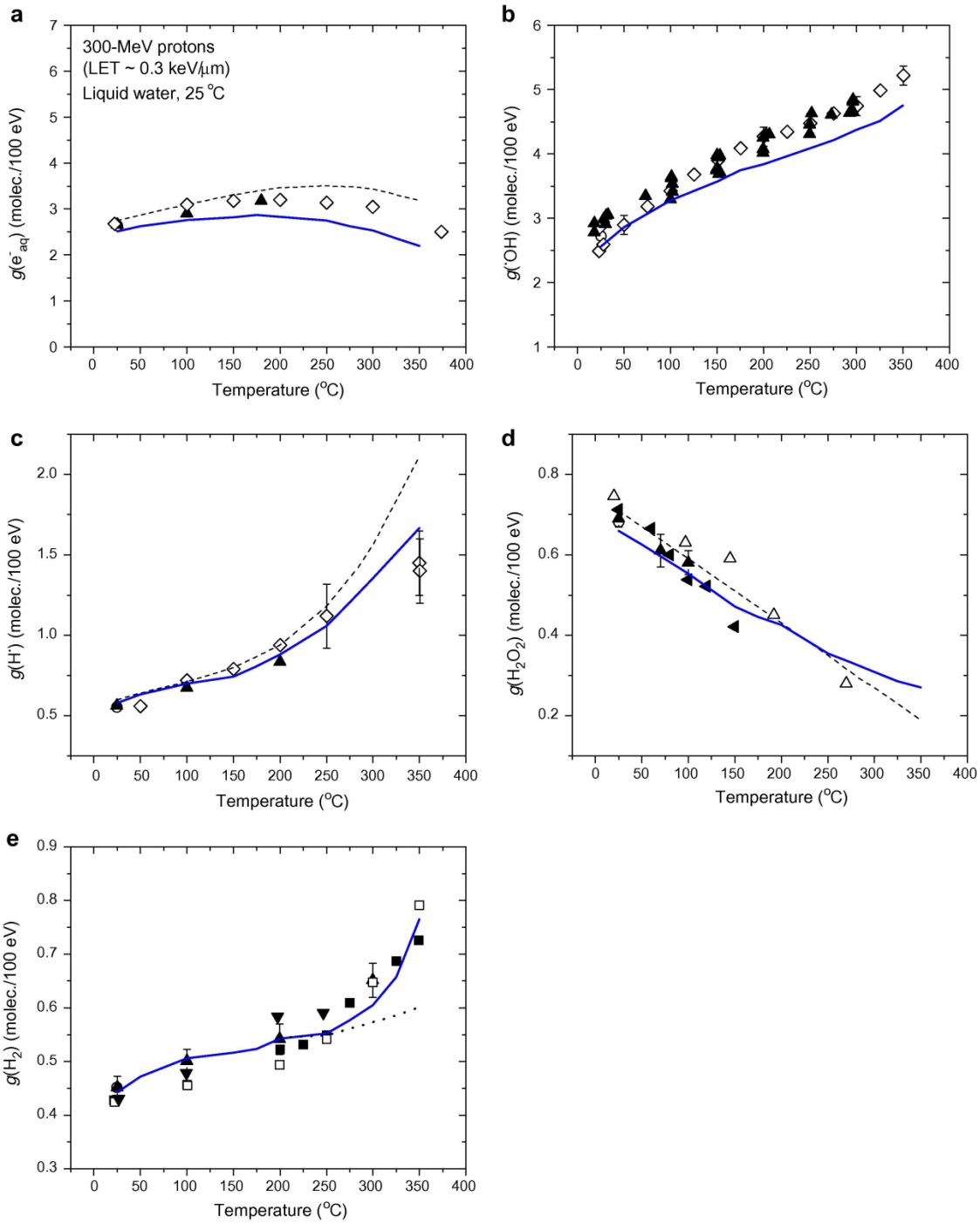

Figure 2.18. Radiolysis product yields varying with temperature. Solid lines are simulated, and data points are taken from various experiments. Products shown are e^- (a) OH^- (b) H* (c) H_2O_2 (d) and H_2 (e)[64]

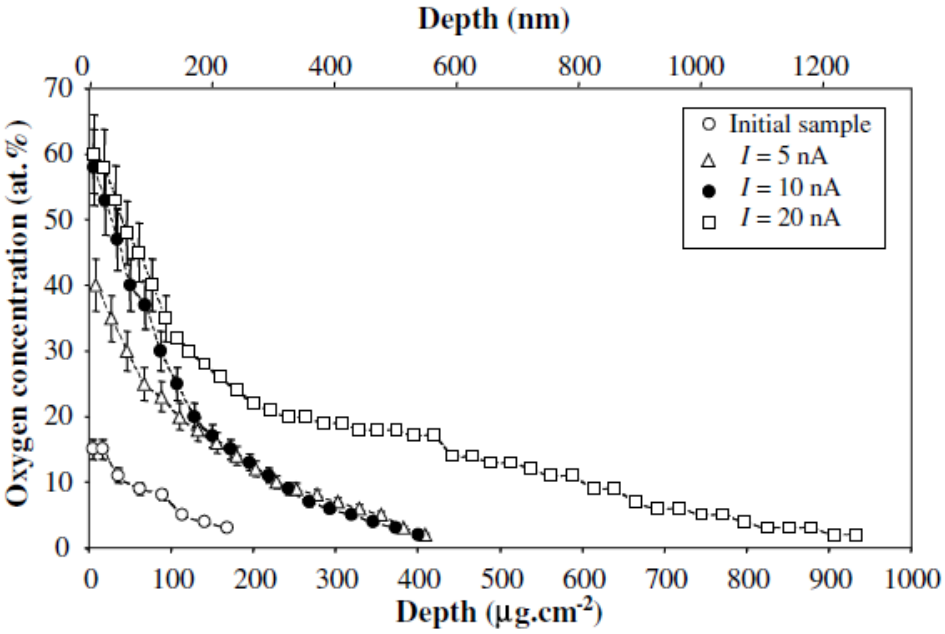

Figure 2.19. Profiles deduced from RBS measurements for the initial sample and for the irradiated samples after 45 min exposures at beam intensities of 5, 10 and 20 nA. The nm depth scale is calculated assuming pure iron. The error bars are represented on the first 150 nm depth on which both oxygen and hydrogen have been analyzed.[4]

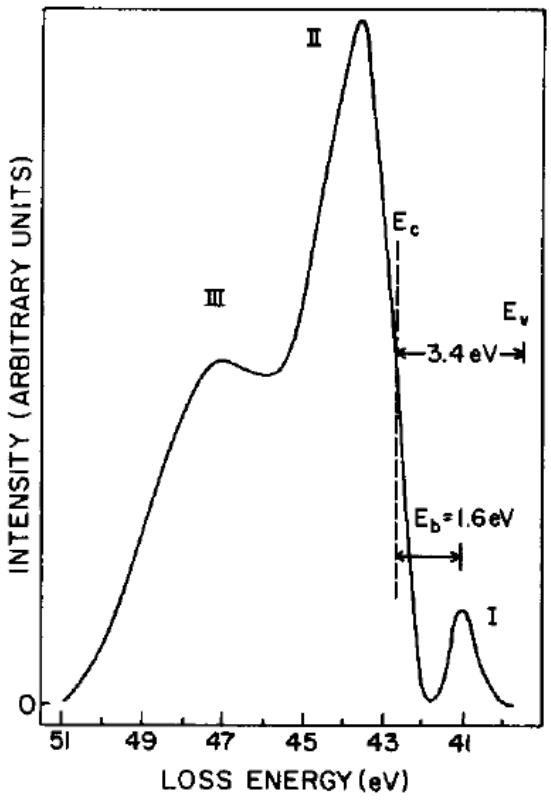

Figure 2.20. Electron energy loss spectrum of Cr_2O_3. E_v and E_c are the valence and conduction band energies, while E_b denotes the exciton binding energy.[70]

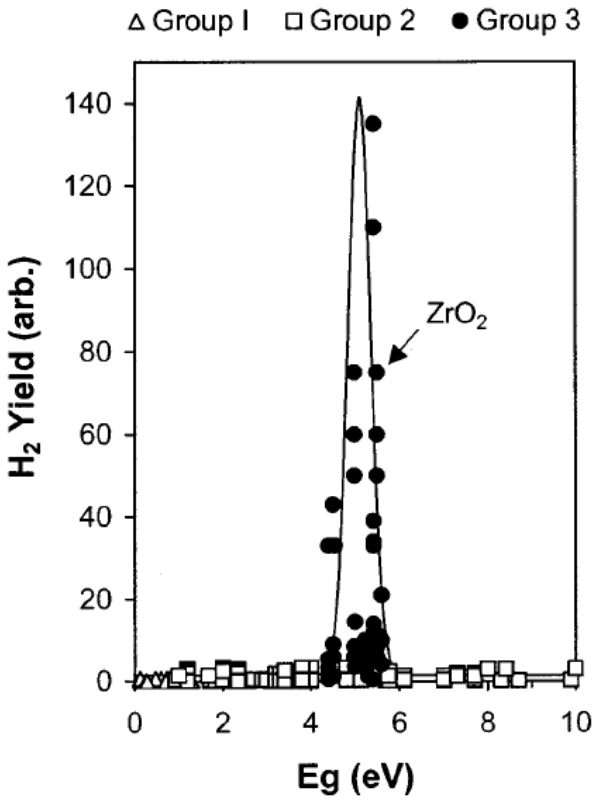

Figure 2.21. Hydrogen yield of oxides in water as a function of bandgap energy[76]

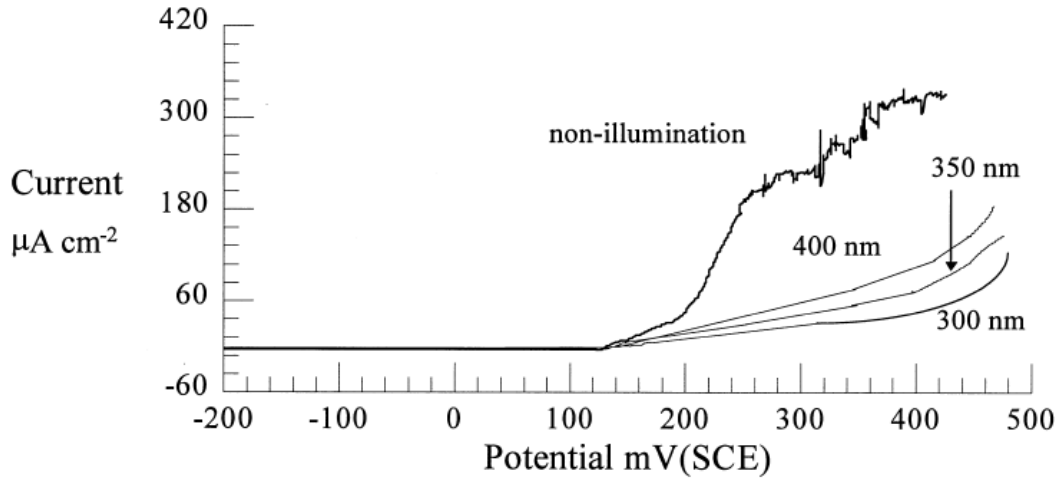

Figure 2.22. Polarization curves for copper alloy under illumination at different wavelengths[78]

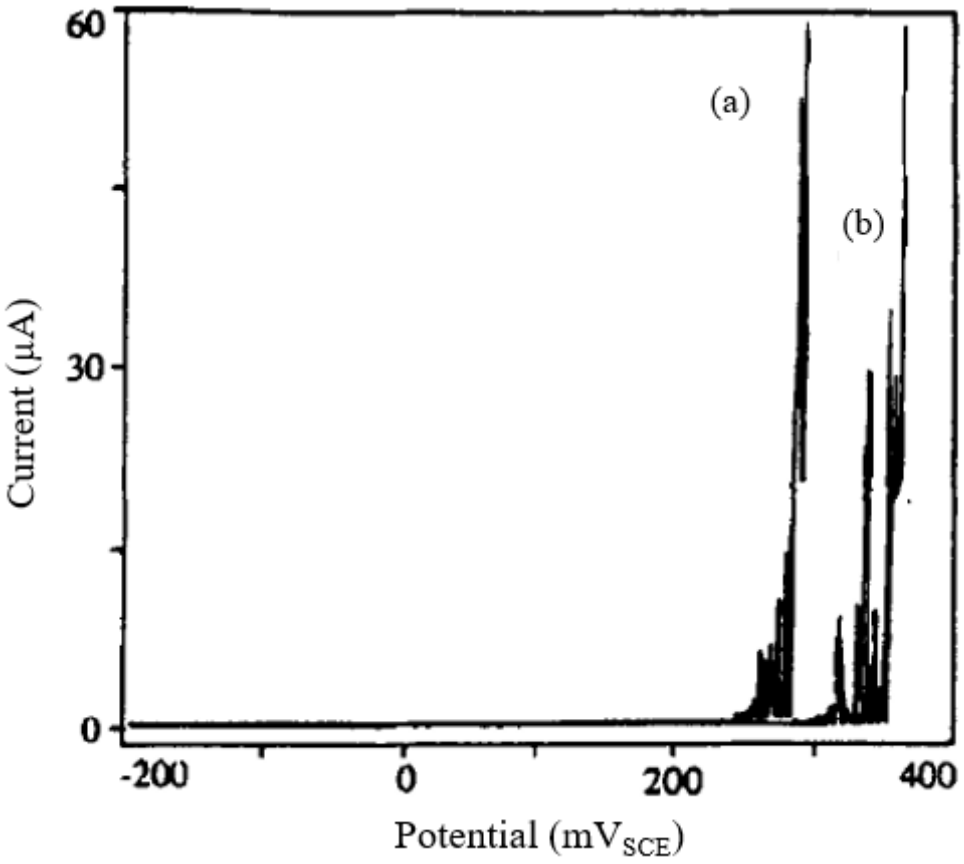

Figure 2.23. Polarization curves for 304 stainless steel in NaCl under (a) no illumination and (b) illumination with 300 nm wavelength[77]

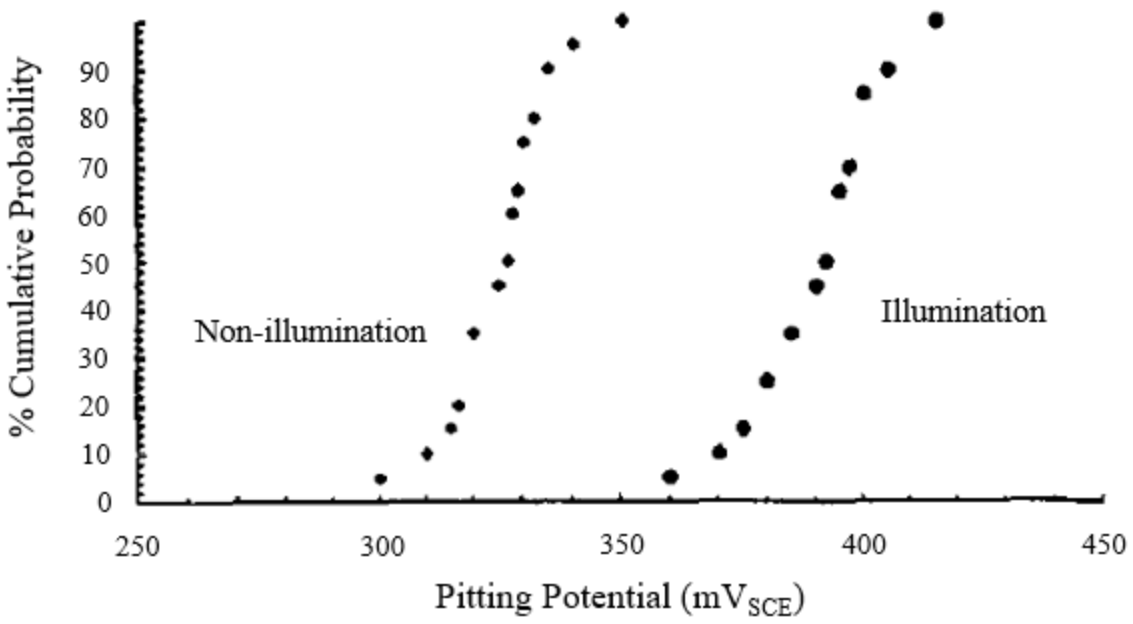

Figure 2.24. Pitting probability in 316 stainless as a function of pitting potential under no illumination and 300 nm illumination.[95]

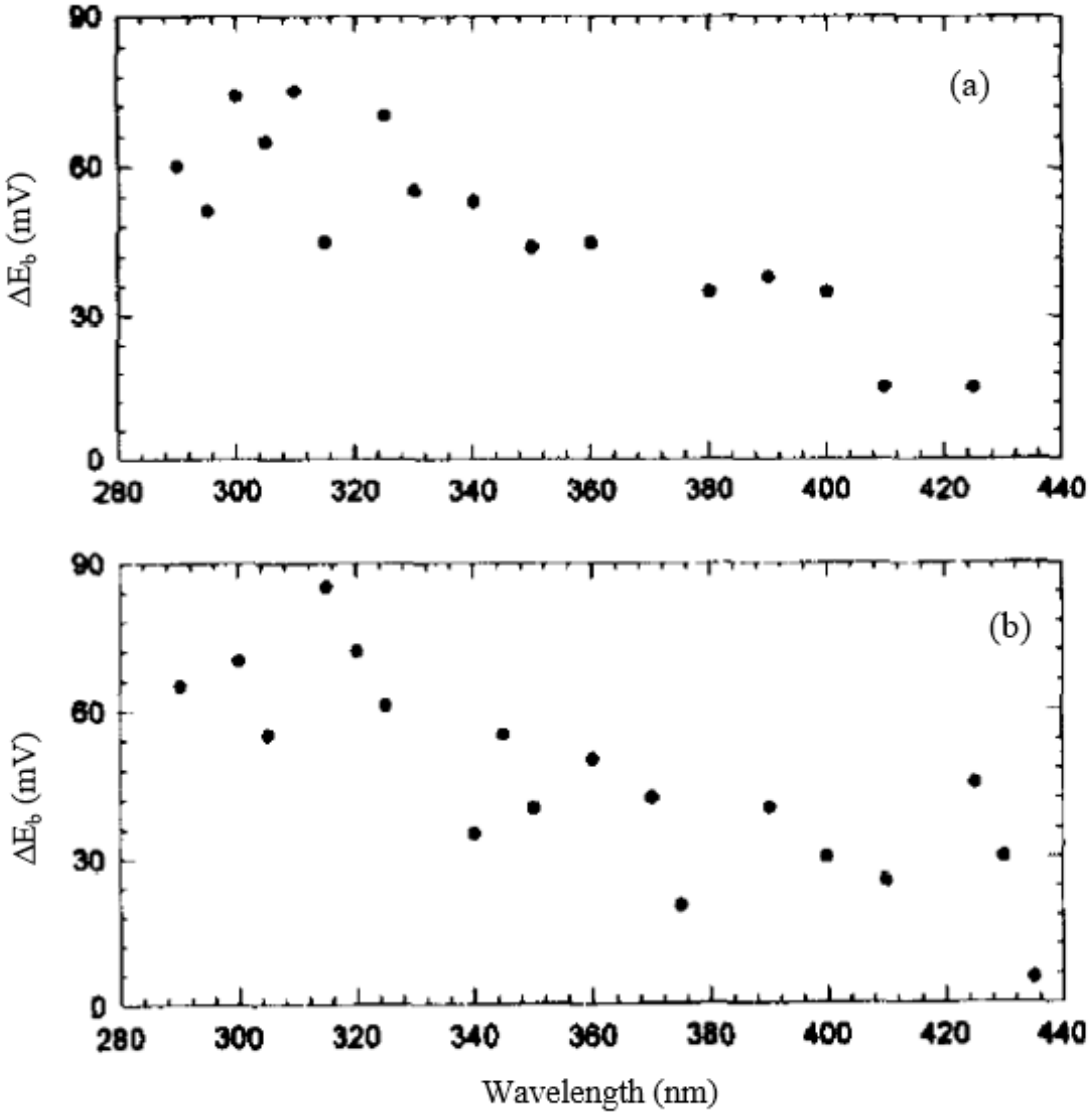

Figure 2.25. Increase in breakdown voltage as a function of illumination wavelength in (a)304 and (b)316 stainless steels.[95]

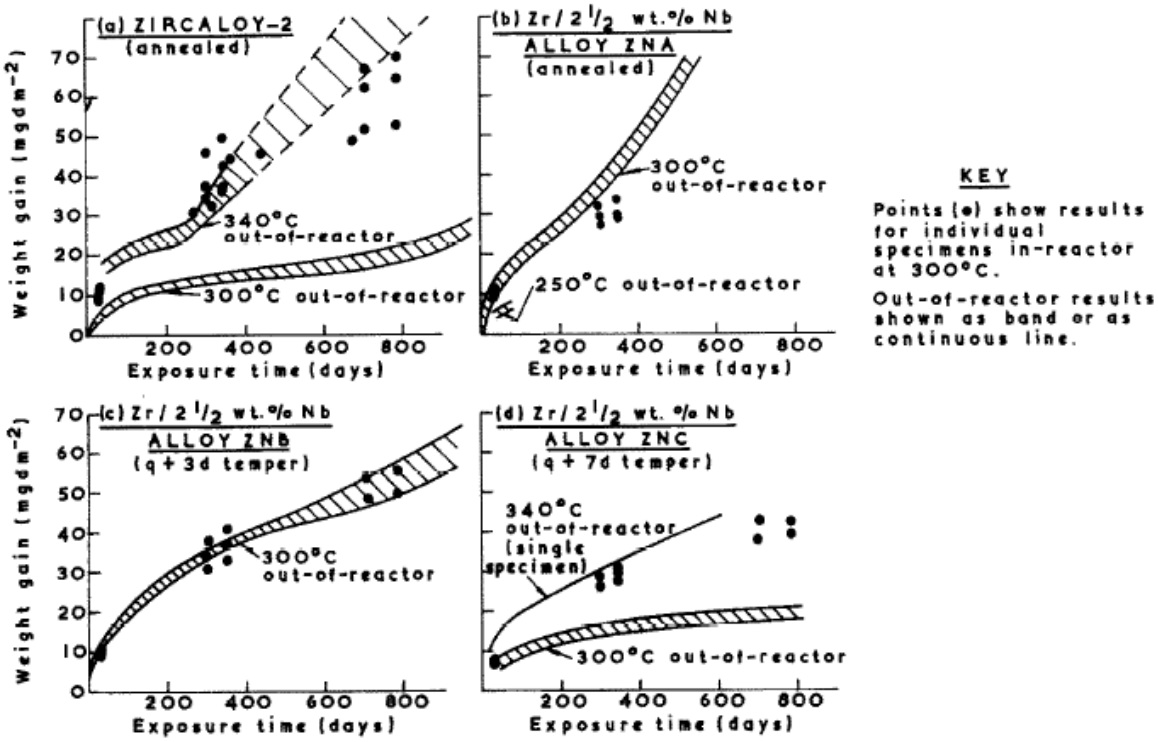

Figure 2.26. Effect of radiation on the corrosion of Zircaloy-2 and Zr-2.5 wt% Nb in a moist carbon dioxide and air mixture at 300˚C. [6]

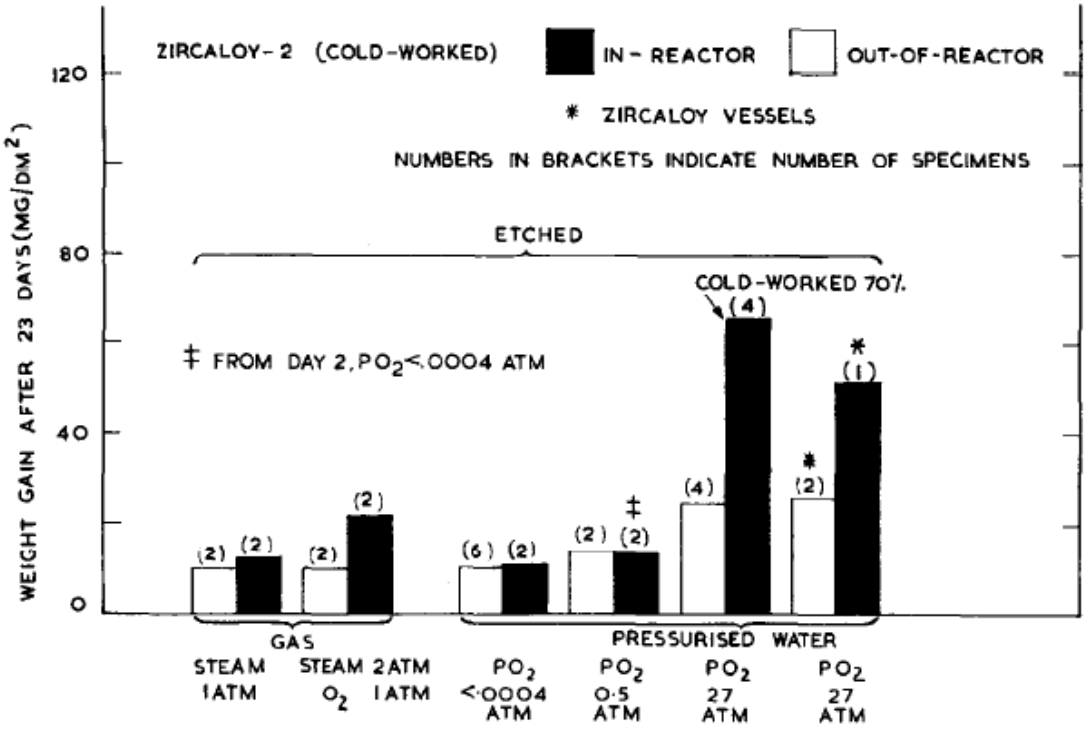

Figure 2.27. Effects of radiation and oxygen on the oxidation of cold-worked Zircaloy-2 in pressurized water at 290˚C. [8]

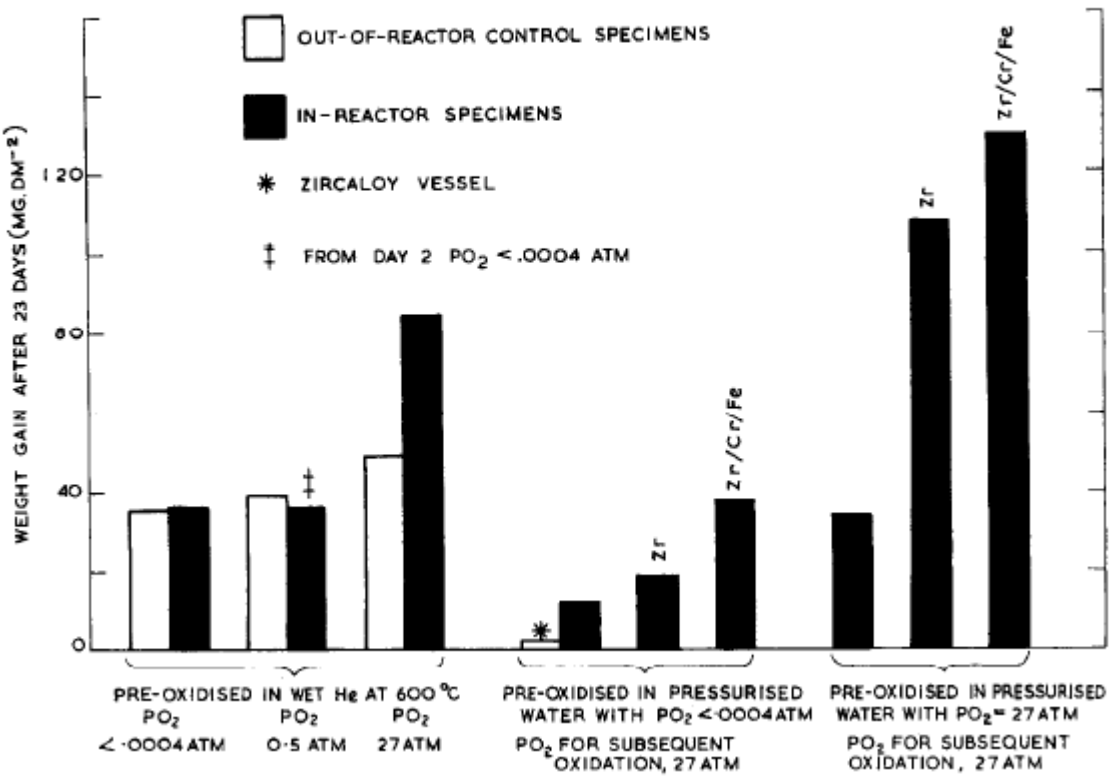

Figure 2.28. Effects of different pre-oxidation conditions on the subsequent corrosion of Zircaloy-2, zirconium (reactor-grade), and zirconium/chromium/iron alloy during a 23-day exposure in pressurized water at 290˚C. [8]

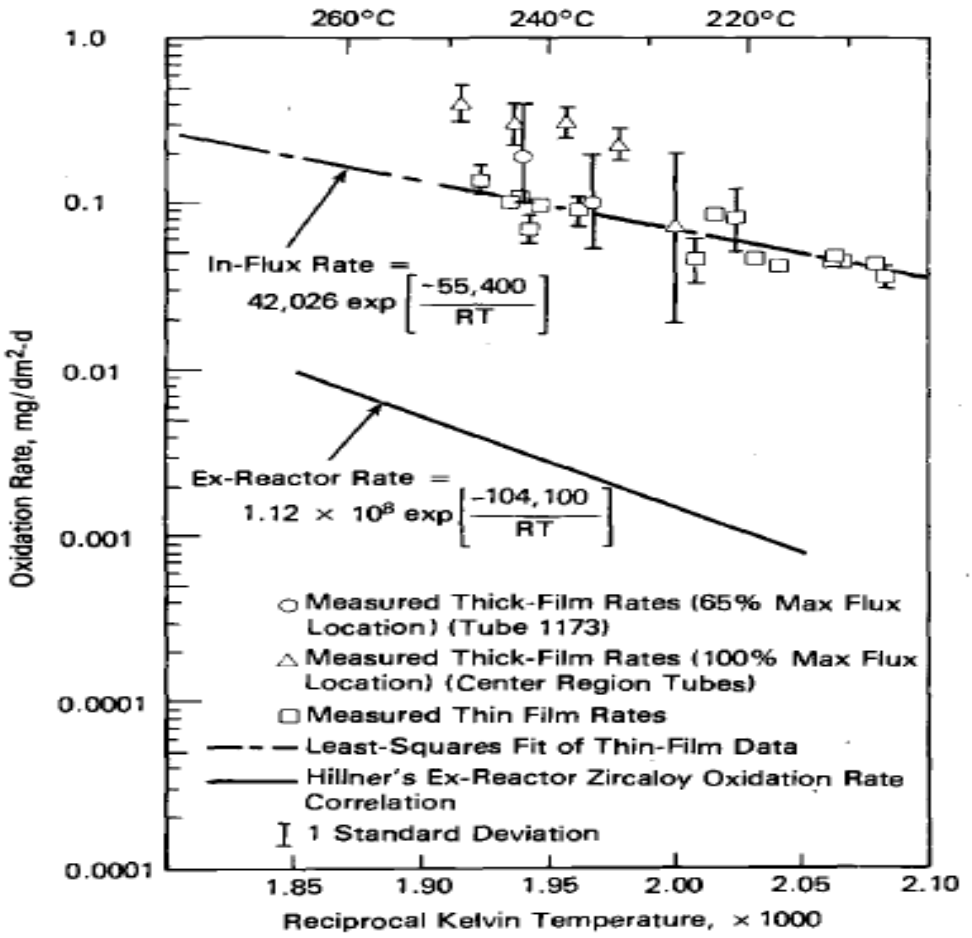

Figure 2.29. Zircaloy pressure tube oxidation rates versus temperature: thin-film least-square lines versus Hillner's ex-reactor correlations and thick-film rates from high-flux locations (100% maximum) to low-flux locations (65% maximum). [79]

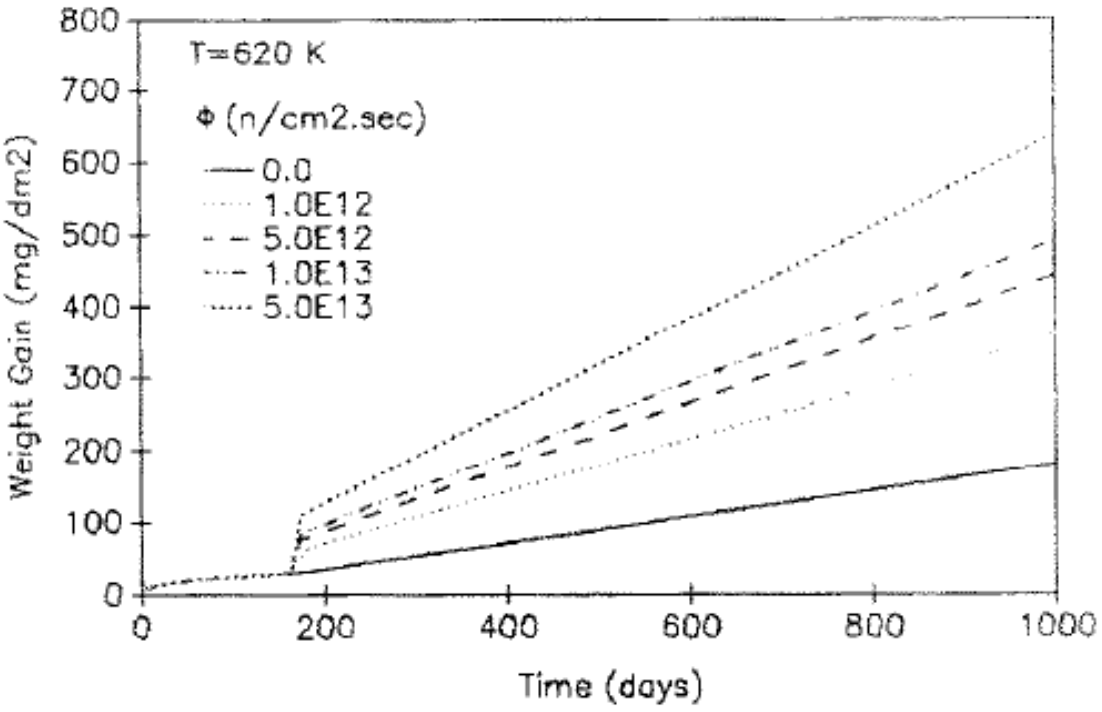

Figure 2.30. Fast neutron flux influence on the corrosion rate of Zircaloy-4 at 620K.[7]

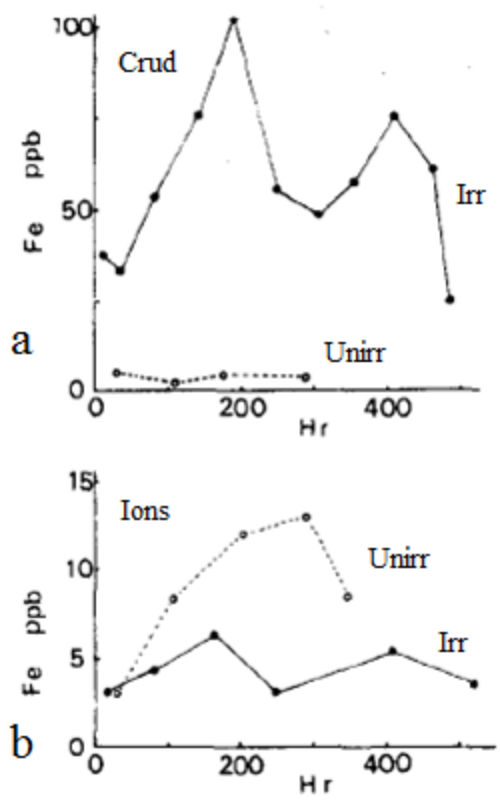

Figure 2.31. Concentration of (a) iron crud and (b) iron ions in 250˚C water flowing at 20 mL/min with 20ppb O_2. Each water condition had samples made from 304 stainless steel that were (•) irradiated with a Co-60 source at 500Gy/hr 304 and (◦) unirradiated. [84]

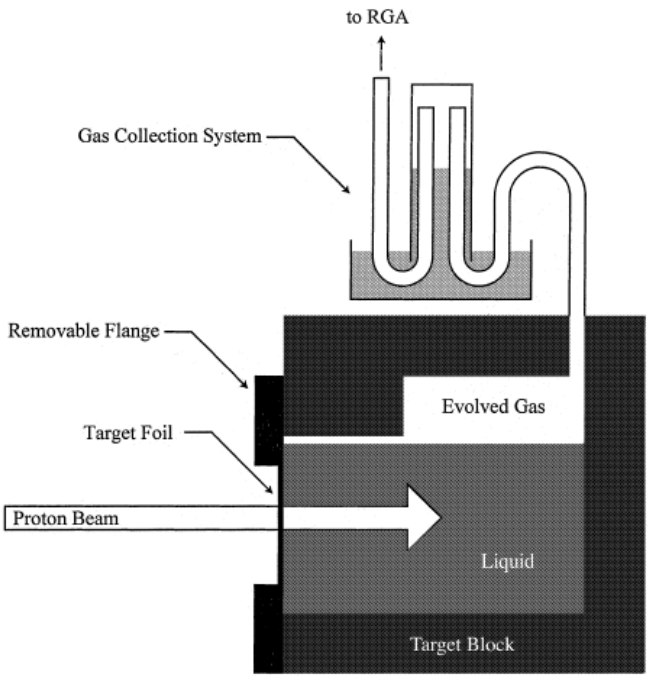

Figure 2.32. A schematic of Lewis and Hunn's experiment.[3]

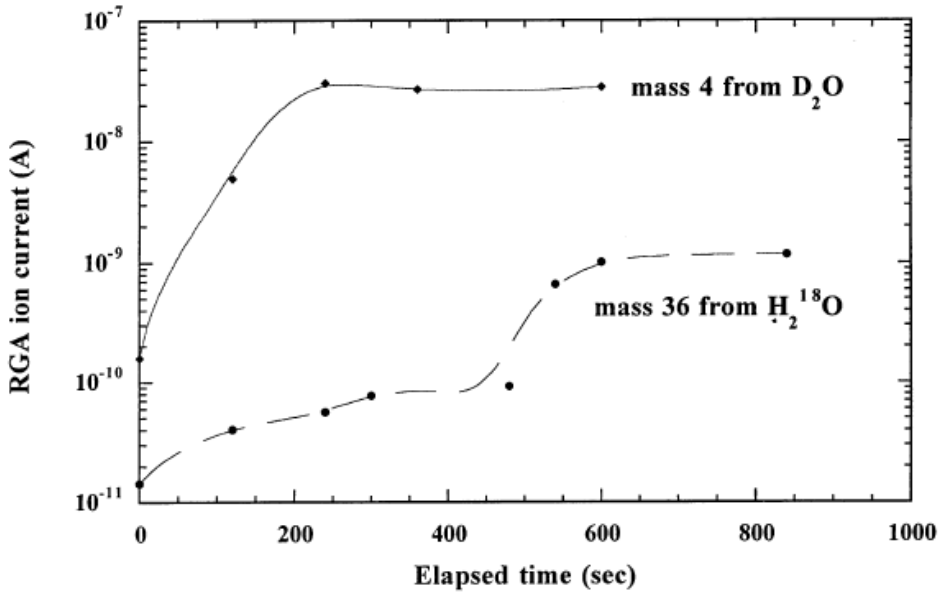

Figure 2.33. Values of residual gas analysis (RGA) currents taken during the first few minutes of two separate proton irradiations, one using a target water containing D_2O and the other containing $H_2{}^{18}O$.[3]

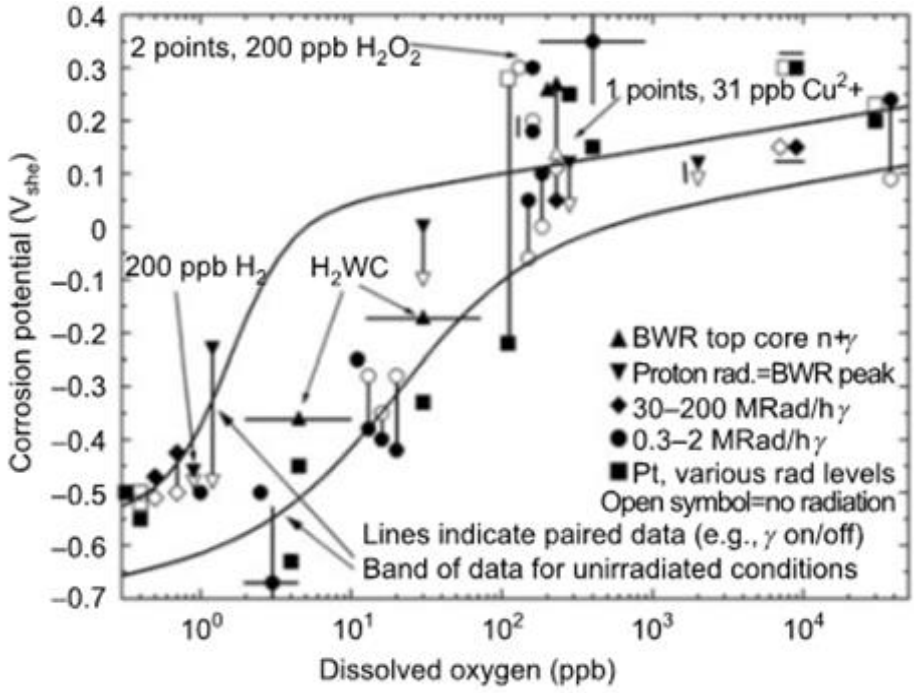

Figure 2.34. Effect of radiation on corrosion potential of 304 SS and Pt in 288˚C water[86]

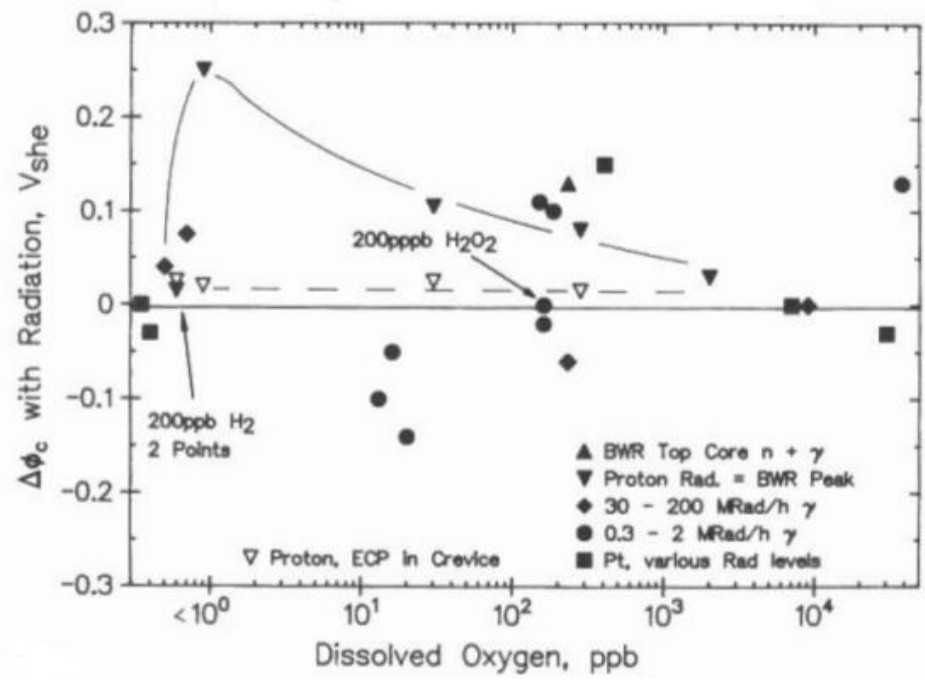

Figure 2.35. Shift in corrosion potential from irradiation of 304 SS and Pt in 288˚C water[86]

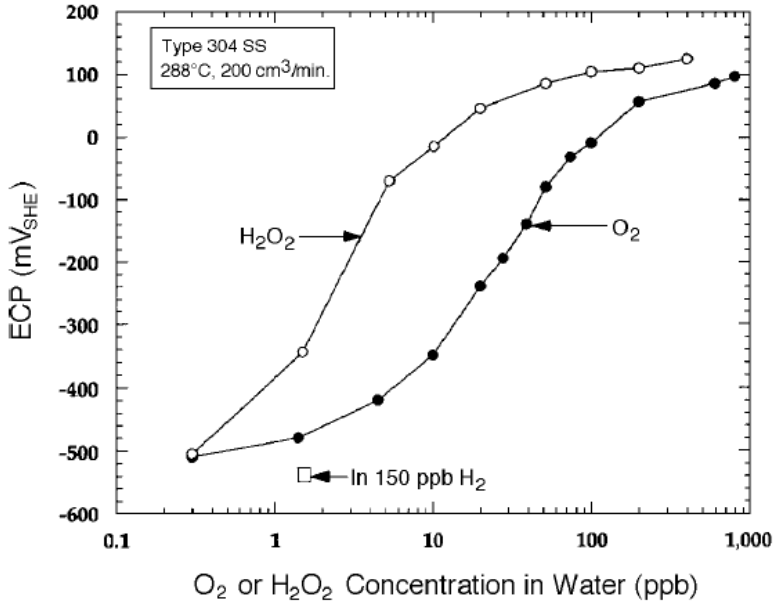

Figure 2.36. ECP during the corrosion of 304 stainless steel in 288˚C water as a function of H_2O_2 and O_2 concentration, with ECP at 150 ppb H_2 included for comparison [89].

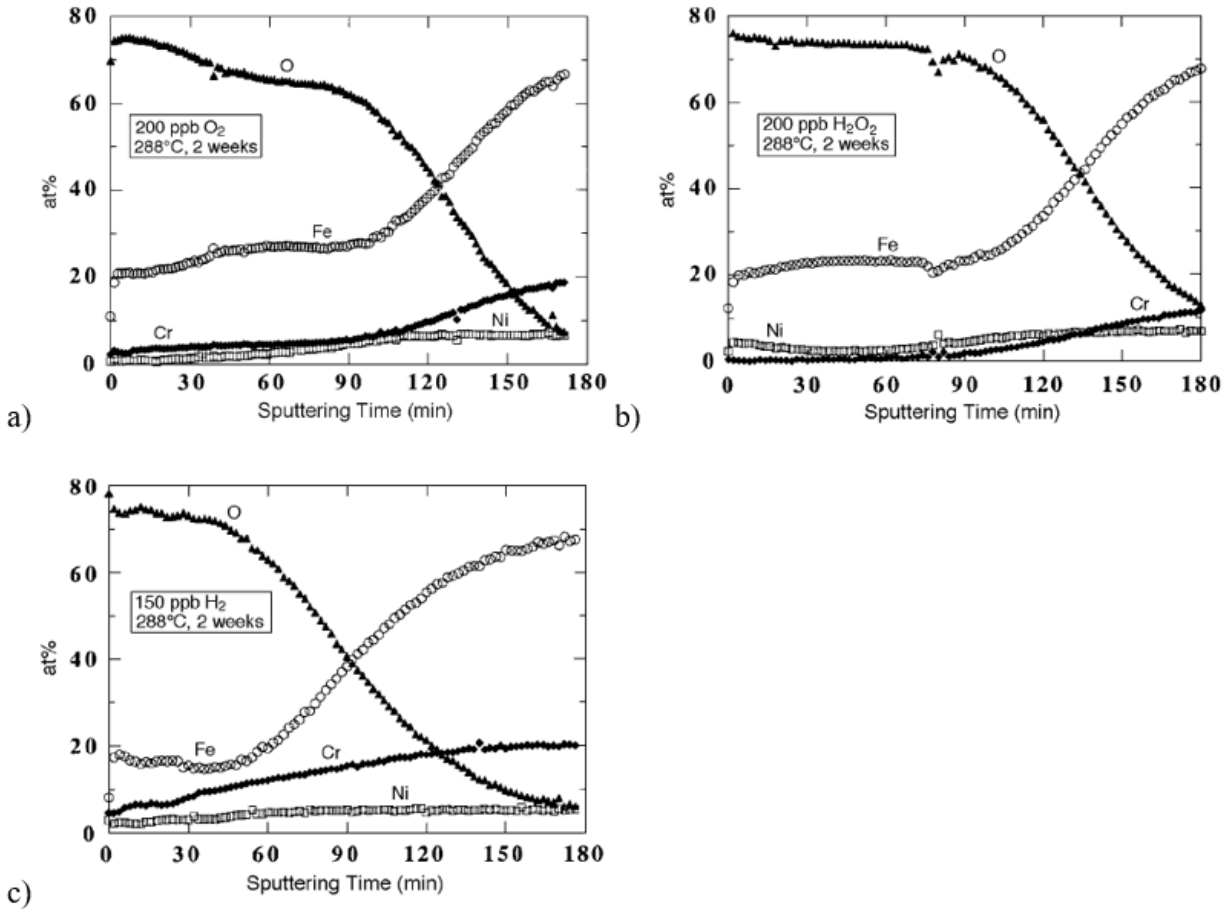

Figure 2.37. AES depth profile for type 304 SS specimen exposed for 2 weeks to 288°C water containing (a) 200ppb O_2 (b)200ppb H_2O_2 and (c) 150 ppb H_2.[89]

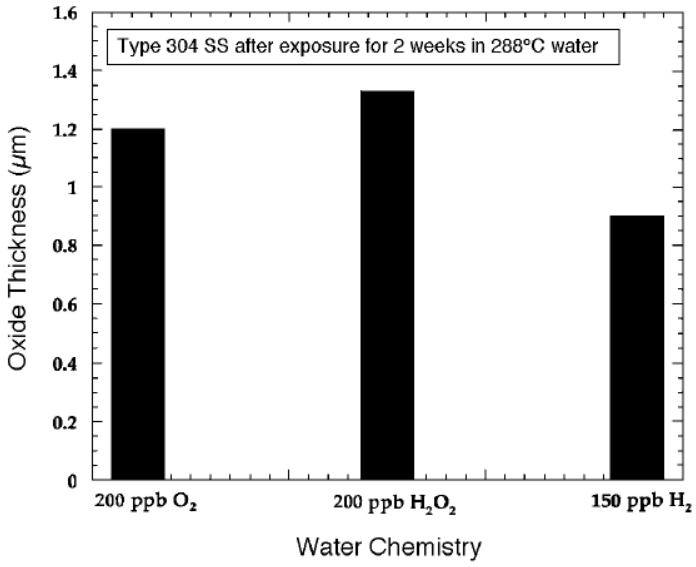

Figure 2.38. Oxide thickness on 304 stainless steel after 2 weeks in 288˚C water with H_2O_2, O_2 and H_2 additions.[89]

CHAPTER 3 - OBJECTIVE AND APPROACH

The objective of this work is to understand the effects of irradiation on the corrosion of 316L stainless steel in simulated primary water. The objective will be accomplished in three parts.

The first sub-objective is to find how radiation affects the thermodynamics of corrosion. To meet this objective, stainless steel samples were exposed to a simulated PWR environment both with and without irradiation. By examining the species that are present in the oxide film in both cases, the thermodynamic conditions under which the film formed can be found, and the effect of radiation on corrosion thermodynamics can be determined.

The next sub-objective is to determine how the altered corrosion thermodynamics affect the growth and dissolution of the oxide film. This objective was accomplished by characterizing the oxide film that formed on the samples, both with and without irradiation. By comparing the morphology and composition of the oxide films, new insights into the effect of radiation on oxide protectiveness and dissolution are presented.

The third sub-objective is to determine the contributions of radiolysis and displacement damage to IAC. To accomplish this objective, regions exposed only to radiolysis are compared to regions exposed to both radiolysis and displacement damage. Additionally, a sample with a pre-grown oxide film was exposed to radiation to examine the effect of a pre-grown kinetic barrier.

A novel experiment for meeting these objectives is presented in Chapter 4. Results from the experiment are shown in Chapter 5, and a discussion of the results follows in Chapter 6.

CHAPTER 4 - EXPERIMENT

This chapter will begin with a description of the design, construction, and testing of the experimental facility used for this work. It will continue on to a list of the experimental procedures, and characterization techniques used to produce the presented results.

4.1 Experiment Design

Very little mechanistic data on IAC exists, in-part due to experimental limitations. The most difficult challenge to overcome is the design of an experiment in which a sample surface can be irradiated while simultaneously exposed to controlled LWR conditions. This chapter presents the design and testing of a facility to study irradiation accelerated corrosion in high-temperature flowing water using in-situ proton irradiation. The major components of the facility will be described in detail, including the sample design, water system, and novel beamline components.

To allow for rigorous studies of irradiation accelerated corrosion in high temperature water using in-situ proton irradiation, the following requirements must be met:

- Samples must be kept in a controlled environment with flowing water and carefully monitored water chemistry,
- The water cell must be able to contain high pressure to allow for water temperatures up to 320˚C,

- The interface between the sample and the water must be irradiated at a controlled dose rate.

These requirements are met by using a very thin sample through which the proton beam passes. All other subsystems are built around this central design element. Since a sample thin enough to allow complete transmission of the proton beam poses a risk of rupture under high pressure, a dedicated beamline was built with unique safety systems to protect the accelerator in the event of a sample rupture. A custom corrosion cell was also built to maintain a stable and monitored environment for sample exposure and irradiation.

4.1.1 Sample Design and Testing

The unique aspect of this experiment is that the sample serves the dual role of sample on which IAC will be measured, and structural component that isolates the beamline vacuum from the high temperature/high pressure environment in the corrosion cell. Because of this dual role as both a specimen and a "window" into the corrosion cell, nearly every sample design parameter represents a compromise. The sample must be thin enough to allow a 3.2 MeV proton beam to pass completely through, while still remaining strong enough to serve as a barrier between the beamline vacuum and the high-pressure, high temperature water in the corrosion cell.

The process of designing the samples used in the experiment sought to determine the proper balance among three parameters:

- Rupture strength – Higher is more desirable to maximize the safety of the experiment
- Sample thickness – Thinner is more desirable to maximize beam penetration
- Sample diameter – Larger is more desirable to maximize the sample area that can be studied

The pressure required to maintain 320˚C water in its liquid phase is 11.4 MPa, so an experimental pressure of 12.8 MPa was selected to avoid local boiling.

4.1.1.1 Sample Design

The design window for thickness was determined by simulating the penetration depth of the proton beam through the sample material. Figure 4.1 shows the damage curve of 3.2 MeV protons travelling through stainless steel as calculated by SRIM 2013[96].

It is preferable to choose a smaller sample thickness so the sample-water interface is as far away from the Bragg peak as possible to minimize the deviation in the damage rate if there is variance or error in the sample thickness measurement.

To meet these design requirements, several geometries were tested before narrowing them down to two designs – a flat plate, and a hemispherical shell. They were then examined using the ANSYS® finite-element modeling software to determine the geometric limitations of each sample design. For a 35 μm sample thickness, and a water pressure of 12.8 MPa, the outside diameter of the sample was varied, and the maximum stress at the center of the sample was plotted as a function of sample diameter in Figure 4.2. For both designs the maximum stress on the sample increases with diameter, but the hemispherical shape offers a significant improvement over a flat sample.

The implementation of this design was inspired by the design of safety rupture discs used in high pressure water systems. The samples began as flat metal discs, and were hydraulically

formed into a dome-shape. The design is shown schematically in Figure 4.3, and a photograph of a sample after forming is shown in Figure 4.4.

The rupture-disc-like geometry of the sample was optimized using Equation 4.1, an analytical formula by Vodyanik[97] which expresses the rupture pressure of the sample as a function of its thickness and diameter, taking into account the tensile strength and formability of the material.

$$p = \frac{8\Delta\sigma_{UTS}}{D}\sqrt{\frac{\sqrt{1+\delta}-1}{1+\delta}} \tag{4.1}$$

where p is the burst pressure, Δ is the sample thickness at burst, D is the sample diameter, σ_{UTS} is the ultimate tensile strength of the material, and δ is the uniform elongation of the material.

Figure 4.5 shows a contour plot of the burst pressure at 320˚C as a function of the sample diameter for different sample thicknesses. The thickness before forming was given along with the thickness immediately before rupture to show how the thickness was reduced during the forming process. The analytical equation assumed room temperature, so the burst pressure at 320°C was calculated by applying an empirical correction factor of 0.7 to account for the change in strength and formability at 320˚C. The actual forming pressure should be less than the burst pressure, but greater than the experimental pressure (with temperature correction factor applied) to avoid yielding the sample during the experiment. This resulted in a slightly higher sample thickness, to give an appropriate margin of safety.

For the initial experiments, a dome diameter of 3.5 mm was chosen. To allow for a sufficient area to weld, samples were cut into 7.6 mm diameter discs from 49 µm thick 316L stainless steel sheet stock. At the center of each disc, a 3.5 mm diameter dome shape was

hydraulically formed using high-pressure water to a final center thickness of 37 μm and a dome height of 0.8 mm, introducing 24% cold-work based on the reduction in thickness.

4.1.1.2 Orange Peel Effect

A fine-grained material was required for the samples, as large grained materials can experience roughening of free surfaces during forming (orange-peel effect)[98]–[100]. An expression for the surface roughness is given by Parmar and Mellor[101].

$$R_f = kd_0\varepsilon + R_0 \tag{4.2}$$

Where R_f = final roughness, R_0 = initial roughness, d_0 = grain size, ε = strain, and k = an empirical constant dependent on material.

Baydogan et al.[102] found $k=2.2x10^{-3}$ for 304 stainless steel, while also discovering a "critical strain" below which no surface roughening occurs, which is dependent on grain size.

Samples made from an alloy with an average grain diameter of 39μm showed significant cracking and surface roughening during forming, and were deemed unusable. An SEM image of a sample that experienced significant orange peel effect during hydroforming is shown in Figure 4.6.

The 316L stainless steel sheet used in this study had an average grain diameter of 11 μm, which was small enough to avoid roughening of its free surfaces during forming.

4.1.1.3 Sample Mounts

After forming, the samples were TIG welded around their circumference onto a specially designed 316 stainless steel sample-mount with the concave side of the dome facing the water, shown in Figure 4.7.

The sample mounts were custom designed to simultaneously form a high-pressure water seal with the corrosion cell on one side, and a high vacuum seal on the accelerator-facing side. On the water side, the seal is formed by a compressed Zircaloy gasket, while a Conflat flange (CF) forms a high-vacuum seal with the beamline flange on the beamline-facing side. After the sample mounts were machined, a zirconium coating was sputtered on all surfaces, and later oxidized in a furnace at 450˚C for two hours to form an electrically insulating layer of zirconia. This insulating layer provided an extra layer of electrical isolation between the sample mount and the cell, while also preventing the sample mount from interfering with ECP measurements near the sample surface.

4.1.1.4 Measurement

After forming, it was important to have a good measurement of sample thickness to ensure proton beam penetration during irradiation. Due to the unique geometry of the sample mounts, measurement of formed sample dimensions after welding was difficult. As an alternative to mechanical measurement, the post-forming thickness of the sample was measured with a proton beam, using a method adapted from Hosemann et al.[103]. The sample was bombarded with a

proton beam with a diameter of 0.5 mm and positioned in an analysis chamber with a 1-mm-thick stainless steel plate behind the sample and serving as a current detector. The energy of the proton beam was increased in steps of 20 keV until current was detected, indicating transmission through the samples. The detected current was recorded as a function of proton energy. Figure 4.8 shows measurements for two stainless steel samples, with the detected current shown as a fraction of the total beam current, which represents the fraction of protons transmitted through the sample.

Using the energy at half the maximum value of the curve, simulations were run using SRIM 2013 [96] to determine the sample thickness using the mean range of the beam at the selected energy. As a check, some test samples were measured using both the proton beam and a Mitutoyo model 342 point micrometer. The results are given in Table 4.1, and show good agreement between the two methods.

4.1.1.5 Pressure testing

To ensure safety during experiments, extensive pressure testing was conducted on samples before use in the IAC experiment. Tests were carried out using a specially-built rupture testing system shown schematically in Figure 4.9.

Samples were sealed in a test-cell using the same high-pressure water seal as used in the experimental corrosion cell. The cell was then placed in a metal canister to contain the water and steam following sample rupture. The canister was sealed and placed in a box furnace. A high-pressure pump circulated water and maintained pressure on the dead-leg, which ran into the furnace to the test-cell. After sample loading, the water pressure was increased to 13.8 MPa. The

temperature was then increased to 320˚C, and allowed to stabilize for ~30 minutes. Pressure was then increased at a rate of 0.2 MPa/min up to 20.7 MPa, followed by 0.04 MPa/min until rupture. The sample shown in Figure 4.10 had a burst pressure of 19.8 MPa, which was well in excess of the minimum rupture strength for the experiment.

4.1.2 Corrosion Cell Design

The corrosion cell was designed to contain a 10 mL volume of flowing water at high temperature and pressure, while providing access for in-situ diagnostic equipment. The cell was constructed of 316 stainless steel and contained six high-pressure feedthroughs machined into the sides, as shown in Figure 4.11.

The feed-throughs were used to allow access for water inlet and outlet, electrochemical potential (ECP) probes, and a thermocouple. To electrically isolate the sample from the corrosion cell body and allow for ECP measurements of the sample surface, the bolts that hold the cell to the beamline flange were fitted with ceramic washers, and the zirconium gasket that forms the water-side high pressure seal was pre-oxidized in a furnace to provide an insulating zirconia layer. The sample remains electrically coupled to the beamline flange only, which is isolated from the rest of the beamline by a ceramic drift tube. The cell was encircled by a resistive heating band, and then wrapped in fiberglass insulating tape and loose fiberglass insulating filler. The time to heat to 320˚C is dependent on the water flow rate, but is typically around 3 hours for flow rates between 5ml/min and 20 ml/min.

4.1.2.1 ECP

ECP was measured using a palladium-hydrogen (Pd-H_2) reference electrode, as described by Vasile and Enke[104]. The palladium electrode was cathodically charged under constant current from a platinum electrode to make it independent of the water conductivity. The electrodes consisted of 0.5-mm diameter wire wrapped into 5-mm-long coils with a diameter of 1.5 mm. The Pd electrode tip was placed approximately 2 mm from the sample surface. The equilibrium state of palladium hydride and hydrogen at the electrode surface resulted in a constant potential for the Pd-H_2 electrode, was used as a reference electrode. The potential of the Pd-H_2 electrode is governed by the modified Nernst equation, shown in Equation 4.3.

$$E = -2.303\frac{RT}{F}pH_T - 2.303\frac{RT}{2F}\log\left(\frac{\theta}{1-\theta}\right) \quad (4.3)$$

where R is the gas constant, F is Faraday's constant, pH_T is the pH value at temperature T, and θ is the degree of hydrogen coverage on the electrode surface. The electrode potential is only sensitive to solution pH, hydrogen activity at the electrode surface, temperature, and charging current. Figure 4.12 shows that the ECP remained constant while the temperature and conductivity of the corrosion cell water were stepped down.

4.1.3 Accelerator and Beamline

The corrosion cell is attached to a dedicated beamline of the 3 MV Pelletron accelerator (Wolverine) at the Michigan Ion Beam Laboratory (MIBL). The accelerator is capable of producing proton energies up to 3.4 MeV with a target current up to 60 μA. A schematic drawing of the beamline is shown in Figure 4.13. The beamline was built specifically for this experiment and contains safety systems to prevent damage to the accelerator and high voltage beamline components in case of a sample rupture.

After being directed by a bending magnet from the accelerator into the beamline, the beam is raster-scanned to ensure a uniform damage rate over the irradiated area. It was shaped into a 6mm x 6mm square defined by a system of movable slits, each with independent motion control. The slits are each isolated, and the current is monitored and recorded on each. The beam is centered by ensuring equal current on each of the four slits. After passing through the slits, the beam passes through a 2mm-diameter circular aperture mounted on the back of the sample mount to define the exposed area of the sample.

A unique feature of the beamline is the safety system that ensures that critical beamline and accelerator components will not be damaged in the event of sample rupture. The system features two fast-closing gate valves, shown in red in Figure 4.13, which are triggered by a pair of cold-cathode gauges (for redundancy) in the sample chamber.

When the cold-cathode gauges detect a pressure increase above a user-specified threshold, a signal triggers the fast-closing valves which close immediately, cutting-off the shockwave from the ruptured sample and preventing damage to sensitive equipment. A signal from the safety circuit also cuts power to electronic components on the beamline, and stops the flow of water into the corrosion cell. For a typical chamber pressure of $< 1 \times 10^{-5}$ Pa during

experiments, a pressure threshold of $1x\ 10^{-3}$ Pa was typically used. Total response time between the detection of a pressure increase and the full closure of the valves was measured to be below 20 milliseconds.

The system was tested by attaching an argon cylinder to a closed valve at the end of the beamline where the corrosion cell would normally be attached. The beamline was then pumped to a pressure of $1x10^{-5}$ Pa, and the tubing behind the value was pressurized with argon. To simulate a sample rupture, the valve was opened and the fast-closing gate valves were triggered and shut. The pressure in the beamline between the two fast-closing gate-valves was measured immediately after the values were shut, and the results are shown in Table 4.2. It was found that increasing the pressure of the argon gas resulted in a greater loss of vacuum in the beamline, but all losses were considered acceptable to protect beamline and accelerator components in the event of a sample rupture.

4.1.4 Water Loop

The water loop was designed to flow water with carefully controlled and monitored chemistry through the corrosion cell. A schematic of the water system is shown in Figure 4.14.

Water is deionized and treated with a UV light to break-down organics before it is added to a large circulating glass column. A gas cylinder is attached to bubble gasses, such as argon, to deaerate the water. For PWR experiments, hydrogen is bubbled, and a column overpressure of 0.12 MPa was maintained to reach 3wppm H_2. A secondary mixing column is available for chemical additions such as boron and lithium. The column is connected to a fast-circulating sub-loop with a DI filter, a Mettler Toledo Thornton® dissolved oxygen (DO) sensor, and an

Omega® conductivity sensor. Water is allowed to circulate in this column until conductivity and DO levels drop below the experiment-dependent maximums, typically under 0.2 µS/cm and 10wppb respectively.

From the column, water flows through 316 stainless steel tubing to a pair of Lab Alliance® dual-piston high-pressure pumps. An accumulator is used to remove pressure oscillations due to the pumps. The water flows through a custom-built tube-in-tube stainless steel heat exchanger, and then into the corrosion cell where it is quickly brought to temperature. All tubing containing water at elevated temperatures is wrapped with fiberglass insulating tape to minimize heat loss. Water exiting the corrosion cell flows through the heat exchanger again, followed by a chiller tube that cools the water to room temperature. Water then flows through a Tescom® back pressure regulator where it is brought to atmospheric pressure. To determine any effects of irradiation on the cell water chemistry, the water flows through a second set of conductivity and DO sensors before recirculation into the primary column.

4.1.5 Verification

Tests were conducted to determine the viability of the facility, using three different water conditions: 130˚C deaerated water, 320˚C deaerated water and 320˚C water with 3wppm H_2. Samples of 316 stainless steel measuring 37µm-thick were held at each temperature for 2 days and irradiated at beam currents between 0.5 µA/cm^2 and 10 µA/cm^2 for approximately 20-30 minutes each. Approximately 15 minutes were required for water to flow from the corrosion cell to the conductivity and DO sensors, so this irradiation time was chosen to give sufficient time for the sensors to reflect steady-state conditions within the 10 mL corrosion cell at each beam

current. The gas cylinder was switched from argon to hydrogen after the first day of experiments at 320˚C to test both deaerated and hydrogenated water. Dissolved oxygen and water conductivity were measured in each condition, and are shown in Figure 4.15. Each peak represents a 20-30 minute irradiation at a single current density.

During the irradiation at 130˚C in deaerated water, application of the beam to the sample resulted in large increases in dissolved oxygen and modest increases in water conductivity. The DO can likely be attributed to water radiolysis, although the measured concentrations were significantly higher than previously reported radiolysis yields [21]. The jumps in conductivity were previously attributed to an increase in aqueous ions due to enhanced corrosion, but after the installation of an in-line UV light to break down organic carbon, the effect of irradiation on conductivity disappeared. The previous conductivity increases under irradiation are likely due to radiolytic decomposition of organic carbon.

At 320˚C the magnitude of the DO peaks under irradiation decreased to only a few wppb, likely due to reactions with the hot stainless steel walls of the corrosion cell and outlet tubing before reaching the DO sensor. When 3wppm dissolved hydrogen was added to 320˚C water, DO was undetectable while water conductivity showed similar response as in the deaerated condition. Kanjana et al. [63] have shown previously that dissolved hydrogen is effective at suppressing oxygen produced by radiolysis, so the lack of any measured oxygen is consistent with their findings.

Figure 4.16 shows the behavior of DO as a function of current density for at 130°C and 320°C. Note that the DO increases linearly with current density for all of the cases, which is inconsistent with the expected square-root dependence of radiolytic oxygen production on

energy deposition [21]. The value of DO at 130°C is 40-60x that at 320°C due to accelerated reaction and recombination of oxygen at the higher temperature. A higher flow rate results in a reduction in the amount of oxygen per unit volume of water, accounting for the reduced values of measured DO.

Sample temperature was also measured during irradiation in 320˚C water to verify that any measured effects of irradiation were not simply the result of sample heating. Measurements were made on the vacuum-facing side of the sample using an infrared pyrometer. At the highest beam current density of 10 μA/cm^2, the sample temperature increased only 3˚C from 320˚C to 323˚C. The small increase can likely be attributed to the very thin sample geometry combined with efficient heat conduction by the water in the corrosion cell.

4.2 Experimental Procedure

With the experimental apparatus fully described, this section will describe the procedures used for the experiments. Following a brief discussion of the sample material, the procedures used for the standard IAC experiments will be discussed in section 3.2.2, followed by a description of the pre-oxidation experiment in 3.2.3 and the static cell experiment is 3.2.4.

4.2.1 Material

Experiments were conducted on three different samples made from Type 316L stainless steel sheet stock, heat 13364044. The composition is given in Table 4.3, and other properties of the material are given in Table 4.4.

4.2.2 Standard IAC experiments

The majority of experiments performed for this study will be referenced as standard IAC experiments to differentiate them from the pre-exposure experiment and the static cell experiment. The standard IAC experiments consist of samples that were exposed for a single heating in the IAC cell, with or without irradiation.

Standard IAC samples were exposed to 320˚C water with 3 ppm H_2 for 4, 12, 24, or 72 hrs. Irradiated samples were irradiated with constant proton beam currents of 10 or 1 μA/cm^2, which produced dose rates at the sample-water interface of 7 x 10^{-6} dpa/s and 7 x 10^{-7} dpa/s. Unirradiated samples were also prepared for 4, 24, and 72 hrs for comparison to the irradiated samples.

A list of standard irradiated and unirradiated samples is given in Table 4.5. The first two letters refer to the level of irradiation used (high dose rate, low dose rate, or none), while the numbers refer to the exposure time in hours.

For each experiment, samples were loaded into the corrosion cell, and allowed to stabilize in room temperature water with a flow rate of 15 mL/min until conductivity and dissolved oxygen content settled to steady state. The cell was then heated to 320˚C over approximately 3 hrs. Once cell temperature stabilized at 320˚C, the beam was turned on for irradiated experiments. The samples remained at temperature for 4, 12, 24, or 72 hrs, with or without irradiation. At the end of the prescribed exposure time, the beam was turned off, and the cell was cooled back to room temperature over approximately 3 hrs. Figure 4.17 shows water chemistry data over the course of the exposure of Hi12. The graph shows water conductivity data

during the exposure, as well as DO, pressure, and temperature. Water data for other samples is given in Appendix B.

4.2.3 Pre-Oxidation Experiment

The standard IAC experiments began with clean samples, and examined the effect of radiation on the entire oxidation process. It is also desirable to study the effect of irradiation on an already-formed oxide to gain insight into the effect of an already-formed kinetic barrier. To test the effect of irradiation on a pre-formed oxide, sample Pr24 was exposed in an autoclave for 72 hrs in 320˚C water with 3 wppm H_2, and then irradiated for 24 hrs in the IAC cell also in 320˚C water with 3 wppm H_2. After the first autoclave exposure, a FIB liftout was taken from the sample before the second exposure in the IAC cell to compare the oxides before and after the irradiated exposure.

4.2.4 Static Cell Experiment

Due to the very small size of the sample, the concentration of chromium dissolving into solution during the IAC experiments was very low – too low to detect reliably with UV-Visible light spectroscopy. To overcome this limitation, a static-cell experiment was devised in which the corrosion cell was connected to a dead-leg off the main circulating loop, minimizing the exchange of water in the cell, allowing aqueous Cr species to reach a detectible level. The modification to the water loop is shown in Figure 4.18. The cell volume was measured to be 8 mL, and the volume of water in the tubing was 2 mL, totaling 10 mL in the collection volume.

Static cell experiments were conducted in 320˚C water with 3 wppm H_2. For each experiment, a water sample was collected at room temperature before heating. The cell was then heated to 320˚C, at which point the proton beam was then turned on at a current density of 10 $\mu A/cm^2$. After 4 or 8 hours, the beam was turned off, and the cell was allowed to cool. At 305˚C, the valve leading to the cell was closed to prevent ingress of water from the water loop due to densification during cooling (it was not closed immediately before cooling to allow some margin-of-error in maintaining pressure inside the cell during cooling). After cooling to 50˚C, the cell water was collected. Unirradiated experiments were also conducted for 4 and 8 hrs using the same procedure, but without irradiation.

For each collection, a 2 mL sample was taken for ICP-MS to determine total Cr content, and another 2 mL sample was mixed with an ammonium-hydroxide buffer for UV-visible light spectroscopy to determine the Cr^{6+} content. Samples were refrigerated after collection, and were shipped in refrigerated packaging to Brooks Applied Labs for testing.

For 2 mL samples, the minimum detectability of Cr^{6+} using UV-Visible light spectroscopy is around 100 parts-per-trillion. To ensure that Cr^{6+} was be above the detectable limit, the concentration was estimated using Equation 4.4.

$$C = \frac{\rho_a * A * x * f_{cr} * d * y * m_m}{\rho_m * V} \tag{4.4}$$

Where

$C = \text{concentration of } Cr^{6+}$

$\rho_a = \text{oxide atomic density}$

$\rho_m = \text{oxide molar density}$

$$A = \text{irradiated area}$$

$$x = \text{oxide thickness}$$

$$f_{cr} = \text{fraction of Cr depleted}$$

$$y = \text{yield, or the amount of acqueous Cr that is collected}$$

(i. e. not lost before collection)

$$m_m = \text{molar mass of the species of interest}$$

$$V = \text{water volume}$$

Using some known values

$$\rho_a = \text{oxide atomic density} = 5.15 \frac{g}{cm^3}$$

$$\rho_m = \text{oxide molar density} = 225.7675 \frac{g}{mol}$$

$$A = \text{irradiated area} = 3.14\ mm^2$$

$$m_m = \text{molar mass of the species of interest} = 116 \frac{g}{mol}\ \text{of}\ CrO_4^{2-}$$

$$V = \text{water volume} = 10\ ml$$

With some reasonable assumptions

$$f_{cr} = \text{fraction of Cr depleted} = 0.6$$

$$y = \text{yield} = 0.3$$

$$x = \text{oxide thickness} = 65 \text{ nm}$$

The oxide thickness is an estimate based on the thickness of the oxide from the unirradiated portion of sample Hi04 (shown later in Chapter 4).

Based on this calculation, a concentration of 3 ppb can be achieved in 4 hours. This is well in excess of the minimum sensitivity of UV-Vis spectroscopy of ~0.1 ppb. The time is chosen allow a large margin above the detectability threshold, while still minimizing changes to the cell water chemistry that might occur during a longer experiment in static water.

4.3 Characterization

A number of characterization techniques were used to determine the composition and morphology of the oxide films both with and without irradiation. This section will discuss them.

4.3.1 TEM microscopy

TEM specimens were prepared with the FIB liftout technique, using FEI Helios and Nova dual-beam SEM/FIB microscopes. A protective layer of platinum was deposited over a 2x20 µm area on the oxide surface using a two-step deposition technique. First, a thin layer of platinum was deposited using a 5kV electron beam to preserve a sharp boundary, and then a 30 kV ion beam was used to increase the thickness of the platinum layer to ~5 µm. After Pt deposition, trenches were cut on both sides of the specimen a depth of ~7 µm. The specimen is them removed with an Omniprobe micromanipulator, welded with Pt to a copper grid, and thinned to

less than 200 nm in thickness using a 30 keV ion beam. Images of the specimen before extraction and after attachment to the grid are shown in Figure 4.19.

TEM images were taken using JEOL 2010f and 2100 FEG electron microscopes, operating at 200 kV in STEM mode. Both bright-field (BF) and high angle annular dark field (HAADF) imaging modes were used. Bright-field was typically used for imaging oxide morphology, while HAADF was used for low-magnification images to determine oxide thickness.

STEM-EDS data was taken with an EDAX EDS system, and quantified using standardless ZAF quantification in Gatan Digital Micrograph software. Linescans were taken with step sizes between 1.5 and 6 nm, and dwell time was set to gather a minimum of 400 counts in each peak to ensure <5% error in each of the elements analyzed.

4.3.2 Raman Spectroscopy

While the use of Raman spectroscopy to study corrosion is not common, it has been successfully employed in studies of stainless steel oxidation in LWR conditions[50], [52], [53], [105]–[107]. The technique is useful for obtaining data on the oxide species present on the sample surface efficiently, although it has some limitations when used to examine an irregularly shaped mixed oxide. Notably, the intensity of peaks cannot reliably indicate quantitative amounts of the oxide species. Despite the limitations, Raman spectroscopy is a useful and efficient technique for determining which oxide species are present in the scale, reveling important insight into the thermodynamic conditions during oxide growth.

For this study, samples were examined after exposure with an InVia Raman spectrometer with a red laser (λ=633nm) operating at a measured power of 8.2 mW. Spectra were taken through a 20x lens, producing a spot size of approximately 20μm. An image taken from the microscope is shown in Figure 4.20.

Magnetite has been shown to oxidize to hematite during Raman spectroscopy due to heat from the laser[108], however a sufficiently low laser power was used for this work. This can be verified by the lack of any apparent hematite Raman modes on unirradiated samples, indicating that the magnetite did not oxidize to hematite.

4.3.3 SEM Microscopy

Sample surfaces were examined with SEM microscopy using FEI Helios, Nova, and Quanta microscopes. Secondary electron imaging was used, with an Everhart-Thornley detector. The electron beam was typically set to an energy of 5 keV, at currents of 0.2-0.4 nA. Most images used for this work were taken at magnifications of 5,000X or 20,000X.

4.4 **Summary**

A facility has been established for the study of irradiation accelerated corrosion using in-situ proton irradiation. Samples were designed to be thin enough to allow the 3.2 MeV proton beam to pass completely through the samples while still being strong enough to contain high pressure water in the corrosion cell. By allowing the sample to serve as a “window” into the

corrosion cell through which the proton beam passes, the simultaneous effects of displacement damage and radiolysis on corrosion can be studied. A corrosion cell with a water loop was constructed with in-situ diagnostics to monitor ECP, dissolved oxygen, water conductivity, and temperature. The corrosion cell is located on a dedicated beamline with a system of fast-closing valves to protect the accelerator and beamline components in the event of sample rupture.

The facility was tested by irradiating a stainless steel sample at varied beam current densities, up to 10 $\mu A/cm^2$ in 130°C deaerated water, 320°C deaerated water, and 320°C hydrogenated water. Increases in the dissolved oxygen varied with the proton beam current suggesting that irradiation was creating radiolysis products in the cell water. Measured DO was much higher at 130˚C than at 320˚C, likely due to a higher rate of recombination of radiolytically-produced oxygen at the higher temperature. The addition of 3wppm H_2 was sufficient to suppress DO below detectable levels. These tests establish the capability of the facility for studies into the effect of irradiation on corrosion in high temperature water.

Experiments were conducted in which samples were exposed for 4,12, 24, or 72 hrs in 320˚C water with 3 wppm H_2, and irradiated at dose rates of 400 or 4000 kGy/s, corresponding to damage rates of $7x10^{-7}$ to $7x10^{-6}$ dpa/s respectively. A pre-oxidation experiment was conducted in which a sample was exposed to 320˚C water with 3 wppm H_2 for 72 hrs without irradiation, and then subsequently exposed to the same conditions for 24 hrs with irradiation at a dose rate of 4000 kGy/s. A static cell test was conducted in which a non-flowing volume of water was irradiated for 4 or 8 hrs to collect water samples containing chromium. The effect of radiation on the structure and composition of the oxide film was characterized using Raman spectroscopy, TEM, and SEM.

Table 4.1. Results of proton beam measurement of three stainless steel test samples – one flat plate, and two dome-shaped samples, each with a 3.5 mm diameter. Proton beam measurements are compared to measurements taken with a point micrometer.

Sample	Half-maximum energy (keV)	Sample thickness – beam method (μm)	Sample thickness – micrometer method (μm)	Difference (%)
Flat plate	2950	33.7±2.4	34±2.5	1%
Dome 1	3270	39.8±2.4	39±2.5	2%
Dome 2	3070	36.0±2.4	38±2.5	7%

Table 4.2. Results of beamline safety system tests. Argon at various inlet pressures was admitted into the beamline from the location of the sample. The pressure in the beamline between the two fast-closing valves was recorded immediately after the safety system valves shut to determine the loss of vacuum. The starting vacuum was 1×10^{-5} Pa for all tests before the admission of argon.

Argon inlet pressure (MPa)	Pressure in beamline (Pa)
0	2×10^{-4}
0.3	1×10^{-5}
0.7	3×10^{-5}
1.4	7×10^{-5}
2.8	1×10^{-4}
6.9	2×10^{-4}

Table 4.3. Composition of heat 13364044

Element	**C**	**Si**	**Mn**	**S**	**P**	**Cr**	**Ni**	**Mo**	**Cu**	**N**	**Co**	**Fe**
Wt %	0.019	0.520	1.40	0.0004	0.0290	16.77	10.28	2.08	0.300	0.020	0.130	bal

Table 4.4. Properties of heat 13364044

Condition	Annealed
Surface	Bright Annealed
Tensile Strength	641 MPa
0.2% Yield Strength	262 MPa
Elongation 2”	51.70%
ASTM Grain Size	9.5
Hardness	70 HRB
Roughness	~20 nm Ra

Table 4.5. Irradiated and unirradiated samples produced.

Sample	**Time (hrs)**	**Dose Rate (kGy/s)**	**Damage Rate (dpa/s)**	**Damage (dpa)**
Hi04	4	4000	7×10^{-6}	0.1
Hi12	12	4000	7×10^{-6}	0.3
Hi24	24	4000	7×10^{-6}	0.6
Hi72	72	4000	7×10^{-6}	1.8
Lo24	24	400	7×10^{-7}	0.06
Un04	4	na	na	na
Un24	24	na	na	na
Un72	72	na	na	na

na: Not applicable

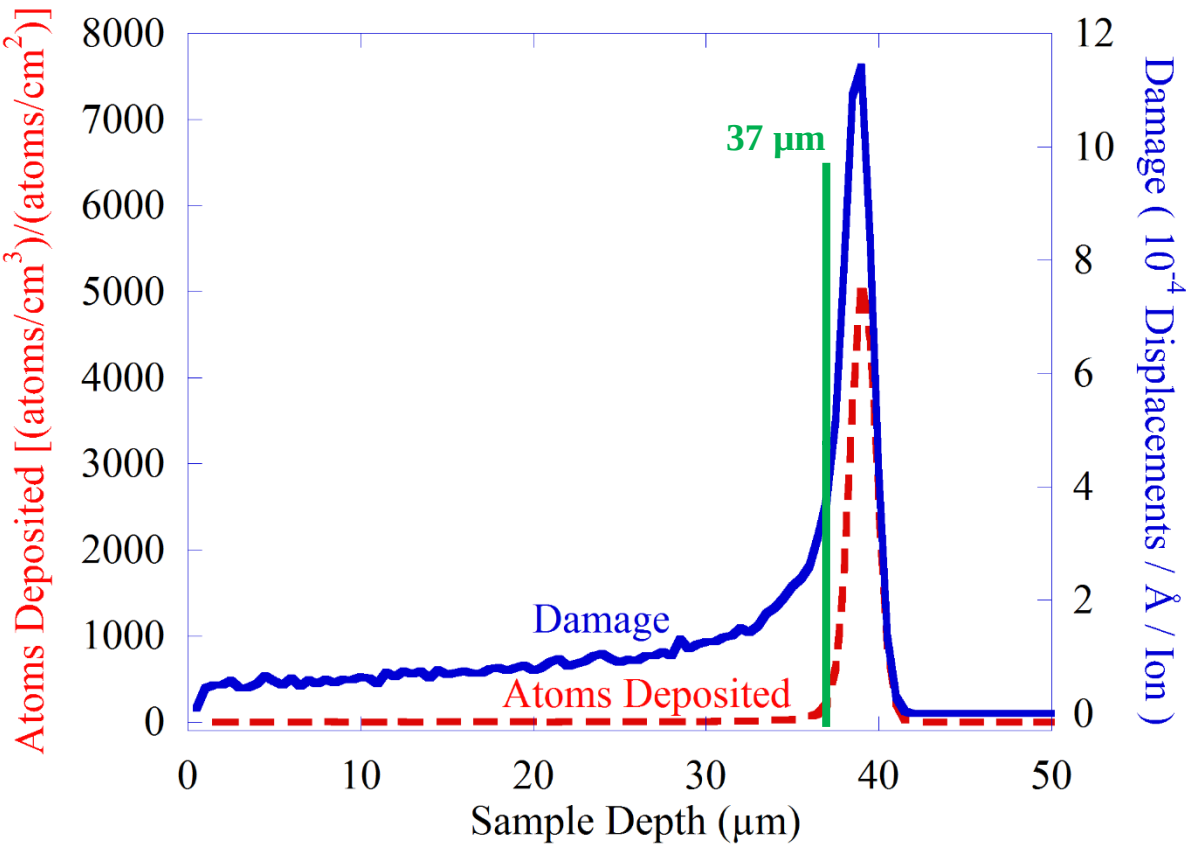

Figure 4.1. Damage and range plots for 3.23 MeV protons into 316 stainless steel as calculated by SRIM 2013 in the Kinchin-Pease mode with 40 eV displacement energy for all major elements. The green line represents the sample thickness used in initial experiments.

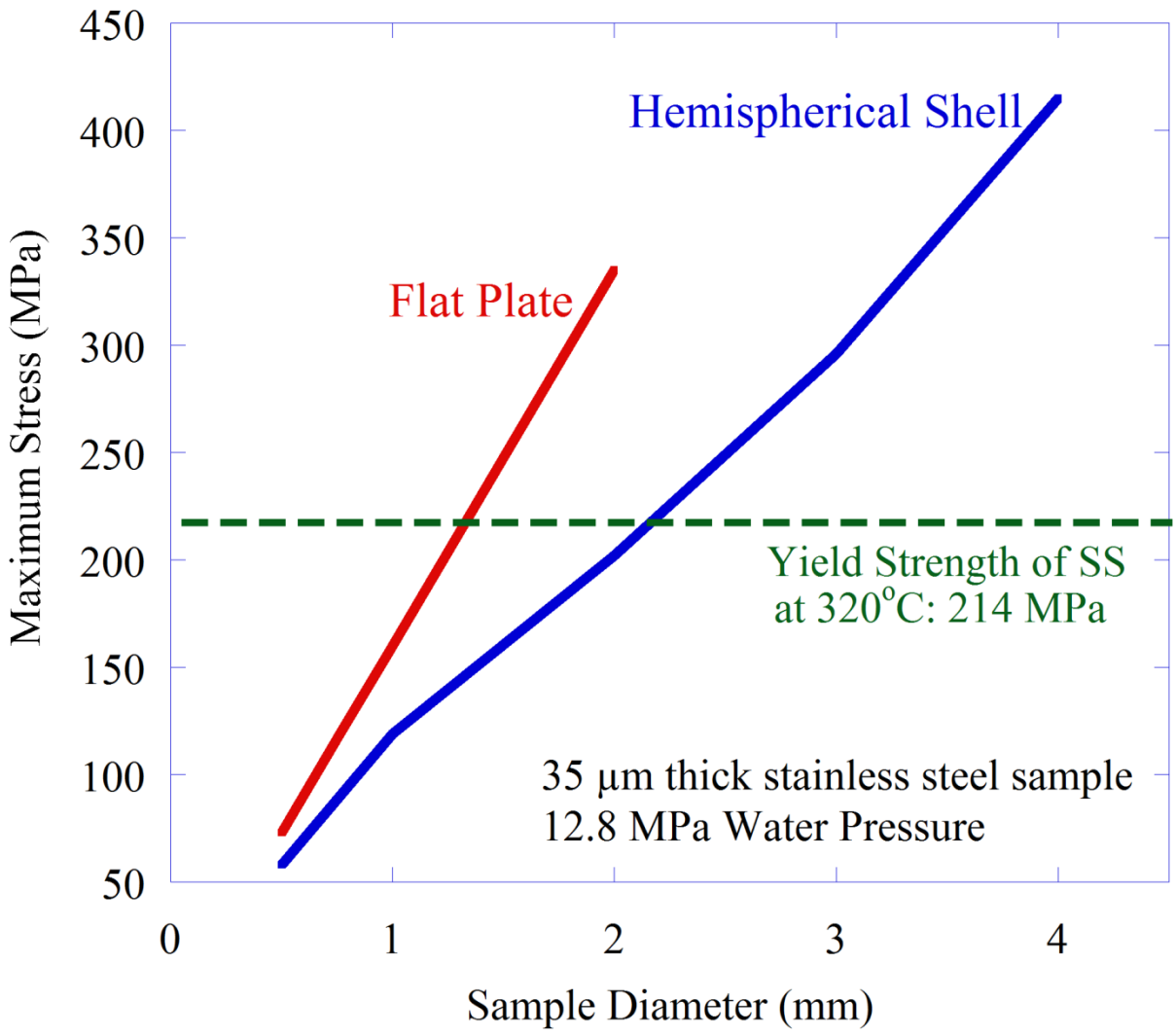

Figure 4.2. Maximum stress on 35 µm-thick samples with 12.8 MPa of pressure as a function of sample diameter. Samples must be designed so as not to exceed the yield strength of the material under experimental conditions, so the hemispherical design allows for a greater sample area at a given maximum stress.

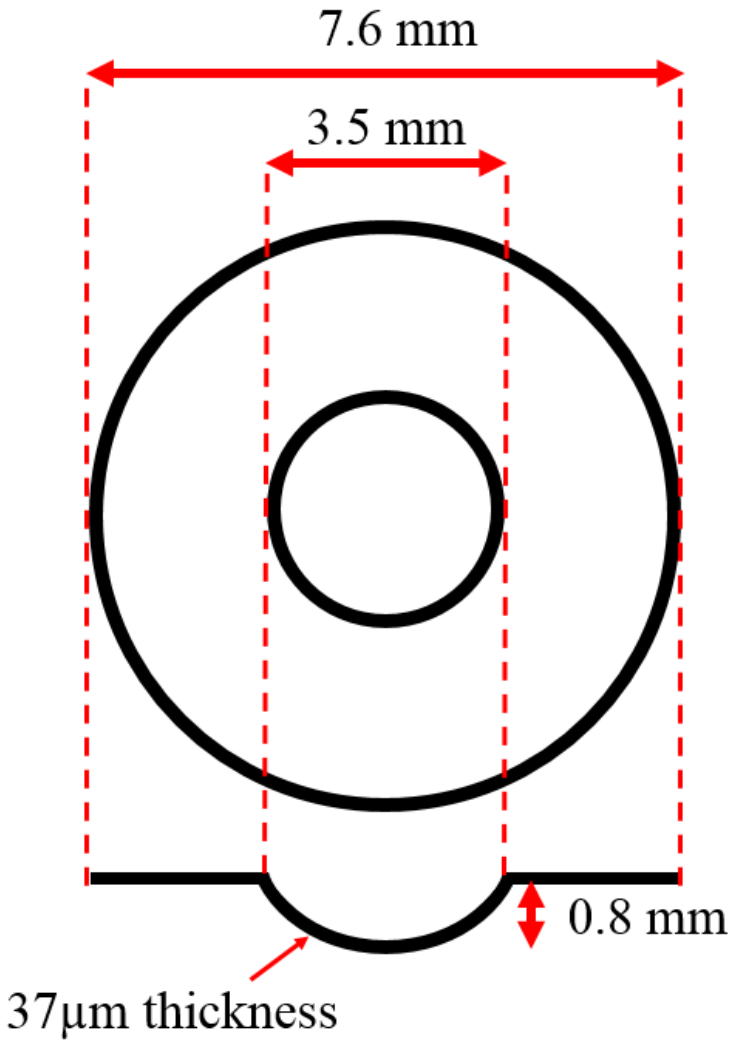

Figure 4.3. Dimensions of the samples made from 316 stainless steel. Sheet stock measuring 50 µm thick was cut into discs with an OD of 7.6 mm. A 3.6 mm diameter dome of approximately 0.8 mm depth was hydraulically formed at the center of each disc.

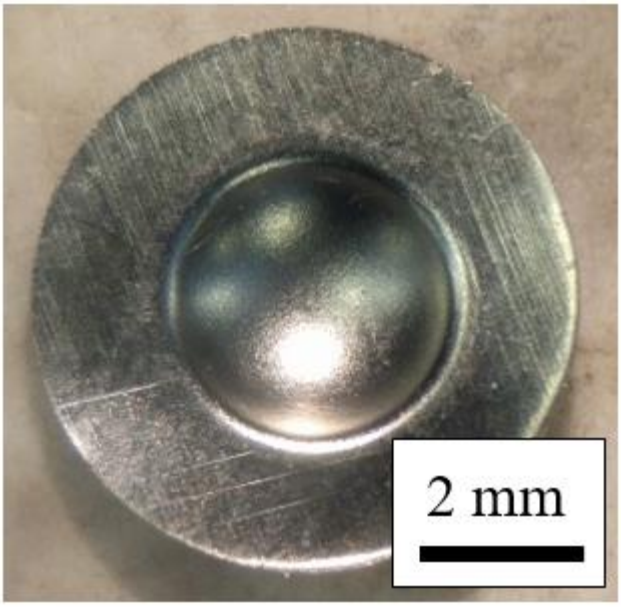

Figure 4.4. An optical image of a stainless steel sample after forming. Sheet stock measuring 50 µm thick was cut into discs with an OD of 7.6 mm. A 3.5 mm diameter dome of approximately 0.8 mm depth was hydraulically formed at the center of each disc.

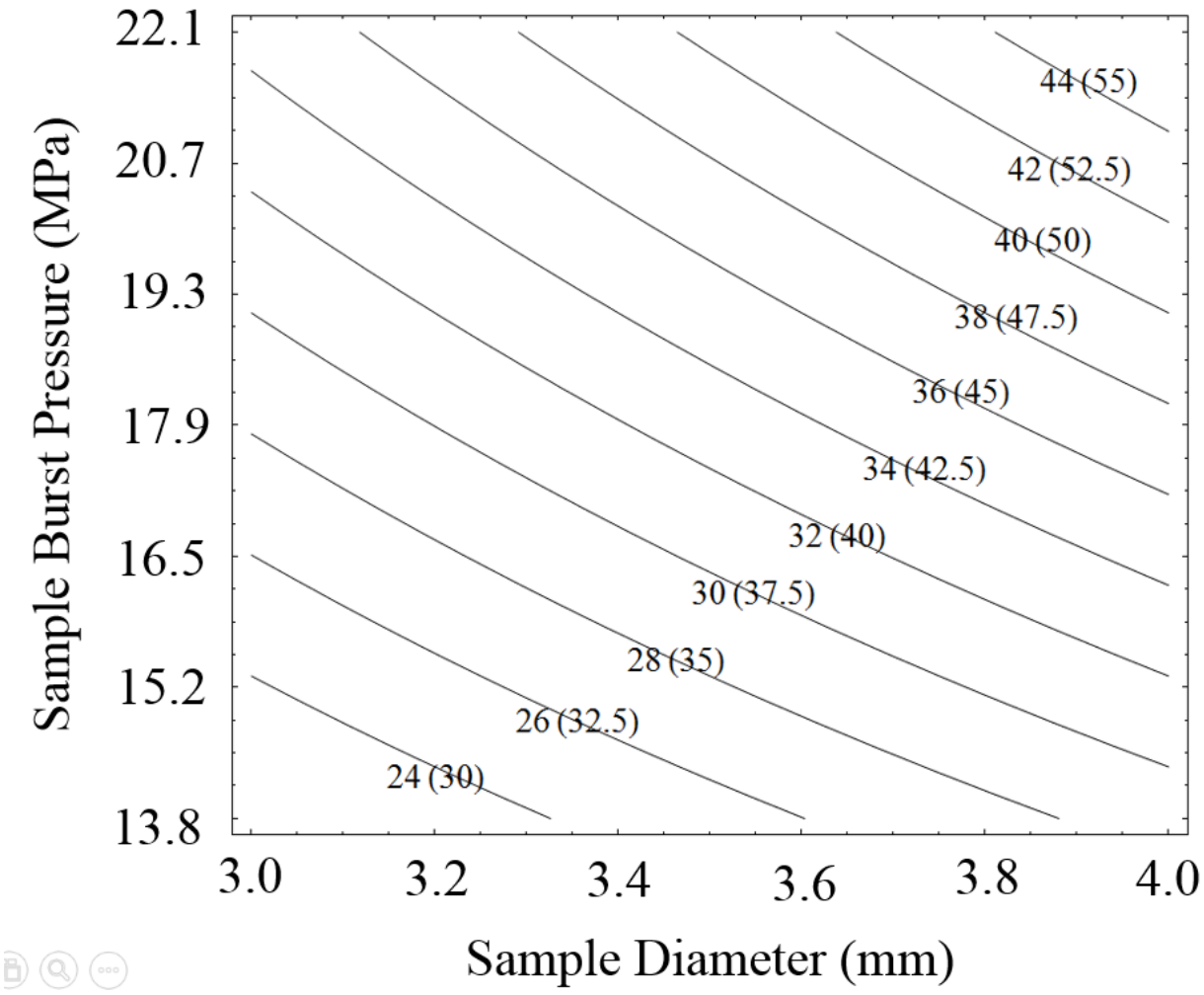

Figure 4.5. Calculated sample burst pressure as a function of sample diameter for different values of sample thickness. Contour lines are the sample thickness at rupture and the pre-formed thickness (in parentheses) given in μm.

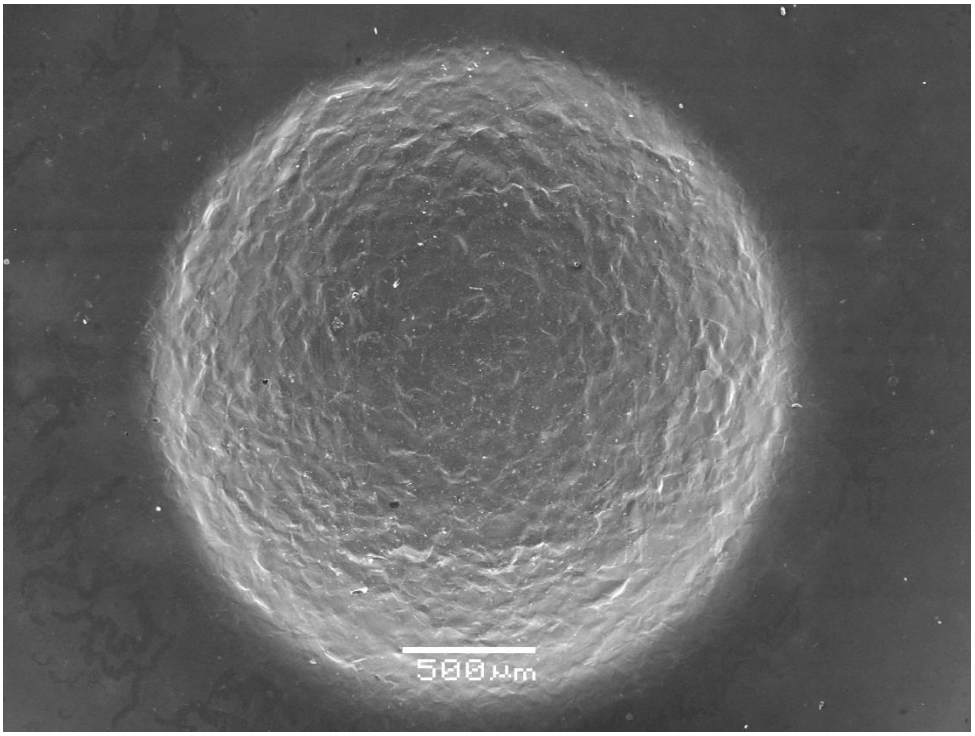

Figure 4.6. SEM image of a stainless steel sample with an average grain diameter of 39µm after hydroforming. Significant surface roughening (orange peel effect) is visible.

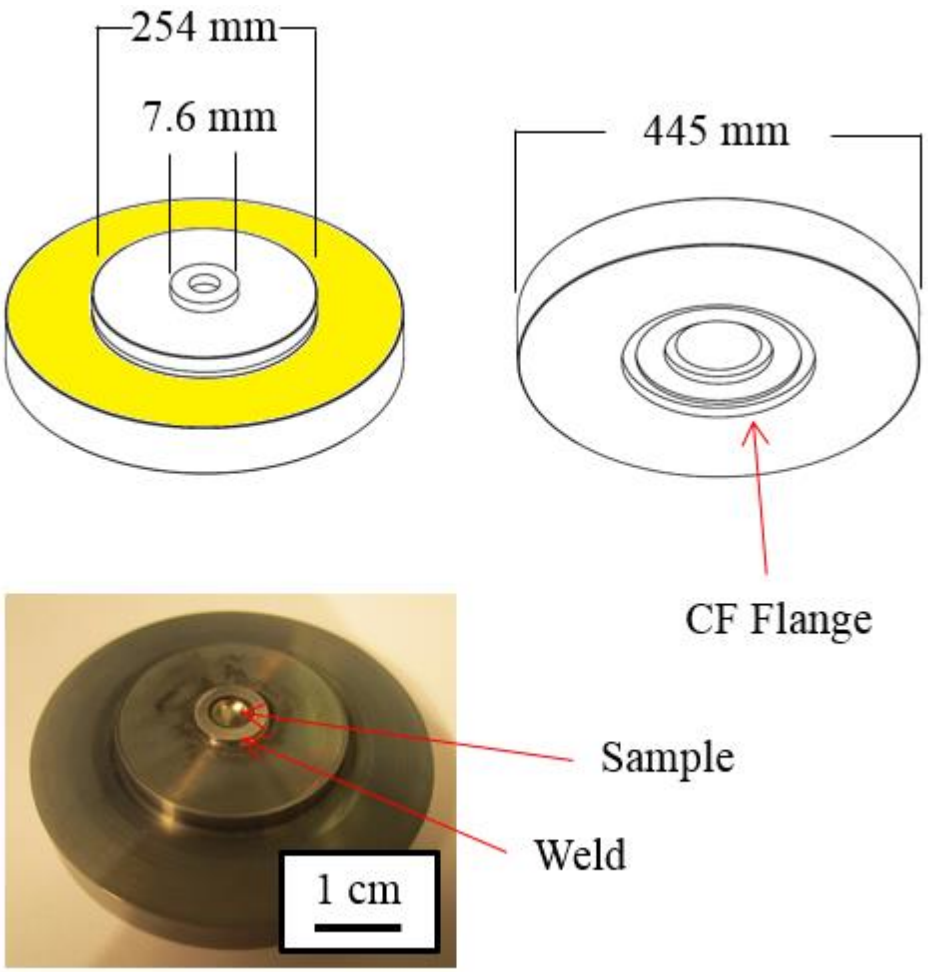

Figure 4.7. Schematic drawing and photograph of the sample mount. A zirconium gasket forms a high pressure water seal with the face highlighted in yellow. A CF flange provides a high vacuum seal on the side facing the beamline. The sample mount is coated in zirconia for electrical isolation.

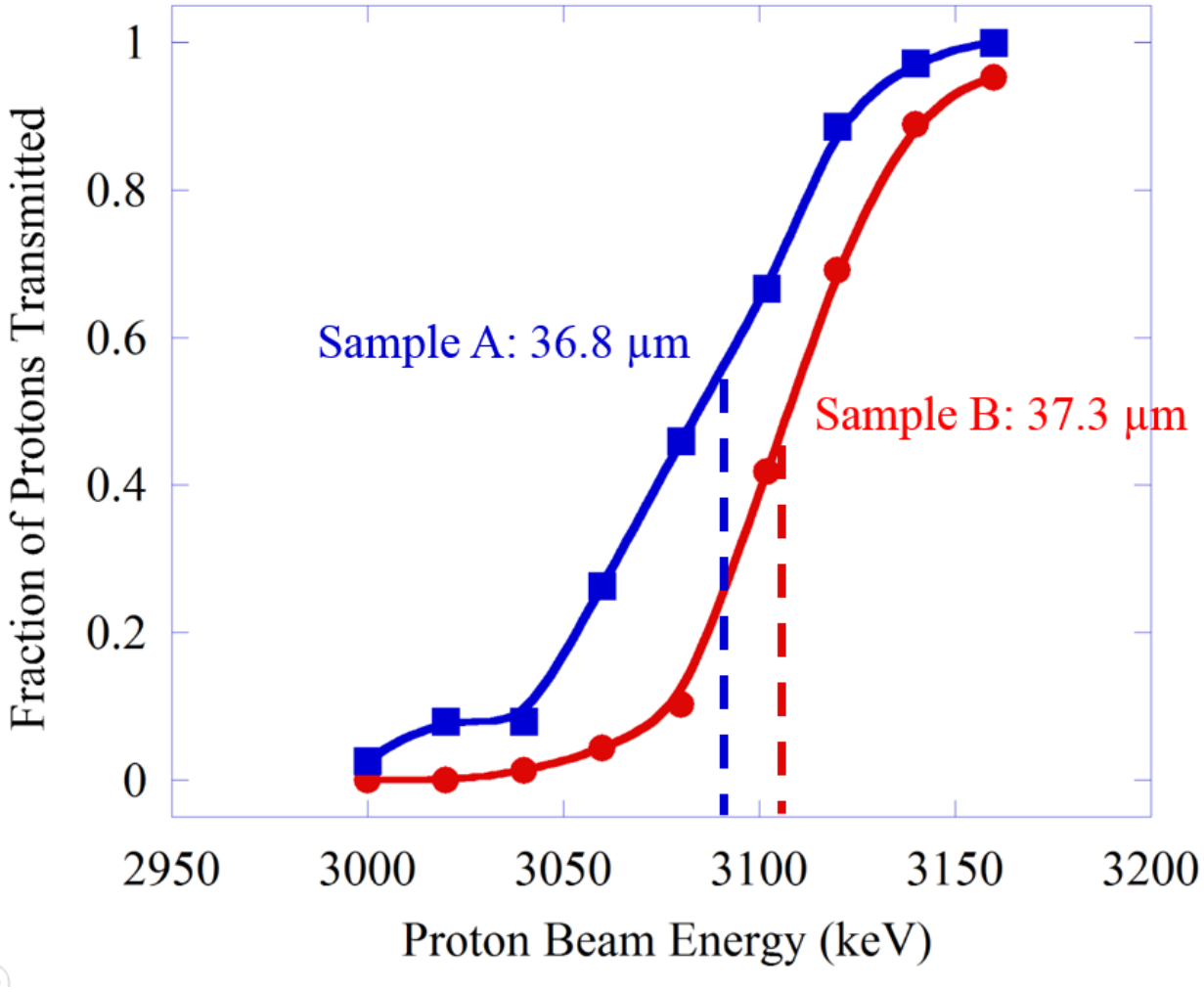

Figure 4.8. Fraction of incident protons transmitted through the sample as a function of the beam energy. The energy of the midpoint of each curve was matched to the range calculated by SRIM 2013 to determine the thickness of each sample.

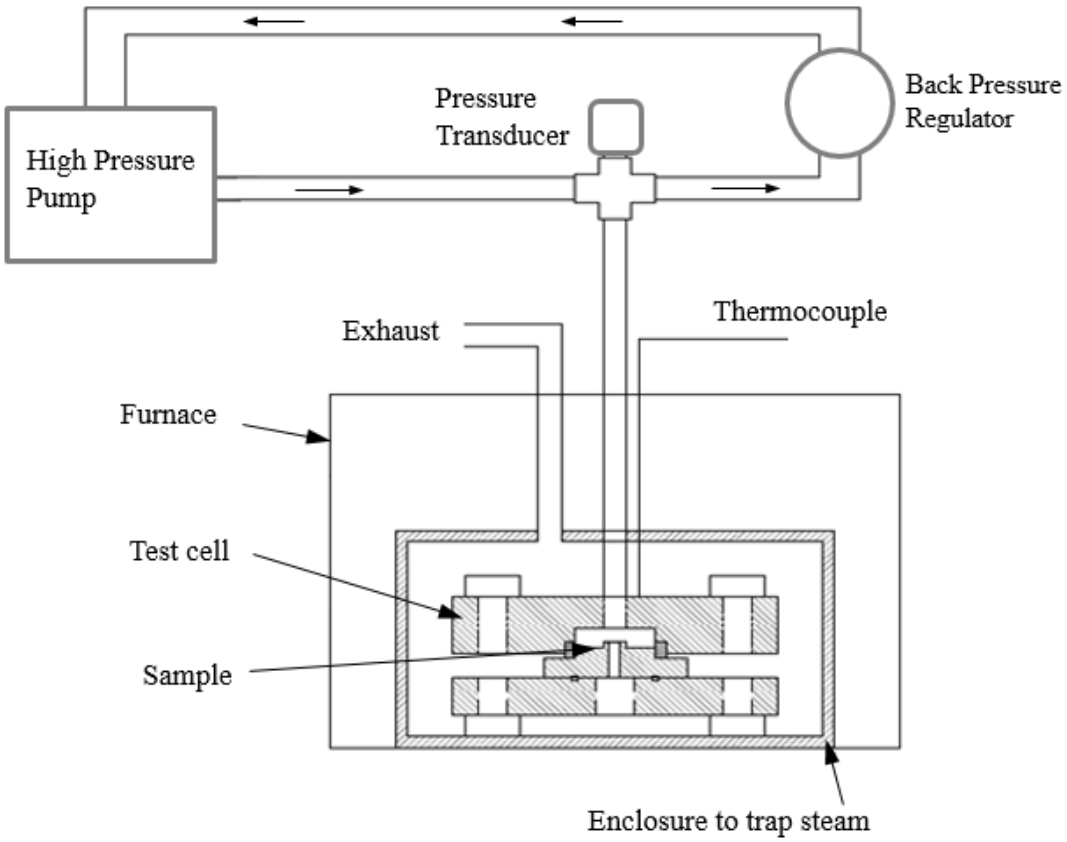

Figure 4.9. Schematic diagram of the system used for sample rupture testing. The sample and test-cell were contained in an enclosure that was placed in a box furnace. The loop was pressurized by a Lab Alliance dual-cylinder pump that applied pressure to the sample via a dead leg off of a flowing water loop located outside the furnace.

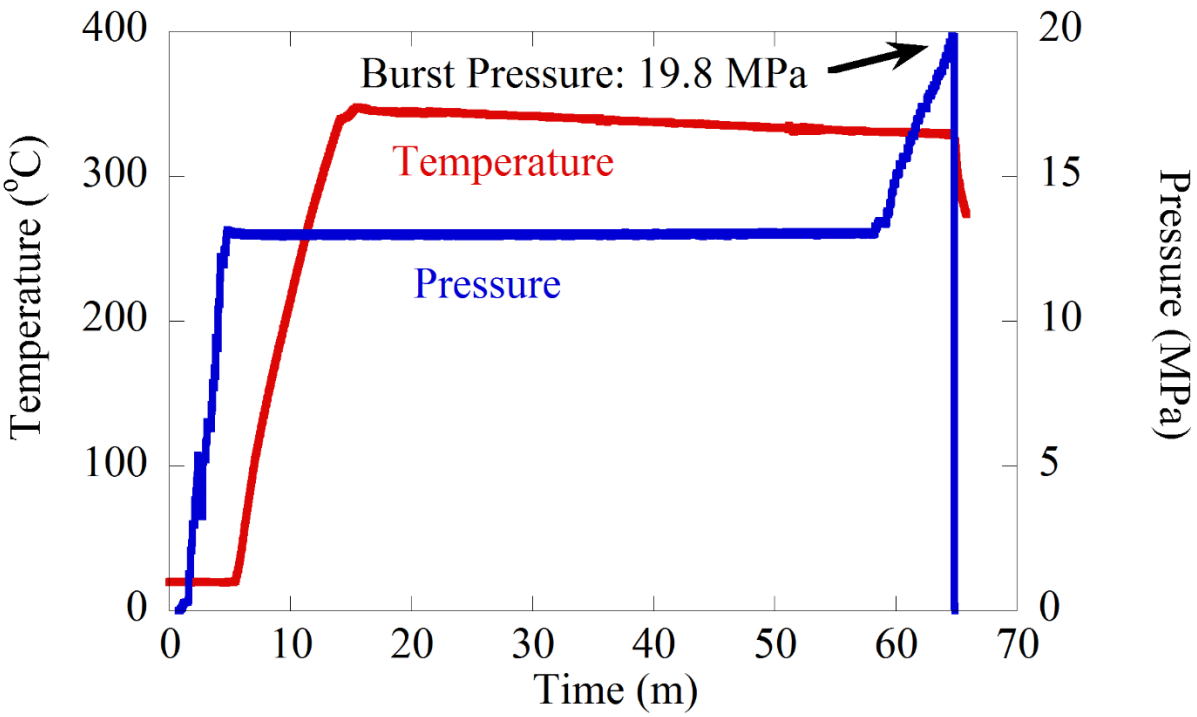

Figure 4.10. Burst test results for a stainless steel sample. After the pressure was increased to 13.8 MPa, the furnace was heated and allowed to reach euilibrium at 320˚C. Pressure was then steadily increased until the sample ruptured.

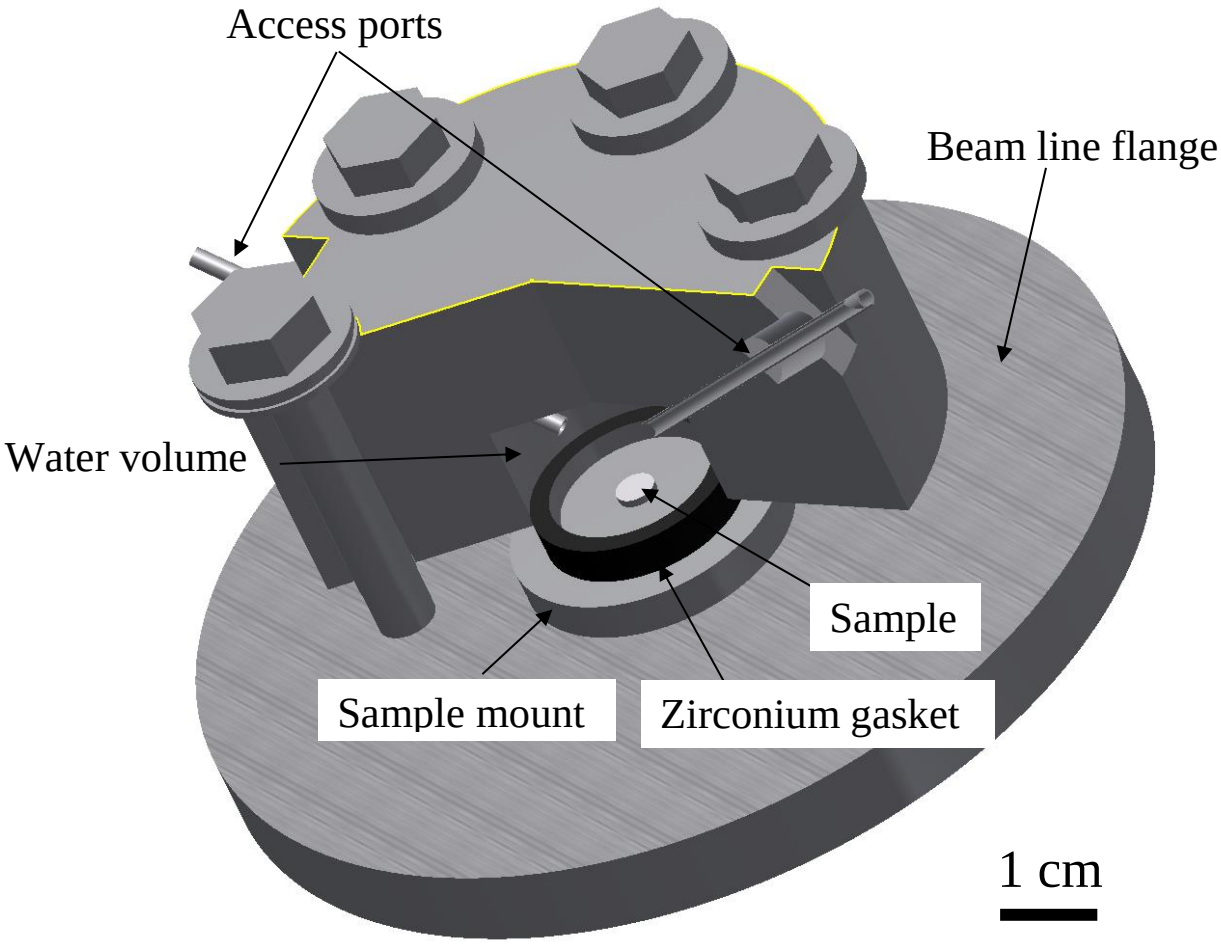

Figure 4.11. A schematic drawing of the corrosion cell attached to the beamline flange. The sample mount is sandwiched between them and the assembly is held together by six bolts. A zirconium gasket seals the high pressure water in the cell volume.

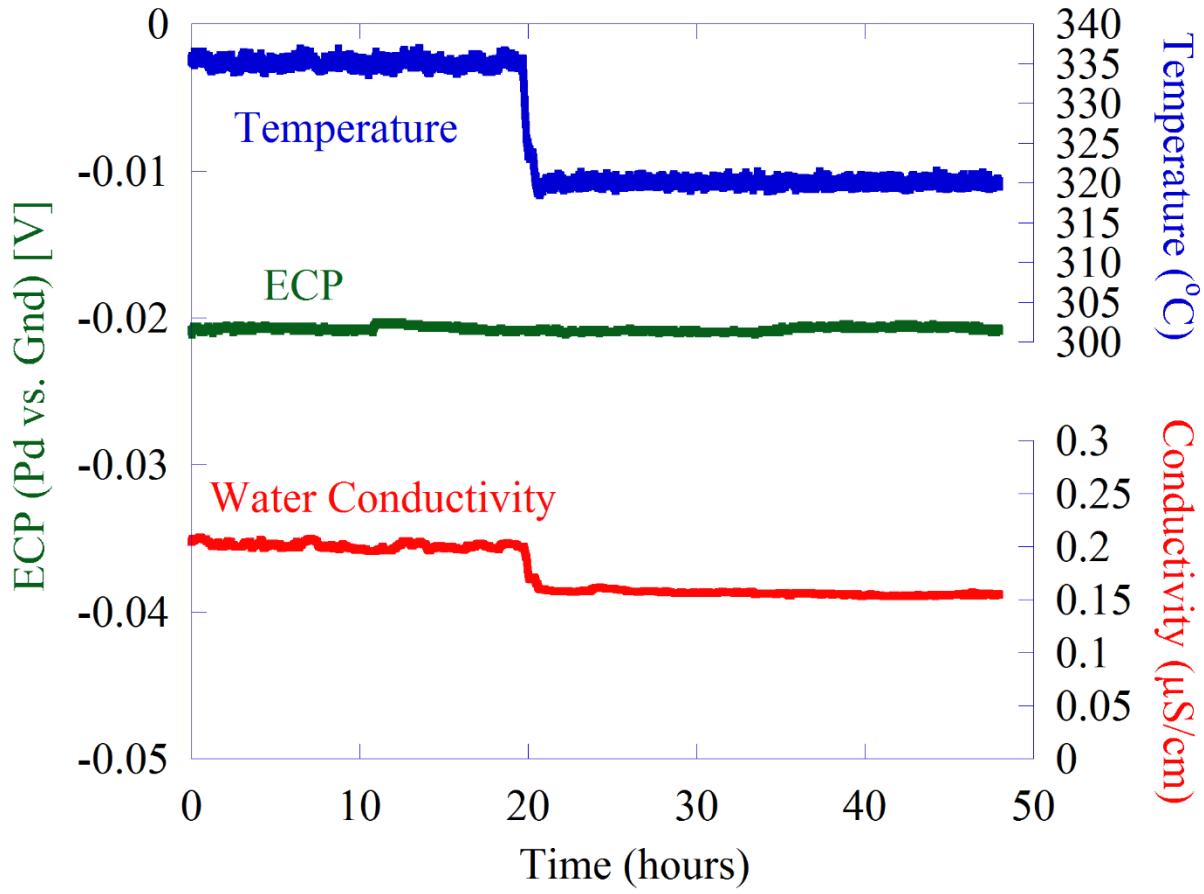

Figure 4.12. Constant current ECP measurement of the Pd-H_2 electrode against ground while the cell temperature was stepped down from 335°C to 320°C. ECP was shown to be independent of the water temperature and conductivity.

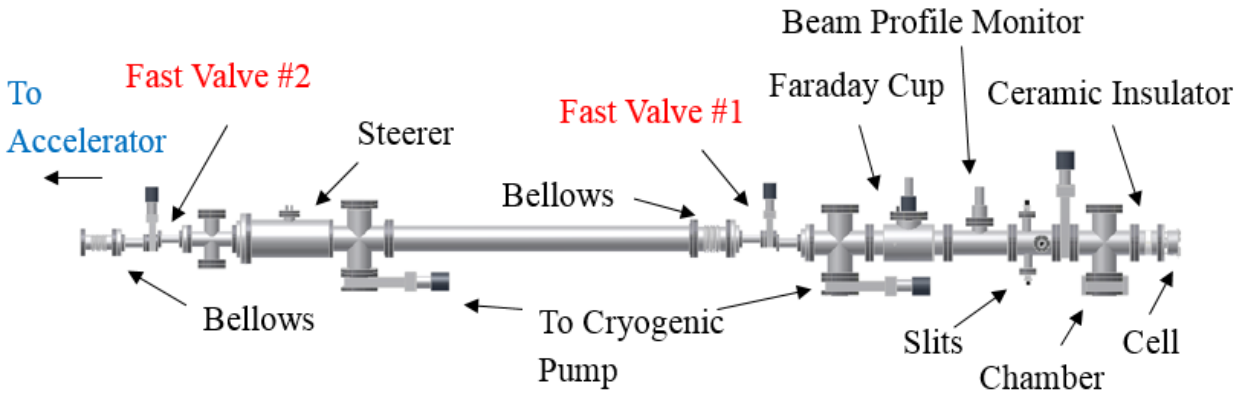

Figure 4.13. A schematic drawing of the dedicated beamline. The bellows at the left side connects to the accelerator, and the corrosion cell is on the right. The beamline is pumped by a pair of cryogenic pumps, with an additional turbo pump connected to the chamber. The fast closing valves are shown in red, and are

connected to a redundant pair of pressure sensors in the chamber. The ceramic insulator electrically isolates the sample from the beamline.

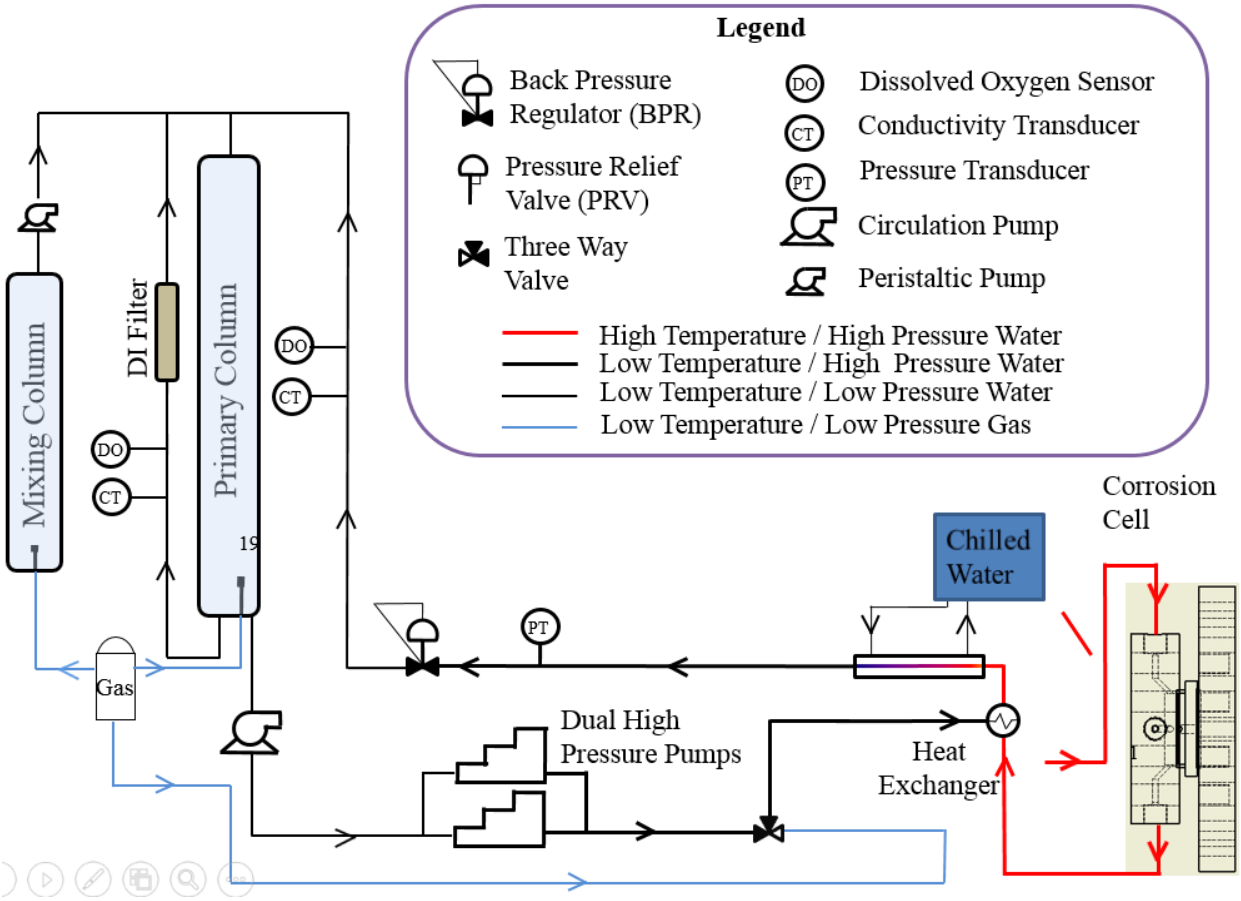

Figure 4.14. A simplified schematic of the water system. Water flows from the primary column where it is pressurized and heated before entering the corrosion cell. After flowing through the cell, water is chilled and de-pressurized before its conductivity and DO are measured. A secondary loop off the primary column continuously filters the water. A gas cylinder is used for bubbling gas though the columns or for purging the water loop. A mixing column is available for chemical additions.

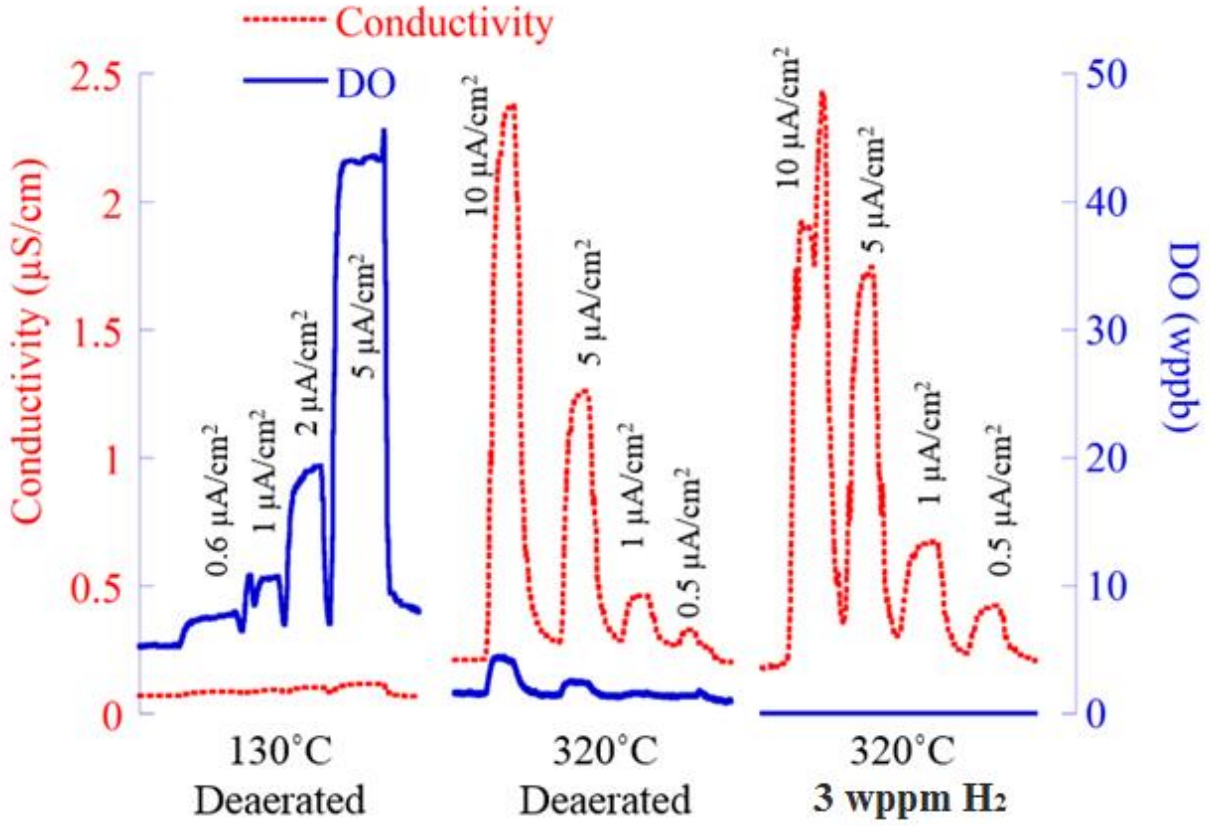

Figure 4.15. Conductivity and dissolved oxygen in the corrosion cell during irradiation at varied beam current densities between 0.5 µA/cm^2 and 10 µA/cm^2 and flow rates near 10mL/min. When temperature was increased from 130˚C to 320˚C, the magnitude of DO spikes went down, while jumps in conductivity increased in magnitude. When 3wppm H_2 was added, no measurable DO was detected.

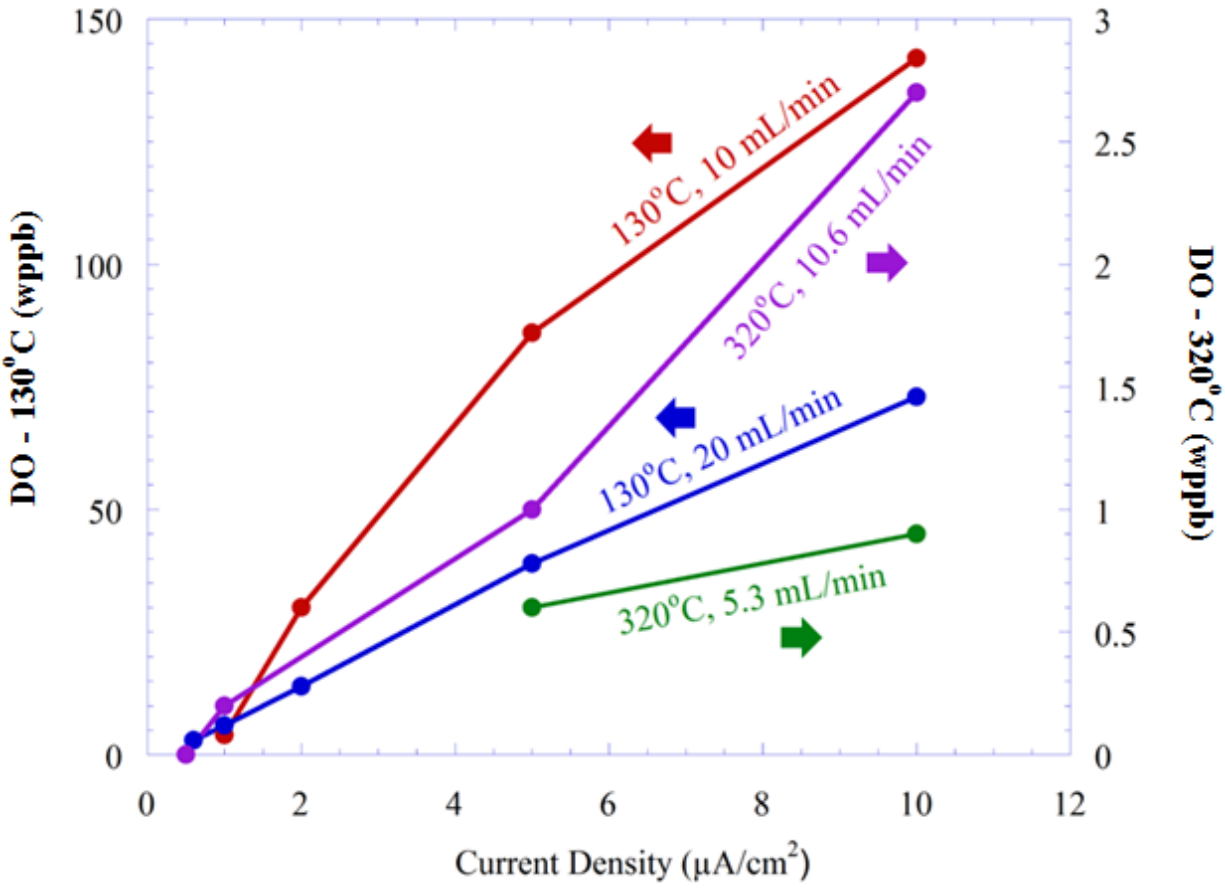

Figure 4.16. Dissolved oxygen as a function of proton beam current density at 130˚C,and 320˚C in deaerated water. Beam current densities between 0.5 μA/cm^2 and 10 μA/cm^2 were applied to a 2mm diameter circular area at the center of the 316 stainless steel samples. The measured DO concentrations at 130˚C are shown on the left axis and measurements at 320˚C are shown on the right axis.

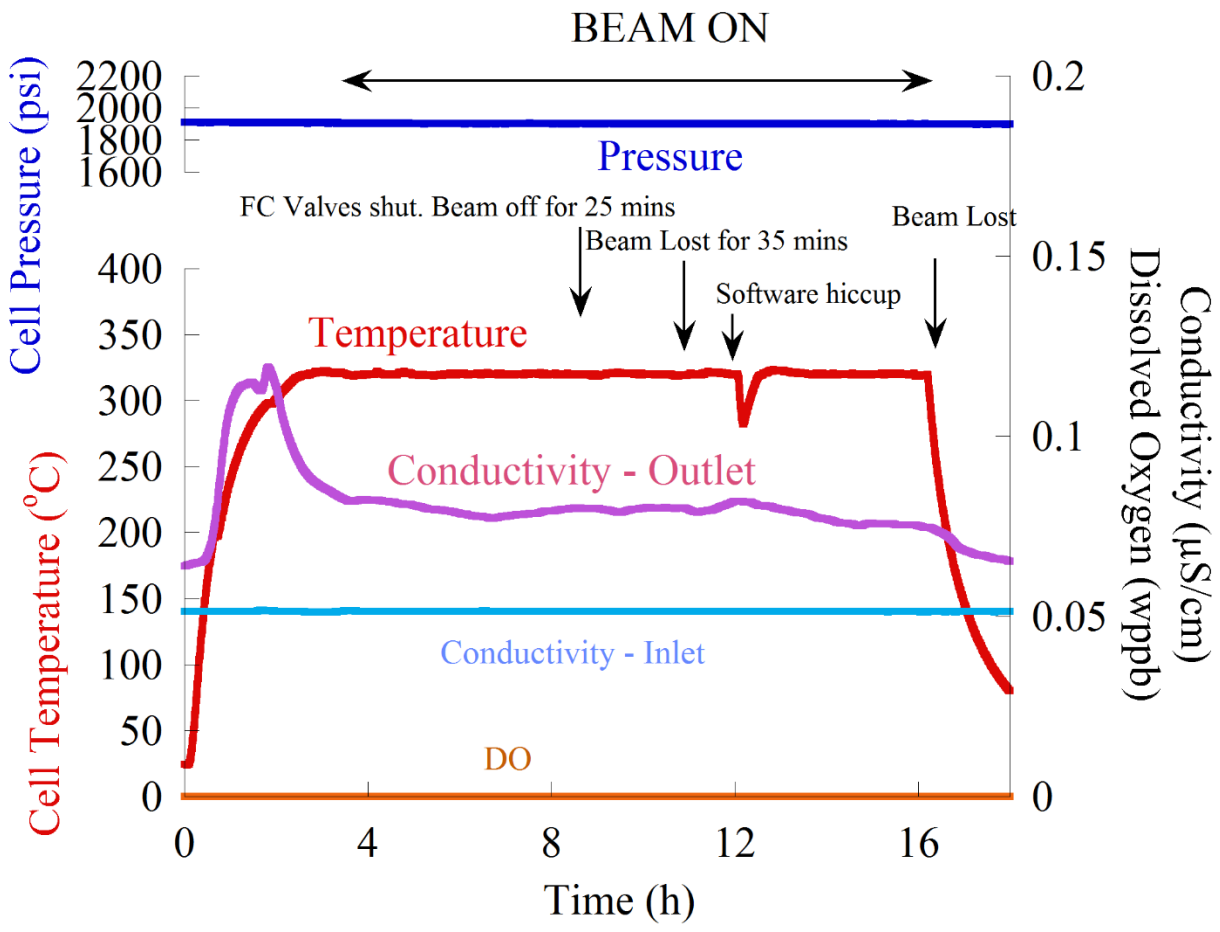

Figure 4.17. Water data during exposure of sample Hi12.

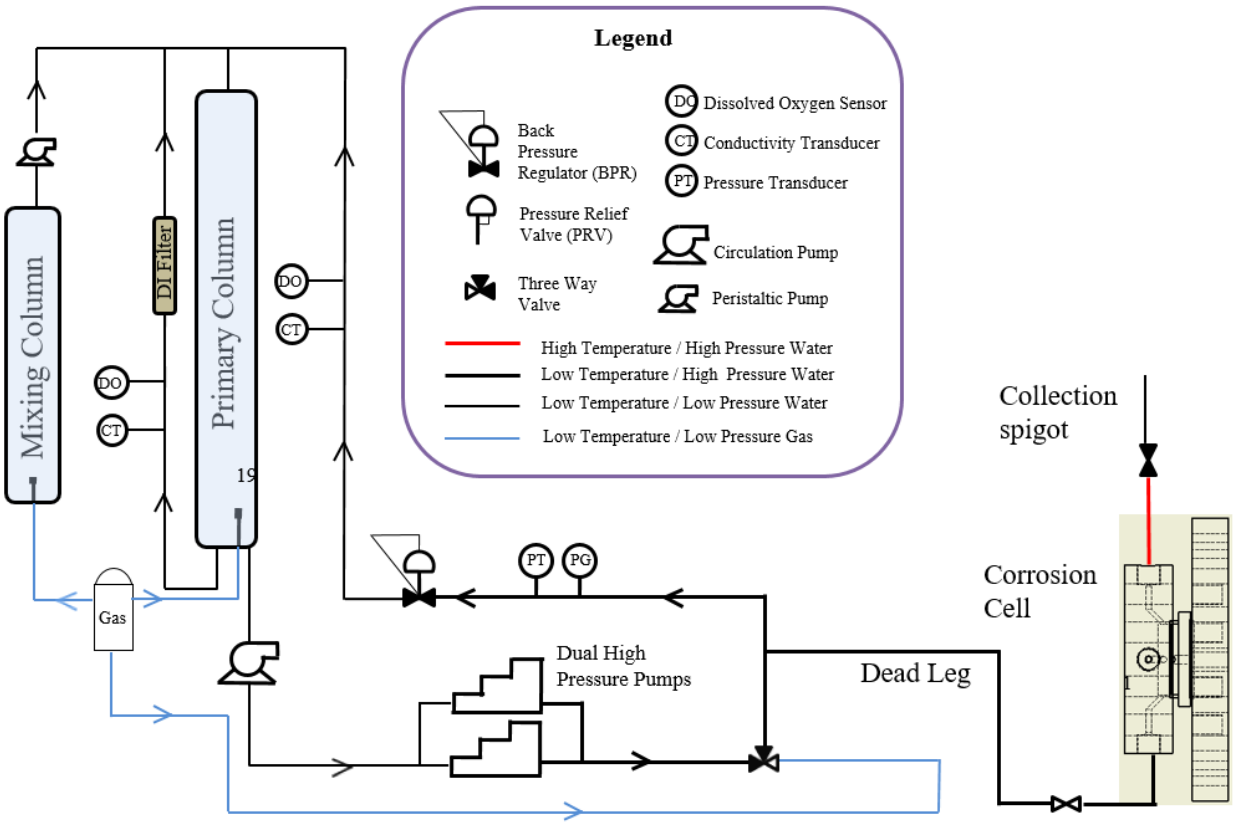

Figure 4.18. Schematic of the water loop modified for static cell experiments.

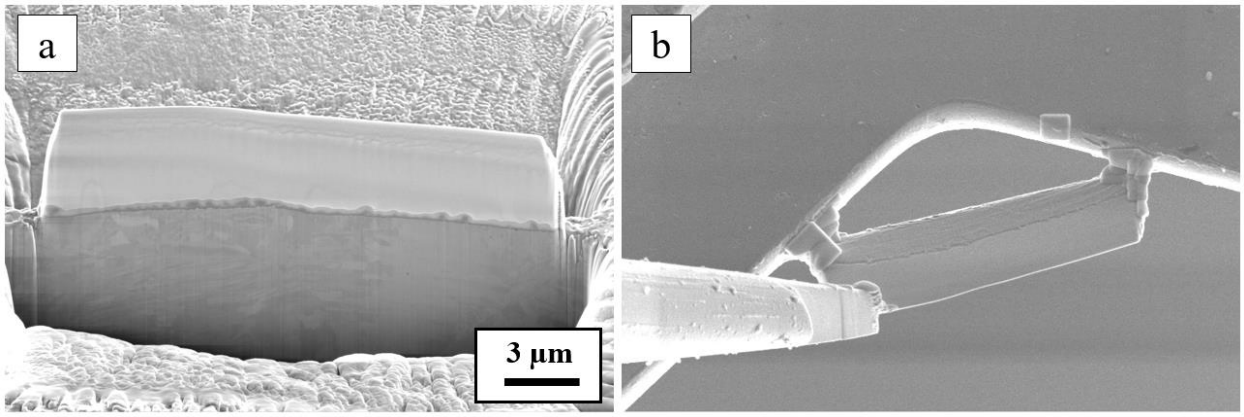

Figure 4.19. SEM images of the preparation of a TEM specimen (a) after deposition and trenching and (b) after attachment to the copper grid.

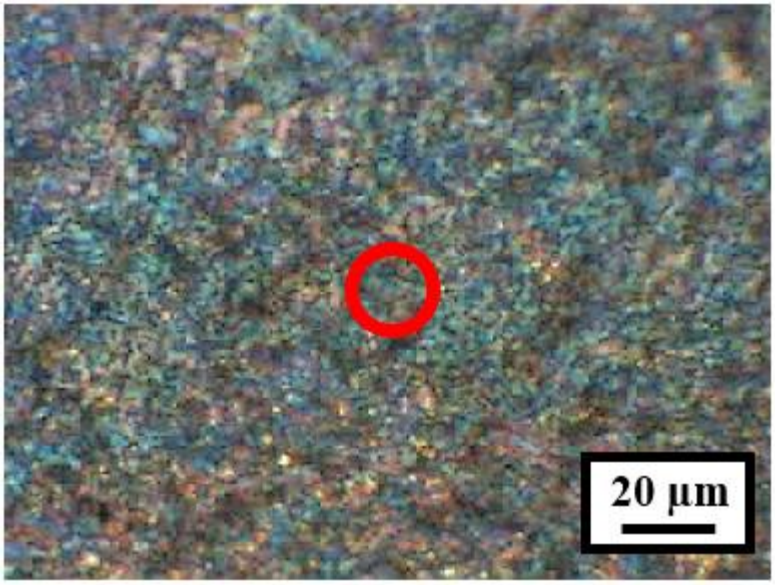

Figure 4.20. An optical image of an oxidized stainless steel sample taken from the Renishaw InVia Raman microscope used in this work. The location of the laser spot is indicated at the center of the image.

CHAPTER 5 - RESULTS

Experimental results are presented to show the effect of irradiation on corrosion of stainless steel in simulated primary water. The first section will present results on the nature of the oxide species present on the surface of the scale. Section 5.2 will present surface images showing the morphology of the oxide surface. Section 5.3 will present results on the oxide thickness and morphology. Section 5.4 will focus on the composition of the oxide from surface through to the metal substrate. Data on the pre-oxidized sample Pr24 with be presented separately in section 5.5. Finally, data on the static cell experiment will be presented in section 5.6.

The analysis of the samples includes the study of three distinct regions on irradiation samples. Optical images of the irradiated and unirradiated samples are shown in Figure 5.1. The irradiated region is visible on the irradiated samples as a distinct circle at the center of each. The irradiated region has a diameter of approximately 2mm on samples Hi04, Hi24-2, and Hi72, and a diameter of 1mm on sample Hi12, consistent with the size of the aperture used in each experiment. A discolored region extending up and to the left is also visible on each irradiated region. Evidence will be presented later that this discoloration is due to the flow of radiolysis products, so this region will be referenced as the “flow” region. Throughout this section, the symbols and color scheme shown in Figure 5.2 will be used to indicate the location of measurements on irradiated and unirradiated samples.

5.1 Oxide Species Present

This section presents Raman spectroscopy results showing the species present on the oxide surface. Samples were examined after exposure with a Renishaw InVia Raman spectrometer with a red laser (λ=633nm) at 20x magnification, producing a spot size of approximately 20μm. Representative Raman scans from the unirradiated, flow, and irradiated regions of samples are shown in Figure 5.3.

The most prominent effects of radiation that can be observed from the Raman spectra are the emergence of hematite, and a shift in the spinel A_{1g} peak. The A_{1g} peak is the most prominent Raman-active mode in the spinel structure, and is visible as the large peak between 650 and 700 cm^{-1}. The peak is a combination of several Fe-Cr-Ni spinel oxide modes, which represents a scale composed primarily of solid solution oxides of type $(Fe_{1-x}Ni_x)(Fe_{1-x}Cr_x)_2O_4$[50], [56]. To more easily see the changes in spinel stability, Figure 5.4 shows the same spectra focused on the spinel A_{1g} peak. The shifts up and down are more easily observed in this more zoomed-in view.

Raman spectra taken on the irradiated and flow surfaces of samples Hi12, Hi24, and Hi72, showed a significant presence of hematite as indicated by the characteristic peaks on the irradiated samples at 226 cm^{-1}, 245 cm^{-1}, 299 cm^{-1}, 411 cm^{-1} and 613 cm^{-1}. While the flow region of Hi04 exhibits hematite, the irradiated region did not exhibit most of the characteristic peaks of hematite. However, small peaks at 300 cm^{-1} and 490 cm^{-1}, and the shift of the spinel peak at 670 cm^{-1} to the right may indicate the formation of maghemite $(\gamma - Fe_2O_3)$, a metastable oxide

phase between magnetite and hematite, which results when magnetite loses an FeO group, but retains the spinel structure. This suggests that hematite will form on the surface with more time.

The second prominent effect of radiation on the spectra is seen in the large peak between 650 and 700 cm^{-1}, the spinel A_{1g} peak. The peak is a combination of several spinel oxide modes, as indicated in the figure.

Unirradiated samples Un04, Un24, and Un72 show a prominent peak around 674 cm^{-1}, which is between the characteristic peaks for Fe_3O_4 and $FeCr_2O_4$, Spectra taken from irradiated and flow surfaces of samples Hi12, Hi24, Lo24 and Hi72 show an apparent down-shift of the spinel A_{1g} peak, toward Fe_3O_4 and away from the $FeCr_2O_4$ peak. The spectra taken from the unirradiated regions of all irradiated samples, as well as from the irradiated and flow regions of sample Hi04 show an up-shift in the spinel A_{1g} peak to toward $NiFe_2O_4$. The shifts in the spinel A_{1g} peak are explained in the discussion chapter by deconvolution of the characteristic spinel oxide modes.

Raman spectra were taken at several locations on the surfaces of the irradiated and unirradiated samples, and the locations where hematite was either present or not present are depicted in Figure 5.5. The locations where the spinel peak was shifted up or down are indicated in Figure 5.6 and summarized in Table 5.1.

5.1.1 Summary

The oxide surface on unirradiated samples was composed of spinel type oxides. Irradiated samples also contained hematite on all irradiated and flow regions except on sample Hi04, which showed minor signs of hematite on the irradiated region, and prominent hematite in the flow

region. The unirradiated surfaces of Hi24 and Hi72 contained hematite, while the unirradiated surfaces of Hi04 and Hi12 did not. The primary spinel peak was observed to shift up on the flow and irradiated regions of sample Hi04 and on the unirradiated regions of samples Hi24 and Hi72. It was observed to shift down on the flow and irradiated regions of sample Hi12, Hi24, and Hi72

5.2 Surface Morphology

This section presents results of the surface oxide morphology after exposure, with a comparison of the surfaces exposed with irradiation, to those exposed without irradiation.

Figure 5.7, shows SEM images of samples exposed for 4 hrs. Un04 and the unirradiated area of Hi04, shown in Figure 5.7a and b, feature mostly large faceted outer oxide crystals. The surface of the flow region of Hi04, shown in Figure 5.7c, features a mix of smaller equiaxed outer oxide crystals and larger faceted crystals. The irradiated region, Figure 5.7d, has an outer oxide consisting of a mix of small equiaxed crystals and plate-like crystals on top of a rough inner oxide surface.

Figure 5.8 shows SEM images of the irradiated, flow, and unirradiated surfaces of sample Hi12. There was no unirradiated sample exposed for 12 hrs. The unirradiated surface, Figure 5.8a, shows large faceted crystals atop a smooth inner oxide surface. The flow surface, Figure 5.8b, features mostly smaller equiaxed outer oxide crystals, with some larger faceted crystals. The inner oxide is slightly rough, and is dusted with smaller outer oxide particles. The irradiated area, Figure 5.8c, features relatively few faceted outer oxide crystals, and is composed of mostly

densely packed equiaxed crystals. The inner oxide is well covered, but when visible it is rough in appearance, as with the previous irradiated regions.

The surfaces of samples Un24 and Hi24-2 are shown in Figure 5.9. The surface of Un24, Figure 5.9a, is fully covered with large faceted outer oxide crystals to the degree that the inner oxide is not visible. The unirradiated surface of sample Hi24, Figure 5.9b, features a mix of large faceted crystals and smaller equiaxed crystals atop a smooth inner oxide. The flow region, Figure 5.9c, features mostly smaller equiaxed outer oxide crystals with some larger faceted particles present, atop a smooth inner oxide. The irradiated surface, Figure 5.9d, features a mix of faceted, equiaxed, and plate-like outer oxide particles on top of a rough inner oxide.

Figure 5.10 shows images of the irradiated, flow, and unirradiated surfaces of Hi72, and the surface of sample Un72. The images of Un72 and the unirradiated region of Hi72 in Figure 5.10a-b show mostly large, faceted outer oxide particles. Where the inner oxide is exposed, the surface appears smooth and homogeneous. The image of the flow region, Figure 5.10c, shows smaller equiaxed outer oxide particles mixed with the larger faceted crystals. On areas where the inner oxide is visible, a “dusting” of very small outer oxide crystals is visible. The irradiated surface, Figure 5.10d, features mostly equiaxed and plate-like outer oxide crystals. The surface of the inner oxide appears to be a rough layer of densely packed oxide particles.

5.2.1 Summary

Unirradiated oxides from both irradiated and unirradiated samples were covered with large faceted outer oxide crystals, and when visible, the inner oxide surfaces appeared smooth. Flow regions were covered with a mixture of larger faceted crystals and smaller equiaxed crystals, and

featured smooth inner oxide surfaces with a minor presence of roughness or small surface particles. Irradiated surfaces were covered with mostly equiaxed or plate-like outer oxide crystals, and featured rough inner oxide surfaces.

5.3 Oxide Thickness and Morphology

In this section, oxide cross sections are examined and results on the morphology and thickness of the inner oxides of the samples are presented. This section will first show images that reveal the morphology of the inner oxide layer on irradiated and unirradiated samples, and will show the differences in thickness between irradiated and unirradiated samples.

The oxide layers on samples were imaged with STEM. Specimens were prepared with the FIB liftout method. Oxide thickness measurements were made using STEM-HAADF images at 10,000X focus.

5.3.1 Morphology

Images of the oxides on the irradiated, flow, and unirradiated regions of sample Hi04 are shown in Figure 5.11. The unirradiated region shown in Figure 5.11a is homogeneous and appears relatively non-porous. The surface of the inner oxide, which forms the boundary between the inner oxide and either the outer oxide or solution is straight, and is presumed to be the original metal surface. The flow and irradiated regions, shown in Figure 5.11b-c are inhomogeneous and highly porous. The porosity is difficult to see in these images, but will be highlighted in more detail on images of samples exposed for 24 and 72 hrs.

The same trend continues with sample Hi12, as shown by the STEM images in Figure 5.12. The unirradiated inner oxide, shown in Figure 5.12a, is non-porous and homogeneous, while the inner oxides on the flow and irradiated regions, Figure 5.12b-c, are porous and inhomogeneous.

To compare the irradiated sample to an unirradiated sample, Figure 5.13 shows sample Un24 and the unirradiated and irradiated regions of sample Hi24-1. Both Un24, Figure 5.13a, and the unirradiated region of Hi24-1, Figure 5.13b have a thick, homogeneous, low-porosity oxide layer. The irradiated region of Hi24-1, Figure 5.13c, is thin, inhomogeneous, and highly porous.

To more easily see the porosity on sample Hi24-1, an under-focused conventional BF TEM image is shown in Figure 5.14. The porous microstructure in the inner oxide is visible, as highlighted by the arrows.

To investigate the structure of the oxides, electron-diffraction patterns were taken from the inner oxides of sample Un24, from the irradiated areas of sample Hi24-1 and Lo24. The results are shown in Figure 5.15. Theoretical and measured d-spacing are tabulated in Table 5.2. The ring-shaped patterns taken from the inner are reflective of nano-crystalline oxides, and all rings were consistent with the spinel structure. The patterns were taken on areas fully within the inner oxide, and did not include the oxide-solution interface. It is notable that while Raman spectroscopy indicated hematite was present on the irradiated areas of Hi24 and Lo24, the diffraction patterns that did not include the oxide surface fit strongly with the spinel structure. Hematite may still be present in smaller amounts within the bulk of the inner oxide, as some

strongly diffracting corundum planes overlap with spinel, but this diffraction data indicates a majority spinel inner oxide.

STEM bright field images of the three regions of sample Hi72 are shown in Figure 5.16. The inner oxide on the unirradiated region, Figure 5.16a, is relatively homogenous in morphology despite its uneven thickness, and appears to be relatively non-porous. By comparison, the inner oxides on the flow and irradiated regions, shown in Figure 5.16b-c, both have a heterogeneous morphology, which is highly porous. The oxides are also significantly thinner than on the unirradiated region.

A closer look at the inner oxides is shown in Figure 5.17. The difference in porosity between the irradiated and unirradiated oxides is visible as white regions in the inner oxide. Note that the images are not on the same scale, and are shown at different magnifications to better highlight the features present.

5.3.2 Inner Oxide Thickness

Inner oxide thickness was measured using HAADF images of the oxides on samples, as shown in Figure 5.18. To find the average thickness, the inner oxide was traced to find its cross sectional area, and is shown in the figure highlighted by yellow dotted lines. The cross sectional area was then divided by the length of the cross-section to obtain the average thickness. Since only limited areas could be examined, the results are highly variable. Images of the total cross sections from which thickness data was extracted can be found in Appendix C.

The average thickness of the oxides on the irradiated, flow, and unirradiated regions of the samples in this work is given in Table 5.3, and is graphed in Figure 5.19. The thicknesses presented should be regarded as semi-quantitative measures of oxide growth, since each data point represents a single liftout taken from a single sample. Nevertheless, several patterns can be seen. First, the irradiated and flow regions are significantly thinner than the unirradiated regions. Second, the irradiated and flow regions do not appears to be significantly different from each other in terms of thickness. Third, the inner oxides on unirradiated regions from irradiated samples are thinner than the unirradiated regions from unirradiated samples, although this data is based on only two unirradiated samples, so it may not be significant.

5.3.3 Summary

Inner oxides on the irradiated and flow surfaces were found to be thinner and more porous than the oxides on irradiated surfaces. SAD patterns were consistent with the spinel structure. With limited data, the irradiated surfaces on irradiated samples were thinner than on unirradiated samples. The inner oxides on flow surfaces were found to be of similar thickness to the irradiated inner oxides.

5.4 Oxide Composition

This section presents composition data of the oxides on irradiated and unirradiated samples. Special attention will be given to the chromium content of inner oxides to reveal how it is affected by irradiation. To determine the oxide composition, EDS line scans were taken across

the oxide layers on irradiated, flow, and unirradiated regions. The number of scans taken from each region is shown in Table 5.4. Only one line scan from each region will be shown in this section, and all other scans are shown in Appendix D.

EDS line scans taken from the unirradiated, flow, and irradiated regions of sample Hi04 are shown in Figure 5.20, Figure 5.21, and Figure 5.22, respectively. The unirradiated scan begins in the outer oxide, which shows a mixture of iron and oxygen, with a small amount of nickel. The oxygen content in this scan, and in all scans, should not be regarded as quantitative, as oxygen is much more difficult for EDS to detect compared to transition metals. Because of this, quantification is difficult, and is dependent on a number of unknown factors, including specimen thickness. The oxygen content is useful for determining the boundaries of the layers in the scan.

The inner oxide is composed of oxygen, with approximately 20% each iron and chromium, with less than 10% nickel. The chromium concentration is approximately the same across the metal-oxide interface. The composition of the metal agrees with the mill specification given in Appendix A.

The outer oxide and metal are similar in composition on all regions, but the inner oxide on the flow and irradiated regions is deficient in chromium. The inner oxide on the flow region is only slightly deficient in chromium, as seen in the downward trending chromium profile moving away from the metal interface toward the outer oxide. Note that the fitting routing overlapped iron and oxygen peaks in the inner oxide during these scans, so the iron content appears artificially high, while oxygen content appears artificially low. The irradiated region displays

even more chromium depletion, as the Cr profile can be seen trending toward zero almost immediately after the metal oxide interface.

EDS scans taken from the unirradiated, flow, and irradiated regions of sample Hi12 are shown in Figure 5.23, Figure 5.24, and Figure 5.25, respectively. The irradiated and flow regions are depleted in chromium, and the unirradiated region is not.

EDS line scans of sample Un24, and the unirradiated, flow, and irradiated regions of sample Hi24-2 are shown in Figure 5.26, Figure 5.27, Figure 5.28, and Figure 5.29, respectively. As with the 72 hour samples, the irradiated and flow regions have inner oxides that are depleted in chromium, while the unirradiated regions from both the irradiated and unirradiated sample are not depleted in inner oxide chromium.

Line scans taken from the irradiated and unirradiated regions of sample Lo24 are shown in Figure 5.30, and Figure 5.31. The inner oxide in the irradiated region is depleted in Cr as in Hi24, while the unirradiated region does not show Cr depletion.

An EDS line scan taken from sample Un72 is shown in Figure 5.32. Line scans taken from the unirradiated, flow, and irradiated regions of Hi72 are shown in Figure 5.33, Figure 5.34, and Figure 5.35, respectively. Un72 and the unirradiated region of Hi72 do not show chromium depletion in the inner oxide, while the irradiated and flow regions both have inner oxide deficient in chromium.

5.4.1 Cr Depletion

To see the effect of irradiation on the Cr content of the inner oxides, a representative line scan showing the Cr content across the metal-oxide interface of each sample region is shown in Figure 5.36. The data represented by the red line was taken from a sample that was never exposed to radiation. Data in green were taken from the unirradiated regions of irradiated samples. The amount of chromium in all unirradiated regions is relatively flat across the metal-oxide interface. The blue and orange lines represent irradiated and flow regions respectively. Specimens taken from these regions exhibit a sharp depletion of Cr in the inner oxide.

5.4.2 Summary

EDS line scans show an outer oxide composed of iron oxide with some substitutional nickel, and an inner oxide composed of iron, chromium, and nickel oxides. Inner oxides on irradiated and flow regions were found to be deficient in chromium compared to unirradiated oxides from both irradiated and unirradiated samples. The chromium content of flow regions is similar to that on irradiated regions.

5.5 Pre-Oxidized Experiment

To study the effect of IAC on a sample with a pre-grown film, sample Un72 was exposed for an additional 24 hrs with irradiation at a dose rate of 4000 kGy/s and a damage rate of 7×10^{-6}

dpa/s. To distinguish the pre-oxidized sample from the others used in this study, the sample after irradiation will be called Pr24

Optical images of Pr24 before (Un72) and after the irradiated exposure are shown in Figure 5.37. The 1 inch diameter irradiated area is visible at the center, and the flow region extends upward from the irradiated region. The flow region on this sample is significantly smaller and shaped differently than the flow regions on other samples.

SEM images were taken of the surface of Pr24, and are shown in Figure 5.38. The outer oxide on the unirradiated region is similar to the outer oxide before irradiation, with a high density of larger faceted outer oxide crystals. The outer oxide crystals on the flow and irradiated regions feature a mix of large and small crystals, but the larger faceted crystals have very rough surfaces.

Raman scans were taken on several spots on the surface of Pr24 before and after irradiation. Figure 5.39 shows maps of the locations of the scans, along with representative spectra from each region. The irradiated and flow regions have hematite on the surface, while the unirradiated region and the sample before irradiation do not have hematite. The spinel A_{1g} peak before irradiation and on the unirradiated region is centered near the $FeCr_2O_4$ mode. The irradiated and flow regions show a shift of the spinel peak down, toward the Fe_3O_4 mode.

STEM-HAADF images of the oxides are shown in Figure 5.40. The before and unirradiated images show a relative thick, homogeneous, non-porous oxide, consistent with previous samples. The flow region also has a thick, non-porous oxide, which is different from previous samples, which all had a thin, porous inner oxide in the flow region. The inner oxide on the irradiated region is highly porous, but is not significantly thinner than oxide from the other

regions. The outer oxide on the flow and irradiated regions are both highly porous, which was not observed on other samples.

The differences in the inner oxide are clearly seen the STEM-BF images shown in Figure 5.41, which show diffraction contrast more clearly. The inner oxides on the before, unirradiated, and flow regions are relatively homogeneous and non-porous, while the inner oxide of the irradiated region is porous and inhomogeneous. Pores are still clearly visible on the outer oxides of the irradiated and flow regions.

EDS linescans were taken across the oxides of sample Pr24 before and after irradiation, and representative scans are shown in Figure 5.42, Figure 5.43, Figure 5.44, and Figure 5.45. More scans from each region are shown in Appendix D. The scan taken before irradiation, and from the unirradiated region after the irradiated exposure both show an inner oxide with an approximately 1:1 ratio of Fe:Cr. The irradiated region has an inner oxide that is depleted in chromium, similar to the irradiated region on other samples. The flow region does not show Cr depletion, which is unlike the flow regions on all other irradiated samples, which had inner oxides depleted in chromium.

To compare the chromium profile in the inner oxide, Figure 5.46 shows linescans taken from Pr24 before and after irradiation. The chromium content of the inner oxide on the before, unirradiated, and flow regions is relatively level across the interface, while it depletes in the irradiated scans. Notably, some scans in the irradiated region did not show Cr depletion, although the majority did. Also, the degree of depletion is not as severe in sample Pr24 as on other samples, which can be seen in the more gradual slope of the Cr profile moving away from the metal-oxide interface.

5.5.1 Summary

The outer oxides on the unirradiated region of Pr24 was similar to the sample before irradiation, with mostly large faceted crystals. The irradiated and flow regions were covered with a mix of equiaxed grains, and roughened faceted crystals. Hematite was found on irradiated and flow regions, but not on the unirradiated region, or on the sample before irradiation. EDS line scans revealed chromium depletion in the irradiated region, but not in the unirradiated or flow regions. The irradiated region was found to be highly porous, but the unirradiated and flow regions were found to be non-porous like the oxide before irradiation. There was not a significant difference in inner oxide thickness among the oxides on any region after irradiation when compared to the oxide thickness before irradiation.

5.6 Static Cell Test

To measure aqueous chromium in the corrosion cell water, a static cell test was used to build the necessary concentration required for detectability with UV-Visible light spectroscopy. Water samples were tested with ICP-MS for total chromium, and with UV-Vis for Cr^{6+}. It can reasonably assumed that all Cr that was not in the 6+ state was Cr^{3+}. The results of the tests are given in Table 5.5.

As shown in chapter 4, the predicted concentration of Cr^{6+} due to irradiation is a few wppb. The concentration of Cr^{6+} exceeded 200 wppb in all experiments except Ir4. There is no discernable pattern in the data, and it is assumed that the measured chromium comes from the corrosion cell walls and tubing, and not from the sample. The chromium from the cell and tubing is sufficient to mask any differences in aqueous Cr from the sample. It is therefore concluded that the static cell experiments did not produce useful data, due to much higher-than-predicted levels of Cr in the collected water, and will not be included in the discussion of this work.

Table 5.1. Changes in the position of the Spinel A_{1g} peak as indicated by Raman Spectroscopy

Time	Unirradiated Sample	Irradiated Sample		
		Unirradiated	Flow	Irradiated
4	No Shift	No Shift	Up	Up
12	na	No Shift	Down	Down
24	No Shift	Up	Down	Down
72	No Shift	Up	Down	Down

na: not applicable

Table 5.2. Theoretical and measured d-spacing of the observed diffraction rings on the inner oxides of sample Un24, the irradiated area of Hi24, and the irradiated area of Lo24. Theoretical d-spacing is based on magnetite, with a lattice parameter of 0.8397 nm. Measured d-spacing is calculated with λ= 2.51 pm, and camera lengths of 30 cm for Hi24-1, and 25 cm for Lo24 and Un24.

Plane	$d_{theoretical}$ **(nm)**	$d_{measured}$ **(nm)**		
		Hi24-1-irr	**Lo24-irr**	**Un24**
137	0.109	nd	0.12	0.12
440	0.148	0.15	0.14	0.14
115	0.162	0.18	0.17	nd
400	0.21	nd	0.21	0.21
113	0.253	0.25	0.24	0.25
220	0.300	0.30	0.28	nd

nd: not detected

Table 5.3. Average inner oxide thickness of samples on the irradiated, unirradiated, and flow regions. Specimens were not taken from some sample regions.

Sample	**Time (hr)**	**Dose Rate (kGy/s)**	**Thickness (nm)**		
			Irr	**Flow**	**Unirr**
Hi04	4	4000	24	25	79
Hi12	12	4000	35	62	81
Hi24	24	4000	68	na	136
Hi24-2	24	4000	20	43	na
Lo24	24	400	51	na	53
Un24	24	na	na	Na	192
Hi72	72	4000	89	51	230
Un72	72	na	na	na	258

na = not applicable

Table 5.4. Number of EDS line scans taken from each region of the samples used in this work.

Sample	**Time (hr)**	**Dose Rate (kGy/s)**	**EDS Scans**		
			Irr	**Flow**	**Unirr**
Hi04	4	4000	3	3	3
Hi12	12	4000	2	2	3
Hi24	24	4000	3	0	1
Hi24-2	24	4000	2	3	0
Lo24	24	400	2	0	1
Un24	24	na	na	na	1
Hi72	72	4000	3	2	1
Un72	72	na	na	na	3

na = not applicable

Table 5.5. Aqueous chromium concentrations from the static cell experiments. Total Cr may exceed Cr^{6+} due to variation in the equipment used for testing.

Sample	Exposure Time (hrs)	Dose Rate (kGy/s)	Before		After	
			Total Cr (wppb)	Cr^{6+} (wppb)	Total Cr (wppb)	Cr^{6+} (wppb)
Un4-1	4	na	5.56	2.56	1710	1790
Un4-2	4	na	0.461	0.481	663	759
Un8	8	na	1.45	1.61	466	544
Ir4	4	4000	6.03	3.4	9.46	6.34
Ir8	8	4000	0.335	0.359	248	278

na = not applicable

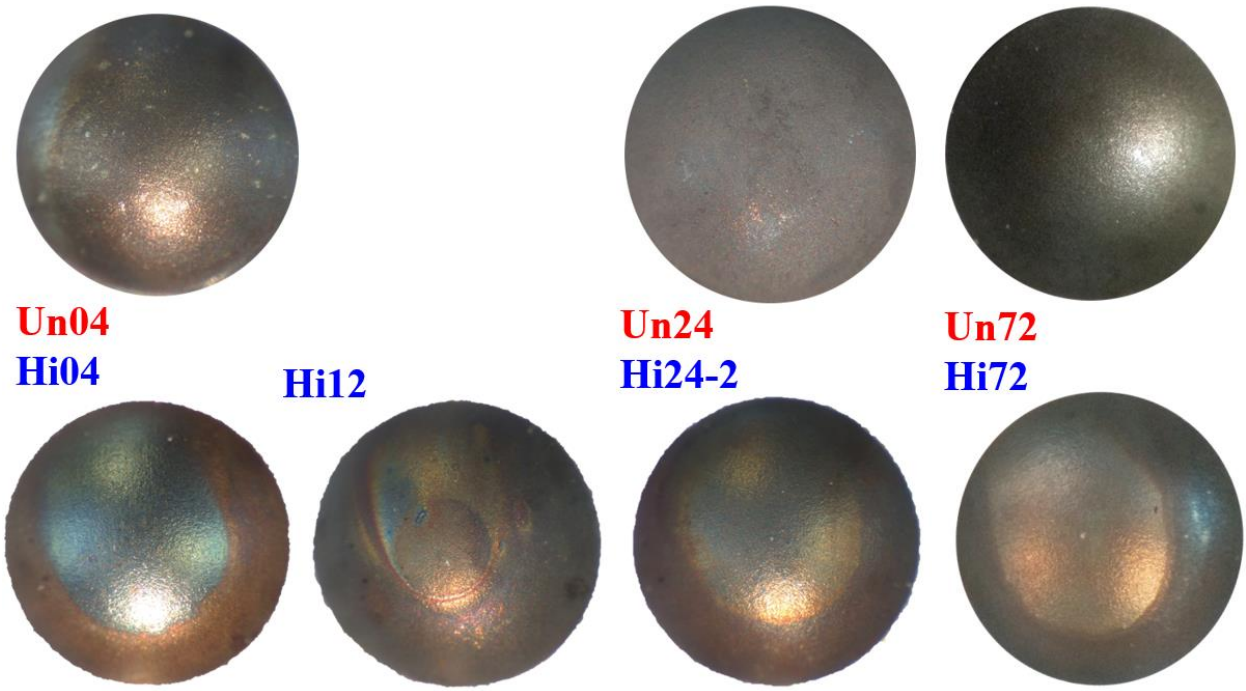

Figure 5.1. Optical images of several samples used in this study. No 12 hr unirradiated sample was produced.

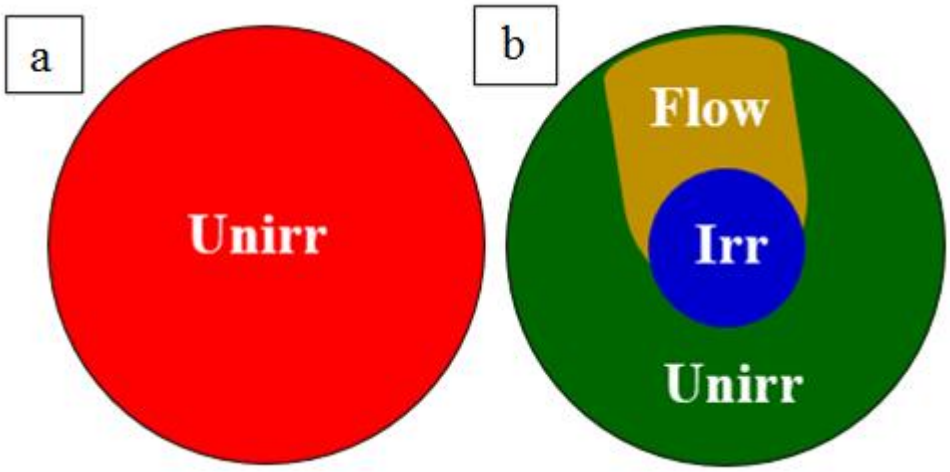

Figure 5.2. Diagrams used in this chapter to indicate the location of measurements taken from (a) unirradiated and (b) irradiated samples.

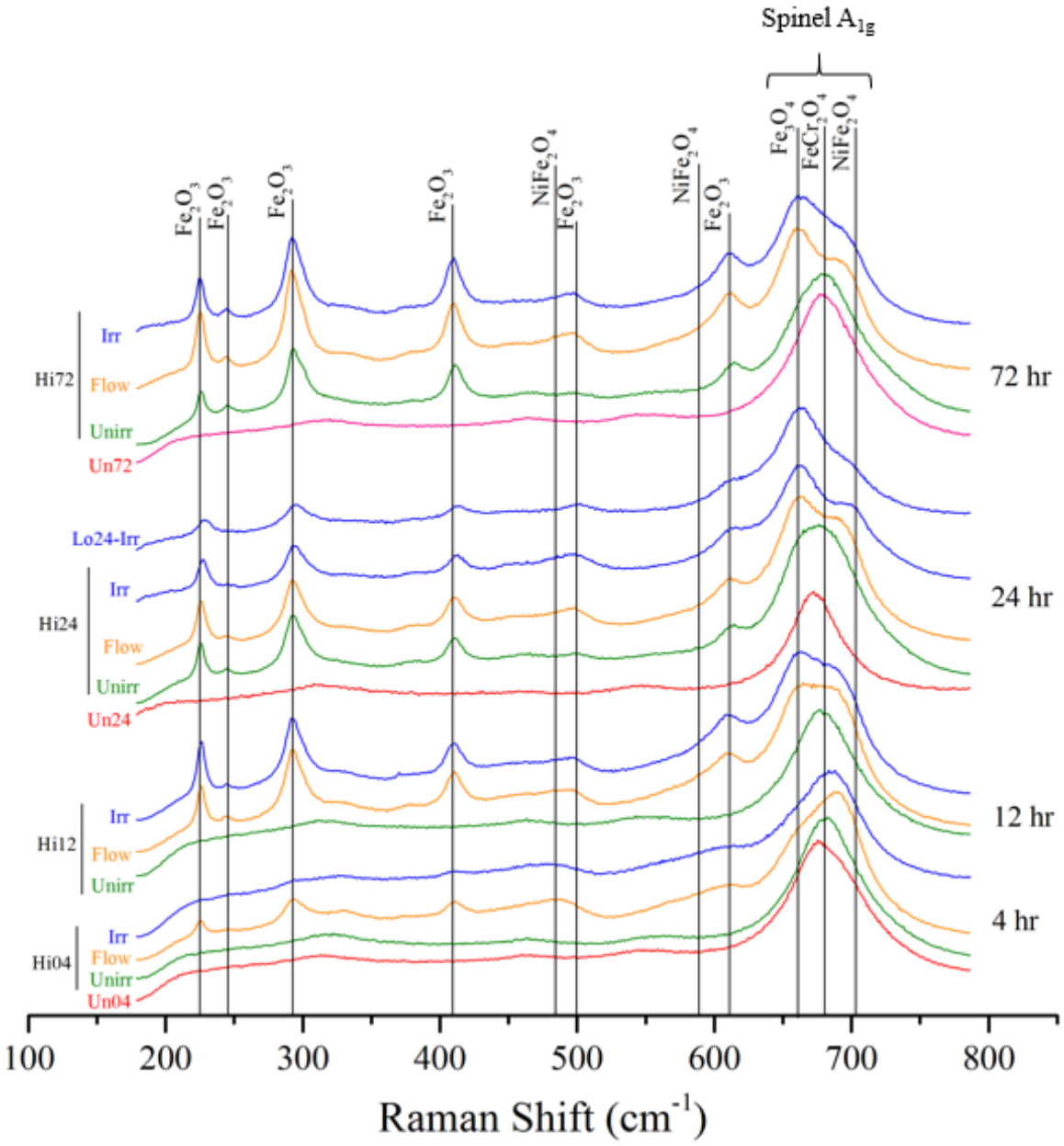

Figure 5.3. Raman spectra taken from unirradiated samples and from the three surface types of irradiated samples.

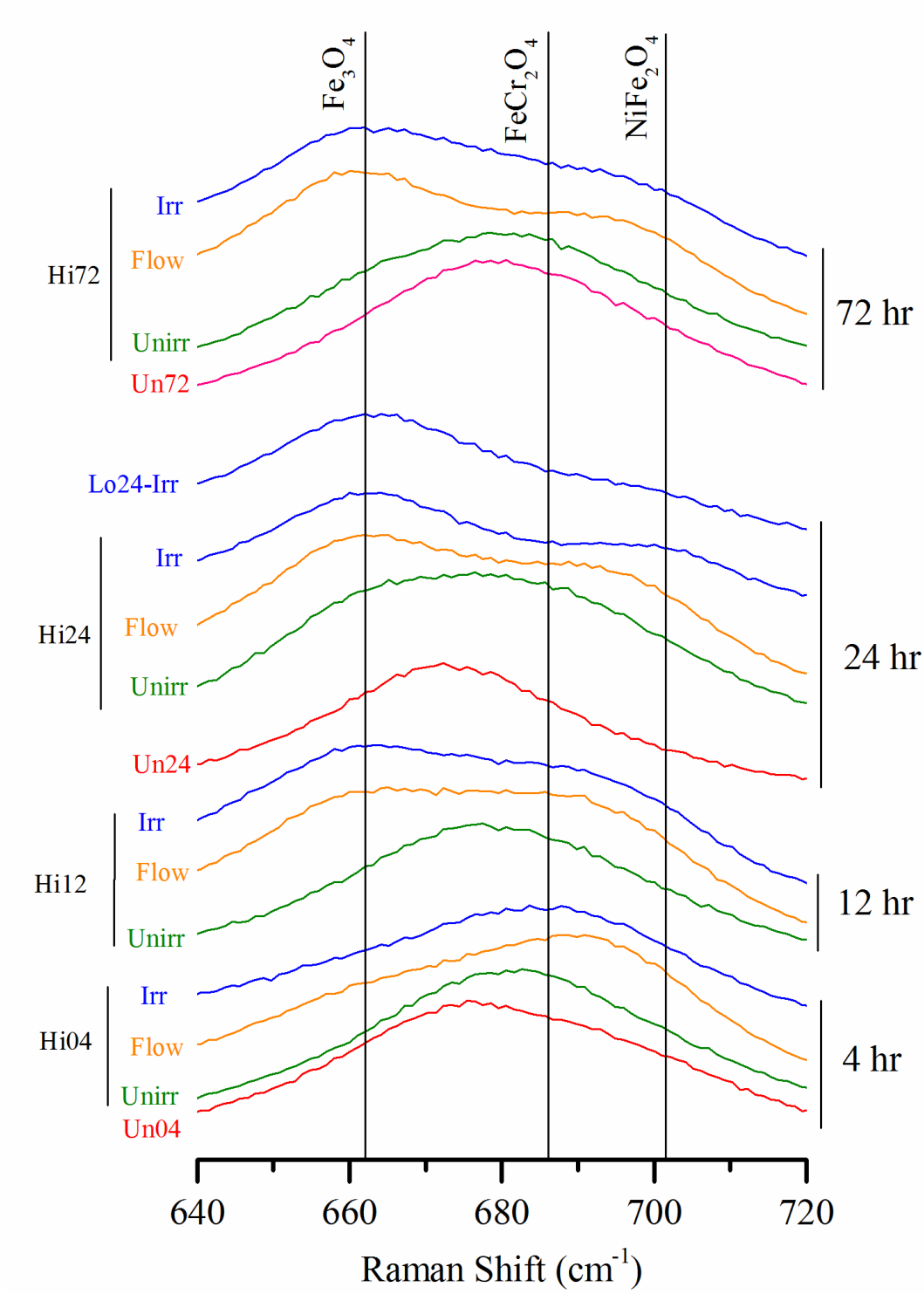

Figure 5.4. Raman spectra showing the spinel A_{1g} peak taken from the unirradiated samples and from the three surface types of the irradiated samples.

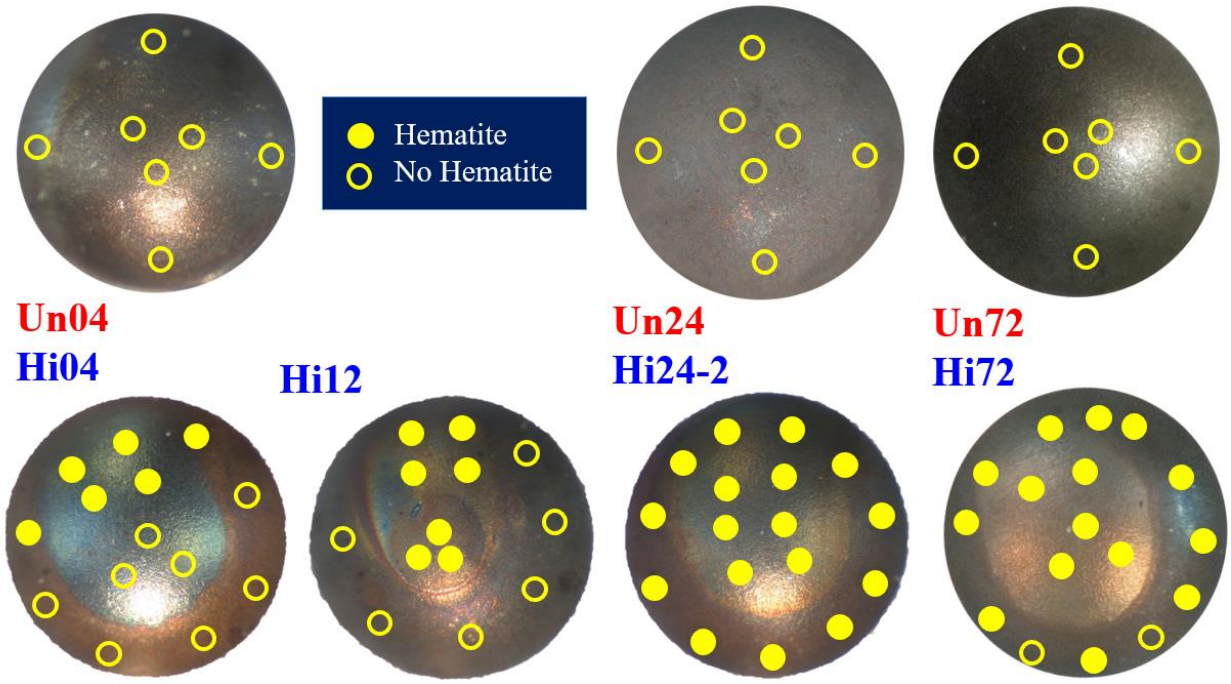

Figure 5.5. Optical images of irradiated and unirradiated samples with closed circles indicating locations where hematite (Fe_2O_3) was detected, and open circles indicating hematite was not detected.

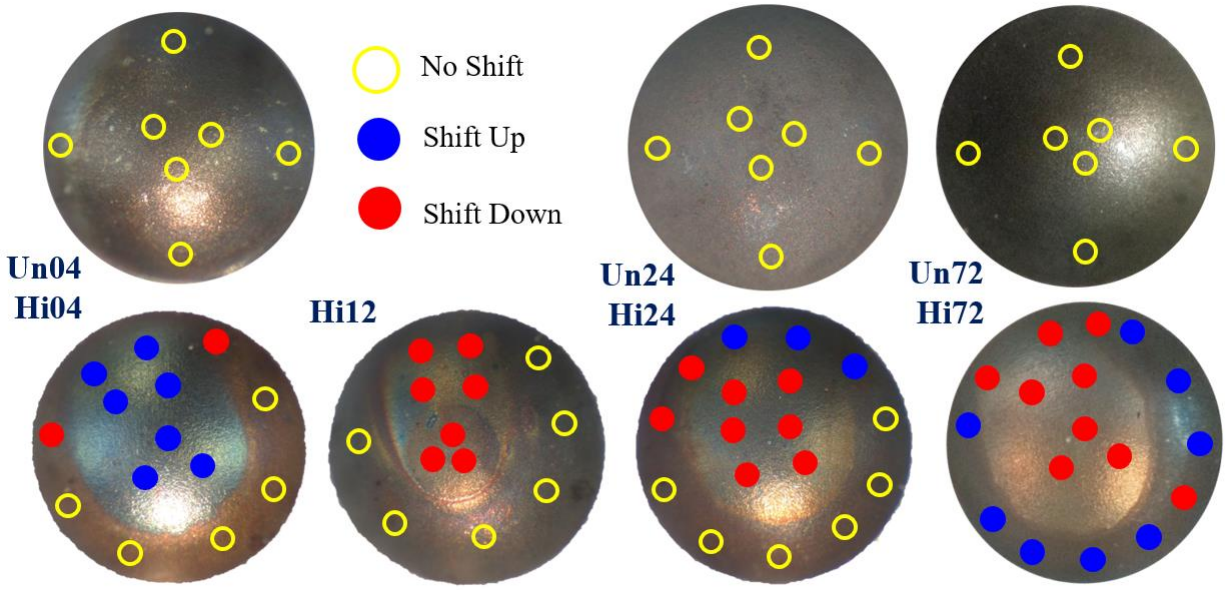

Figure 5.6. Optical images of irradiated and unirradiated samples with blue circles indicating locations where the Raman Spinel A_{1g} shifted up, and red circles where the spinel A_{1g} peak shifted down.

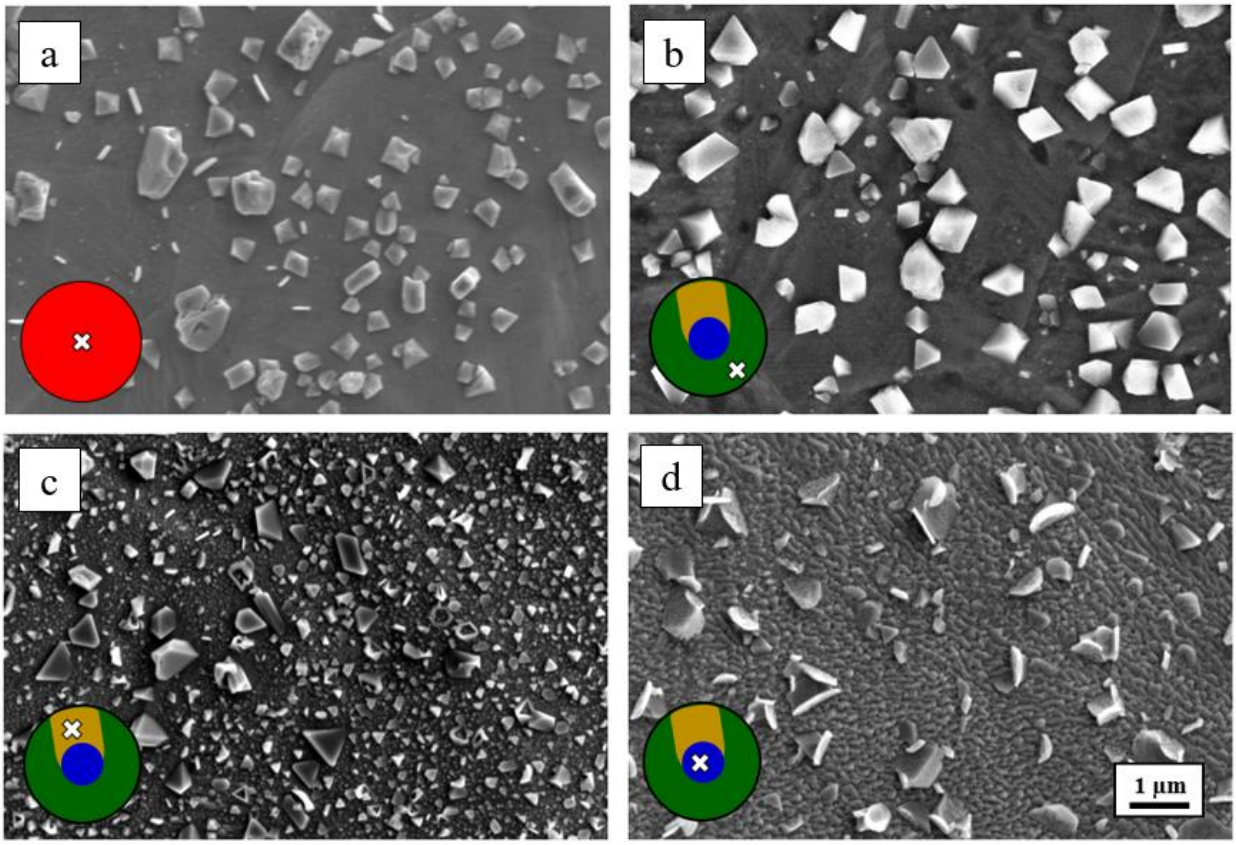

Figure 5.7. SEM images of (a) sample Un04, (b) the unirradiated surface of Hi04, (c) the flow surface of Hi04, and (d) the irradiated surface of Hi04.

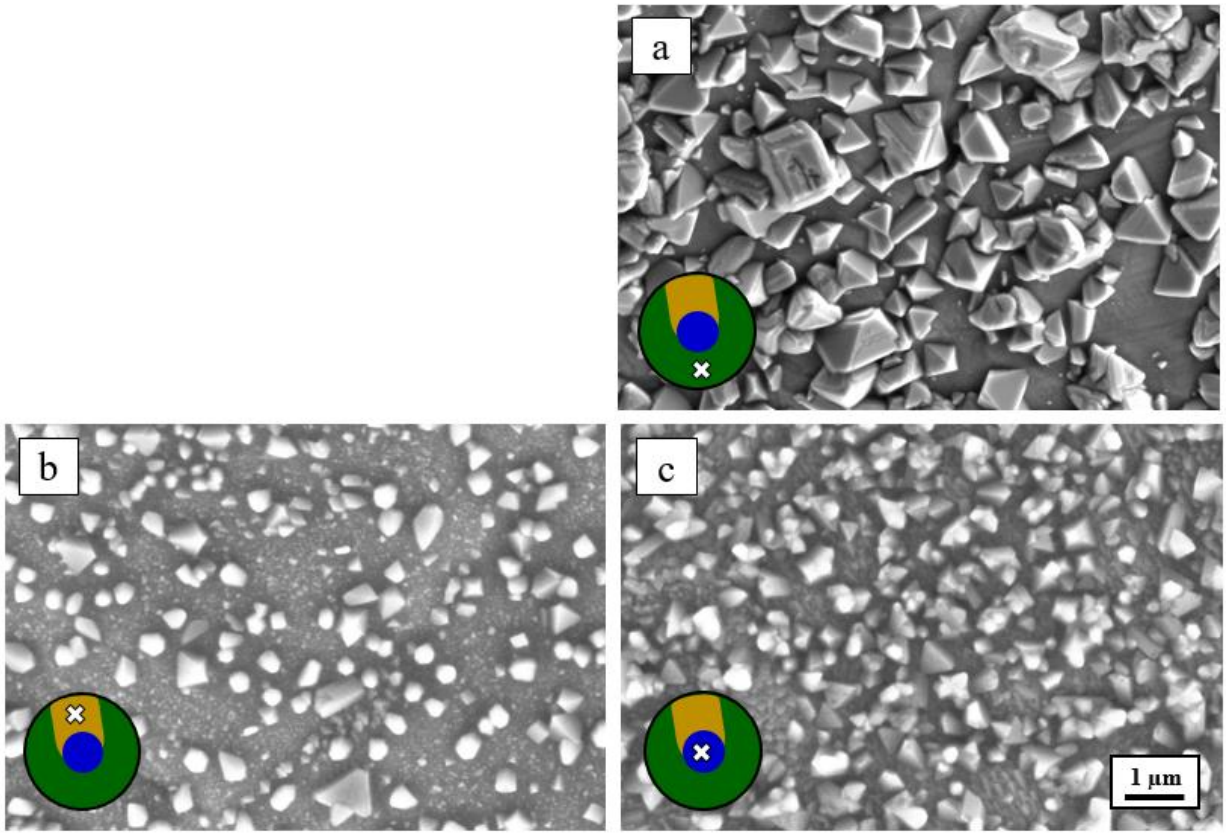

Figure 5.8. SEM images of sample Hi12, taken on the (a) unirradiated surface, (b) flow surface, and (c) irradiated surface

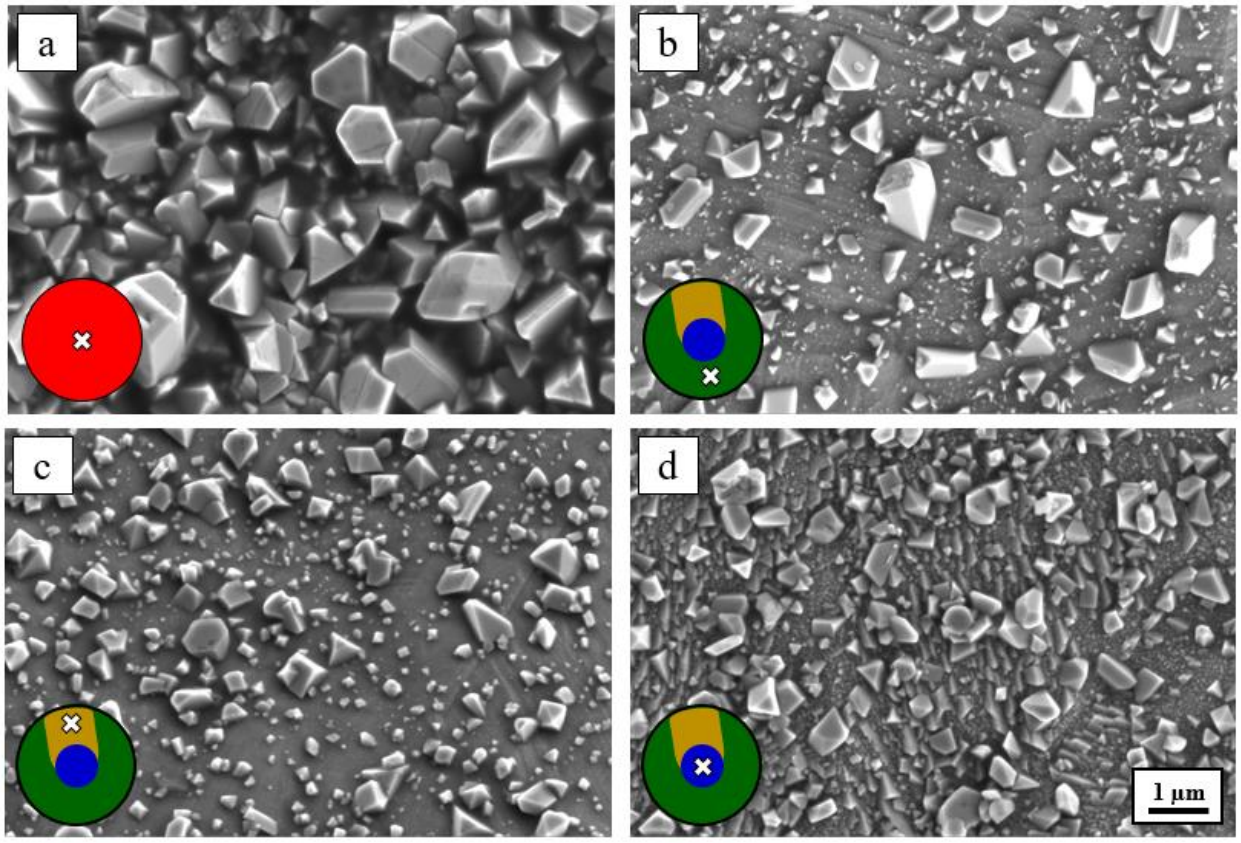

Figure 5.9. SEM images of (a) sample Un24, (b) the unirradiated surface of Hi24-2, (c) the flow surface of Hi24-2, and (d) the irradiated surface of Hi24-2

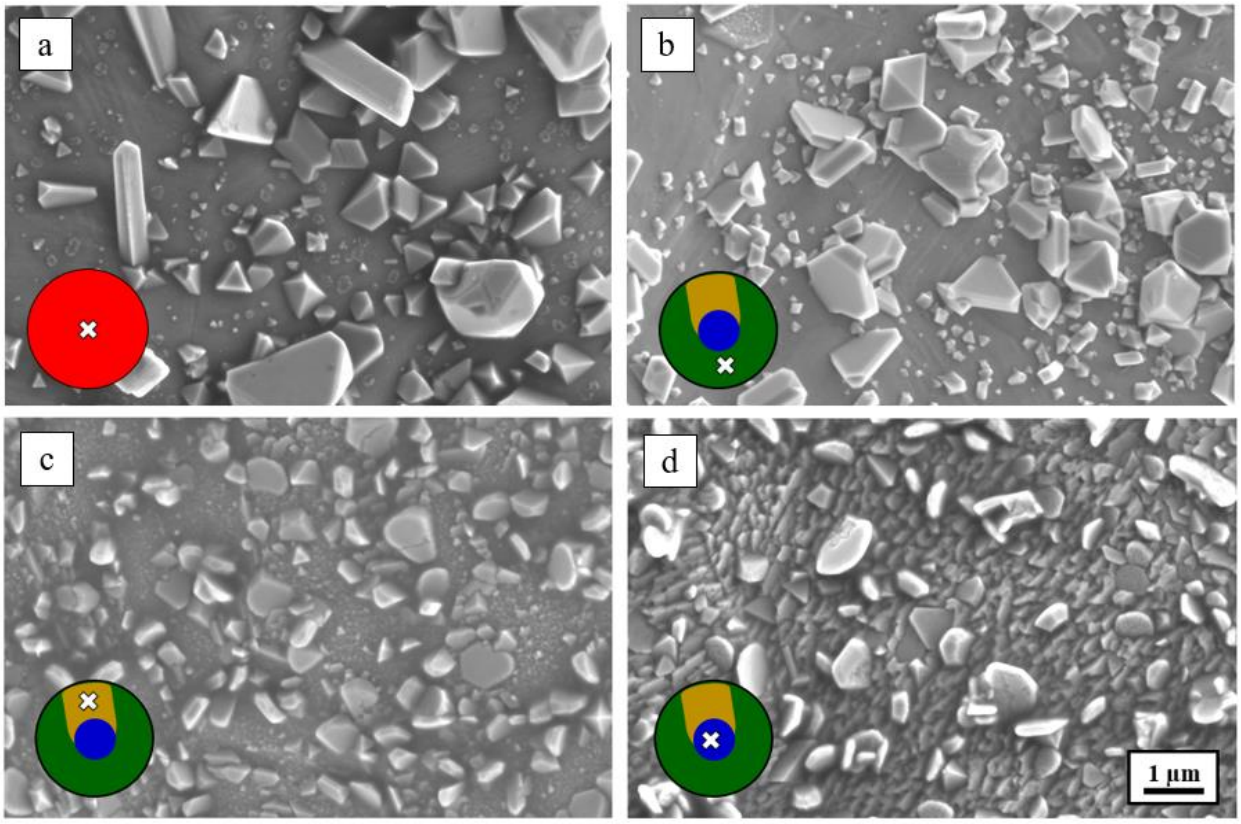

Figure 5.10. SEM images of (a) sample Un72, (b) the unirradiated surface of Hi72, (c) the flow surface of Hi72, and (d) the irradiated surface of Hi72

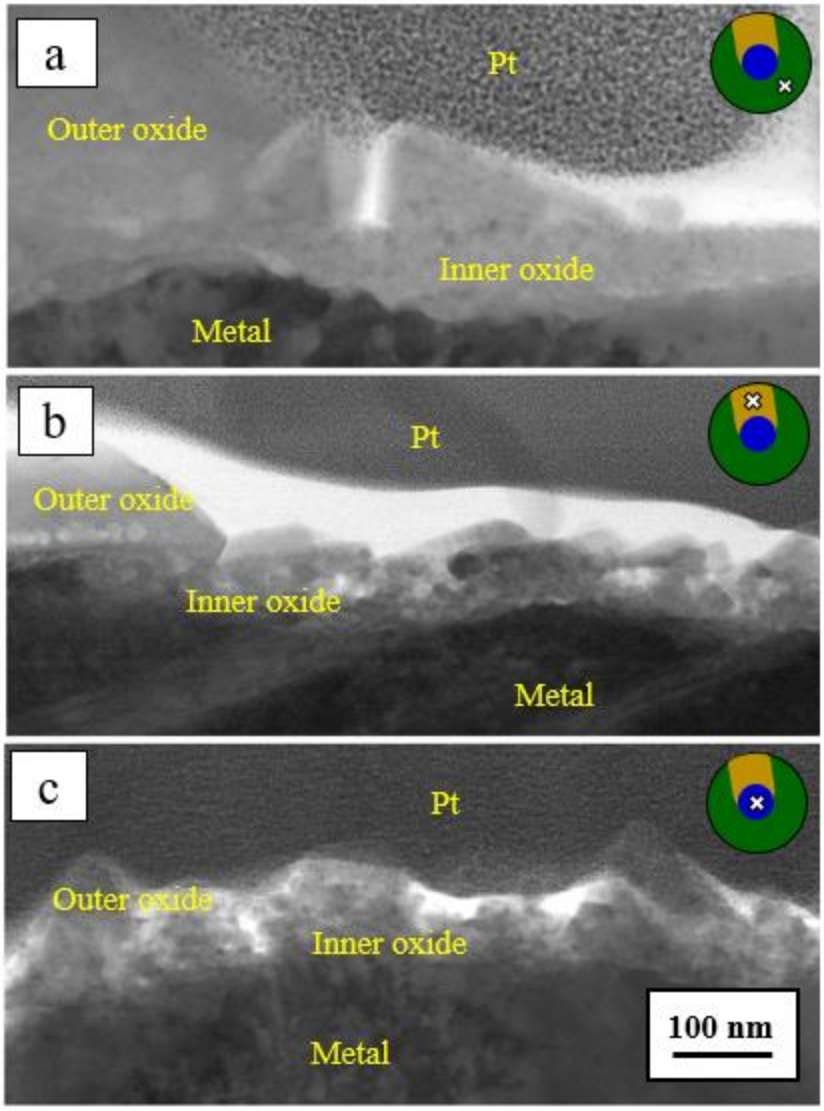

Figure 5.11. STEM images of the oxide layers on the (a) unirradiated (b) flow and (c) irradiated areas of sample Hi04.

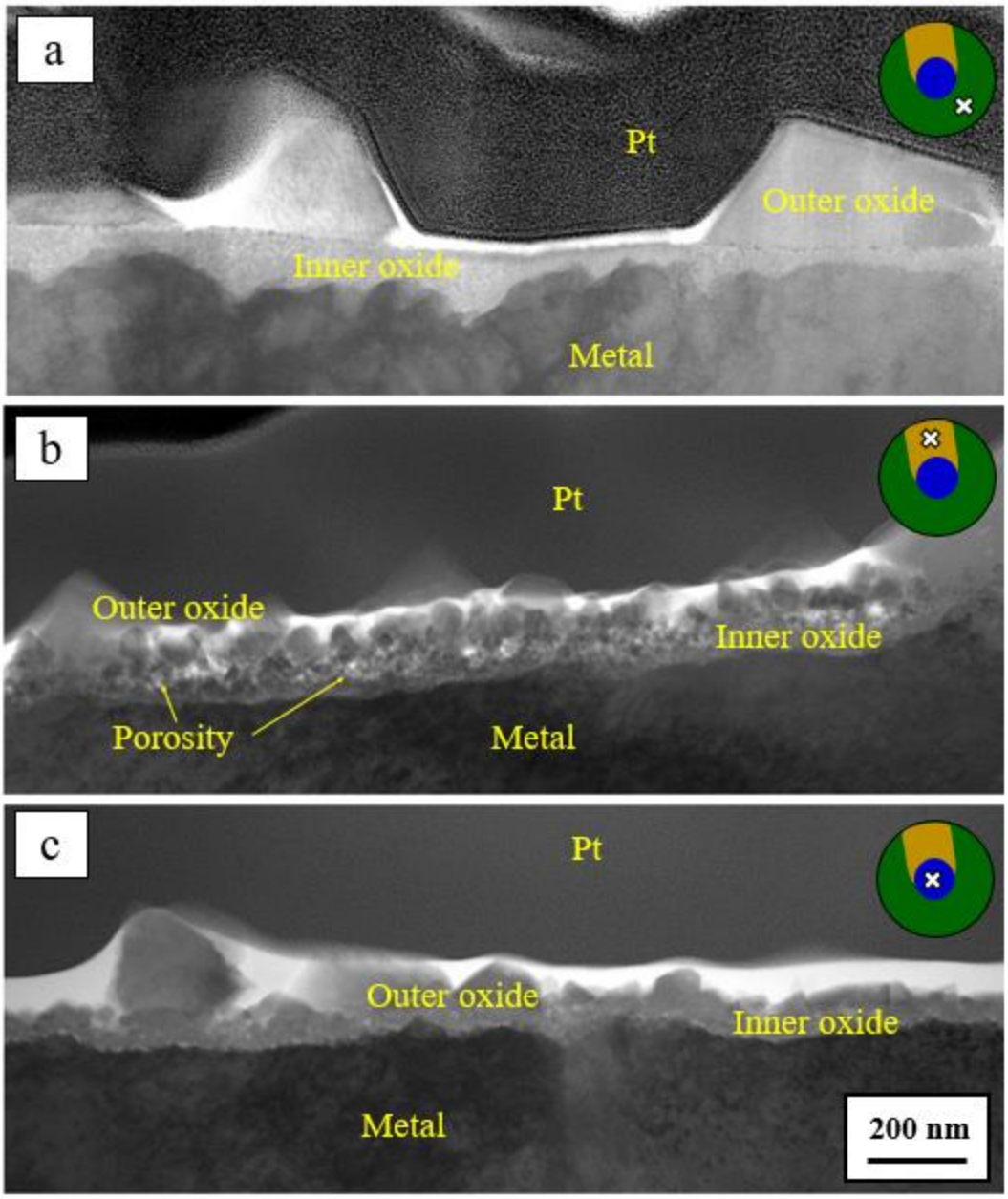

Figure 5.12. STEM images of the oxide layers on the (a) unirradiated (b) flow and (c) irradiated areas of sample Hi12.

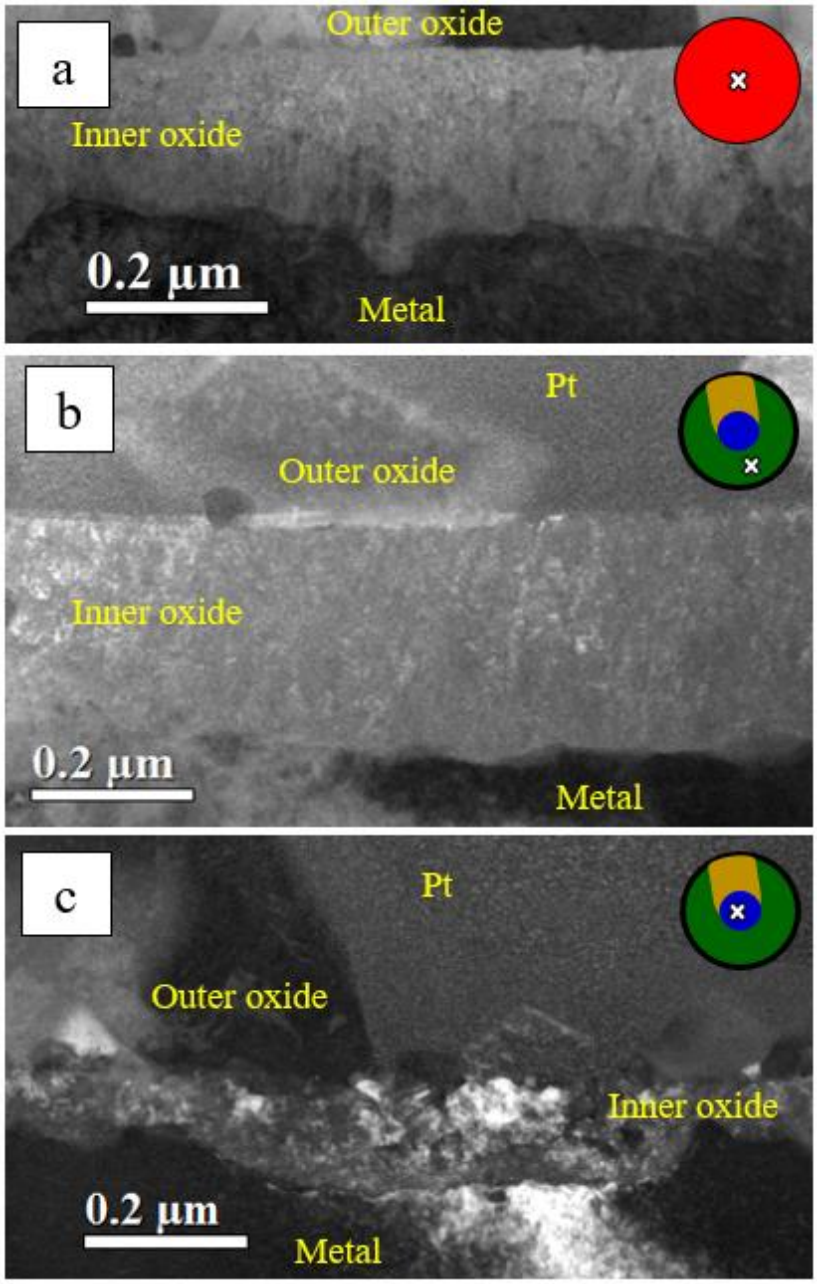

Figure 5.13. STEM images of the oxide layers on (a) sample Un24 and sample Hi24-1, taken from the (b) unirradiated and (c) irradiated regions.

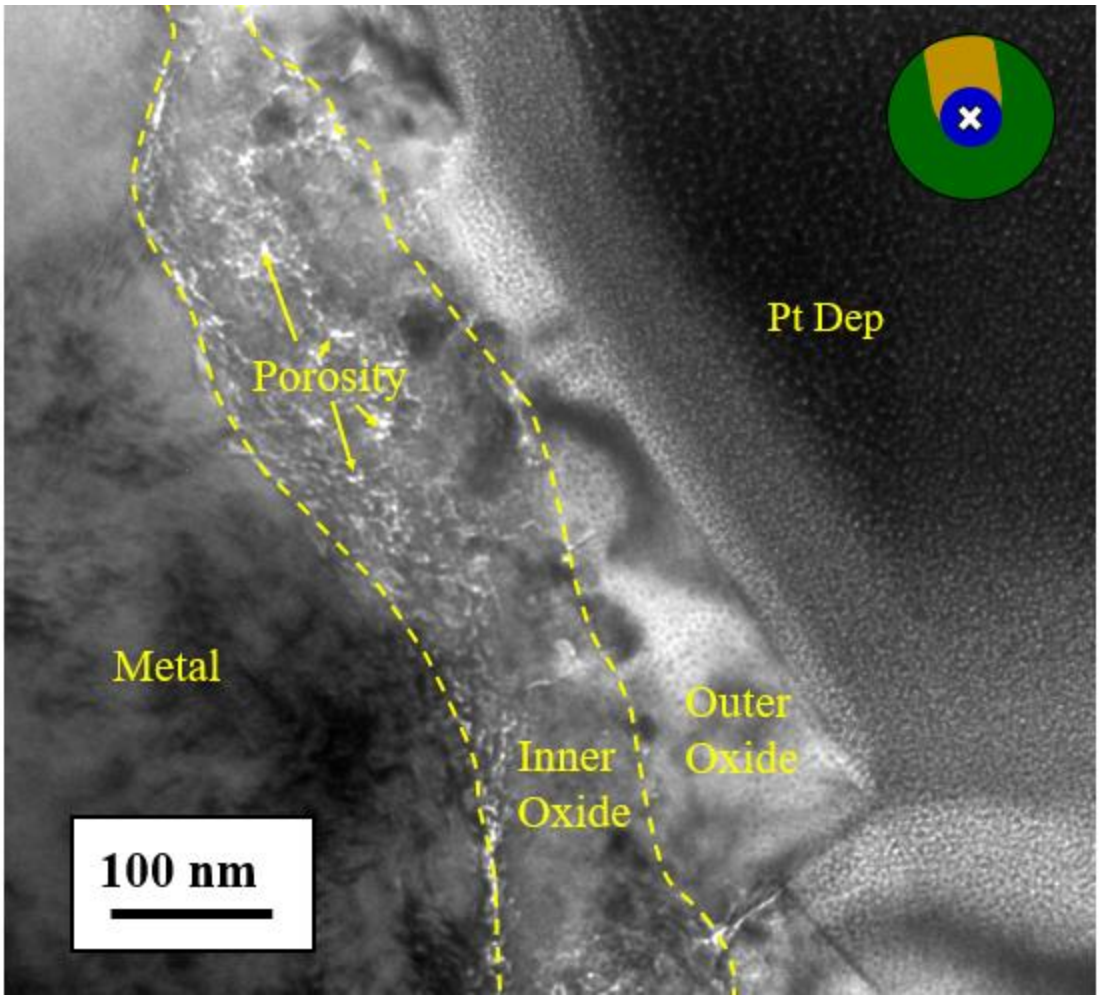

Figure 5.14. Under-focused BF TEM image of the irradiated region of Hi24-1.

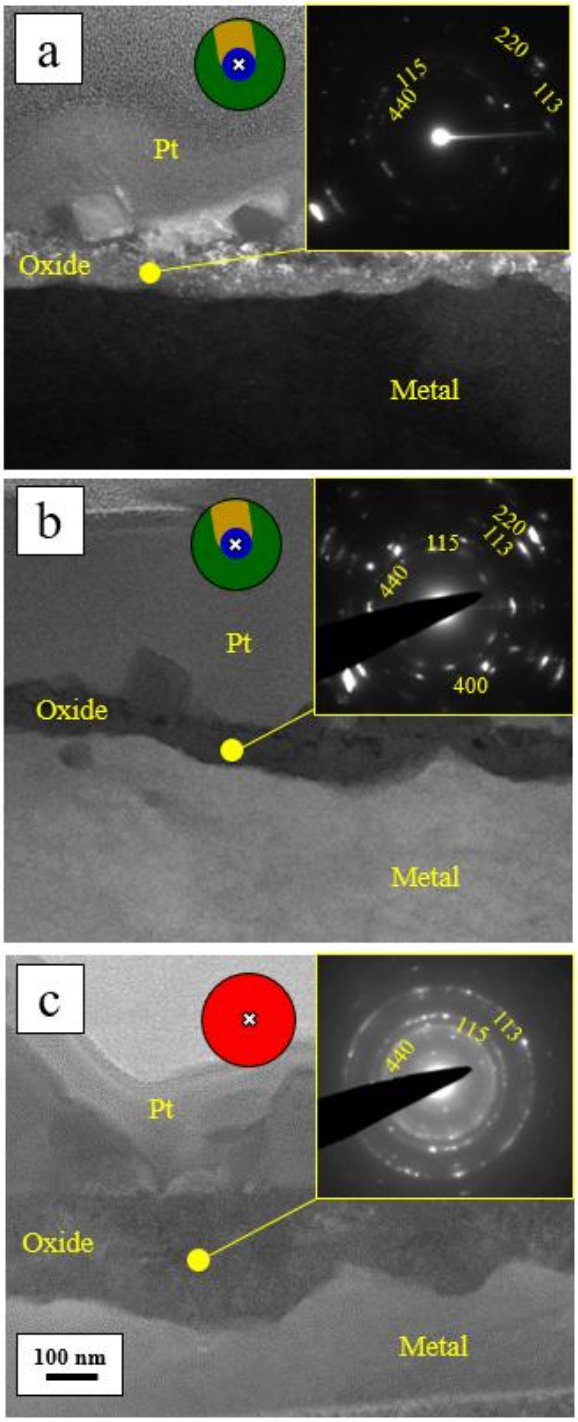

Figure 5.15. Select area electron diffraction patterns taken on the inner oxides of (a) the irradiated area of Hi24-1, (b) the irradiated area of Lo24, and (c) Un24. Diffraction rings are consistent with the spinel structure, and are indexed with the corresponding plane

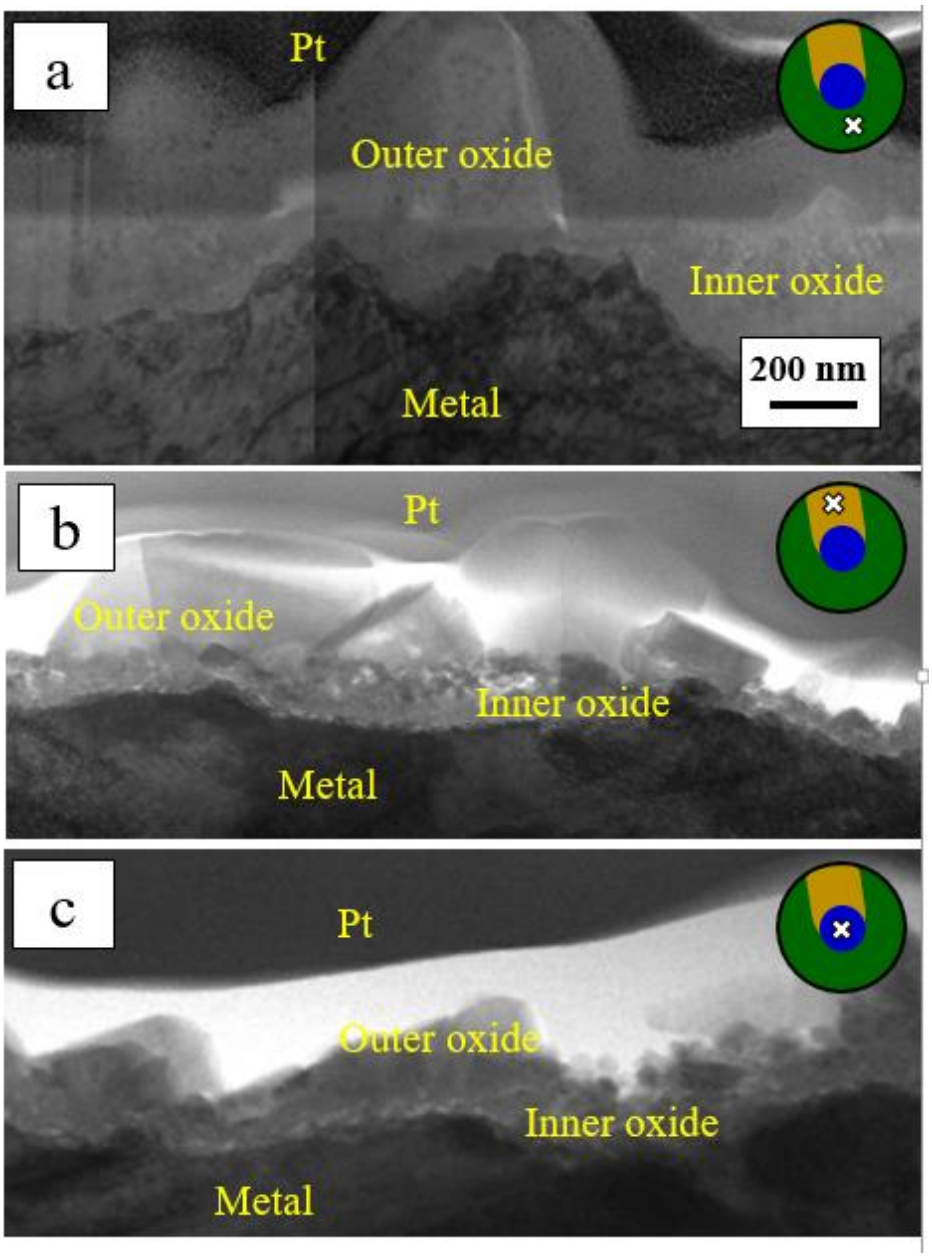

Figure 5.16. STEM images of the oxide layers on the (a) unirradiated (b) flow and (c) irradiated areas of sample Hi72.

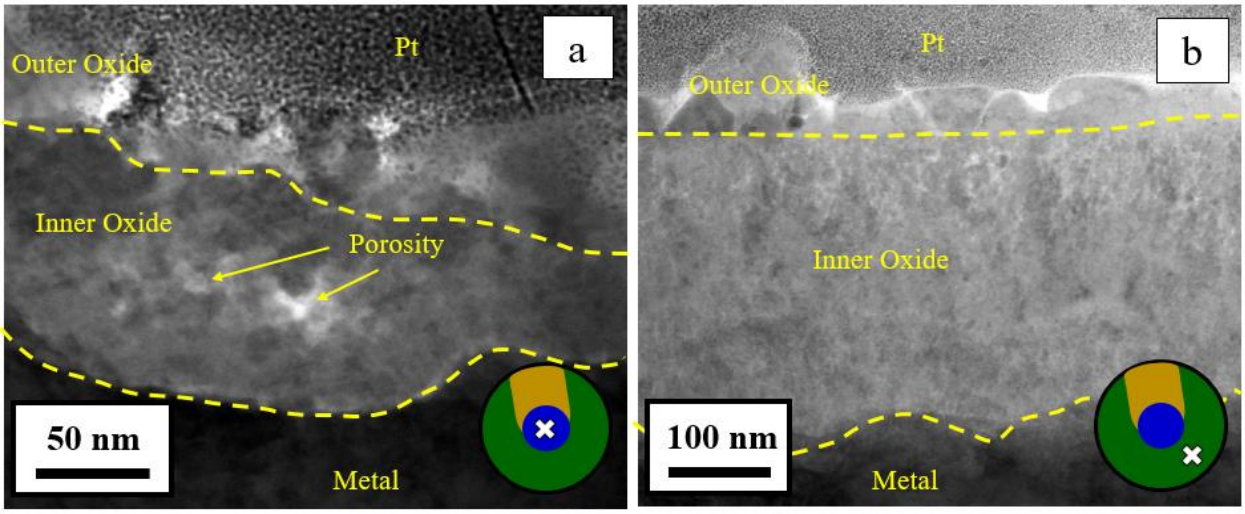

Figure 5.17. STEM images of the inner oxides on the (a) irradiated and (b) unirradiated areas of sample Hi72 to show the difference in porosity.

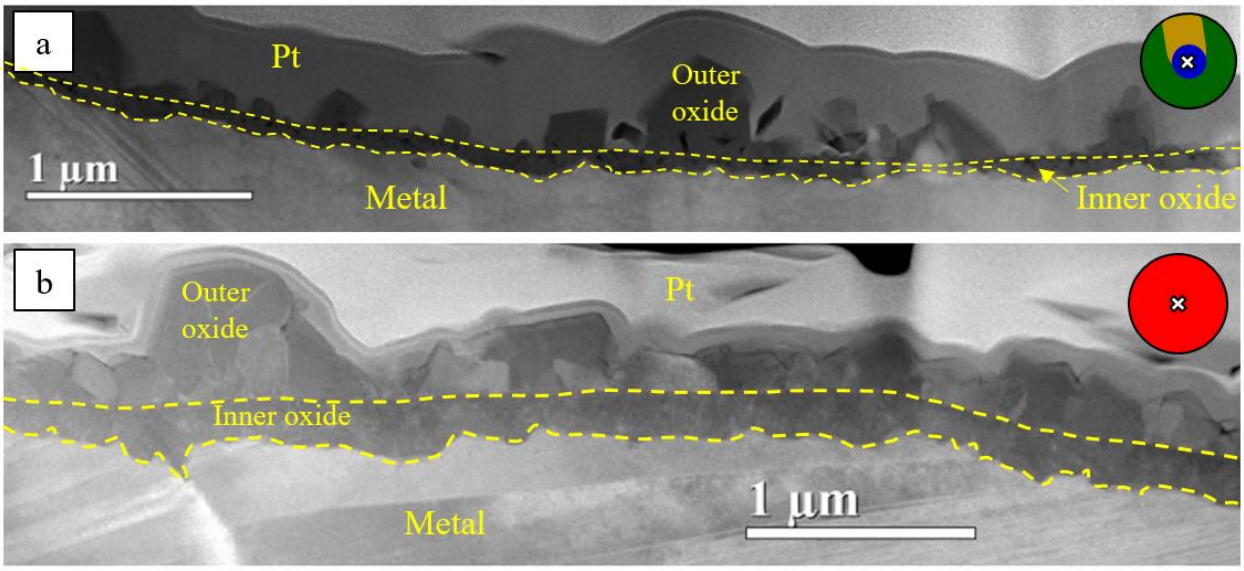

Figure 5.18. HAADF cross-sectional images of the oxides on (a) the irradiated region of Lo24and (b) Un24

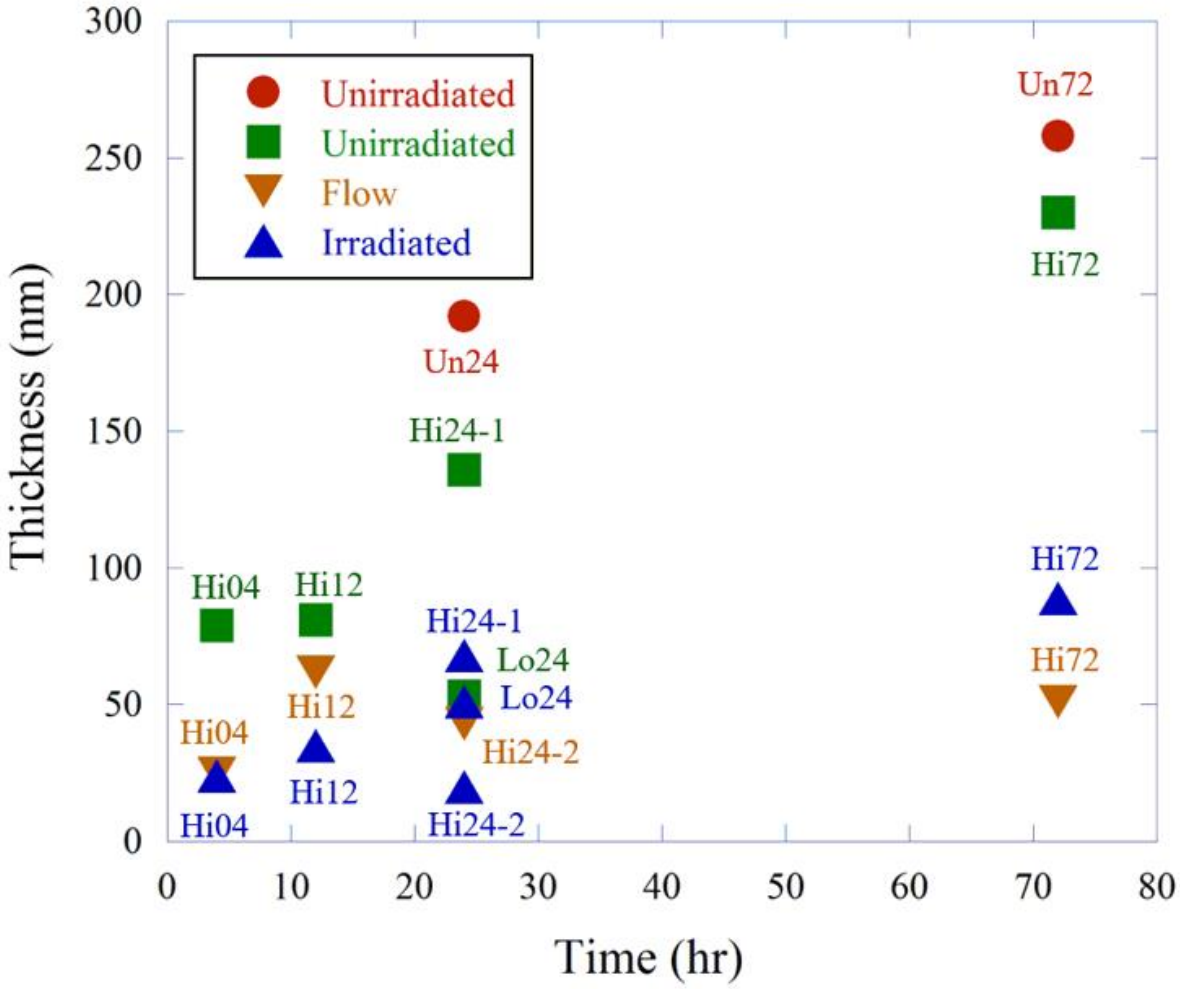

Figure 5.19. Average inner oxide thickness of the irradiated, flow, and unirradiated regions of samples used in this study. The red circles indicate data points from unirradiated samples, while the green circles are indicate specimens taken from the unirradiated areas of irradiated samples.

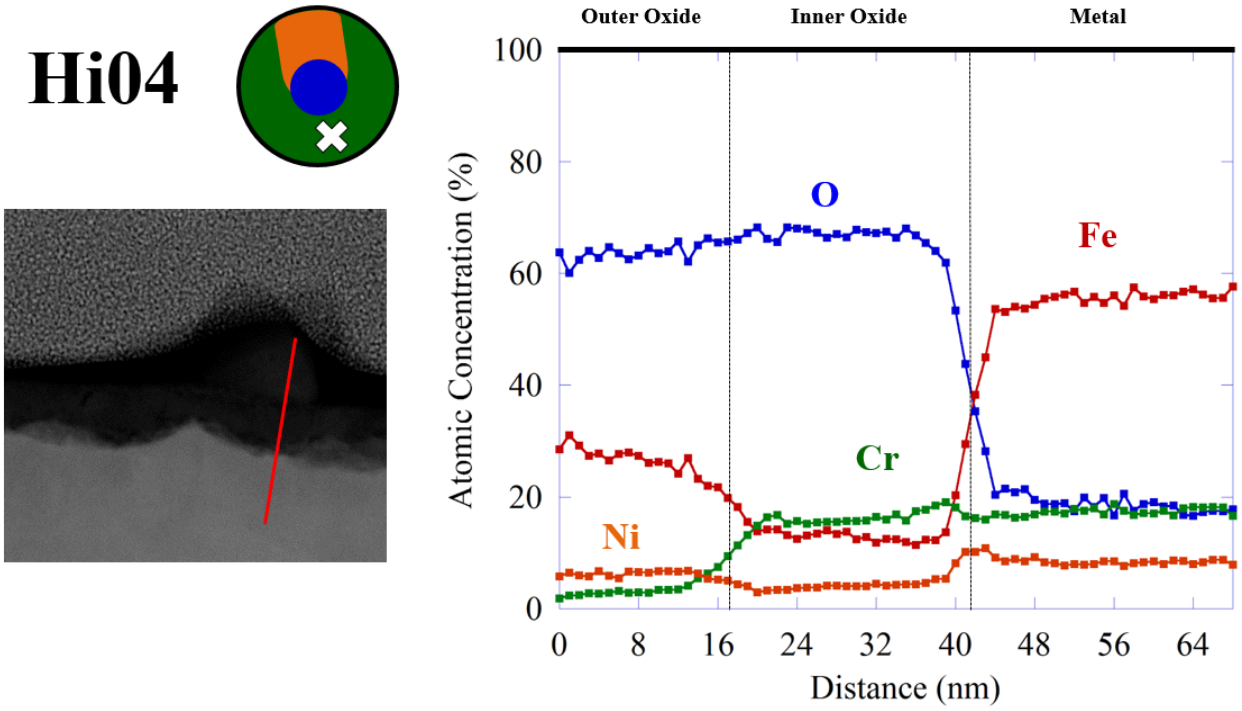

Figure 5.20. Cross sectional atomic composition of the unirradiated region of sample Hi04, measured by STEM-EDS.

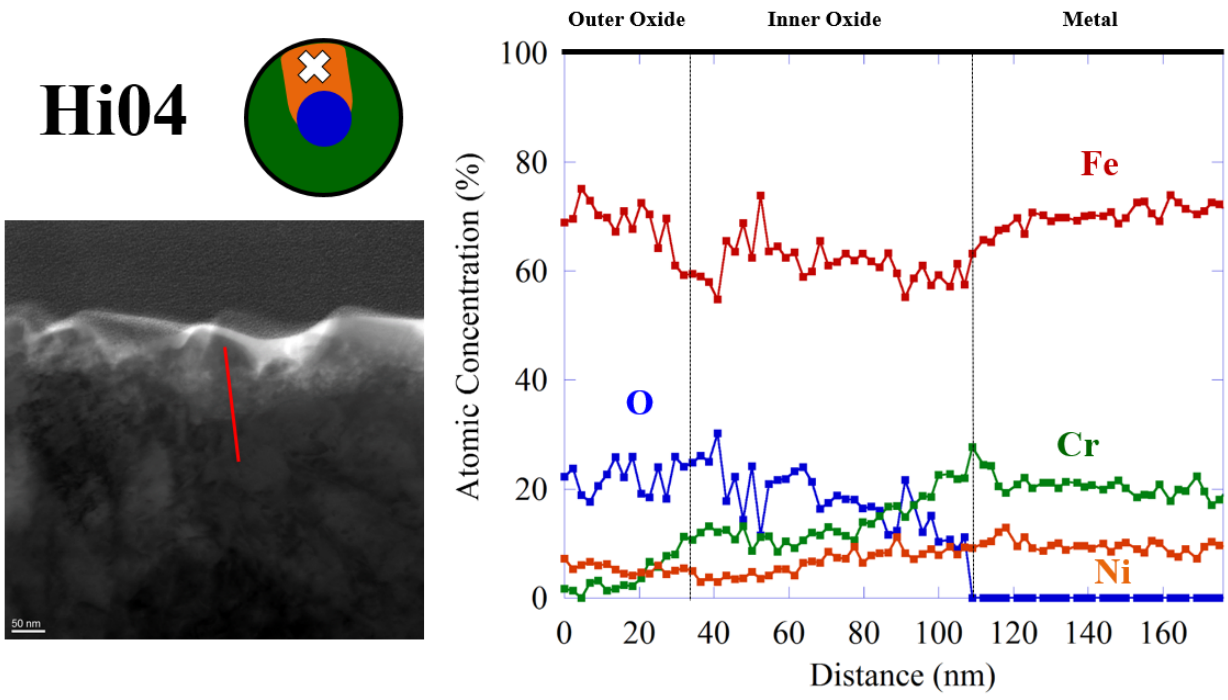

Figure 5.21. Cross sectional atomic composition of the flow region of sample Hi04, measured by STEM-EDS.

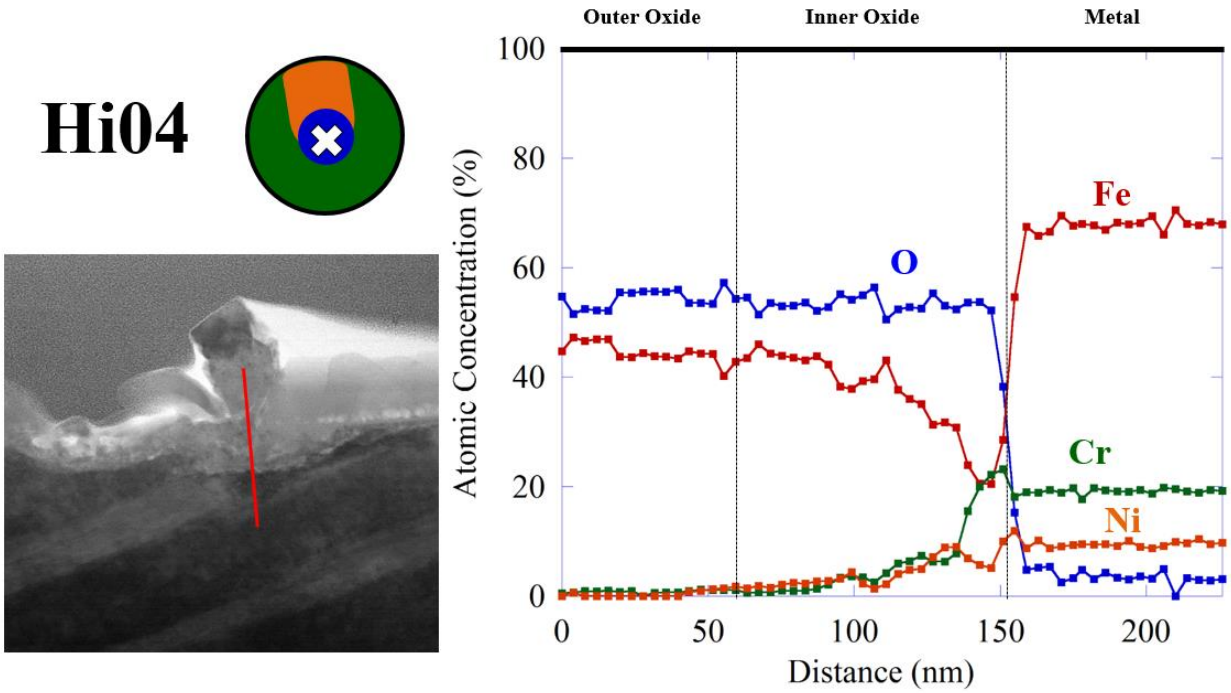

Figure 5.22. Cross sectional atomic composition of the irradiated region of sample Hi04, measured by STEM-EDS.

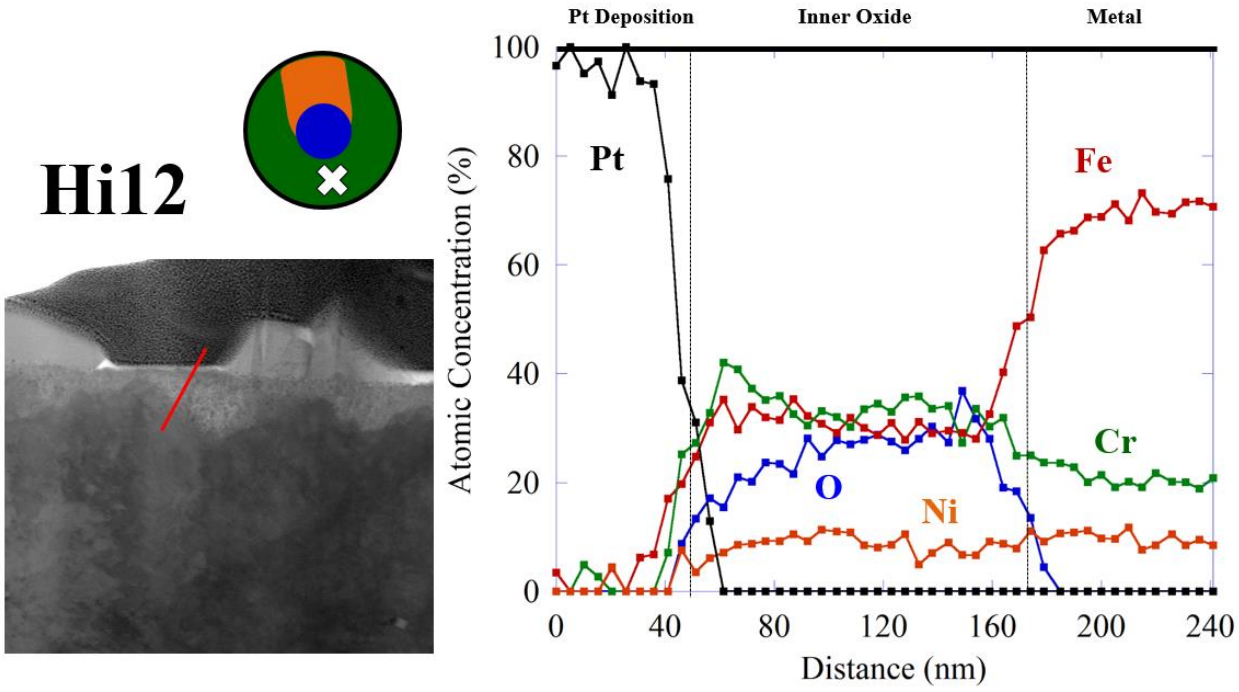

Figure 5.23. Cross sectional atomic composition of the unirradiated region of sample Hi12, measured by STEM-EDS.

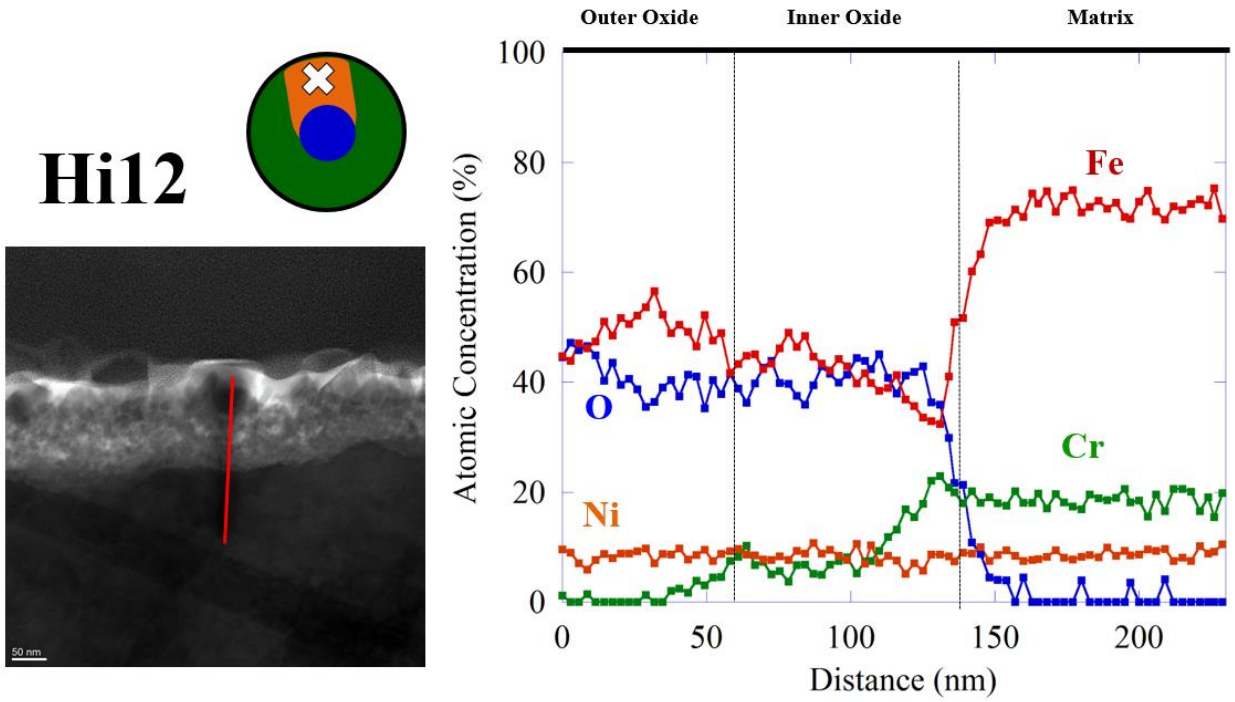

Figure 5.24. Cross sectional atomic composition of the flow region of sample Hi12, measured by STEM-EDS.

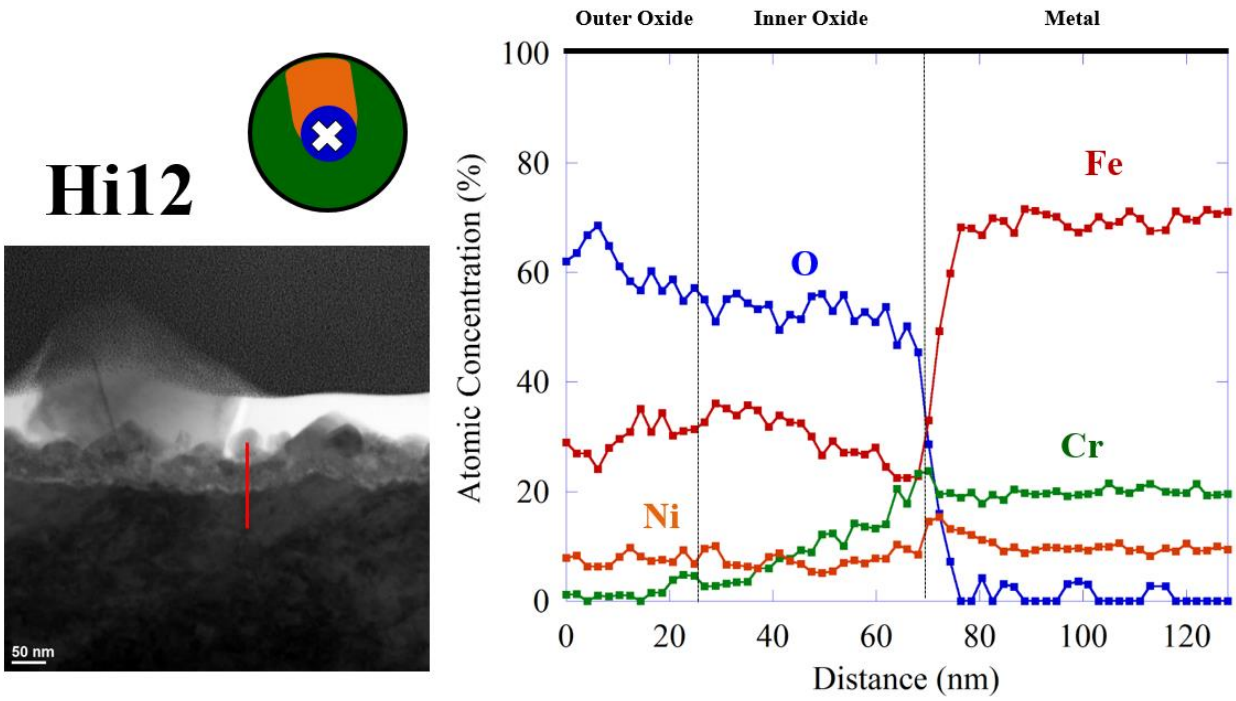

Figure 5.25. Cross sectional atomic composition of the irradiated region of sample Hi12, measured by STEM-EDS.

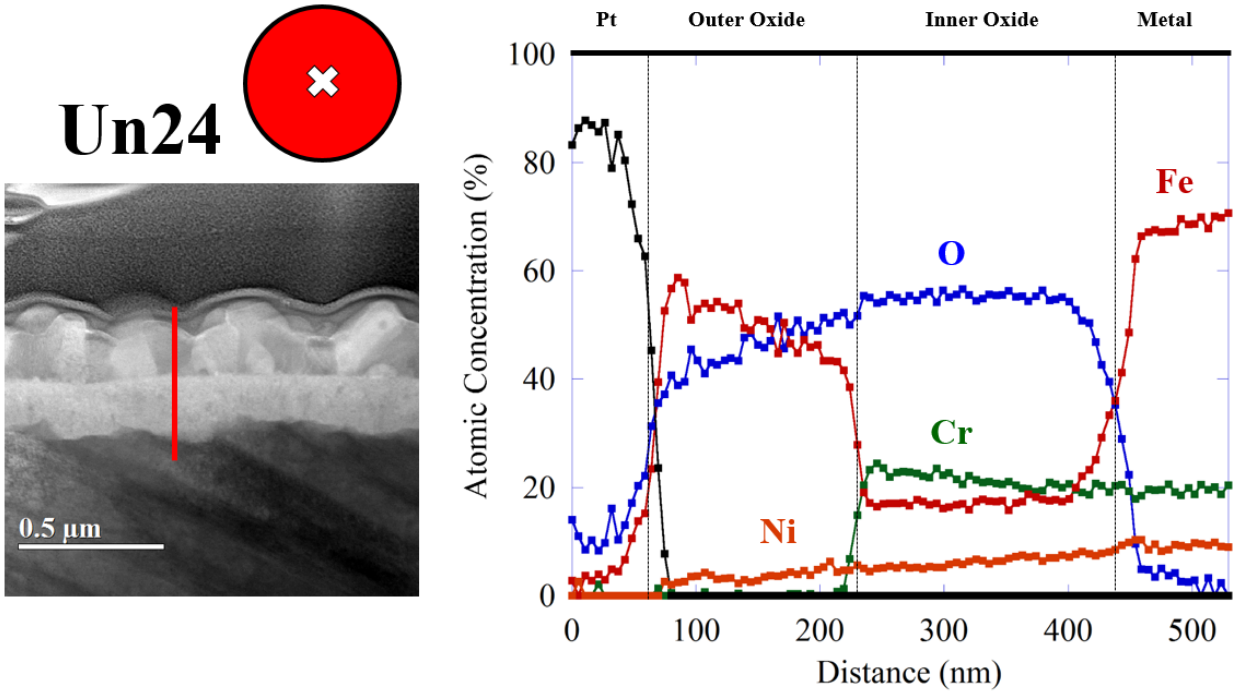

Figure 5.26. Cross sectional atomic composition of sample Un24, measured by STEM-EDS.

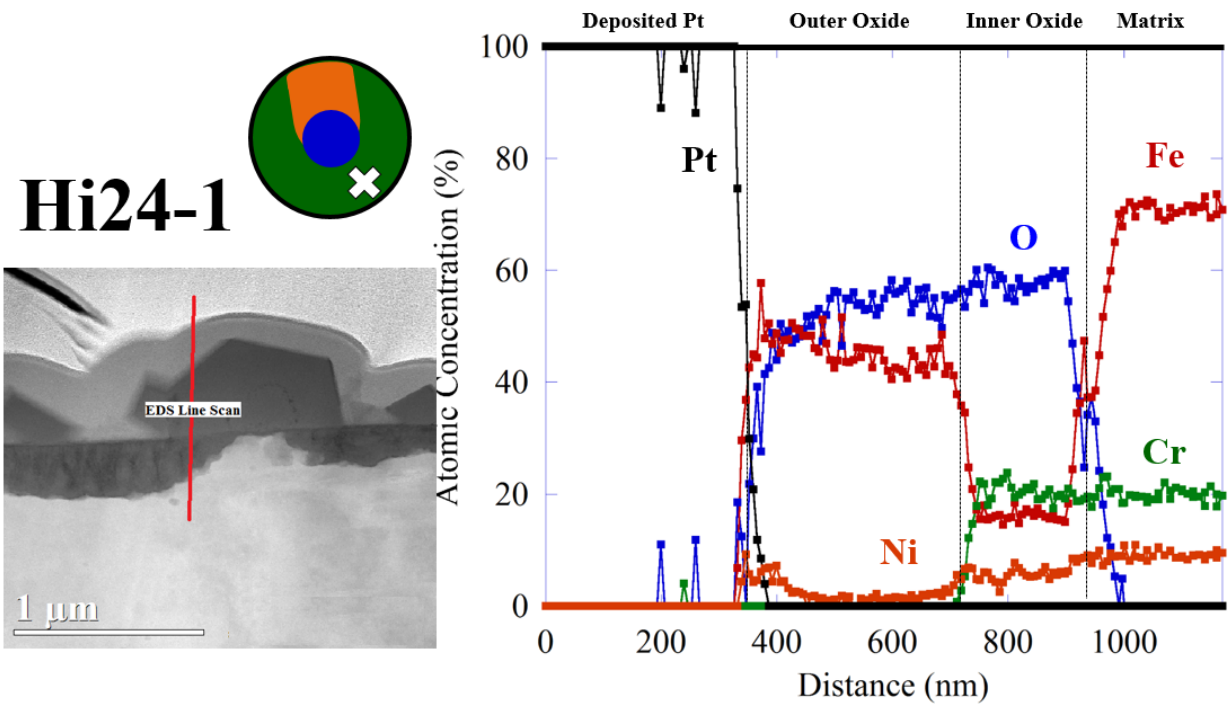

Figure 5.27. Cross sectional atomic composition of the unirradiated region of sample Hi24-1, measured by STEM-EDS.

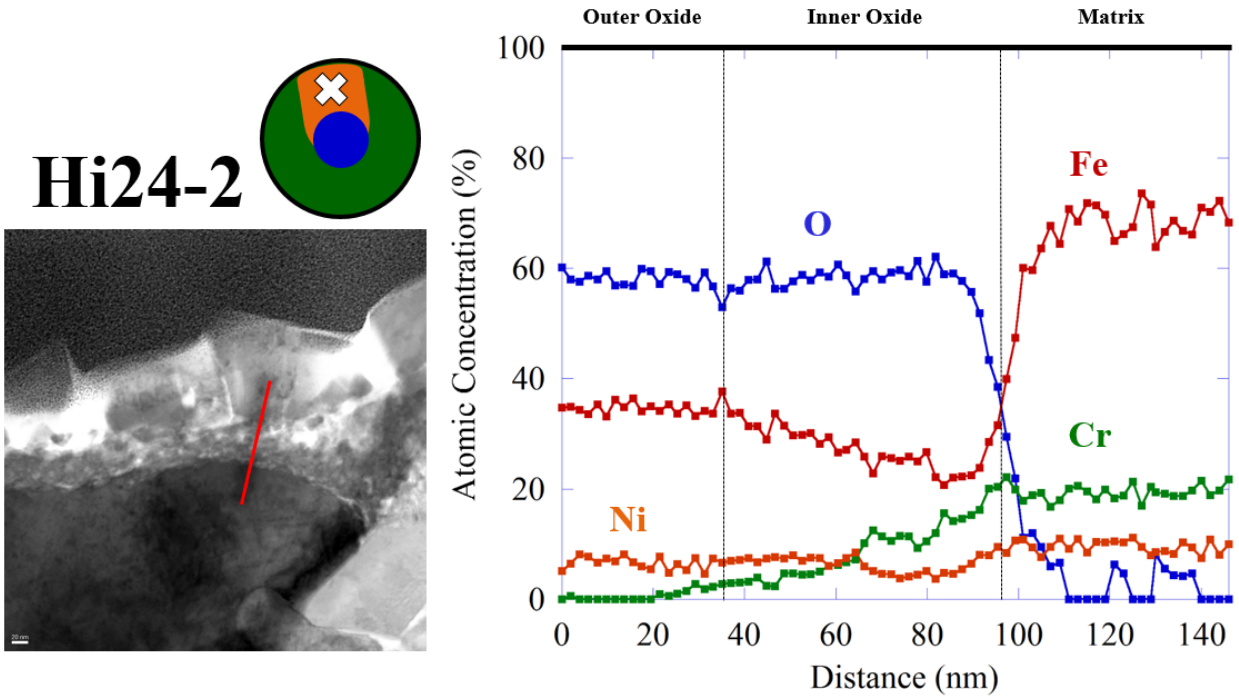

Figure 5.28. Cross sectional atomic composition of the flow region of sample Hi24-2, measured by STEM-EDS.

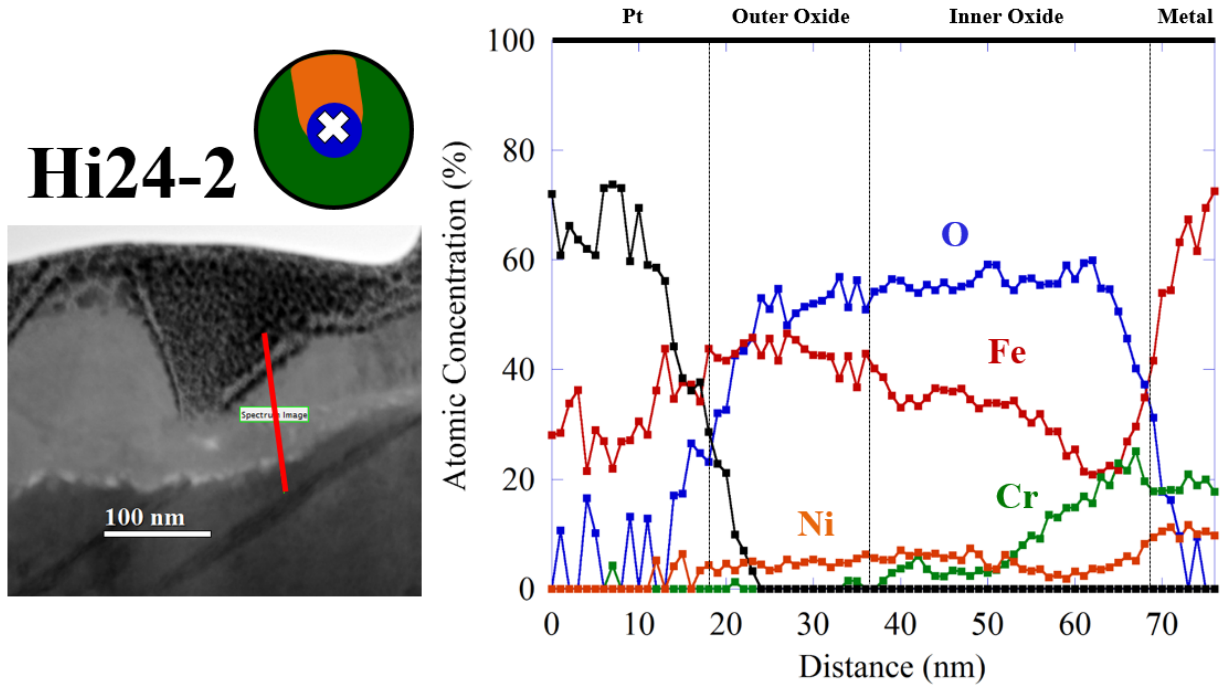

Figure 5.29. Cross sectional atomic composition of the irradiated region of sample Hi24-2, measured by STEM-EDS.

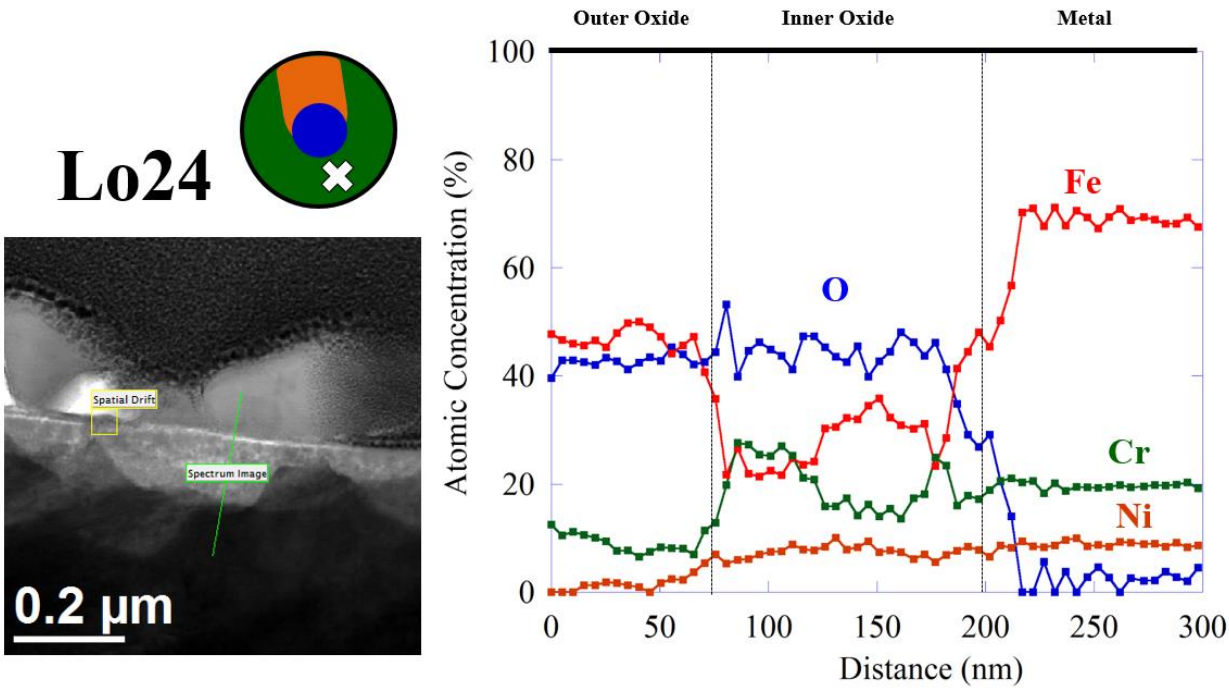

Figure 5.30. Cross sectional atomic composition of the unirradiated region of sample Lo24, measured by STEM-EDS.

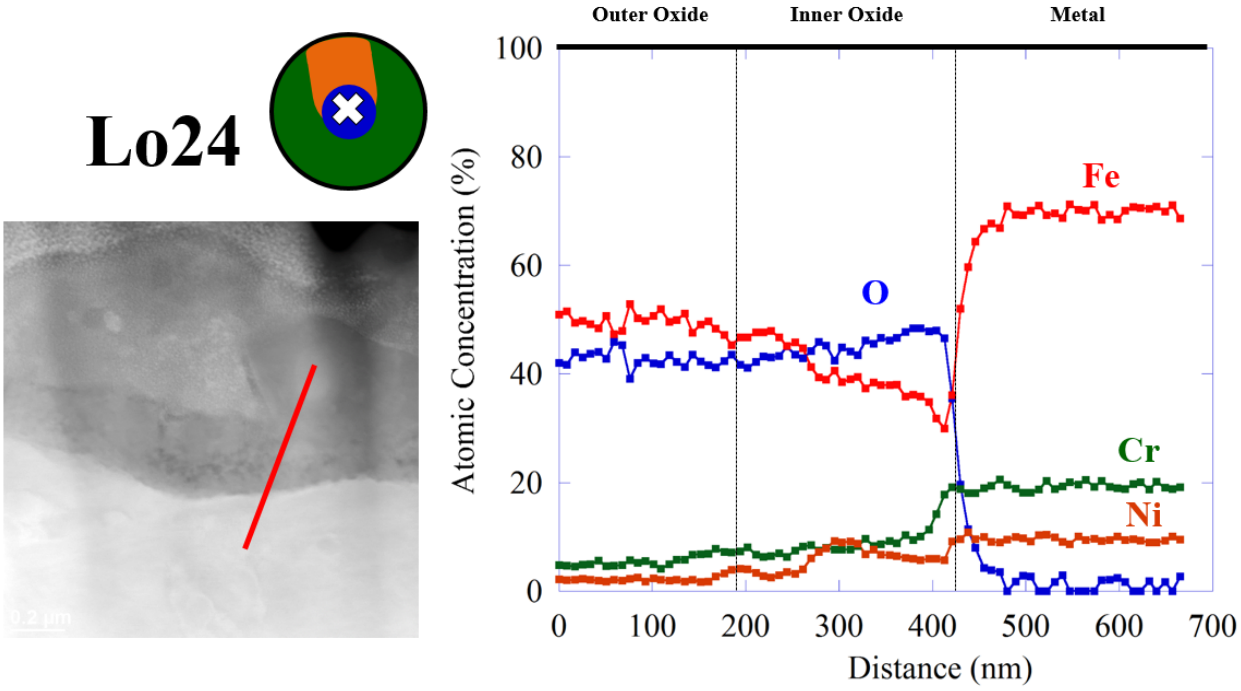

Figure 5.31. Cross sectional atomic composition of the irradiated region of sample Lo24, measured by STEM-EDS.

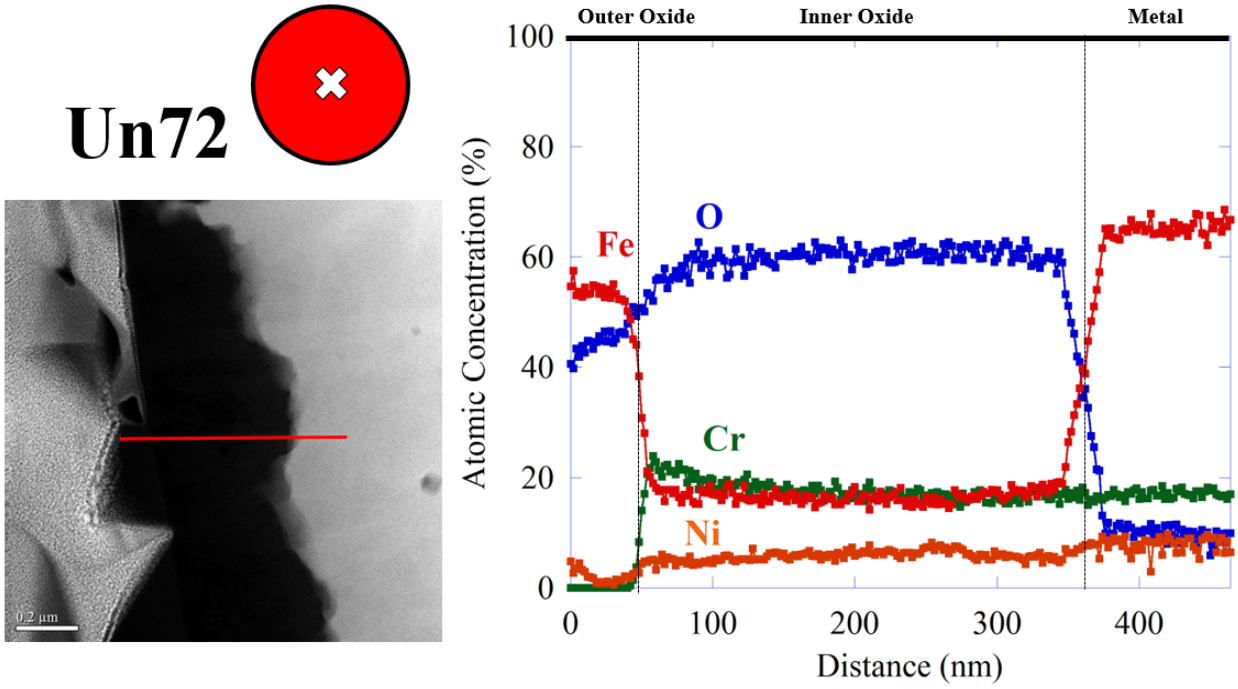

Figure 5.32. Cross sectional atomic composition of sample Un72, measured by STEM-EDS.

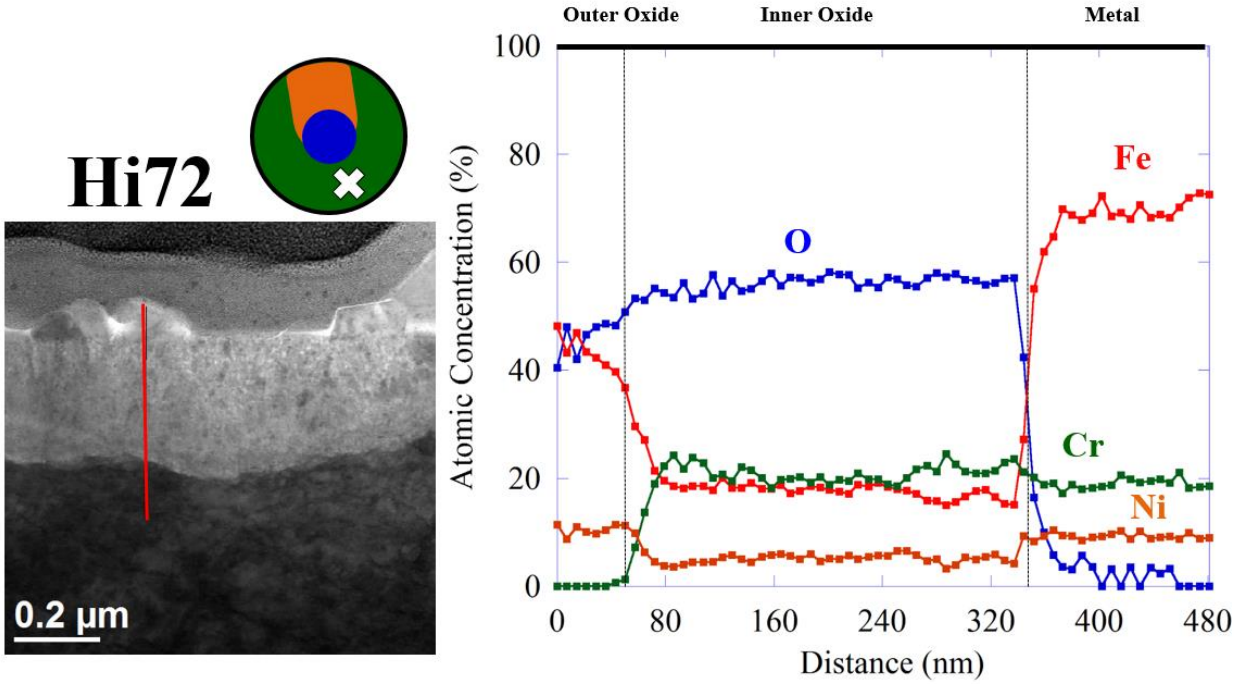

Figure 5.33. Cross sectional atomic composition of the unirradiated region of sample Hi72, measured by STEM-EDS.

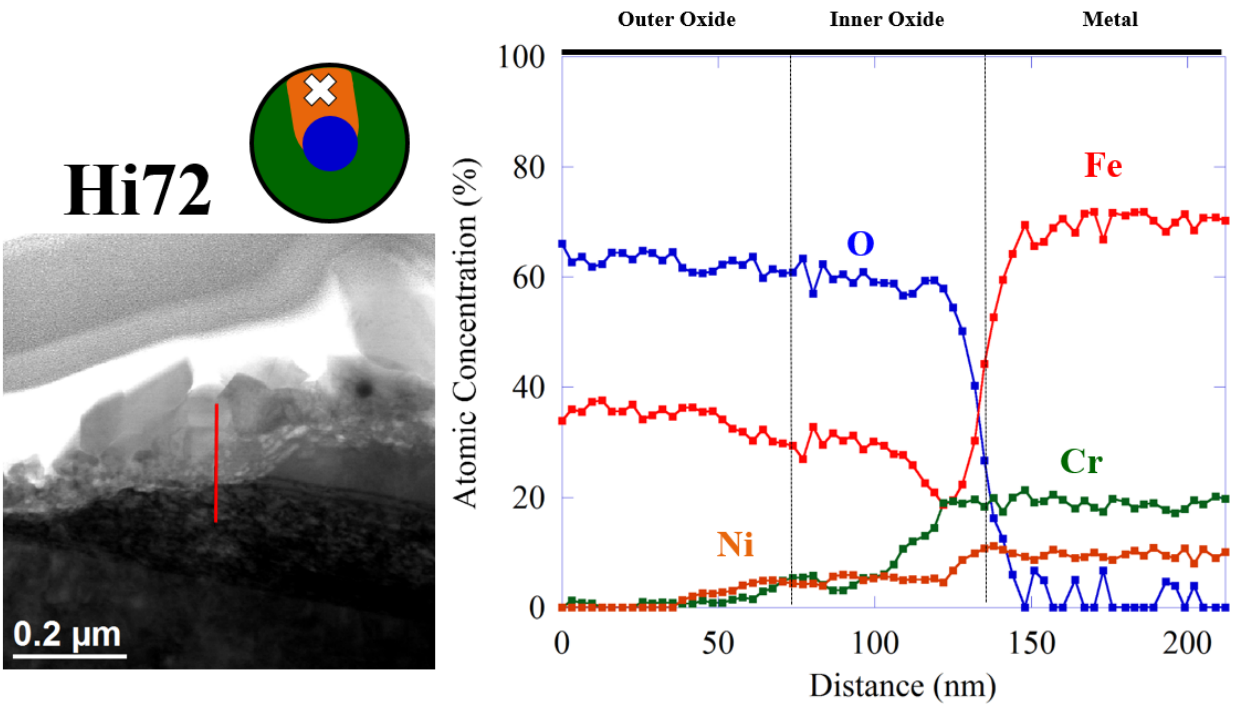

Figure 5.34. Cross sectional atomic composition of the flow region of sample Hi72, measured by STEM-EDS.

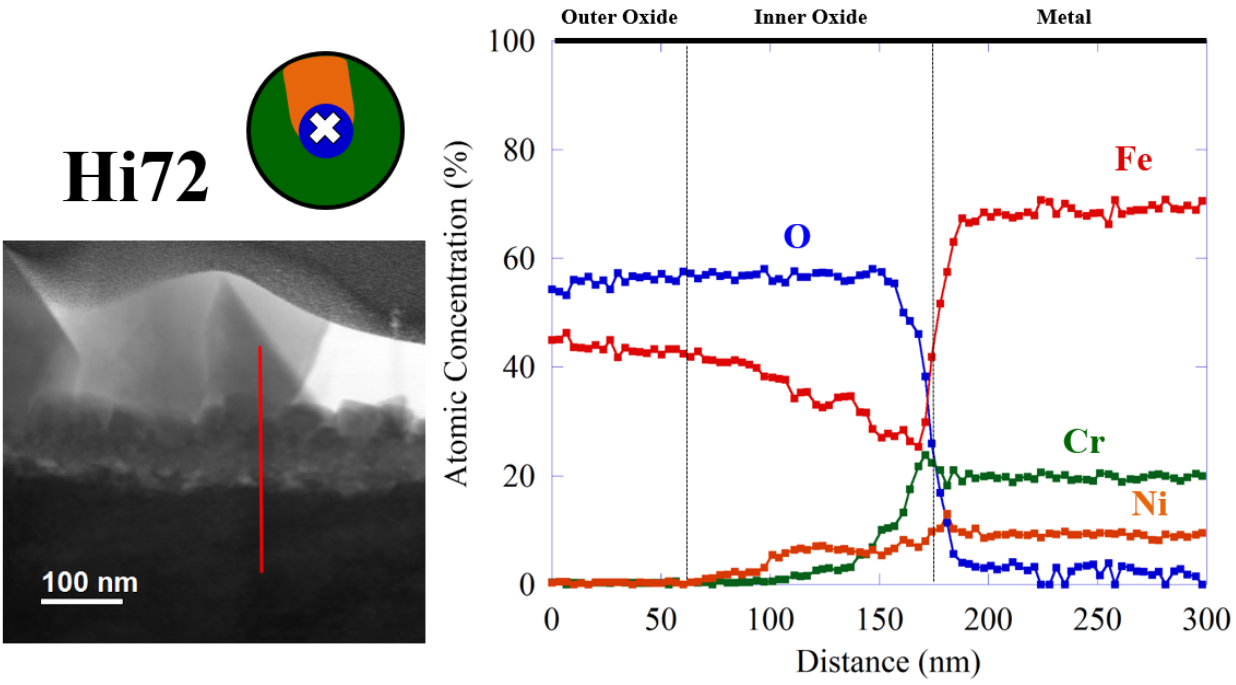

Figure 5.35. Cross sectional atomic composition of the irradiated region of sample Hi72, measured by STEM-EDS.

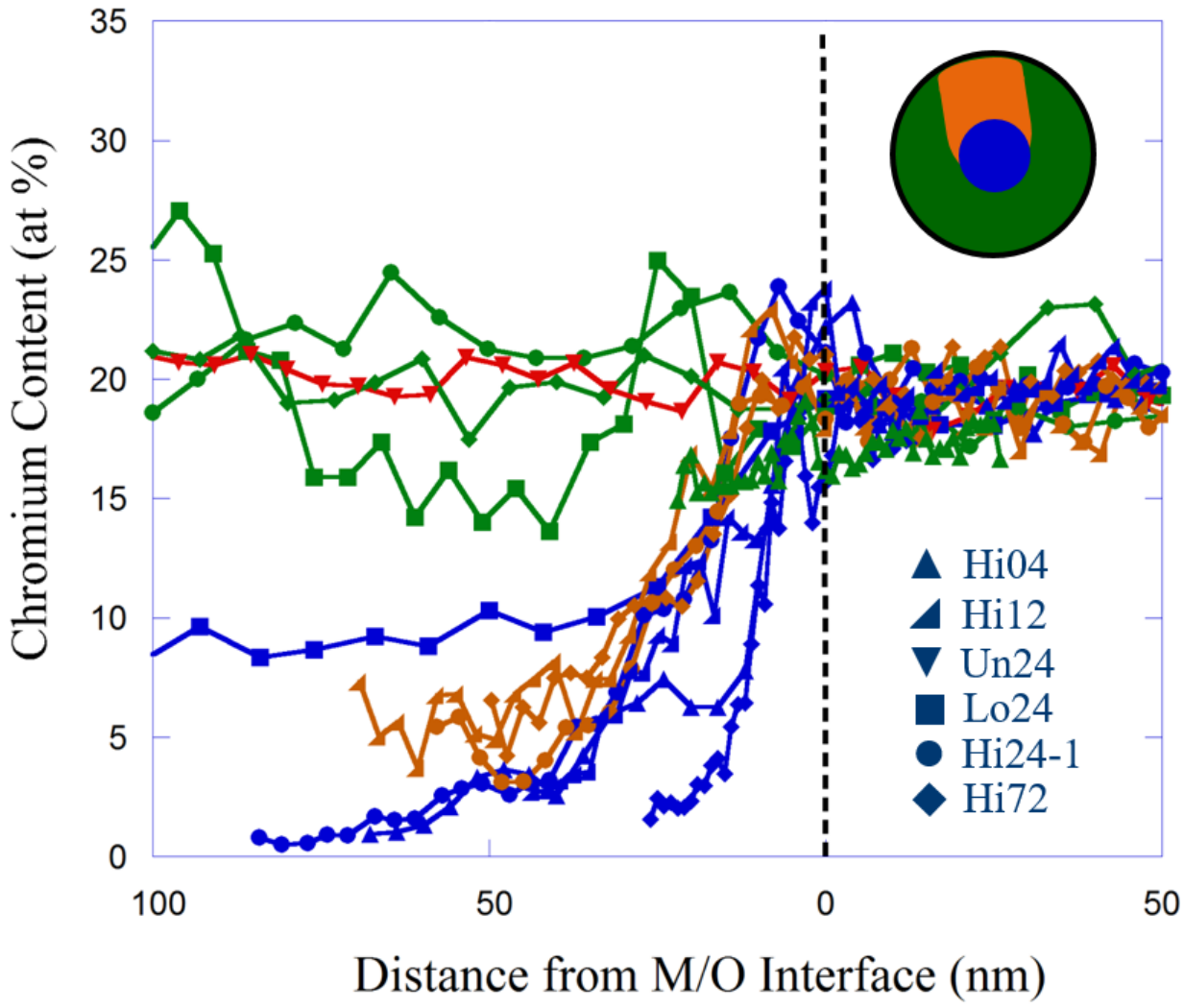

Figure 5.36. Representative STEM-EDS line scans showing the Cr content across the metal-oxide interface of several sample regions.

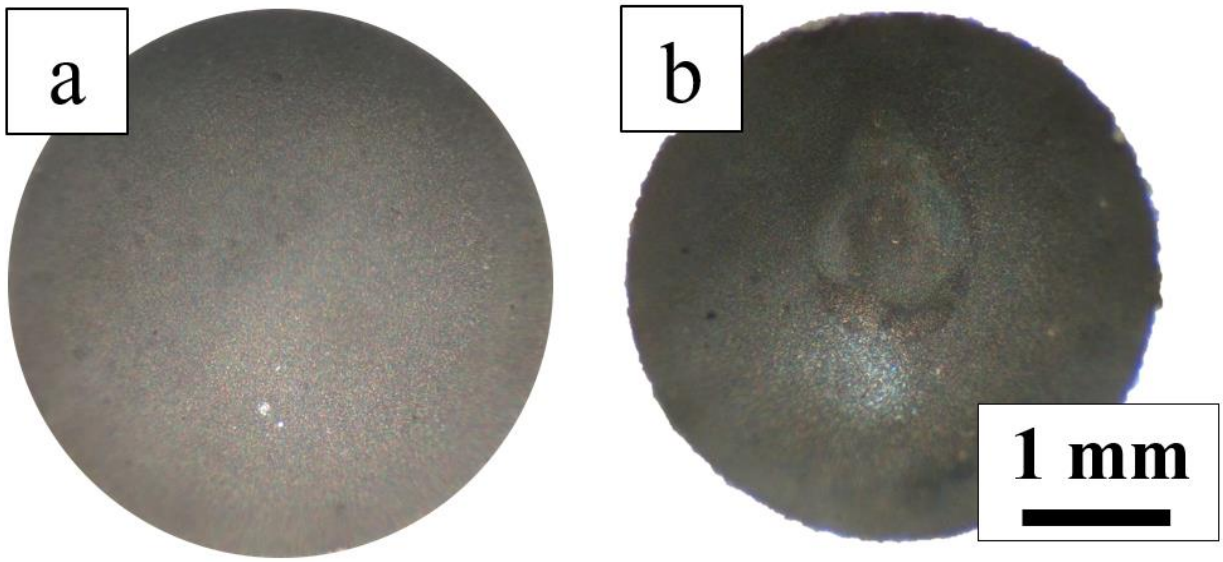

Figure 5.37. Optical images of sample Pr24, exposed for 72 hrs in 320˚C water with 3 wppm H_2 (a) before and (b) after the second exposure in the same water conditions with irradiation at a dose rate of 4000 kGy/s and a damage rate of $7x10^{-6}$ dpa/s.

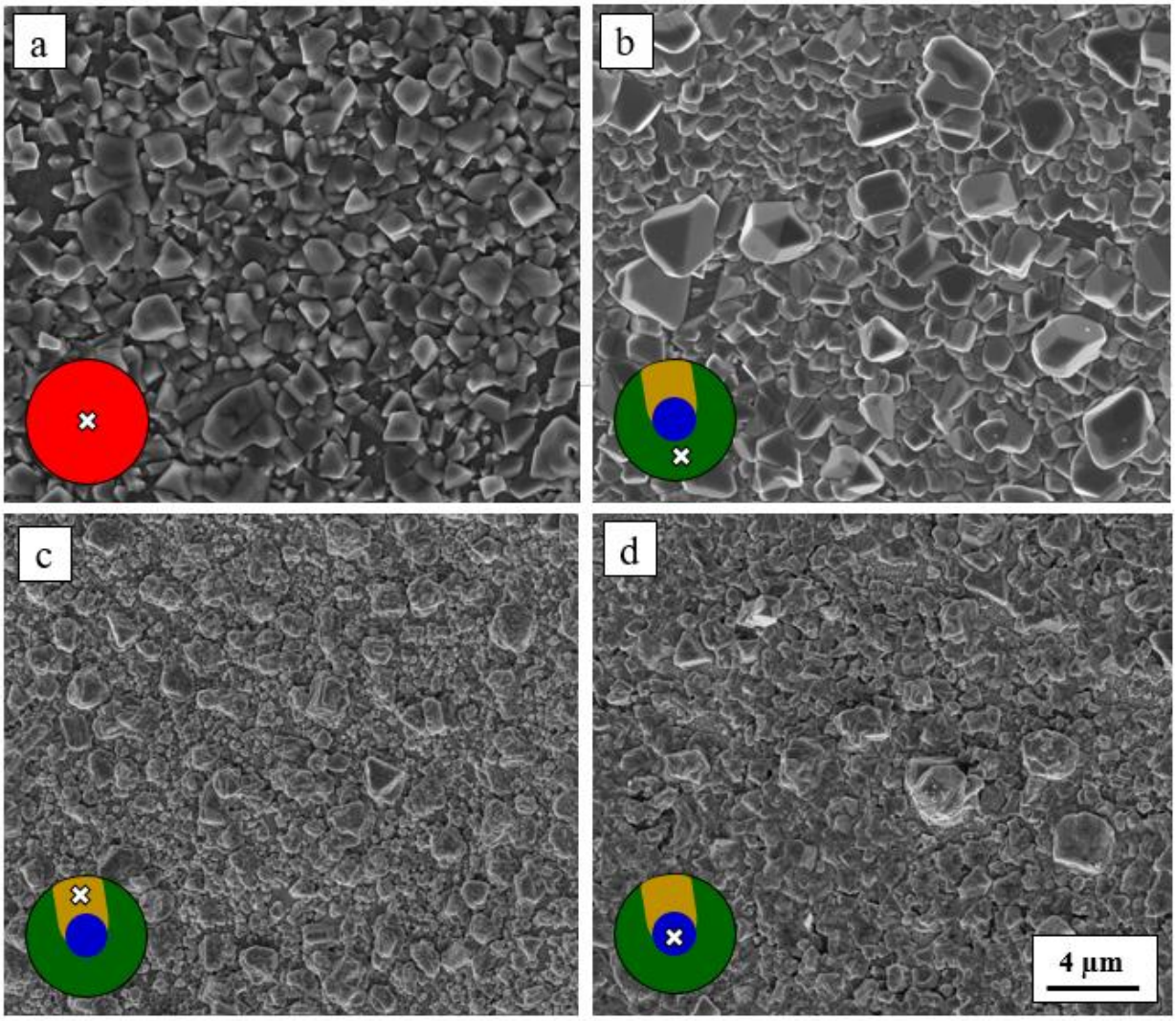

Figure 5.38. SEM images of the outer oxide of sample Pr24, taken (a) before the irradiated exposure, and after the irradiated exposure on the (b) unirradiated, (c) flow, and (d) irradiated surface.

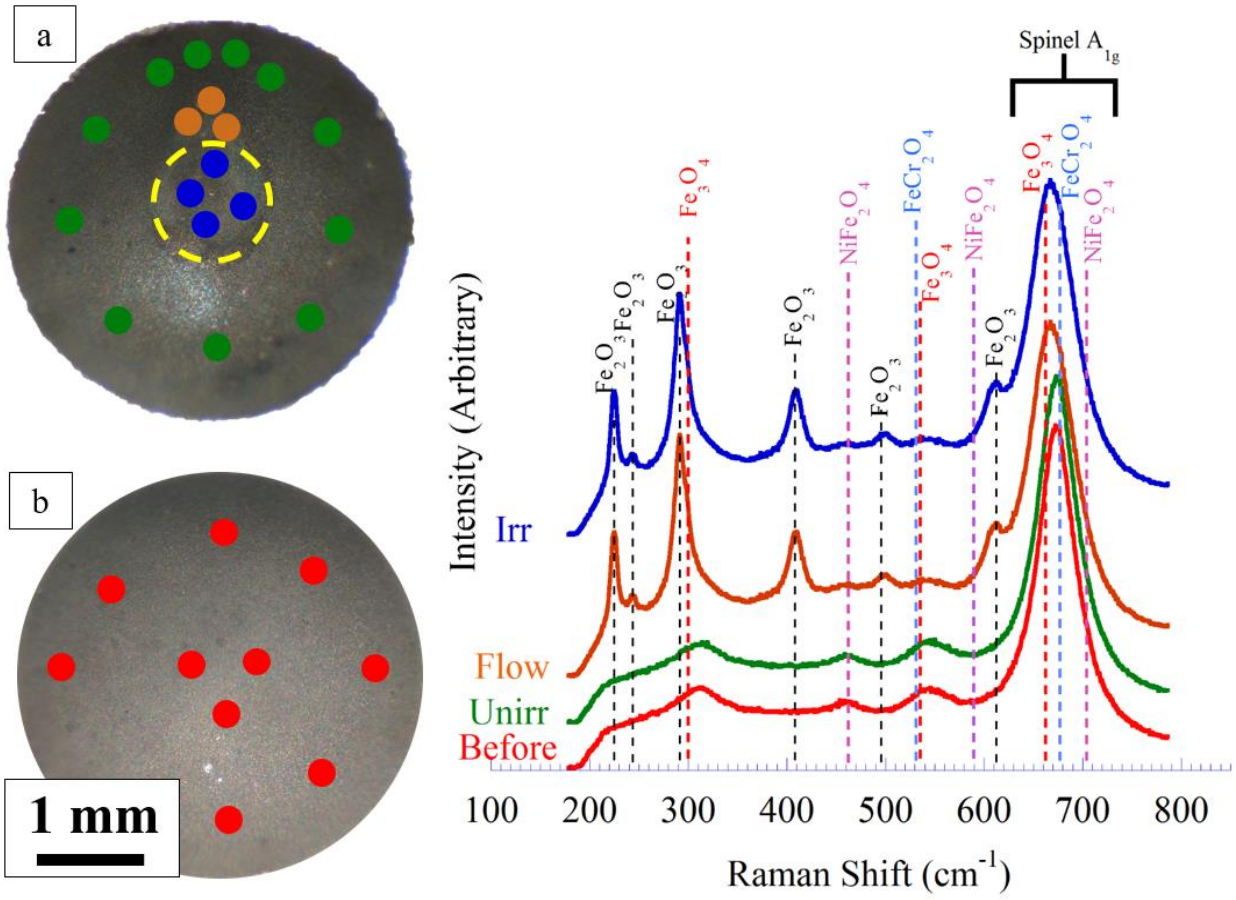

Figure 5.39. Raman scans taken from sample Pr24 both (a) after and (b) before the irradiated exposure. The spectra shown are representative of the area from which they were taken

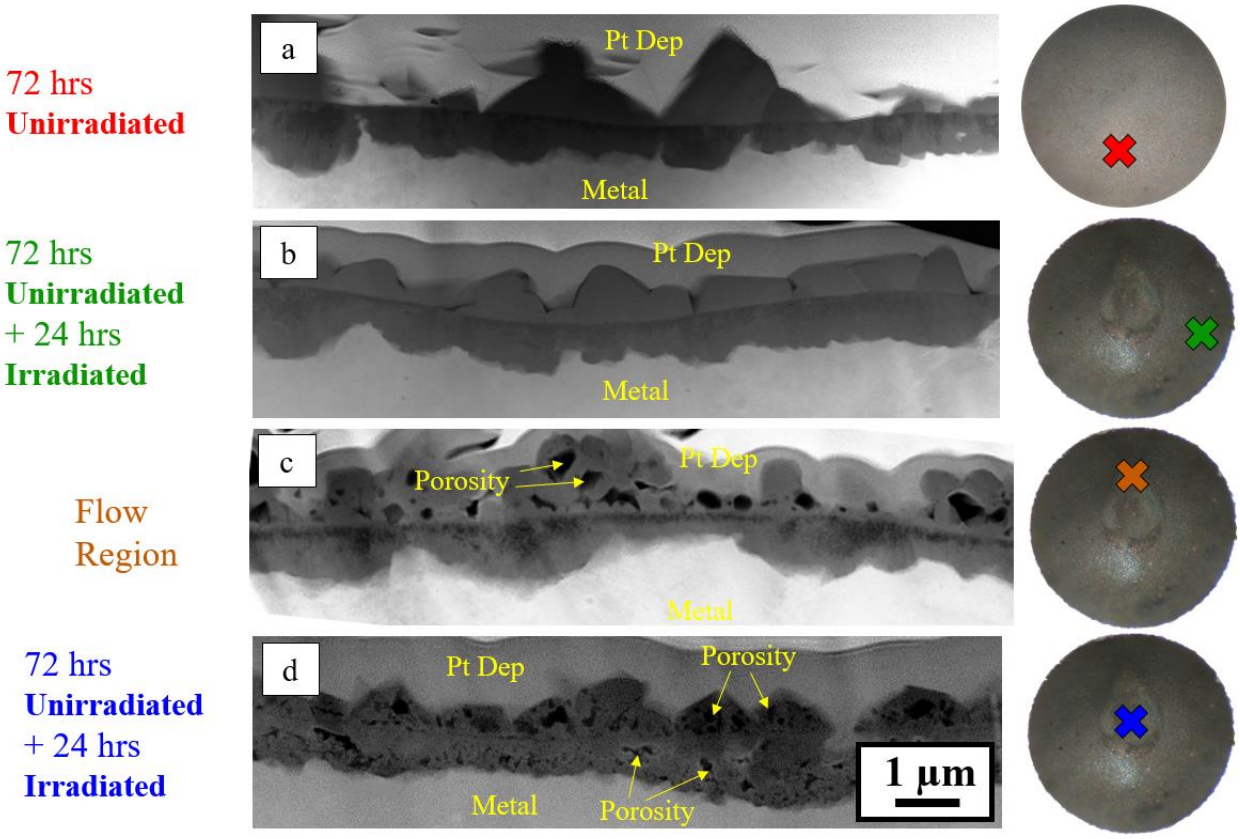

Figure 5.40. STEM-HAADF images of the oxides on sample Pr24 taken (a) before irradiation and after irradiation from the (b) unirradiated, (c) flow, and (d) irradiated regions.

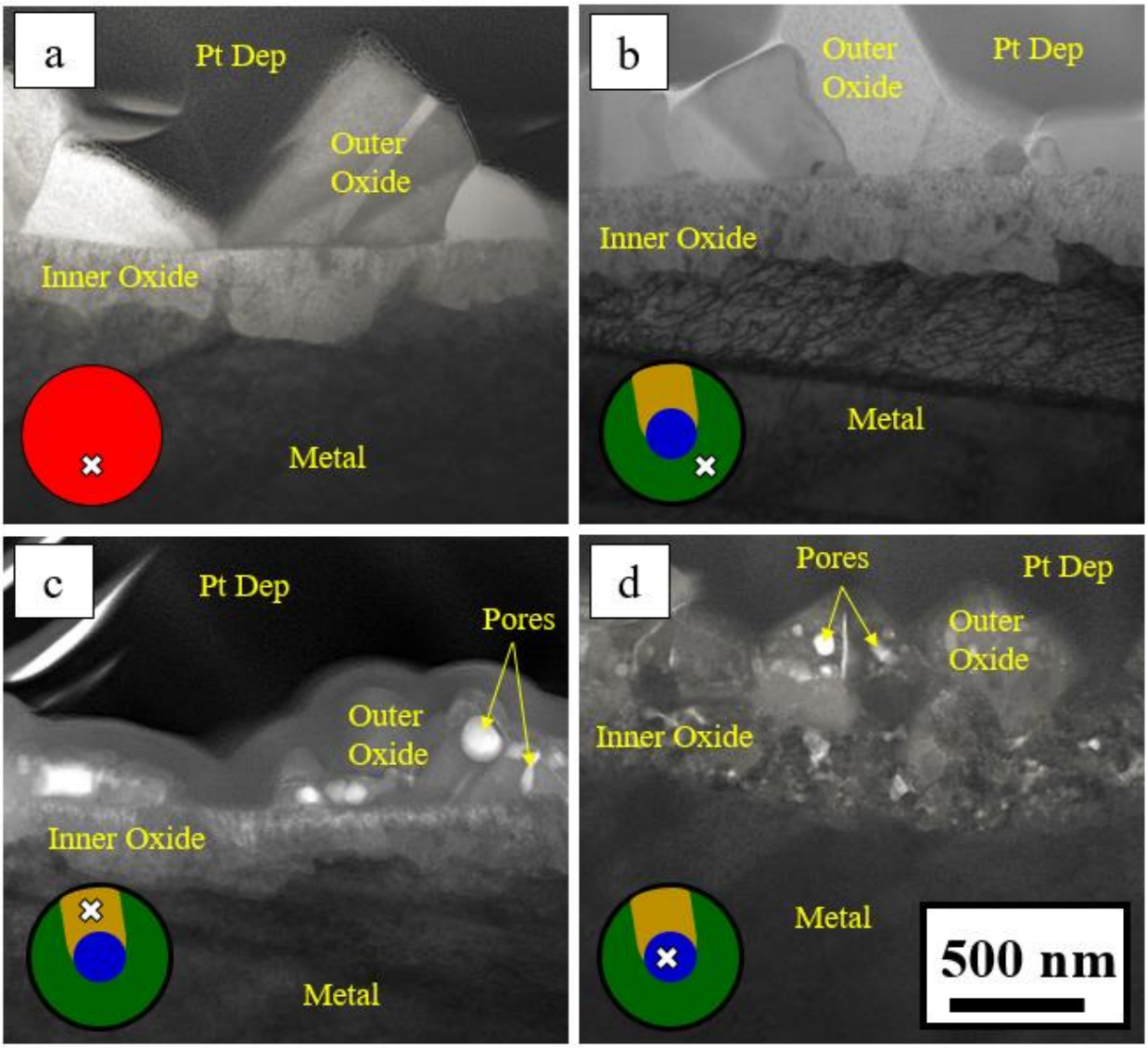

Figure 5.41. STEM-BF images of the oxides on sample Pr24 taken (a) before irradiation and after irradiation from the (g) unirradiated, (c) flow, and (d) irradiated regions.

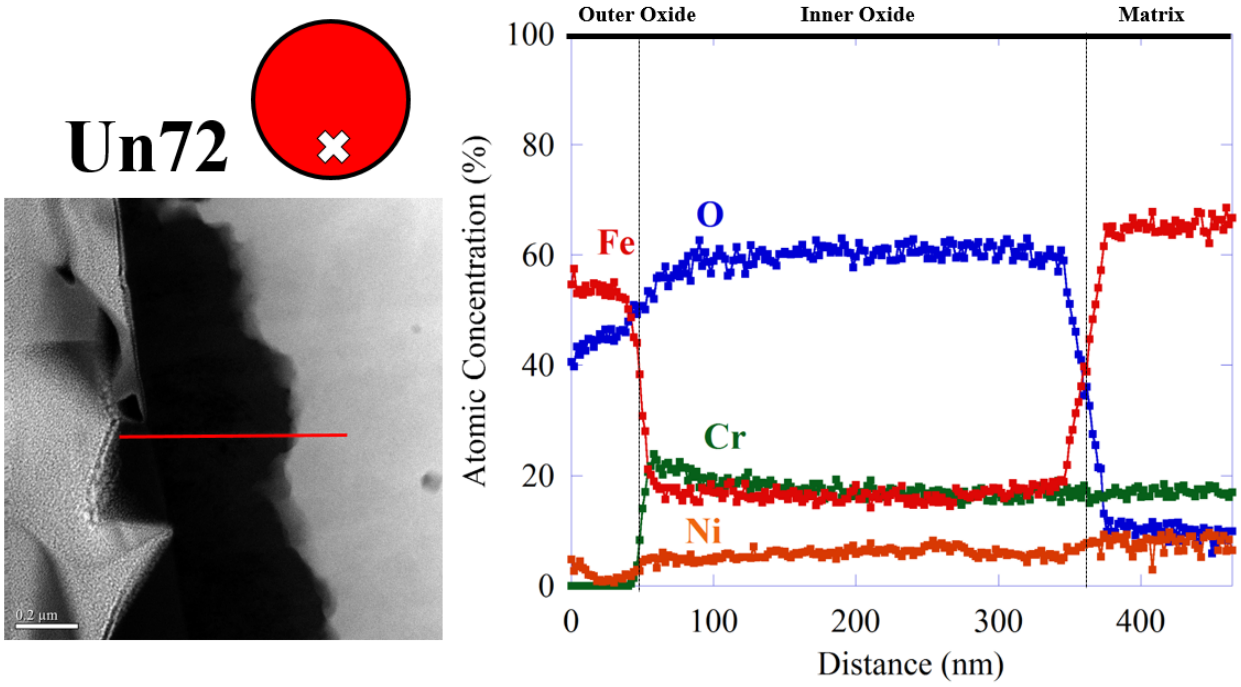

Figure 5.42. Cross sectional atomic composition of sample Un72 before irradiation, measured by STEM-EDS.

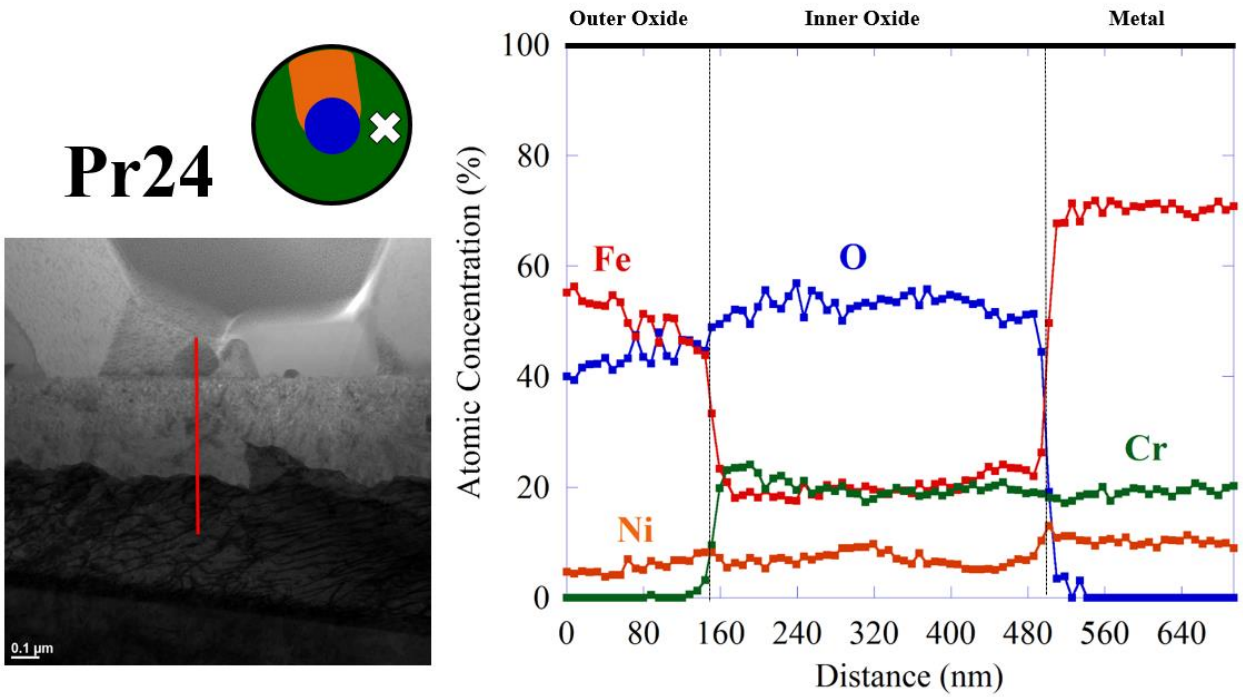

Figure 5.43. Cross sectional atomic composition of the unirradiated region of sample Pr24, measured by STEM-EDS.

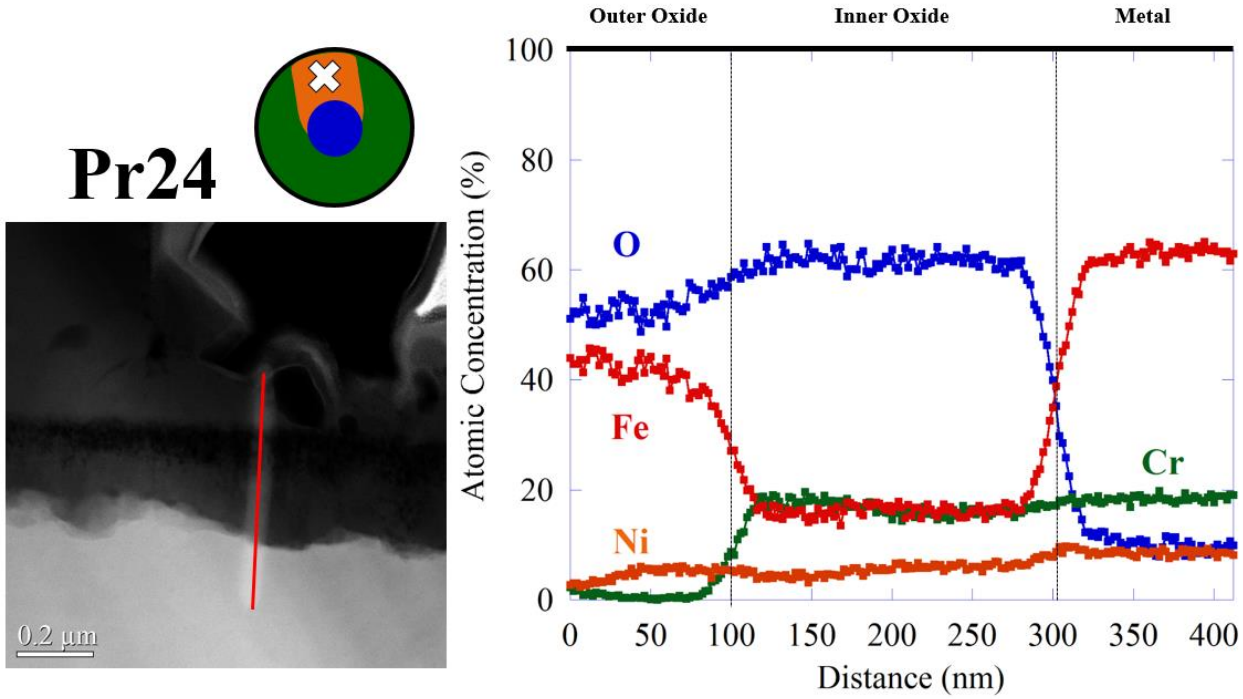

Figure 5.44. Cross sectional atomic composition of the flow region of sample Pr24, measured by STEM-EDS.

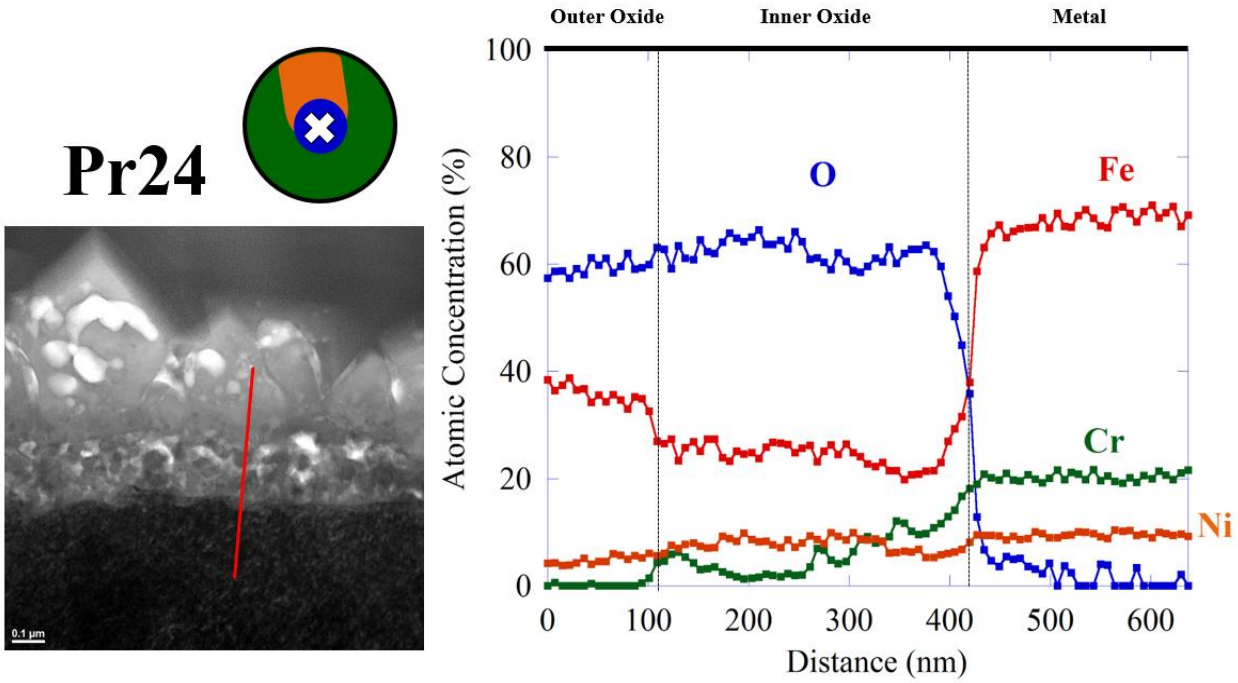

Figure 5.45. Cross sectional atomic composition of the irradiated region of sample Pr24, measured by STEM-EDS.

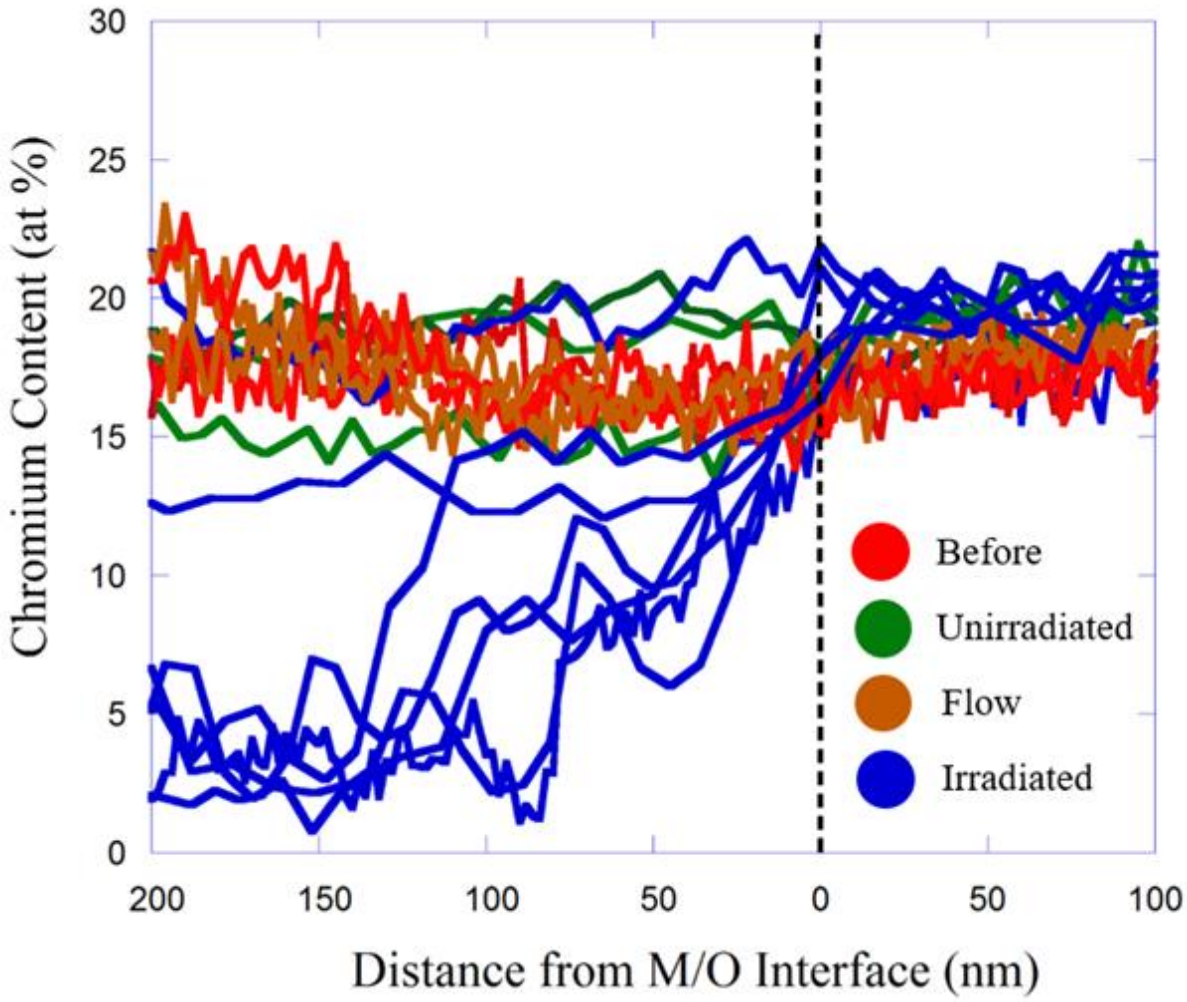

Figure 5.46. Chromium profiles from several EDS linescans taken on sample Pr24. Scans are shown from (red) before irradiation, and after irradiation from the (green) unirradiated region, (brown) flow region, and (blue) irradiated region.

CHAPTER 6 - DISCUSSION

6.1 Hypothesis

It is hypothesized that the major effect of radiation is to create a more oxidizing environment at the oxide-solution interface by means of water radiolysis, resulting in a less protective oxide scale, and an acceleration of the rate of corrosion.

This hypothesis will discussed in four parts. First, it will be established that radiation has created a more oxidizing environment. Observation of the species present on the oxide film will be compared to known thermodynamic stability to prove that corrosion potential has been elevated due to radiation. Next, it will be established that the more oxidizing environment leads to a less protective oxide film. A discussion of kinetics and thermodynamics of oxidation will show how observed changes to the oxide morphology and composition affect passive behavior. The argument will be made that decrease in protectiveness of the oxide film implies an acceleration of the rate of corrosion. Third, it will be established that the observed effects of radiation were caused primarily by water radiolysis rather than displacement damage. Irradiated regions of samples will be compared to regions affected by radiolysis only to show that the observed phenomena were driven by water radiolysis. Results of the pre-oxidation experiment will be discussed to suggest a possible contribution of displacement damage. Finally, the relevance of the experimental findings to actual reactor conditions will be discussed. Particular

attention will be paid to dose rate issues, and to the extrapolation of the findings to longer time scales.

6.2 Thermodynamic Description of the Radiation Environment

This section will discuss the effects of radiation on corrosion in terms of the thermodynamics of the radiation environment. Section 6.2.1 will show that the presence of hematite on irradiated surfaces indicates a more oxidizing environment, and thus an increase in corrosion potential. Section 6.2.2 will discuss how the more oxidizing conditions have affected the stability of spinel oxides. Section 6.2.3 will discuss radiolysis yields, and show that the observed changes in oxide stability are consistent with the experimental conditions in this work.

6.2.1 Hematite Formation

Hematite ($\alpha - Fe_2O_3$) is an iron oxide species that is stable at higher potentials than those typically found in hydrogenated high temperature water[49], [92], [109]. Hematite was found on the irradiated regions of all irradiated samples except Hi04, and on the flow regions of all irradiated samples, as seen in Figure 5.3 and Figure 5.5. The irradiated region of Hi04 showed Raman modes characteristic of maghemite, a precursor to hematite formation. An increase in potential has previously been linked to the formation of hematite, although with chemical addition of oxidizing species, rather than irradiation. Kumai and Devine[52] showed that the amount of hematite on the surface of samples increased as corrosion potential was increased by adding oxygen to purified water at 288˚C. Kuang et al.[18] also showed that adding oxygen or H_2O_2 to purified LWR water resulted in an increase in surface hematite. This section will begin

with a discussion on the stability of iron oxide species, and will then connect observed changes in oxide speciation to changes in corrosion thermodynamics, proving there was an increase in corrosion potential under irradiation.

6.2.1.1 Iron Oxide Stability

The thermodynamic stability of oxides is conveniently discussed using Pourbaix diagrams, which map the stability of oxide species based on electrochemical potential and pH. Consider Figure 6.1 which shows a Pourbaix diagram of iron at 300˚C calculated by Cook and Olive[92]. At a pH of 6, the line of stability between Fe_3O_4 (magnetite) and Fe_2O_3 (hematite) is around -350 mV. Stainless steel in PWR primary water should typically be at a potential around -600 mV, so the presence of hematite indicates that ECP has increased above the level that is expected in PWR primary water.

It should be noted that the Pourbaix diagrams deal solely with thermodynamics, and ignore kinetics. It is possible that an oxide transformation that is thermodynamically predicted may not happen due to slow kinetics. However, kinetics will not drive a transition that is not thermodynamically favorable, so while the lack of hematite is not necessarily evidence that an increase in potential did not occur, the presence of hematite is indeed a positive indicator that potential was elevated.

To verify this diagram, a Pourbaix diagram of Fe in 300˚C water was calculated using the Act2 Module in Geochemists' Workbench 11[110] with the LLNL thermodynamic dataset, and is shown in Figure 6.2. The calculated Pourbaix diagram is in good agreement with that by Cook

and Olive, and confirms that the presence of hematite on the irradiated and flow surfaces indicate elevated potential.

To illustrate the oxidation of magnetite to hematite, the reaction at the magnetite/hematite phase boundary was simulated with the Rxn module in Geochemists' Workbench 11, using the LLNL database, at a temperature of 300˚C and a pH of 6, the same conditions used for the calculation of the Pourbaix diagram. The result is given as Equation 6.1.

$$Fe_3O_4 + \frac{1}{2}H_2O \rightleftharpoons H^+ + \frac{3}{2}Fe_2O_3 + e^- \qquad \Delta E = -0.35\,V\ vs.SHE \qquad (6.1)$$

The reaction proceeds to the right at a potential above -0.35 V_{SHE}, as in Figure 6.2. The value of the magnetite/hematite phase boundary at pH=6 as calculated in this work agrees with the value calculated by Cook and Olive[92] shown in Figure 6.1. The values relevant to the discussion of the oxidation of magnetite to hematite are tabulated in Table 6.1.

6.2.1.2 Surface Oxide Morphology

Trends in the morphology of the outer oxide, as seen in Figure 5.7 - Figure 5.10, are also consistent with the formation of hematite. Unirradiated oxides from both irradiated and unirradiated samples are covered by an outer oxide composed mostly of larger faceted crystals. This crystal shape is associated with magnetite[53], [111]. The flow regions on irradiated samples are still covered with large faceted crystals, but also feature smaller equiaxed crystals on the surface. Irradiated regions tend to have even fewer large faceted crystals, and instead are covered by mostly equiaxed crystals and plate-like crystals.

These equiaxed crystals are consistent with the formation of hematite on the sample surface[53], [111]. A similar phenomenon was seen by Kumai and Devine[52], who observed the appearance of hematite along with an increase in equiaxed grains on stainless steel in 288˚C water when low potential hydrogenated water was replaced by increasingly oxygenated water. A similar change in outer oxide grain morphology was also observed by Kuang et al.[18] and Miyazawa et al.[112] when water chemical potential was raised with O_2 or H_2O_2 additions.

A roughening of the inner oxide surface was also observed on the irradiated areas of the samples in Figure 5.7d - Figure 5.10d. This roughening may actually reflect layer of small particles precipitated from solution – essentially a more homogeneously distributed outer oxide layer. Ishigure et al.[84] found that gamma irradiation decreased the concentration of Fe ions in solution, and increased the concentration of iron oxide corrosion products, indicating that radiolysis may enhance the rate of iron oxide precipitation. It is therefore possible that the apparently rough surface of the inner oxide is, in fact, a thin layer of outer oxide. The roughness may also be attributed to enhanced dissolution of the inner oxide film, which is discussed in-detail in Section 6.4.

It is notable that once magnetite forms from hematite, the reverse reaction back to magnetite is much less likely[113], which explains why the hematite remained stable during cooling after irradiation was stopped.

6.2.1.3 Conclusion

Hematite was observed on the irradiated regions of all irradiated samples except Hi04 (which displayed only maghemite, a precursor of hematite formation), and on the flow regions of

all irradiated samples. Hematite is formed by the oxidation of magnetite, and the presence of hematite indicates elevated corrosion potential at the oxide-solution interface. Reaction modeling and Pourbaix diagrams show that the phase boundary between magnetite and hematite lies at approximately -0.35 mV_{SHE} at a pH of 6. Outer oxides on areas exposed to radiolyzed water showed an increase in equiaxed crystals, consistent with the formation of hematite.

6.2.2 Spinel Stability

In addition to the formation of hematite on irradiated surfaces, a change in the spinel mix was also observed on irradiated regions. As shown in Figure 5.6 and Table 5.1, most irradiated and flow regions experienced a down shift of the spinel A_{1g} peak. The irradiated and flow regions of Hi04 showed an up shift, while the unirradiated region of sample Un72 displayed the same up shift. This section will begin with a discussion of the thermodynamics of spinel oxide dissolution, and will then discuss the observed Raman shifts in terms of the thermodynamic framework set forth.

6.2.2.1 Thermodynamics of Fe-Cr spinel mixing

To begin, unirradiated samples displayed a spinel A_{1g} peak between the characteristic modes for Fe_3O_4 and $FeCr_2O_4$. In reality, this represents a scale composed primarily of solid solution oxides of type $(Fe_{1-x}Ni_x)(Fe_{1-x}Cr_x)_2O_4$[50], [56]. The occurrence of these oxide types is supported by EDS scans that showed primarily iron and chromium oxides, with some substitutional nickel.

To show that the EDS data and the Raman data agree, it will be shown that a solid solution of iron chromium spinels of type Fe_3O_4 and $FeCr_2O_4$ can reasonably produce the cation profile found in the inner oxide by EDS while remaining thermodynamically stable. This will begin with an examination of the thermodynamics of the iron, chromium, nickel spinels that make up the oxide layers.

Recall background section 2.2.2.2. It was found, using free energy of mixing in B^{3+} cation sites, that the most stable configuration of Fe-Cr spinels at 600K is $Fe(Fe_{0.3}Cr_{0.7})_2O_4 = Fe_{1.6}Cr_{1.4}O_4$. When accounting for the fact that some of the A^{2+} sites are occupied by nickel cations, this Fe:Cr ratio is in very good agreement with the STEM-EDS data in Section 5.4 showing a roughly 1:1 ratio of Fe:Cr in the inner oxides. Therefore, the Raman data that shows a mixture of iron and chromium spinels is consistent with the measured cation concentration in the inner oxides.

This 1:1 ratio of Fe:Cr in the inner oxides is very different from the concentration of each in the metal. For the alloy used in this study, the Fe:Cr ratio in the metal is 69:16, or approximately 4:1. Since no enrichment of iron was seen in the metal near the oxide interface, it follows that the extra iron must have dissolved into solution, in a process referred to by Stellwag as "preferential dissolution"[12]. Preferential dissolution of iron explains why the outer oxide, which forms by ions in solution precipitating on the oxide surface[12], is composed of mostly iron, with some substitutional nickel, but no chromium.

6.2.2.2 Chromate Formation

It is hypothesized that the down-shift of the spinel A_{1g} peak is a result of a decrease in the concentration of chromite relative to magnetite. If these spinels are regarded as solid solution spinels, then this may be regarded as a decrease in the Cr:Fe cation ratio in the spinel lattice. If this cation ratio is to decrease, then a mechanism by which chromium dissolves into solution must be identified.

Consider the Pourbaix diagrams of Cr species for the Fe-Cr-Ni system by Beverskog and Puigdemenech[48] in Figure 6.3. In both Figure 6.3a and b, chromium has an aqueous form in the 6+ oxidation state as either CrO_4^{2-} or $HCrO_4^-$ at high potential. At a pH of 6, the $FeCr_2O_4/HCrO_4^-$ phase boundary is at approximately 0 V_{SHE} when the activity of aqueous species are set to 10^{-6} mol/kg, and approximately -0.1 V_{SHE} with aqueous species at 10^{-8} mol/kg.

The stability of $Cr(OH)_3$, as seen on Figure 6.3 is a topic of some debate. While Beverskog and Puigdemenech show that the $Cr(OH)_3$ region is between $FeCr_2O_4$ and $HCrO_4^-$, other authors do not show it in their calculations[49], [51], and instead only show the direct phase boundary between $FeCr_2O_4$ and $HCrO_4^-$. The calculations performed for this work also show the latter case. While the static cell experiments attempted to resolve this uncertainty by measuring the ionic chromium content of the corrosion cell water, these experiments were unsuccessful. Therefore, this work will not consider the formation of $Cr(OH)_3$, and will instead focus on the more widely-agreed-upon reaction between $FeCr_2O_4$ and $HCrO_4^-$ as the primary method of chromium dissolution, with the concession that this is a topic that would benefit from future study.

Also of note, is the stability of $NiCr_2O_4$. While some thermodynamic calculations show that it should be present in the oxide scale, it is omitted from this chapter for two main reasons.

First, calculations in literature give widely varied results on the stability, or lack thereof, of $NiCr_2O_4$[48], [49], [53], [114]. Second, in a solid solution oxide scale, $NiCr_2O_4$ does not need to be considered since $NiCr_2O_4$ does not have any unique bonds or vibrational modes that are not shared with the other spinel types[56]. The full range of solid solution spinels with Fe and Ni in A^{2+} sites and Fe and Cr in B^{3+} sites can be considered strictly in terms of mixtures of Fe_3O_4, $NiFe_2O_4$, and $FeCr_2O_4$.

To further understand the stability of chromium spinels, a Pourbaix diagram of Cr species in the Fe-Cr system was calculated using the Act2 Module in Geochemists' Workbench 11 with the LLNL thermodynamic dataset, and is shown in Figure 6.4. The diagram was drawn with all ionic species set to an activity of 10^{-6} mol/kg, except chromate (CrO_4^{2-}). To investigate how CrO_4^{2-} concentration affects the boundary between chromite ($FeCr_2O_4$) and the aqueous hexavalent chromium species ($HCrO_4^- / CrO_4^{2-}$), the diagram was calculated with CrO_4^{2-} activities between 10^{-6} and 10^{-16} mol/kg. Please note that the phase boundaries between some other regions also shift with changing chromate activity, but only the original phase boundaries at 10^{-6} activity are shown for simplicity. For this work, the phase boundary between $FeCr_2O_4$ and $HCrO_4^-$ is of primary importance, and this is the only boundary that is shown at each CrO_4^{2-} activity.

The reaction that forms the $FeCr_2O_4/HCrO_4^-$ phase boundary in Figure 6.4 was also simulated using the Rxn module in Geochemist's Workbench. A temperature of 300˚C was used with a pH of 6, and with the activity of all ionic species set to 10^{-6} mol/kg, except chromate which was varied between 10^{-6} and 10^{-16} mol/kg.

An activity of 10^{-6} mol/kg corresponds to a fractional concentration of approximately 170 wppb. From Table 5.5, this value is lower than measured in all static cell experiments except IR8. The measured concentration of chromate, however, is likely due mostly to the cell and stainless steel tubing, as discussed in Section 4.2.4. It is therefore difficult to accurately predict the true chromate activity at the sample surface. The calculation used in section 4.2.4 predicts an activity of ~ $2x10^{-8}$ mol/kg for the 4 hr static cell experiment and an activity of ~ $5x10^{-12}$ for the standard high dose rate experiments. Therefore, a chromate activity range of 10^{-6} – 10^{-16} is a reasonable bounding of the actual chromate concentration at the sample interface. Despite the inaccuracy, it is likely that other sources of deviation from ideal behavior account for an error in the position of the $FeCr_2O_4/HCrO_4^-$ greater than several orders of magnitude of chromate activity. This understanding is inherent in the use of Pourbaix diagrams as an approximate predictive tool.

The redox reaction, given as Equation 6.2, shows chromite dissolving in water to form H^+, chromate, ferrous ions, and 6 electrons. The reaction proceeds in the forward direction above 0.29 V_{SHE} for a chromate activity of 10^{-6} mol/kg, as indicated in Figure 6.4.

$$FeCr_2O_4 + 4\,H_2O \rightleftharpoons 6\,H^+ + 2\,HCrO_4^- + Fe^{2+} + 6\,e^- \qquad \Delta E = 0.29\,V\ vs.SHE \qquad (6.2)$$

This reaction was also calculated with different $HCrO_4^-$ activities, to tabulate the position of the $FeCr_2O_4/HCrO_4^-$ phase boundary at pH 6 as chromate activity varies. The results are shown in Table 6.2 along with the positions of the lower phase boundary of $HCrO_4^-$ from Beverskog and Puigdemenech. There is a difference of approximately 0.4 V between the two extremes in activity.

In noticing the large discrepancy between the two works, it should be noted that in the Beverskog and Puigdomenech diagrams, the lower phase boundary of $HCrO_4^-$ borders on either $NiFe_2O_4$ or $Cr(OH)_3$, as opposed to $FeCr_2O_4$ as in the diagram produced for this work. Further comment on this discrepancy will be made in section 6.3.

At this juncture, a thermodynamic framwork by which chromium-rich spinels dissolve into aqueous chromate has been established, and arange of potentials and chromate activities at which chromium spinel dissolution is reasonable has been established.

6.2.2.3 Nickel Dissolution

Following the discussion on the behavior of iron and chromium, nickel can now be introduced into the discussion. EDS linescans show that nickel concentration in the inner oxide is similar to the matrix, with a slight, though inconsistent, trend toward depletion. Nickel also exists in the outer oxide in small quantities.

Nickel primarily exists as trevorite ($NiFe_2O_4$) in the oxide scale[18], [48], [114]. Trevorite retains the inverse spinel structure of magnetite, but with a Ni ion in the A^{2+} cation site. A Pourbiax diagram of nickel in the ternary system calculated by Beverskog and Puigdemenech[48] is shown in Figure 6.5. At a pH of 6, the stability region of trevorite is between -0.45 and 0.6 V vs SHE. The red dot indicating simulated primary water conditions near the phase boundary between NiO and nickel metal. However, since all Raman spectroscopy performed for this work, no NiO modes were observed, all nickel in the oxide lattice is assumed to be in spinel form. Beverskog and Puigdemenech also calculated a Pourbaix diagram of Ni in

the Fe-Cr-Ni ternary systems, which includes a trevorite/hematite phase boundary, shown in Figure 6.6. This calculation found a phase boundary at 0.7 V_{SHE}.

The Geochemists' Workbench software was unable to properly calculate a Pourbaix diagram for Ni species in the ternary system, for unexplained reasons. Calculations made with the Rxn module produced the trevorite dissolution reaction:

$$NiFe_2O_4 + 2\,H^+ \rightleftharpoons H_2O + Fe_2O_3 + Ni^{2+} \quad (6.3)$$

which is independent of corrosion potential, and indicates that trevorite is stable above pH=5 at all potentials, and would be represented as a vertical line on a Pourbaix diagram.

Although Equation 6.3 and the diagram calculated by Beverskog in Figure 6.6 are not in agreement, it will be shown later that the differences between the reaction calculated with Geochemists' Workbench and the Pourbaix diagram by Beverskog do not affect how the experimental results in this work are interpreted. Radiolysis models will show that a potential of 0.7 V_{SHE} is likely never reached, so Trevorite is expected to remain stable according to either Equation 6.3 or Figure 6.6. Going forward, a potential of 0.70 V_{SHE} will be used for the phase boundary between trevorite and hematite at pH=6.

6.2.2.4 Spinel Peak Shifts

In section 6.2.1, a thermodynamic explanation was given for the appearance of hematite on sample regions exposed to radiolyzed water. The Raman signature for hematite is unmistakable, and therefore there is very little difficulty in determining which samples have been exposed to the conditions required to oxidize magnetite to hematite. Changes in spinel stability,

however, are more difficult to resolve experimentally. In section 6.2.2.1-6.2.2.3, the theoretical framework by which Fe-Cr-Ni spinel oxides dissolve has been established. In this section, it will be shown how experimental observations showing a spinel peak shift fit within the established thermodynamic framework.

To recap, the three spinel dissolution reactions discussed so far in this chapter are given in Table 6.3. The order in which the reactions are listed is deliberate. Hematite (Fe_3O_4) dissolution occurs at the lowest potential, then chromite ($FeCr_2O_4$) dissolves at a higher potential, and trevorite ($NiFe_2O_4$) dissolves at the highest potential, or not at all. This work proposes that the dissolution of these three spinel oxides is reflected in the observed up-and-down shifts of the spinel A_{1g} peak.

Recall Figure 5.3 and Table 5.1, reprinted here as Table 6.4. Samples that were unirradiated had a spinel A_{1g} peak between the characteristic modes of chromite ($FeCr_2O_4$) and magnetite(Fe_3O_4). The irradiated and flow regions of samples Hi12, Hi24, and Hi72 had spinel A_{1g} peaks that were shifted down toward magnetite. The irradiated and flow regions of sample Hi04, as well as the unirradiated regions of samples Hi24 and Hi72 had a spinel A_{1g} peak that was shifted up, toward trevorite.

Before proceeding, it must be emphasized that the spinel A_{1g} peak is a compound peak, composed of Raman vibrational modes from several mixed spinel oxides. When this work mentions a shift up or down of the spinel peak, it refers to a general movement of the center of mass of the peak, caused by a change in the relative intensity of its constituent modes. While this is a mild oversimplification in a mixed oxide composed of substitutional spinels, it sufficient to account for the trends observed in this work. Further details regarding the movement of the

spinel A_{1g} peak in Fe-Cr-Ni spinels has been studied in-depth by Hostermann[56] and Belo[35], but for the purposes of this work, the spinel A_{1g} peak will be treated as a superposition of the characteristic peaks of magnetite, chromite, and trevorite, as explained in Chapter 2.

Now, consider Table 6.5, which shows the regions on which hematite was found using Raman spectroscopy. The areas that had a spinel peak shift either down or up are the same areas that had hematite on the surface. It has already been established in this chapter that the presence of hematite is a positive indicator of elevated corrosion potential, so the coincidence of spinel peaks shifts in Table 6.4 with the presence of hematite in Table 6.5 further supports the idea that elevated corrosion potential is responsible for the observed spinel peak shifts. Note that the irradiated region of Hi04 is also included, despite only showing maghemite, a precursor to hematite formation. The fact that maghemite was found on that region, coupled with the fact that hematite was found in the flow region of the same sample suggest that corrosion potential was still elevated in the irradiated region of Hi04. Also note that hematite was found on the unirradiated regions of samples Hi24 and Hi72. This indicates that radiolysis products must have affected the unirradiated regions, as there is no other credible explanation for the presence of hematite. The concentration of radiolysis products that affected the unirradiated regions, however, is apparently much lower than on the flow regions of the samples. Issues of flow inside the corrosion cell are discussed in greater detail in Section 6.4.1.

Examining the data in these two tables, it is clear that everywhere that there is a peak shift either up or down, there is also hematite. Since it has been established that hematite is the result of magnetite oxidation at a potential of -300 mV or greater, then it can be concluded that spinel peak shifts are occurring only where there is evidence of spinel oxide dissolution. Since it has been found that chromite and trevorite dissolve at higher potentials than magnetite, it makes

sense to hypothesize that the differences in spinel peak shifts might be caused by differences in potential on the surfaces of irradiated samples.

To explain the changes in spinel oxide stability, this work proposes grouping the sample regions by the following criteria:

Time: The time the sample was exposed.

Concentration: The more complex of the criteria, this refers to the qualitative concentration of radiolysis product at the surface. Obviously the irradiated regions were exposed to the highest concentration of radiolysis product, followed by the flow regions which received a substantial, but likely lesser concentration of radiolysis product. The unirradiated regions, as discussed previously, received a small concentration of radiolysis product (as indicated by the hematite on samples Hi24 and Hi72), while the unirradiated samples received no concentration of radiolysis product.

To discuss this idea, sample regions are tabulated in Table 6.6. Examining the regions on samples exposed for 24 and 72 hrs, the unirradiated samples, as expected, have no shift in their spinel peak. The unirradiated regions, which presumably experienced a low concentration of radiolysis products, had spinel peaks that were shifted up. The flow and irradiated regions, which experienced high concentrations of radiolysis products, had spinel peaks shifted down. Following increasing time, the unirradiated regions on Hi04 and Hi12 experienced no peak shift, while the unirradiated regions on Hi24 and Hi72 were shifted up. The spinel peaks on the flow and irradiated regions of Hi04 were shifted up, while the spinel peaks on the flow and irradiated regions of Hi12, Hi24, and Hi72 were shifted down. This reveals a trend in which the spinel

peaks shift up when exposed to irradiation at low concentration or short time and then the up—shift turns to a down shift as time or qualitative concentration increases.

While three distinct regions are visible in Table 6.6, it is reasonable to make a distinction between the regions that were exposed for a short time at a high concentration, and the regions exposed for a long time at a low concentration. While they both exhibited an up-shift of their spinel A_{1g} peak, the mechanism may not be the same. Therefore, the samples are grouped into 4 distinct regions, abbreviated No-effect, Short-high, Long-low, and Long-high. These regions are tabulated in Table 6.7, and are shown schematically in Figure 6.7.

With these 4 regions defined, the next step is to explain the observed behavior of the spinel A_{1g} peak on each region using the reactions listed in Table 6.3. The spinel A_{1g} peak from a representative Raman spectrum on each region will be deconvoluted, and discussed to show how the conditions during the experiments performed for this work may have led to the observed behavior.

Analysis will begin with the *no-effect* regions, which display no effects of irradiation. While the unirradiated regions of Hi04 and Hi12 may have been affected by small amounts of radiolyzed water, it was not enough to create any measurable effects, so they are grouped with the unirradiated samples. The spinel A_{1g} peak on sample Un24 is shown in Figure 6.8, along with fitted peaks representing magnetite, chromite, and trevorite. The combined curve which has a peak at 672 cm^{-1} between the magnetite and chromite modes is a result of the high magnetite and chromite peaks, with a much smaller trevorite peak. This combination reflects the magnitude of the peaks as they might exist without the influence of radiation.

The regions that experienced a low concentration of radiolysis products for a long time (*long-low*), had hematite on their surfaces. As was discussed in section 6.2.1, hematite forms from the oxidation of magnetite, so it follows that this region that has hematite on its surface should have less magnetite, and thus a smaller magnetite peak. The decrease in the magnetite and relative increase in the trevorite peaks causes the spinel A_{1g} peak on the *long-low* regions to shift up in wavenumber. Figure 6.9 shows this effect. The small peak near 613 cm^{-1} indicates hematite. The magnetite peak is much smaller than in Figure 6.8, causing the combined peak to shift up to 680 cm^{-1}. Also important to note, EDS line scans did not reveal chromium depletion, which is evidence that chromite did not dissolve in this region. Therefore, the chromite peak is large compared to the magnetite peak.

Next, the regions that experienced a high concentration of radiolysis products for a short time *(short-high)*. These regions were also observed to have hematite on their surfaces. Therefore, a decrease in the amount of magnetite is expected, when compared to the unirradiated samples. These samples also exhibited chromium depletion in the inner oxide, so a decrease in the amount of chromite is also expected, and is reflected in a reduction of the size of the magnetite and chromite peaks, causing an overall shift up of the spinel A_{1g} peak. Figure 6.10 shows the spinel A_{1g} peak on the flow region of Hi04, which has a peak at 688 cm^{-1} and a center-of-mass position of 680 cm^{-1}. It is notable that the magnetite peak on the *short-high* regions is smaller than on the *long-high* regions.

Finally, the regions that experienced a high concentration of radiolysis products for a long time *(long-high)*. Like the *short-high* regions, these areas had hematite on the surface, indicating magnetite dissolution, which should result in a decrease in the size of the magnetite peak. These regions also and had inner oxides depleted in chromium, reflected in a decrease in

the size of the chromite peak. While the same dissolution reactions are active on the *long-high* regions as on the *short-high* regions, the *long-high* regions have a much larger magnetite peak. This can be explained by the longer exposure time, resulting in more inner oxide chromite that can be "converted" to magnetite. While magnetite still oxidizes to form hematite on the oxide surface, as on the *short-high* samples, the thicker oxide on the *long-high* regions still likely contains a high concentration of magnetite. This results in a larger magnetite signal, and a down-shift of the spinel A_{1g} peak, which is reflected in Figure 6.11. Note that while the peak position is at 660 cm^{-1}, which represents a significant down shift from the unirradiated regions, the center-of-mass position of 670 cm^{-1} is very close to the center of mass position of the unirradiated regions. This still represents a significant down-shift of the center-of-mass when compared to the short-high and long-low regions.

While the Raman data does not provide the location from which the Raman signal originates, other data from Chapter 5 provides some clarity. Recall electron diffraction data in Figure 5.15 which showed inner oxides retained the spinel structure. Combined with EDS data that showed primarily iron cations in the inner oxide, this suggests the inner oxide on the high concentration, long time regions is composed primarily of magnetite. Further, since SEM images of the outer oxides on irradiated and flow regions showed primarily equiaxed outer oxide crystals, it is likely the hematite Raman signal comes primarily from the outer oxide. Therefore, it can be estimate that the Raman signal on the *long-high* regions comes primarily from hematite on the outer oxide, magnetite on the inner oxide, and trevorite in both the inner and outer oxide.

6.2.2.5 Maghemite formation

An alternate explanation for the up-shift seen on the *long-low* and *short-high* regions is the emergence of maghemite, ($\gamma - Fe_2O_3$). Maghemite is a transitional oxide between magnetite and hematite, resulting when magnetite is oxidized and loses and FeO group, but the lattice still retains the spinel structure[60], [115], [116]. It may be regarded as a defective spinel structure. When maghemite transitions to the corundum structure, it becomes hematite. Choupra et al. [115] and Guo et al.[117] have reported an up-shift in the spinel A_{1g} peak of magnetite as it was oxidized due to heat from a laser. They attributed the shift to maghemite formation.

The characteristic modes of maghematite did not appear strongly in the Raman spectra taken for this work, although several of them are obscured by hematite peaks, so it is possible that they are present. The formation of trevorite was observed to cause an up-shift of the spinel A_{1g} peak by Hostermann[56] and Belo[35]. The trevorite peak was chosen for this work because the characteristic A_{1g} mode at 702 cm^{-1} fit well with the measured spectra. It should still be noted that maghemite formation cannot be ruled-out as a contributing mechanism to the spinel peak shifts observed in this work.

6.2.2.6 Conclusion

Iron-chromium-nickel spinels are thermodynamically stable in primary water conditions, but tend to dissolve as potential is increased. Pourbaix diagrams and reaction modeling were used to show how spinel oxide dissolution may explain observed inner oxide chromium depletion. Raman peak fitting was used to show how observed shifts in the spinel A_{1g} peak are consistent with the oxidation of magnetite to form hematite and the dissolution of chromite to

form aqueous chromate. Unirradiated oxides exhibited a spinel A_{1g} peak between the characteristic modes of magnetite and chromite. The unirradiated regions of samples Hi24 and Hi72 had spinel A_{1g} peaks shifted up toward the characteristic mode of trevorite, attributed to the dissolution of magnetite. The irradiated and flow regions of sample Hi04 also showed a shift up, attributed to the dissolution of magnetite and chromite. The flow and irradiated regions of samples Hi12, Hi24, and Hi72 had spinel A_{1g} peaks shifted down, attributed to the dissolution of inner oxide chromium and the conversion of the inner oxide chromite spinels to magnetite.

6.2.3 Radiolysis and Thermodynamics

Observed changes in oxide speciation have been linked to an increase in corrosion potential under irradiation. The next step is to show that the experimental conditions used in this work are consistent with the claimed potential increase. Since the thermodynamics of oxide stability are based primarily on the oxidizing potential of the water at the oxide-solution interface, this chapter will focus only on radiolysis. The minimal effect of displacement damage on thermodynamics is briefly covered in the background section, and the subject of radiolysis vs. displacement damage will treated in-depth in section 6.4.

To determine the yield of radiolysis products, simulations were run by Bartels[118]. The simulations modeled a 1 second pulse of 1.4 MeV protons (their energy after passing though the sample) in 300˚C water with 3 wppm H_2 (1.6 mM) at dose rates of 4000 and 400 kGy/s. The concentration of radical species at each dose rate is shown in Figure 6.12 and Figure 6.13, and the concentration of stable species is shown in Figure 6.14 and Figure 6.15.

From the figures, it is apparent that H_2O_2 is the dominant oxidizing species produced by radiolysis, at concentrations of 10 and 1.2 μM (340 and 40 wppb) for the high and low dose rates respectively. The OH radical appears at a small concentration, but should only affect irradiated areas, as the concentration immediately goes to zero when the beam is turned off. HO_2 is an oxidizing species with a short lifetime, but may last long enough to affect the flow region as well as the irradiated region

Based on this data, the impact of radiolysis will be measured primarily in terms of hydrogen peroxide production (H_2O_2). The finding that H_2O_2 is more abundant is in agreement with experimental and modeling data in prior works [21], [65]. Therefore, with a few noted exceptions, it will be assumed that the effect of radiolysis on corrosion is dominated by H_2O_2, with some contributions from radicals $HO_2^{\cdot}$ and $HO^{\cdot}$.

6.2.3.1 Corrosion Potential

With the calculated concentration of H_2O_2, the change in corrosion potential can now be determined. Since H_2O_2 is a species of interest in radiolysis studies, several works have measured corrosion potential as a function of H_2O_2 concentration[20], [87], [119]. Measurements by Tachibana et al. along with other measurements are shown in Figure 6.16.

The measurements show ECP either saturating or nearly saturating around 10 wppb H_2O_2 at ECP values between -0.05 and 0.13 V_{SHE}, reaching values around 0.15 to 0.2 V_{SHE} at 200 wppb H_2O_2. Since the $Fe_3O_4 - Fe_2O_3$ stability line was calculated to be around -300 mV_{SHE}, and since the concentration of H_2O_2 is calculated to be 340 or 40 ppb for the high or low dose rate experiments respectively, the observation of hematite on the sample surface during

experiments is consistent with the amount of H_2O_2 production predicted with this model. Note that the measurements in Figure 6.16 were made in BWR-like conditions, so hydrogen was not present as it is in this work. Corrosion potential is controlled by the concentration of oxidizers in solution, and hydrogen primarily serves to reduce oxidizing species. Since the hydrogen content of the water was already taken into account by the radiolysis models when determining the surviving concentration of H_2O_2, the measurements made in BWR water are still a valid comparison for this work.

Calculations presented earlier in Table 6.2 determined the $FeCr_2O_4 - HCrO_4^-$ stability line to be between -0.09 and 0.29 V_{SHE}, depending on the activity of chromate. At the H_2O_2 concentration calculated for the low dose rate experiment, 40 ppb, Figure 6.16 indicates an ECP of between 0 and 0.17 V_{SHE}, depending on which dataset is used. This indicates that it is likely that the $FeCr_2O_4/HCrO_4^-$ stability line was crossed, as shown in Figure 6.4 and Table 6.2. Further, the potentials suggest a chromate activity of between 10^{-8} and 10^{-14}.

6.2.3.2 Conclusion

Models of H_2O_2 production for the conditions in this work were compared to data showing the ECP of stainless steel in high temperature water as a function of H_2O_2 concentration. The data show that the irradiation conditions used in this experiment were sufficient to increase the corrosion potential above the phase stability lines of magnetite and chromite.

6.2.4 Deposited charge

Since this work utilizes charged particle irradiation, it seems reasonable to assume that the net charge introduced by the proton beam might affect corrosion potential. Therefore the effect of deposited charge should be addressed. Consider that ions in a medium do not lose their charge until the very end of their range[120], so charge can be assumed to be deposited approximately 10-15 μm from the sample surface, creating a potential difference between the water and the sample. Since exchange current is limited by the availability of surface sites on the sample, and since the sample and mount are electrically isolated, the excess charge likely goes to the cell walls, which are grounded,

To understand why charge buildup near the sample does not significantly affect corrosion, consider the yield of solvated electrons given in Table 2.6. With a G-value of 2.5, a single proton with an energy of 1.4 MeV after transmission through the sample, produces 35,000 solvated electrons. It stands to reason that any charge deposited by the proton beam is insignificant compared to the number of charged particles produced by radiolysis, and will not significantly affect interactions at the sample surface. Therefore, it is concluded that the effect of deposited charge is minimal.

6.2.5 Summary of Thermodynamics

The presence of hematite on irradiated surfaces implies an increase in corrosion potential, which agrees with the nature of the outer oxide showing an increase in rough equiaxed crystals. Raman data showing changes in the relative concentration of spinel oxides are consistent with EDS data showing a loss of inner oxide chromium. Calculated radiolysis yields for the experimental conditions in this work show that H_2O_2 production is sufficient to elevate corrosion

potential above the stability line of magnetite and chromite. Such an elevation in corrosion potential is consistent with the dissolution of magnetite and chromite to form hematite and chromate, respectively, as hypothesized. It is therefore concluded that radiolysis is the likely cause of chromium depletion.

6.3 Oxide Growth and Dissolution Kinetics

Section 6.2 has established that radiation increased the thermodynamic driving force for oxidation at the oxide-solution interface, and showed how this change affected the stability of species in the oxide scale. Section 6.3 will now discuss how these changes have affected the growth and dissolution of the oxide film. Kinetics of growth and dissolution will be discussed to explain the observations made in this work.

6.3.1 Inner Oxide Chromium and Passivity

STEM-EDS data from Chapter 5 clearly shows a decrease in the chromium content of the inner oxide layer on irradiated and flow regions. Raman data from chapter 5 shows a shift in the spinel A_{1g} peak on irradiated and flow regions, which was shown in section 6.2 to also indicate a decrease in oxide chromium content. With irradiation-induced chromium depletion of the inner oxide well established, this section will focus on the importance of chromium in the inner oxide,

and will show how the loss of chromium in the inner oxide likely leads to an increase in the rate of corrosion.

It is well understood that stainless steel forms a thin passive layer of Cr_2O_3 in air at room temperature, and it is from this film that stainless steel derives its corrosion resistant properties in ambient conditions. It has already been covered in Chapter 2 that this film does not form in LWR conditions, which instead favors the formation of Fe-Cr spinel oxides of type $Fe(Fe_{1-x}Cr_x)_2O_4$. While these Fe-Cr oxides may not form as robust a film as Cr_2O_3, they have been shown to have protective properties.

In this section, polarization data on stainless steel in relevant conditions from literature will be examined. The passive regions in the polarization curves will be compared to thermodynamic data calculated for this work to see how the dissolution of chromium-rich spinels corresponds with the upper bound of the passive region on stainless steel in PWR-relevant conditions. This will allow meaningful connections to be drawn between the observed loss of inner oxide chromium, and the growth and dissolution rates of the oxide film.

Recall from Section 2.2.3 the work of Xu et al. [59], Sun et al. [19], and Liu et al[93] that found the upper bound of the passive region of stainless steel corresponds roughly with the stability region of chromium rich spinels. This correspondence makes good sense, as chromium spinels are known to be protective for a number of reasons, previously discussed in Chapter 2. In summary, chromium is known to diffuse much slower through the spinel lattice[32] than iron or nickel. Also, comparing the bandgaps of the oxides[60], chromite has a bandgap of 3 eV[61], compared to 0.2 for magnetite[62], indicating that higher chromium content presents a barrier to charge transport across the oxide film. Finally, solubility of the oxide films is known to decrease

as chromium content increases[12]. Therefore, the loss of passivity as chromium-rich spinels become thermodynamically unstable is consistent with literature data on oxide thermodynamics and kinetics.

Figure 6.17 shows a polarization curve of 304 stainless steel in 300 ˚C water at pH 7.1 by Liu et al. [93] A dotted line showing the upper bound of the passive region and the beginning of the transpassive region is overlaid, at a potential of 0.10 V_{SHE}.

Figure 6.18 shows a polarization curve in 250˚C water at a pH of 6.8 calculated by Xu et al.[59]. The upper bound of the passive region is marked, at a potential at 0 V_{SHE}.

Lastly, Figure 6.19 shows polarization curves by Sun et al [19] in aerated and deaerated 300˚C water at pH 6.8 and 9.1. The upper bounds of the passive regions are at potentials of -0.04 and -0.22 V_{SHE} respectively.

To compare the polarization data to the thermodynamic calculations in this work, the potential of the upper bound of the passive region from each work is plotted on Figure 6.4, and the results are shown in Figure 6.20. Note that the data from Sun was taken at 250˚C, while all other data was taken at 300˚C. The data all fall on $FeCr_2O_4$ / $HCrO_4^-$phase boundaries with log[CrO_4^{2-}] between -8 and -13. The data is tabulated in Table 6.8.

This indicates that polarization data from literature showing the passive region on stainless steel is in good agreement with the stability region of chromite calculated for this work. It is therefore reasonable to assert that a loss of inner oxide chromium due to irradiation should lead to an increase in the rate of corrosion.

6.3.1.1 Conclusion

Polarization data from literature shows a transition from the passive region to the transpassive region at potentials between -0.22 and 0.04 V_{SHE} at pH between 6.8 and 9.1. The data were plotted on a Fe-Cr Pourbaix diagram calculated for this work, and found to be in good agreement with the $FeCr_2O_4$ / $HCrO_4^-$ phase boundary. It is therefore concluded that the stability of $FeCr_2O_4$ is important for the passivity of stainless steel, and the loss of this spinel oxide suggests an increase in the rate of corrosion.

6.3.2 Porosity

After establishing that irradiation leads to a loss of protectiveness in the inner oxide, the next step is to discuss observed changes in the oxide morphology that are consistent with the loss of protectiveness. STEM imaging of the oxide layers in Chapter 5 showed that the inner oxides on irradiated and flow regions were highly porous compared to the oxides on unirradiated regions from both irradiated and unirradiated samples. Regions in which porosity was observed were also regions in which chromium was depleted, so it should be determined if the two phenomena are related to each other, and if so, whether the observed decrease in chromium leads to the enhanced porosity, or whether the enhanced porosity leads to the chromium depletion.

In support of the former premise, this work has already discussed in the background chapter why a chromium-rich oxide film has lower solubility, higher oxidation potential, and a slower rate of cation diffusion, so it is reasonable to suggest that the increase in porosity on irradiated and flow areas is caused by accelerated dissolution of the already chromium-deficient inner oxide scale.

This effect may be similar to dealloying, or selective leaching, most commonly observed in copper alloys, and cast iron[121]. Erlebacher et al[122] observed both experimentally and computationally the formation of nano-porosity by way of selective-leaching in Au-Cu alloys, so it may be possible that the observed porosity in stainless steel arises from selective leaching. To this author's knowledge, no prior work exists on selective leaching of stainless steel in relevant high temperature conditions, although purposeful selective leaching has been explored for removal of Cr during reprocessing of stainless steel[123], [124]. It is important to note that the phenomenon observed in this work is a loss of chromium in the *oxide*, rather than a loss of Cr in the *metal*, as with selective leaching. Still, the fact that both phenomena involve the selective dissolution of a more noble metal leads to a compelling parallel.

In support of the latter premise, an increase in porosity can lead to a higher rate of chromium dissolution by allowing for solution access to the metal-oxide interface, shifting the rate controlling mechanism from diffusion to interfacial reactions[11]. Castle and Masterson found that transport of aqueous species aided by porosity can have a significant effect on corrosion of mild steel[125]. Since it has been argued that the mechanism of Cr depletion is dissolution of Cr rich spinels to form aqueous chromate, it follows that solution access should be required for chromium depletion to proceed, and increased porosity allows for greater solution access to the inner oxide.

Insight into this question is gained through an examination of Pr24. Recall that the irradiated inner oxide of sample Pr24 had significant porous and non-porous regions, a characteristic not shared by the other samples in this work. Consider Figure 6.21, showing a STEM-EDS line scan taken across a non-porous section of the inner oxide on the irradiated region of sample Pr24. Comparing this figure to Figure 6.22 which shows a STEM-EDS profile

taken from a porous section of the irradiated region of sample Pr24, it is clear that both scans show chromium depletion.

More EDS linescans were taken across porous and non-porous sections of the irradiated region of Pr24 (included in Appendix D), and Cr depletion was found on several scans taken across non-porous inner oxides. Therefore, it is logical to conclude that porosity is not necessary for Cr depletion to occur, suggesting that porosity is a result of chromium depletion, rather than its cause.

This conclusion does present a new problem. It has been concluded in section 6.2 and 6.3.1 that the mechanism of chromium depletion is aqueous. If this is true, a mechanism must be identified to explain how the chromium depleted in the irradiated area of Pr24 without porosity to provide the necessary solution access. Further, it must be explained why there is no observed chromium depletion or porosity on the flow region of sample Pr24?

These topics are covered fully in section 6.4, but for now a simple explanation will suffice to allow the current discussion to continue. The difference between Pr24 and the other irradiated samples is the pre-grown unirradiated oxide which served as a kinetic barrier. This kinetic barrier lessened the porosity on the irradiated region, and prevented Cr depletion and porosity on the flow region. If a protective inner oxide has this effect, then it is logical to suspect that on the samples that were not pre-oxidized, a protective film never formed in the irradiated and flow regions in the first place. If the protective film never formed, then the inner oxide and metal are never denied access to solution, allowing aqueous dissolution of chromium at interfaces in the porous oxide. This explanation, however, requires a higher rate of oxide

dissolution which should limit the oxide thickness. This phenomenon is discussed in the next section.

6.3.2.1 Conclusion

Oxides on irradiated and flow regions were more porous than unirradiated oxides. It is hypothesized that enhanced dissolution due to the depletion of inner oxide chromium is responsible for the increased porosity. The effect may be similar to the selective-leaching phenomenon observed in some alloy systems. The decreased porosity on the irradiated region of sample Pr24, and lack of porosity on the flow region show that a pre-grown oxide scale can lessen oxide dissolution, and suggests that irradiation prevented a protective film from forming in the first place on the samples that were not pre-oxidized.

6.3.3 Oxide Thickness

It has been established that inner oxides are deficient in protective chromium spinels, and that the loss of chromium leads to the formation of inner oxide porosity due to enhanced dissolution. It has been hypothesized that these processes prevent a passive oxide from forming, and a higher rate of oxide dissolution should follow as a result of the loss of oxide protectiveness. To further support this assertion, oxide thickness over time should be considered. It naturally follows that if the rate of oxide dissolution has been enhanced under irradiation, that

the thickness of the inner oxide on irradiated and flow areas should be less than on unirradiated areas. In this section, the oxide thickness observed in Chapter 5 will be discussed, and it will be shown that the reduction in oxide thickness in irradiated areas is consistent with the other phenomena observed in this work.

6.3.3.1 Rate Law and Dissolution

Oxide growth theoretically proceeds according to Equation 6.4

$$x = kt^{1/n} \tag{6.4}$$

For stainless steel in unirradiated LWR conditions, *n* is theoretically equal to 2. The oxidation process becomes kinetically limited as the oxide gets thicker, so the rate of growth slows over time. It is well understood that in practice, *n* is not exactly equal to 2. Further, with the addition of radiation which is hypothesized to decrease the protectiveness of the inner oxide layer, it is very possible that *n* is significantly less than 2. It is reasonable, however, to assume that $n > 1$. To show why this is a reasonable assumption, consider the case where *n=1*. In this case, the corrosion rate would be constant regardless of the oxide thickness. For this assumption to be true, we would have to assume that the oxide provides a negligible kinetic barrier, and we know this to be untrue, as even very thin oxides have been shown to slow the rate of corrosion in stainless steels. Therefore, if the oxide layer provides any kinetic barrier to corrosion, then *n* cannot be less than 1.

The next step is to add a term to the growth rate equation to include dissolution. This extra term is not necessary in most oxidation studies, since the rate of dissolution is small

compared to the rate of growth. With radiation believed to be accelerating the rate of dissolution, an additional term will be added. Since oxide dissolution occurs at the oxide-solution interface, and is only dependent on interfacial reactions, the thickness of the oxide does not provide a kinetic barrier. Therefore, it is reasonable to assume that the rate of dissolution is linear with time.

A constant representing the dissolution rate, j, is defined in Equation 6.5.

$$-x = jt \tag{6.5}$$

By combining Equation 6.4 and Equation 6.5, an expression for the oxide thickness under irradiation can be written as in Equation 6.6.

$$x = (kt)^{1/n} - jt \tag{6.6}$$

The assumption is made that it is reasonable to combine these terms in this way because the processes that control dissolution and growth are independent of each other. While it is true that the oxide growth rate depends on the oxide thickness, which is affected by dissolution, the dependence is already built into *n*.

At steady state, Equation 6.6 can be written as Equation 6.7.

$$\frac{dx}{dt} = 0 = \frac{(kt)^{\frac{1}{n}-1}}{n} - j \tag{6.7}$$

This equation can be solved to find a steady-state inner oxide thickness under irradiation at short times. At longer times, the outer oxide may continue to grow and become partially protective, thus making the dissolution term, *j*, non-constant, but that is beyond the scope of this work.

6.3.3.2 Oxide Growth rate Data

Now, with a theoretical framework in place, the next step is to examine the data collected in this work. Recall the inner oxide thickness data in Table 5.3 and Figure 5.19. The thickness of the irradiated and flow regions are significantly less than the thickness of the unirradiated regions, from both the irradiated (green) and unirradiated (red) samples. This observation is consistent with the hypothesis that irradiation has increased the rate of dissolution at the oxide-solution interface.

It should be noted again that the oxide thickness data presented is highly variable. Each region represents only one liftout, with a length of approximately 10-15 μm. A cross section of this length likely covers only one or two grains, and should not be regarded as quantitative. When taken as a whole, the figure still conveys the qualitative message that irradiated and flow regions are significantly thinner than unirradiated regions.

Equation 6.4 and Equation 6.6 were fit to the thickness data to examine their validity. Due to the small amount of data in this work, Equation 6.4 was fit to the unirradiated regions from both the irradiated and unirradiated samples, and Equation 6.6 was fit to the thickness data from irradiated and flow regions. The results are shown in Figure 6.23 and Equations 6.8.

$$x_{unirr} = k_{unirr} * t^{1/n} = 23.8 * t^{1/1.85} \quad (6.8a)$$

$$x_{irr} = k_{irr} * t^{1/n} - j * t = 12.7 * t^{1/1.85} - 0.8 * t \quad (6.8b)$$

The fit to unirradiated data was performed with k and n as variables, while the irradiated fit used the same n as the unirradiated curve, and fit the k and j coefficients. The unirradiated rate

constant is nearly double the irradiated rate constant, and the irradiated dissolution coefficient came out to be 0.8 nm/hr. The fitted value of n=1.85 is very close to the theoretical value of $n = 2$.

While there is no comparable data for *j* or k_{irr}, k_{unirr} can be compared to literature. Tapping et al.[126] examined 304 stainless steel in 300˚C water with 18 cm^3/kg and pH=10.3, and reported a value for n of 1.89. For the sample exposed for 48 hrs, inner oxide thickness was 80 nm, less than half the thickness predicted by Equation 6.8a. Plugging Tapping's values into Equation 6.4 produces

$$k = \frac{80}{48^{1.89}} = 10.3$$

Kim[20] reported an oxide thickness of 900 nm after exposure in 288˚C water with 150 ppb H_2 for two weeks (336 hrs). Using the value of *n* from this work, 1.85, Kim's data produces

$$k = \frac{900}{336^{1.85}} = 38.8$$

The rate constant $k_{unirr} = 23.8$ found in Equation 6.8a is between the rate constants calculated based on the work of Tapping and Kim. Variation is likely due to differences in experimental conditions, and error due to the short times involved.

It should be stated, once again, that these values are based on a very limited data set, with high experimental variance, and should not be used for quantitative predictions. The observations about oxide thickness and accompanying rate laws exist solely as supporting evidence of the dissolution mechanisms proposed in this work, and as a proposed framework for future study of irradiation accelerated corrosion.

6.3.3.3 Conclusion

Oxides were thinner on irradiated and flow regions than on unirradiated regions, which is consistent with previous data suggesting accelerated oxide dissolution under irradiation. A model for oxide growth and dissolution is suggested, which adds a linear dissolution term to the standard parabolic rate equation for oxide growth. The model was fit to the experimental data to show loose correlation with measurements.

6.3.4 Increased Corrosion Rate

Despite the lack of data on corrosion rate, it merits a brief mention, since predicting and/or lowering the rate of corrosion for stainless steel in reactor cores is an over-arching goal of all corrosion science. This work did not measure oxide growth rate to determine corrosion rate, but the observed phenomena have implications on the rate of corrosion.

It has been established that irradiation caused a loss of passivity in the irradiated and flow regions of the samples. Figure 6.18 shows that the corrosion current in the first transpassive region is 10-times higher than in the passive region. For the 40hr data, the corrosion current in the sub-passive region is a factor of two higher than in the passive region.

Further, it stands to reason that if the rate of oxide dissolution is higher under irradiation, that the rate of metal dissolution should also be higher. Solution access to the metal surface in irradiated regions should allow interfacial reactions to proceed uninhibited, resulting in a higher rate of metal loss

6.3.5 Summary of Oxide Growth and Dissolution Kinetics

Raman spectroscopy and STEM EDS data agree that a loss of Cr-rich spinels occurs under irradiation, leading to a decrease in passive behavior. Inner oxides deficient in chromium are more susceptible to dissolution, indicating irradiation induced chromium depletion is the likely cause of the increase in porosity observed in irradiated oxides. Oxides on irradiated and flow regions were thinner than unirradiated oxides, and the difference is attributed to enhanced dissolution. A radiation enhanced dissolution constant is proposed to describe this phenomenon.

6.4 Contributions of Radiolysis and Displacement Damage

To determine the relative effects of radiolysis and displacement damage, it is important to consider the effects of radiation in terms of kinetics and thermodynamics. Section 6.2 discussed the thermodynamic effects of radiation on oxidation. Chapter 2 discussed previous findings showing that displacement damage has little effect on phase stability, and on thermodynamics in general. Therefore, the possible effect of displacement damage on oxidation is limited to kinetics On the other hand, radiolysis can be assumed to affect only the thermodynamics of oxidation, while having no direct kinetic effect. While this work has asserted that an increase in potential has led to the dissolution of the inner oxide, which acts as a kinetic barrier to diffusion, the effect on kinetics is merely indirect.

This section will discuss the relative contributions of radiolysis and displacement damage to IAC. It will begin with a discussion of flow in the corrosion cell, and then proceed to insights

gained by comparing sample Pr24, which was pre-oxidized before irradiation, to irradiated samples that were not pre-oxidized. An analysis of the effect on displacement damage on the spinel oxide layer will follow, and the section will conclude with a discussion of the differences in concentration of radiolysis products between the irradiated and flow regions.

6.4.1 Flow in the Corrosion Cell

All irradiated samples had a flow region above and to the left of the irradiated region. The upward flow is likely the result of the proton beam heating the water, decreasing its density and causing it to rise, thereby creating an upward flow across the sample face. This effect is heightened by the fact that the cell inlet is positioned at the top of the corrosion cell and the outlet is at the bottom. Because of this positioning, there was likely a temperature gradient in the cell, as water flowing into the cell can be expected to be slightly colder than the rest of the cell volume. This temperature gradient would also tend to favor an upward flow across the sample face.

Fluid flow was modeled by Grunloh[127], and is shown in Figure 6.24. The streamlines near the sample face show water flowing upward, and to either side, and water from the inlet streaming down and to the sides of the cell, forming looping convection currents in the bottom of the cell. The flow across the sample face is dominated by the heating from the beam, and it not affected in a substantial way by the 15 mL/min flow in and out of the corrosion cell.

The model reflects a perfectly symmetrical corrosion cell, and it is likely that asymmetries in the cell, such as thermocouples or ECP probes could cause the convection currents arising from the sample surface to favor one side or the other. This likely explains why

the flow surface on the samples always tended toward the left. This flow pattern is important, because the flow from the irradiated region carries radiolysis products with it, and creates a region on the sample that is exposed to these products, without being affected by displacement damage.

On all samples that were not pre-oxidized, the flow region was similar to the irradiated region. All flow regions have porous inner oxides that were deficient in chromium, as seen in Section 5.3.1 and Section 5.4, and summarized in Table 6.9.

Further, the inner oxide thickness of the flow regions was similar, as was the thickness on the irradiated regions. Both were much thinner than the unirradiated regions taken from the same samples. Since the flow regions displayed all of these phenomena despite a lack of direct irradiation, it is concluded that they are caused by radiolysis, and not by displacement damage.

Also notable, samples Hi24 and Hi72 had hematite over all their surfaces, including unirradiated surfaces. This indicates that, while the prevailing flow across the sample face was up and to the left, some radiolysis products affected the rest of the sample surface. The products were likely carried by the varied flow patterns within the corrosion cell, as it is highly unlikely that hematite could have formed on the sample surface by any means other than the flow of radiolysis products.

It should be noted that it is highly unlikely that the proton beam directly affected any of the unirradiated or flow areas of the samples. Since the samples all displayed the same flow pattern, it is not reasonable to think that an unforeseen divergence in the proton beam would produce the same pattern on the sample surfaces across many individually prepared experiments.

Therefore, fluid flow is the likely cause of elevated corrosion potential and hematite formation on the flow surfaces of all samples, and on the unirradiated surfaces of samples Hi24 and Hi72.

6.4.1.1 Conclusion

CFD models are consistent with the observed flow pattern on the sample surfaces, indicating an upward flow across the sample face, carrying radiolysis products upward across the unirradiated region of the sample. The oxide thickness in the flow and irradiated regions were similar and displayed similar porosity and chromium depletion. It is concluded that the loss of passivity and subsequent accelerated dissolution are caused predominantly by radiolysis.

6.4.2 Pre-Oxidized Experiment

While most evidence suggests that radiolysis is the primary driver of accelerated oxide dissolution, this section will discuss how the results of sample Pr24 may indicate a contribution of displacement damage.

Consider the STEM images of the irradiated inner oxide on sample Pr24 shown in Fig. 6.23. The outer oxides display significant porosity that was not seen on samples which were irradiated without a pre-grown film. This porosity is attributed to the enhanced dissolution of the magnetite crystals that comprise the outer oxide to form hematite. This is in agreement with Raman data on Pr24 in Section 5.5 showing hematite on irradiated and flow surfaces, and surface morphology data in Section 5.5 showing a visible roughening of the outer oxide crystals. Most

of the inner oxide layer is porous, as with the irradiated regions of all other irradiated samples. There are, however, parts of the inner oxide on the irradiated region that are not porous. Consider Figure 6.25, a HAADF image of the irradiated oxide on sample Pr24, which highlights the porous and non-porous sections of the inner oxide.

Recall from Figure 5.40a showing the inner oxide before irradiation, that the entire thickness of the oxide before irradiation was homogeneous and non-porous. Also recall that the thickness of the inner oxide on Pr24 before irradiation was similar to the inner oxide thickness on each region of the sample after irradiation. It has previously been concluded that the observed porosity is a result of dissolution of the inner oxide after it has been depleted in chromium. It was also found that the inner oxide on the irradiated region of Pr24 was depleted in chromium on both porous and non-porous sections.

It is therefore reasonable to suggest that the oxide on Pr24 was in the process of dissolving into solution, but this occurred more slowly due to the pre-formed film. This conclusion is also consistent with the observation that the thickness did not change during the exposure under irradiation. It is logical that the kinetic barrier to oxide dissolution also served as a kinetic barrier slowing further oxide growth. Some thinning of the inner oxide is visible on Figure 6.25, on the left side at the end of the dotted line. This area is not covered by any outer oxide particles, allowing greater solution access to the Cr-depleted inner oxide, thus allowing interfacial reactions to dissolve the oxide.

Now, consider the flow region of sample Pr24. This region, like the irradiated region of Pr24, experienced elevated corrosion potential. This is indicated by the Raman data in Figure 5.39 showing the presence of hematite on the sample surface, as well as Figure 5.38 showing

roughened outer oxide crystals that indicate oxidation of magnetite to hematite. Despite the more oxidizing conditions, Cr depletion was not observed on the flow region of Pr24. A small amount of inner oxide porosity was observed near the solution interface, and is indicated in the image in Figure 6.26. This amount of porosity is very small compared to all other irradiated and flow regions.

6.4.2.1 Conclusion

The inner oxides on the irradiated region on sample Pr24 displays the effects of oxide dissolution, but they were not observed on the inner oxide of the flow region, despite both regions showing signs of increased potential. This supports the assertion that the pre-formed oxide scale is an effective kinetic barrier to chromium depletion and oxide dissolution.

6.4.3 Displacement Damage

Now that is has been established that there is an effective kinetic barrier on sample Pr24, and that there is a difference between the irradiated and flow regions, the difference must be explained. The most obvious difference between the flow regions and the irradiated regions of samples is that the flow regions are exposed only to radiolysis, while the irradiated regions are exposed to displacement damage as well as radiolysis. This section will examine how displacement damage in the irradiated regions affects the dissolution processes in the oxide film.

To begin, it is more natural to assume that displacement damage should have little effect. It has been shown in Section 6.3 that the extensive porosity in the irradiated regions grants solution

access through the inner oxide layers. Because of the easy availability of surface sites, it stands to reason that interfacial transport would overwhelm diffusive transport, especially at a temperature as low as 320˚C. It would, of course, be insufficient, to leave the analysis here, so it a more quantitative approach will be taken.

As a first approximation, looking at radiation disordering, Wang et al.[31] conducted a study in which chromite (Cr_2FeO_4) was irradiated with Xe ions at 300 K, and it was found that a dose of 6.4 dpa was required for disordering. Wang et al. found that susceptibility to disordering was correlated with the lattice parameter and the standard entropy of the spinel oxides[128][31]. Since the entropy and lattice parameter of magnetite (Fe_3O_4) and other spinel oxides are similar to chromite, it is reasonable to rule out radiation disordering as a factor in this work, as no samples approached the several dpa needed for disordering.

Radiation disordering is not necessary to affect diffusion however, so for a more precise analysis, point defect concentration will be estimated. To begin, some assumptions will be made. First, only displacement damage in the oxide film will be examined. While displacements in the metal near the oxide interface may affect the growth rate of the inner oxide film, this analysis will be focusing on chromium depletion and dissolution of the already grown oxide film, so only displacement damage in the spinel oxide film will be considered. Second, only cation diffusion will be considered. As with the first assumption, chromium depletion and oxide dissolution are the phenomena of interest. These phenomena are dependent on the movement of interstitial cations, and their rate of diffusion is governed by interstitial self-diffusion[90], [129], [130]. Oxide growth, which proceeds by oxygen vacancy diffusion[39], is not being considered.

With these assumptions, the first step is to calculate the concentration of point defects in the oxide film. Defects will be calculated using Sizmann's model for point defect concentration[131] adapted by Was[67] assuming low temperature and high sink density. Sizmann's equations for vacancy and interstitial concentration are given in Equations 6.9 a and b respectively.

$$C_v = \left[\frac{K_0 K_{is}}{K_{iv} K_{vs}} + \frac{K_{is}^2 C_s^2}{4K_{iv}^2}\right]^{1/2} - \frac{K_{is} C_s}{2K_{iv}} \tag{6.9a}$$

$$C_i = \left[\frac{K_0 K_{vs}}{K_{iv} K_{is}} + \frac{K_{vs}^2 C_s^2}{4K_{iv}^2}\right]^{1/2} - \frac{K_{vs} C_s}{2K_{iv}} \tag{6.10}$$

Where

K_0 = defect production rate
K_{iv} = recombination rate coefficient
K_{vs} = vacancy-sink reaction rate coefficient
K_{is} = interstitial-sink reaction rate coefficient
C_s = sink concentration

Recall from Chapter 2 that the spinel unit cell is an oxygen lattice with 8 fcc sub-units. Cations occupy 24 of the 96 interstitial octahedral and tetrahedral sites in the unit cell. In a normal spinel structure such as chromite ($FeCr_2O_4$), A^{2+} cations occupy 8 of the 64 tetrahedral sites, and B^{2+} cations occupy 16 of the 32 octahedral sites[31], [132]. This means in each unit cell there are 72 unoccupied interstitial sites, and 56 atoms (32 oxygen, 24 cations), thus there are intrinsically 1.5 unoccupied interstitial sites per atom, which serve as sites for cation recombination. When an interstitial cation is knocked from its preferred interstitial site, this creates a Frenkel pair. For cations in the spinel lattice, a Frenkel pair is different from other materials, since cations always occupy interstitial sites in the oxygen lattice. Therefore, when

discussing radiation damage, a vacancy-interstitial pair refers to a cation which is knocked from its preferred interstitial site, and the now-vacant cation site. The previously vacant interstitial sites can easily accept cation interstials, and can therefore be treated as defect sinks. The movement of an interstitial cation from one interstitial site to another still upsets the symmetry of the spinel unit cell (8 fcc subunits), which may be referred to as cation disordering. To recognize the high concentration of cation recombination sites in the spinel lattice[31], [133], $C_s = 1.1 * 10^{22}\ cm^{-3}$ was used. Despite serving as efficient sites for recombination of cation interstitials, the unoccupied interstitial sites should not affect recombination of oxygen vacancies and interstitials. Since this analysis is only concerned with the movement of cations, the fact that oxygen vacancies and interstitials are unaffected can be ignored.

Diffusion coefficients for iron vacancies and interstitials in magnetite were taken from Dieckmann and Schmalzried[134], and represent a reasonable approximation of all cations in Fe-Cr-Ni spinels.

$$D_i = 6.31 * 10^{-17}\ cm^2/s$$

$$D_v = 5.19 * 10^{-10} cm^2/s$$

For calculating the rate coefficients, Equation 6.11 – Equation 6.13 from Was[67], were used.

$$K_{iv} = 4\pi r_{is} D_i = 6.46 * 10^{-23}\,\frac{cm^3}{s} \tag{6.11}$$

$$K_{is} = 4\pi r_{is} D_i = 6.46 * 10^{-23}\,\frac{cm^3}{s} \tag{6.12}$$

$$K_{vs} = 4\pi r_{is} D_v = 5.31 * 10^{-16}\,\frac{cm^3}{s} \tag{6.13}$$

K_0 was calculated based on the high dose rate used in this work.

$$K_0 = 7\ x\ 10^{-6}\frac{dpa}{s} = 5.17 * 10^{16}\frac{displacements}{cm^3}$$

Using Equation 6.9 and Equation 6.10 with these parameters produces

$$C_v^{cations} = 0$$

$$C_i^{cations} = 0$$

These numbers indicate complete annihilation of cation defects due to the high number of recombination sites in the spinel structure. This finding is consistent with the work of Clinard and Hobbs who reported very low interstitial concentration in spinels[135], and Wang et al. who reported a high degree of radiation resistance in $FeCr_2O_4$ spinels due to abundant recombination sites[31]. Since the phenomenon of interest in this section is the movement of cations to explain chromium depletion, this calculation suggests that the effect of radiation enhanced diffusion on chromium depletion is small.

It stands to reason, however, that despite efficient annihilation at abundant sinks, point defect creation should still contribute to diffusion. Even if interstitial defects recombine immediately after creation, the motion of cations during formation of damage cascades should affect transport of species in the oxide lattice, in a phenomenon known as ballistic mixing.[136] Prior work has shown that ballistic mixing effects can affect interactions at interfaces[137]. Unfortunately, this exists little quantitative information in this area, so its mention remains speculative. However, it should not be discounted, as ballistic effects may very well explain the observed difference between the irradiated and flow regions of sample Pr24. It is possible that by ballistically transporting chromium to interfaces where it can interact with the solution, radiation

aided the process of chromium dissolution in the pre-formed inner oxide, which may explain the lack of chromium depletion in the flow region of sample Pr24.

6.4.3.1 Conclusion

Point defect concentration was calculated using Sizeman's point defect concentration equations. Since the spinel oxide microstructure has a high concentration of cation defect recombination sites, the steady state point defect concentration was found to be zero, indicating the effect of displacement damage on diffusion of cations is likely minimal. Despite high recombination, ballistic mixing of may account for the difference observed between the irradiated and flow regions of sample Pr24.

6.4.4 Concentration of Oxidizing Species

It was observed in 6.4.2 that the pre-grown oxide slowed the process of oxide dissolution, so the difference between the irradiated and flow regions may arise from a difference in dose rate. It was discussed in section 6.2.3 that the concentration of oxidizing radiolysis products is likely higher in the irradiated region compared to the flow region, due to dispersion of the oxidizing species in the water, as well as the production of short-lived radicals that only affect the irradiated surface. It has also been found that the thermodynamic conditions at the flow and irradiated regions are sufficient to prevent a passive film from even forming. Therefore, in the case of the samples without a pre-grown film, it is logical to assume that a difference in the

concentration of oxidizing species between the irradiated and flow regions may not make a difference – because the lower concentration in the flow region is enough to effectively suppress the formation of a passive film.

In the case of the already formed film, it has been observed that dissolution was in-progress in the irradiated region, and there were some signs of dissolution in the flow region – the coarsening of the outer oxides. Therefore, while the concentration of oxidizing species was enough to suppress passive film formation in the case of samples without a pre-grown oxide, it requires time to dissolve the already-grown oxide. If this is the case, then it stands to reason that a difference in the concentration of oxidizing species may now make a difference in the rate at which the oxide film dissolves. This suggestion is merely speculative, since conditions at the oxide-solution interface are not well known. Since the effect of radiolysis is purely thermodynamic, and not kinetic, a difference in the concentration of oxidizing species would only make a difference if surface sites on the oxide were not already saturated. While actually measuring this rate is beyond the scope of this work, since only one "snapshot" in time was taken, it serves as a possible explanation for the observed behavior. Therefore, the differences between the irradiated region and the flow region of sample Pr24 may be attributed to a difference in the concentration of oxidizing species in solution, and/or the presence of radicals in the irradiated region. While ballistic mixing seems like a more plausible explanation, a simple difference in the concentration of radiolysis products cannot be ruled out.

A difference in concentration of radiolysis products may also explain the difference in the outer oxide morphology between the flow regions and irradiated regions observed in Section 5.2. The flow regions exhibited a mix of larger faceted outer oxide crystals typical of spinels and smaller equiaxed crystals typical of hematite, while the irradiated regions exhibited much fewer

large faceted crystals, and featured mostly smaller equiaxed crystals, and plate-like crystals, also typical of hematite. This difference can be attributed to a higher concentration of radiolysis products in the irradiated region, possibly due to the presence of radicals in the irradiated region. Also, as mentioned in Section 6.4.3, ballistic effects may have played a part in the outer oxide morphology, as enhanced mixing of the spinel crystals may have led to faster oxidation of magnetite to hematite in the irradiated regions. In the present study, there is not enough evidence to say decisively.

6.4.4.1 Conclusion

The observed difference between the irradiated and flow regions of Pr24 may be attributed to the higher concentration of radiolytically-produced oxidizing species in the irradiated area compared to the flow area. It is hypothesized that this difference in radiolysis product concentration does not produce a difference between the irradiated and flow regions of the other samples due to their relatively thin oxide layers, which become saturated at surface sites at lower oxidizer concentrations, but may have made difference on sample Pr24 due to pre-grown kinetic barrier. A difference in radiolysis product concentration may have also accounted for the observed difference in the outer oxide morphology between irradiated and flow regions in Section 5.2.

6.4.5 Summary of the Contributions of Radiolysis and Displacement Damage

CFD models are consistent with the observed flow pattern on the sample surfaces, indicating an upward flow across the sample face, carrying radiolysis products upward across the unirradiated region of the sample. Flow regions were similar in thickness to irradiated regions, and displayed similar porosity and chromium depletion. It is concluded that the loss of passivity and subsequent accelerated dissolution are likely caused by radiolysis.

The irradiated region of sample Pr24 had both porous and non-porous inner oxides, and was depleted in Cr, while the flow region had neither porosity nor Cr depletion. It was calculated that radiation enhanced diffusion in the spinel oxides likely had a minimal effect, and the difference is attributed to either athermal ballistic mixing in the irradiated region, or to a higher concentration of oxidizing species in the irradiated area.

6.5 Relevance to LWR Conditions

While the objective of this work is fundamental in nature, there is value in discussing the relevance of the findings of this work to reactor conditions. Unfortunately, there is very little literature data available that contains characterization of the oxides from in-service reactors. The reasons for this deficiency can only be left to speculation. While there are a number of aspects of the experiments in this work that differ from an actual reactor, there are two that merit special discussion. Section 6.5.1 will discuss dose rates, and how the observations in this work can be applied to reactors that experience a much lower dose rate. Section 6.5.2 will discuss the

application of the phenomena discovered in this work to longer times that are more relevant to reactors.

6.5.1 Dose Rate Considerations

To accelerate the effects of radiation on corrosion, a dose rate of 4000 kGy/s was used for most of the samples in this work, except for sample Lo24, which was irradiated with a dose rate of 400 kGy/s, measured in the water at the sample-water interface. This can be compared to a typical peak LWR dose rate of 4.7 kGy/s as reported by Andresen[86] and Pastina[138], and a peak gamma dose of 1.5 kGy/s, reported by Pastina[138].

This difference of nearly three orders of magnitude is likely to have some effects on corrosion potential. Particularly, the change in dose rate may have a large effect on how the hydrogenated water suppresses radiolysis products.

Expressed in a rather simplistic way, H_2 suppresses H_2O_2 production by reducing the HO radicalby the reaction given in Equation 6.14 before it can form H_2O_2 by Equation 6.15. [21], [63]

$$HO^{\cdot} + H_2 \rightarrow H_2O + H^{\cdot} \tag{6.14}$$

$$HO^{\cdot} + HO^{\cdot} \rightarrow H_2O_2 \tag{6.15}$$

Note that Equation 6.15 is second-order with regard to HO, while Equation 6.14 is first order with regard to HO. The concentration of HO is dependent on dose rate, while the concentration of H_2 is largely fixed (despite radiolytic production of H_2). For this reason, it

follows that as dose rate is lowered, the reaction rate of Equation 6.15 will decrease exponentially, while the reaction rate of Equation 6.14 will decrease linearly. It is then logical to conclude that as dose rate is lowered, as in a reactor, the effectiveness of dissolved hydrogen at suppressing radiolysis increases, diminishing the effect of radiation on corrosion.

The purpose of the lower dose rate experiment was to determine whether the phenomena observed on the high dose rate samples were still present at a dose rate one order of magnitude less. Sample Lo24 displayed chromium depletion, increased porosity, hematite, and thinning of the inner oxide – all of the effects of radiation found on the high dose rate samples. Dose rates below 400 kGy/s were not tested for this work.

There is limited evidence that some of the effects of irradiation found in this work are present at lower dose rates. Andresen found a slight elevation of corrosion potential (<50 mV) during proton irradiation at 4.7 kGy/s[86] in water with 200 wppb H_2. Andresen found even higher increases in potential in water without dissolved hydrogen. Wang et al. also observed slight potential increases during very low dose proton irradiation[139]. Wang also conducted electron irradiations at low dose rate, and found an increase in the occurrence of hematite on irradiated oxide films[140].

6.5.2 Extrapolation to Longer Operating Times

It is also useful to speculate on the applicability of this work to longer oxidation times. While this work has studied samples that have oxidized for 4-96 hrs, stainless steel components may be in service for 60-80 years if life extensions are included.

This work has largely shown that irradiation leads to a loss of oxide protectiveness by preventing a passive oxide film from forming. At longer times though, even if radiation induced dissolution prevents a protective inner oxide from forming, the outer oxide will still grow in thickness and coverage. This can be seen by comparing the outer oxide coverage in Figure 5.7 - Figure 5.10 to see how the outer oxide coverage increases with time. Limited data in Chapter 5 showed that while the outer oxide is generally non-protective, it can provide limited localized protection to the inner oxide underneath. It is reasonable then to suggest that over a much longer time, the outer oxide will cover all of the oxide surface with increasing thickness. Despite its porosity and lack of Cr-rich spinels, it may provide limited protection by reducing oxidizing species produced by irradiation before they reach the inner oxide.

On the other hand, consider the case of oxide spallation during longer service times. Irradiation may prevent a passive oxide from forming on the location of the spalled oxide, leading to an increase in localized corrosion.

As a final consideration, the case of sample Pr24 which showed that a pre-growth oxide was an effective barrier to oxide dissolution may be applicable to reactor situations. It stands to reason that pre-oxidizing reactor components before exposure to radiation may prevent or retard some of the effects of radiation-induced oxide dissolution.

6.5.3 Summary of Relevance of LWR Conditions

While the dose rate in this experiment is higher than peak LWR dose rates by 2 to 3 orders of magnitude, limited evidence suggests that irradiation still induces increases in corrosion potential even at lower dose rates, and those potential increases are sufficient to affect

the phases on the oxide film. At very long times, accumulation of outer oxide particles may allow the oxide to regain passivity. Prevention of passive film formation may still cause localized corrosion during oxide spallation. It may be advantageous to allow components to pre-oxidize before exposure to irradiation.

Table 6.1. Relevant ECP values for the magnetite to hematite transition

Simulated Primary Water Conditions 300˚C, 3 wppm H_2, pH 6	$E = -600\ V\ vs. SHE$
Fe_2O_3/Fe_3O_4 Phase boundary at pH 6 (Cook and Olive)[92]	$E = -350\ V\ vs. SHE$
Fe_2O_3/Fe_3O_4 Phase boundary at pH 6 (this work)	$E = -350\ V\ vs. SHE$

Table 6.2. Calculated potential of the $HCrO_4^-$ lower phase boundary at pH 6 and 300˚C, at different $HCrO_4^-$ activities

$log[HCrO_4^-]$	$HCrO_4^-$ lower phase boundary (V_{she}) at pH 6	
	This Work	Puigdemenech & Beverskog[48]
-6	0.29	0
-8	0.21	-0.1
-10	0.14	nc
-12	0.06	nc
-14	-0.02	nc
-16	-0.09	nc

nc: not calculated

Table 6.3. Three spinel oxide dissolution reactions that will be used to understand spinel oxide stability

1. The oxidation of Fe_3O_4 to form Fe_2O_3 as discussed in 6.2.1, and calculated in this work, and by Beverskog and Puigdemenech[109] to occur at approximately -0.35 V_{SHE} at a pH of 6.
2. The oxidation of $FeCr_2O_4$ to form $HCrO_4^-$ as discussed in 6.2.2.2, and calculated in this work to occur between -0.09 and 0.29 V_{SHE} at a pH of 6 and chromate activities between 10^{-16} and 10^{-6} mol/kg.
3. The reaction of $NiFe_2O_4$ to form Fe_2O_3 as discussed in 6.2.2.3, which was calculated to occur at 0.7 V_{SHE} by Beverskog and Puigdemenech[48], and was found in this work to not be affected by an increase in corrosion potential.

Table 6.4. Changes in the position of the Spinel A_{1g} peak as indicated by Raman Spectroscopy (reprint of Table 5.1)

Unirradiated Sample	Unirradiated Sample	Irradiated Sample	Irradiated Sample Area		
			Unirradiated	Flow	Irradiated
Un04	No Shift	Hi04	No Shift	Up	Up
ns	ns	Hi12	No Shift	Down	Down
Un24	No Shift	Hi24	Up	Down	Down
Un72	No Shift	Hi72	Up	Down	Down

ns: no sample

Table 6.5. Sample areas on which hematite was found.

Unirradiated Sample	Unirradiated Sample	Irradiated Sample	Irradiated Sample Area		
			Unirradiated	Flow	Irradiated
Un04	No	Hi04	No	Yes	Yes*
ns	ns	Hi12	No	Yes	Yes
Un24	No	Hi24	Yes	Yes	Yes
Un72	No	Hi72	Yes	Yes	Yes

ns: no sample

*The irradiated area of Hi04 displayed small indicators of hematite, along with maghemite

Table 6.6. Sample regions organized by exposure time and qualitative radiolysis exposure, color-coded by spinel peak shift direction

Increasing time ↓		Unirradiated Sample	Irradiated Sample		
			Unirradiated Region	Flow Region	Irradiated Region
	4 hr	Un04 Shift: none	Hi04-unirr Shift: none	Hi04-flow Shift: up	Hi04-irr Shift: up
	12 hr	ns	Hi12-unirr Shift: none	Hi12-flow Shift: down	Hi12-irr Shift: down
	24 Hr	Un24 Shift: none	Hi24-unirr Shift: up	Hi24-flow Shift: down	Hi24-irr Shift: down
	72 Hr	Un72 Shift: none	Hi24-unirr Shift: up	Hi24-flow Shift: down	Hi24-irr Shift: down
	Increasing Concentration →				

ns:no sample

Table 6.7. Sample regions organized by exposure time and qualitative radiolysis exposure for the study of spinel oxide stability. Samples are divided into four groups based on their exposure time and qualitative radiolysis exposure: (gray) No-effect, (pink) Long-low, (green) Short-high, and (blue) Long-high

Increasing time ↓		Unirradiated Sample	Irradiated Sample		
			Unirradiated Region	Flow Region	Irradiated Region
	4 hr	Un04 No-effect	Hi04-unirr No-effect	Hi04-flow Short-high	Hi04-irr Short-high
	12 hr	ns	Hi12-unirr No-effect	Hi12-flow Long-high	Hi12-irr Long-high
	24 Hr	Un24 No-effect	Hi24-unirr Long-low	Hi24-flow Long-high	Hi24-irr Long-high
	72 Hr	Un72 No-effect	Hi24-unirr Long-low	Hi24-flow Long-high	Hi24-irr Long-high
	Increasing Concentration →				

ns: no sample

Table 6.8. Stainless steel polarization data from literature showing the potential at the transition from the passive to the transpassive region

Reference	Temperature	pH	Upper bound of passive region (V_{SHE})	log[CrO_4^{2-}] at the transpassive region
Liu et al.[141]	300˚C	7.1	0.04	-8
Xu et al.[59]	250˚C	7.1	0	-11
Sun et al.[19]	300˚C	6.8	-0.04	-13
Sun et al.[19]	300˚C	9.1	-0.22	-10

Table 6.9. Sample regions that displayed chromium depletion and porosity

Sample	**Time (hr)**	**Dose Rate (kGy/s)**	**Cr Depletion / Porosity**		
			Irr	**Flow**	**Unirr**
Hi04	4	4000	Yes	Yes	No
Hi12	12	4000	Yes	Yes	No
Hi24	24	4000	Yes	nl	No
Hi24-2	24	4000	Yes	Yes	nl
Lo24	24	400	Yes	nl	No
Un24	24	na	na	na	No
Hi72	72	4000	Yes	Yes	No
Un72	72	na	na	na	No

na: Not applicable
nl: No Liftout taken

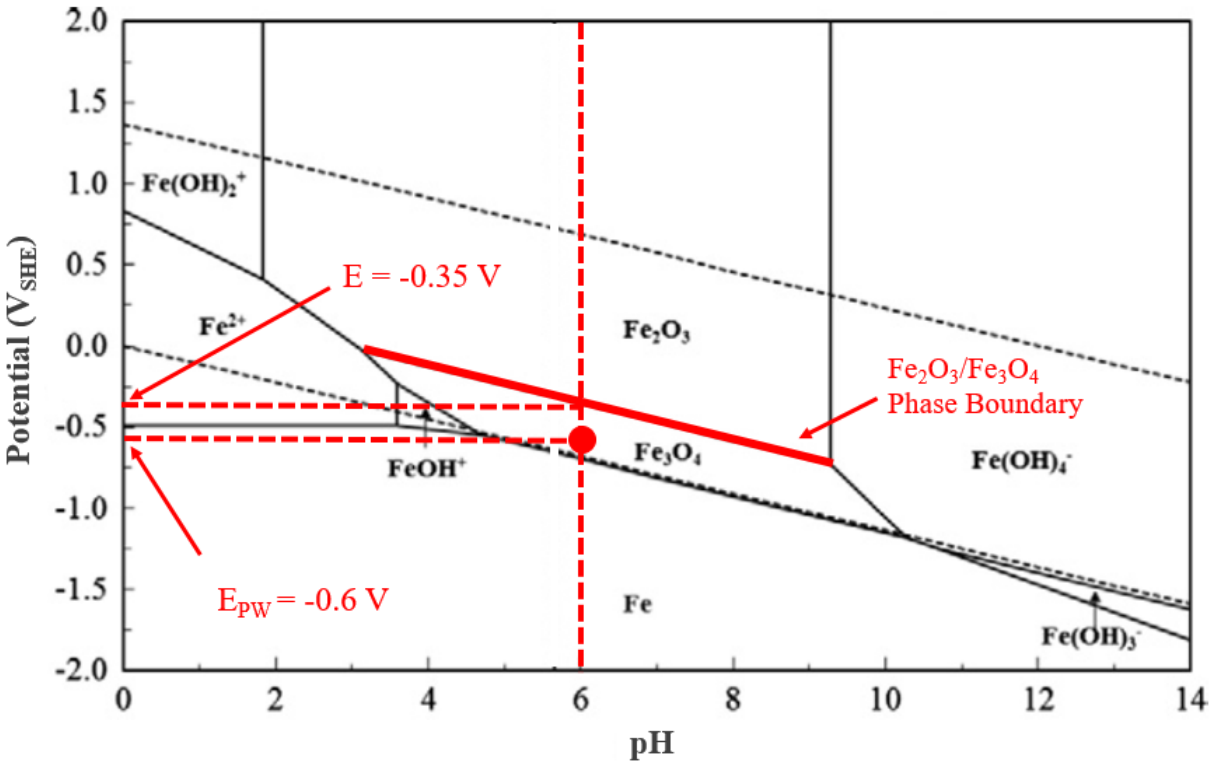

Figure 6.1. Pourbaix diagram by Olive and Cook of iron at 300˚C with activity of iron at 10^{-6} mol/kg. The potential of primary water and of the Fe_2O_3/Fe_3O_4 phase boundary are indicated in the figure[92].

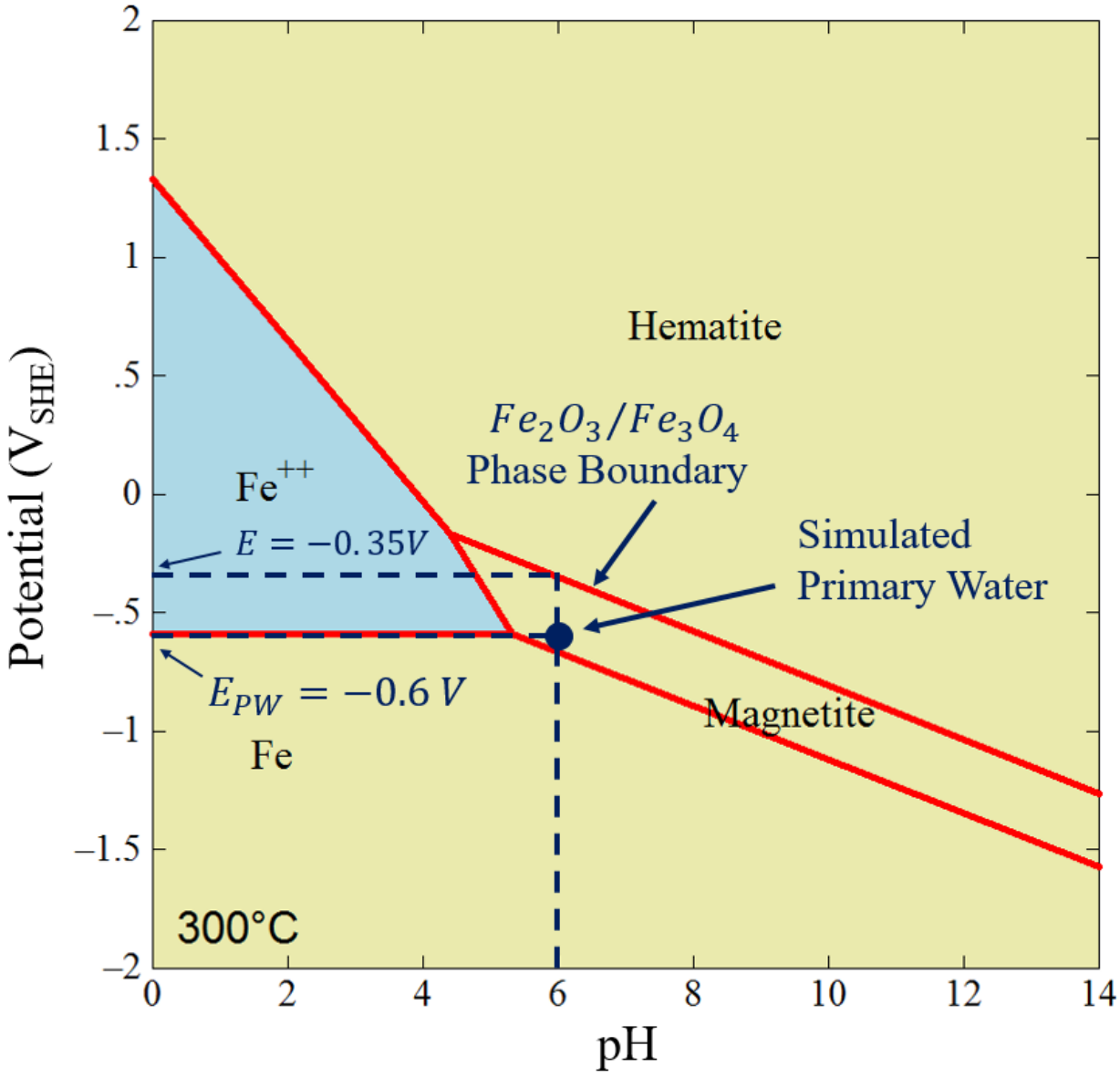

Figure 6.2. Pourbaix diagram of iron in 300˚C water, calculated with Geochemists' Workbench 11[110]. Ionic species are set to an activity of 10^{-6} mol/kg. Blue dotted lines indicate relevant primary water conditions.

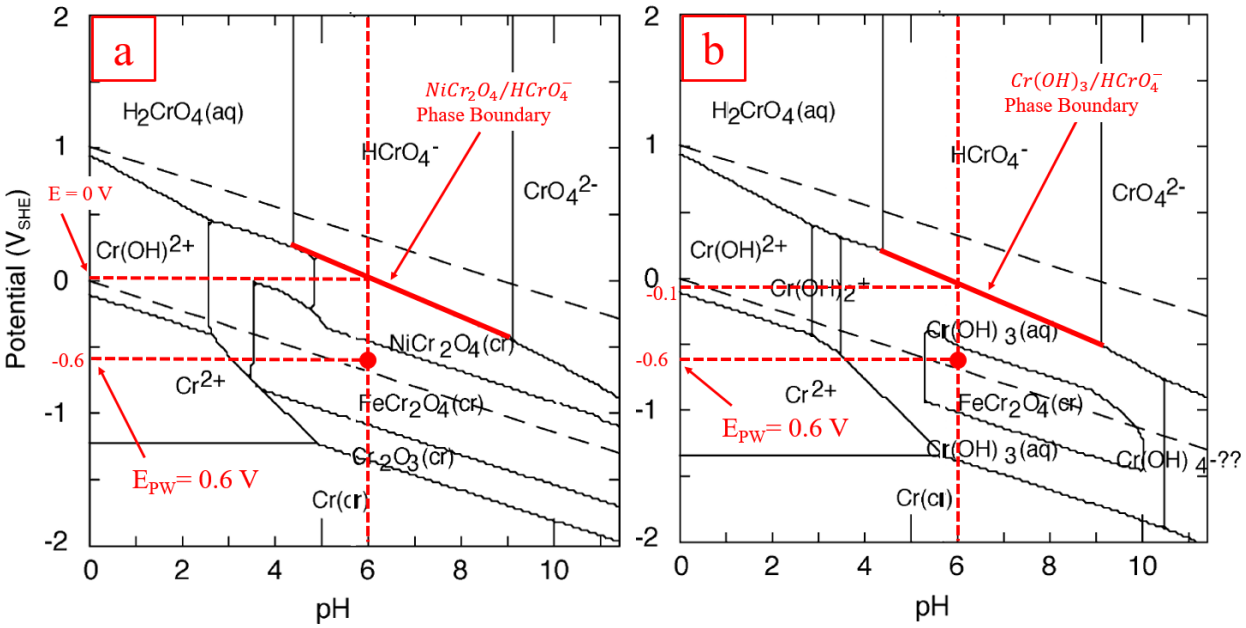

Figure 6.3. Pourbaix diagram of Cr species in the Fe-Cr-Ni system at 300˚C with activity of ionic species set to (a)10^{-6} mol/kg and (b) 10^{-8} mol/kg [48].

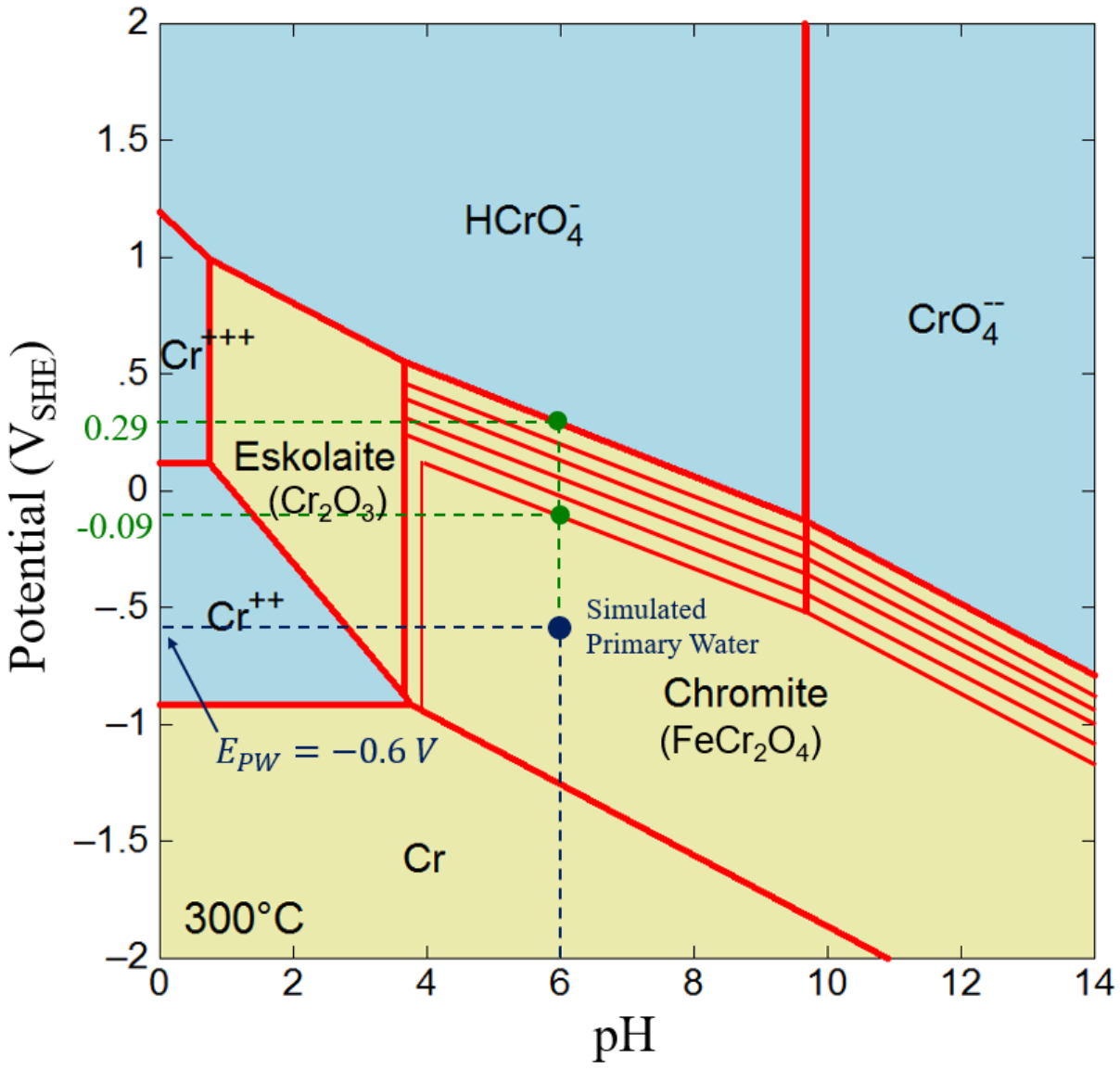

Figure 6.4. Pourbaix diagram of chromium in the Fe-Cr system in 300˚C water. Ionic species are set to an activity of 10^{-6}. Additional lines are drawn for the upper phase boundary of chromite at decreasing CrO_4^{2-} activity. Blue guide lines indicate primary water conditions, and green guide lines indicate the range of the upper chromite phase boundary at a pH of 6.

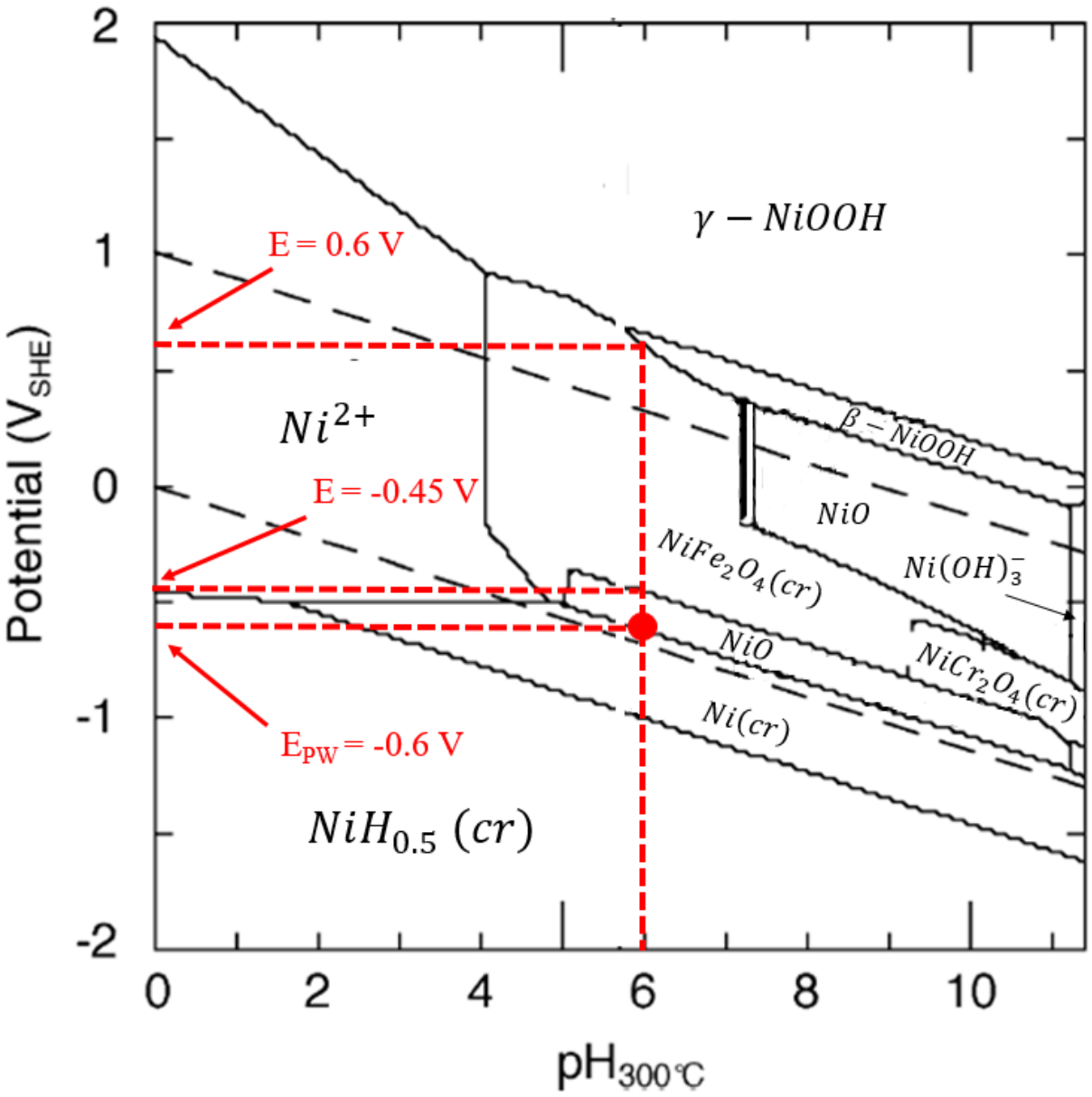

Figure 6.5. Pourbaix diagram of Ni species in the Fe-Cr-Ni system at 300˚C and 10^{-6} mol/kg. The potential of primary water, and the bounds of trevorite stability are indicated at a pH of 6. [48]

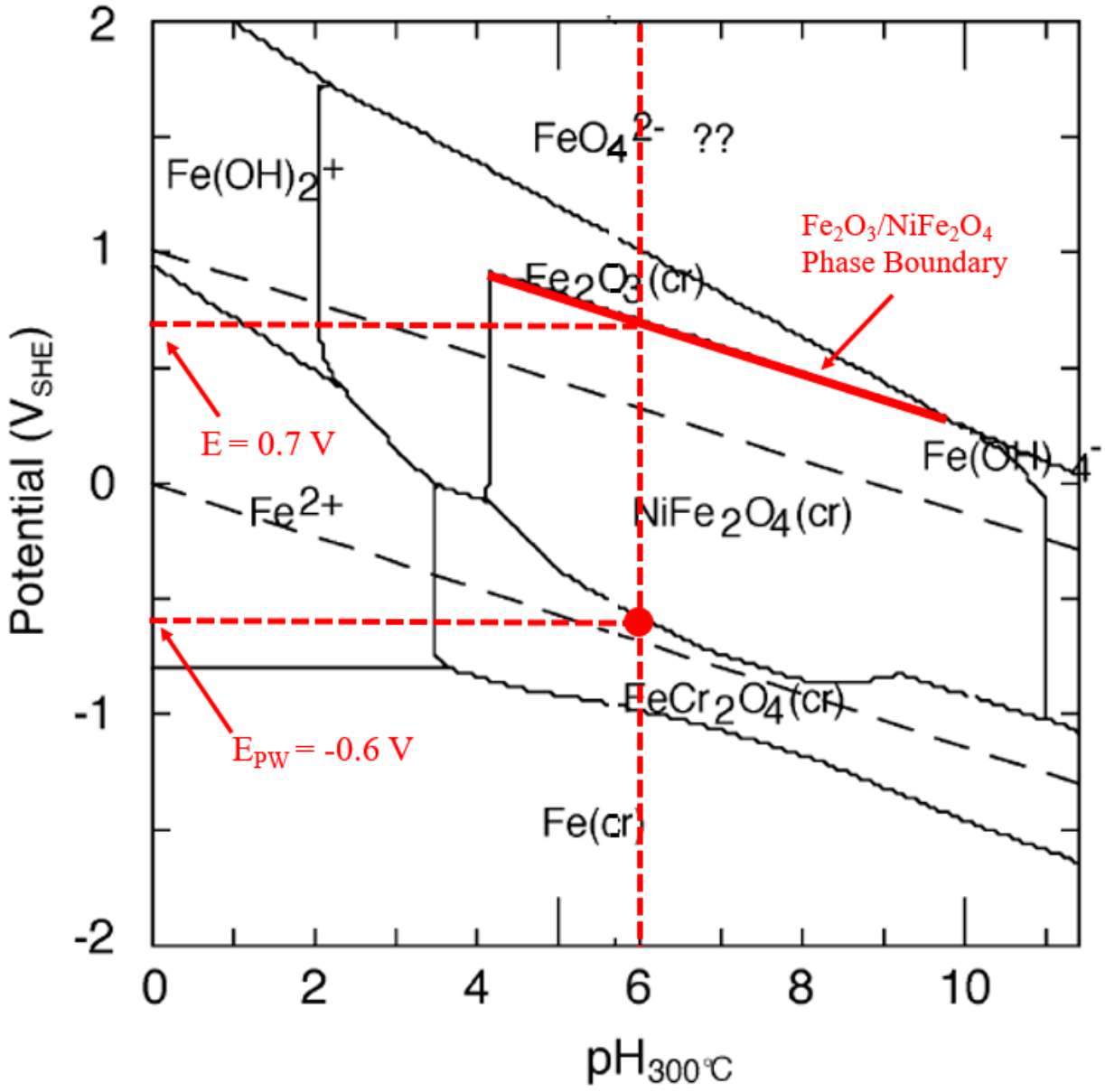

Figure 6.6. Pourbaix diagram of Fe species in the Fe-Cr-Ni system at 300˚C and 10^{-6} mol/kg. [48]

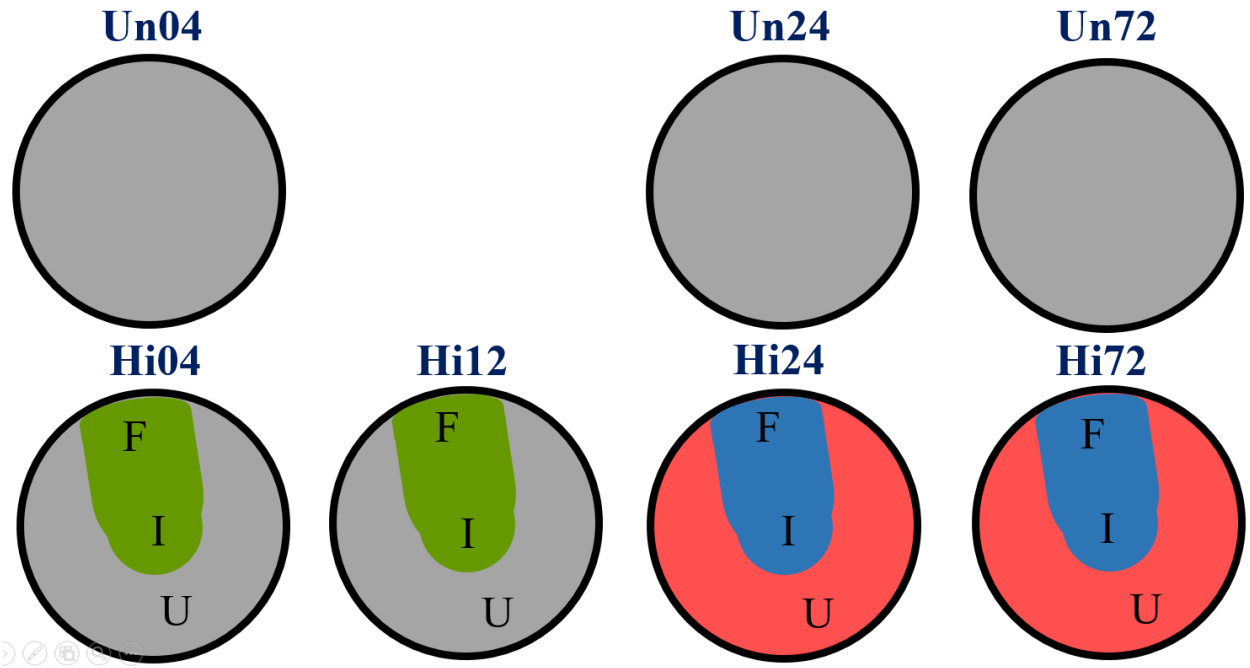

Figure 6.7. Diagram of the sample regions divided into four groups based on their exposure time and qualitative radiolysis exposure for the study of spinel oxide stability: (gray) No-effect, (pink) Long-low, (green) Short-high, and (blue) Long-high.

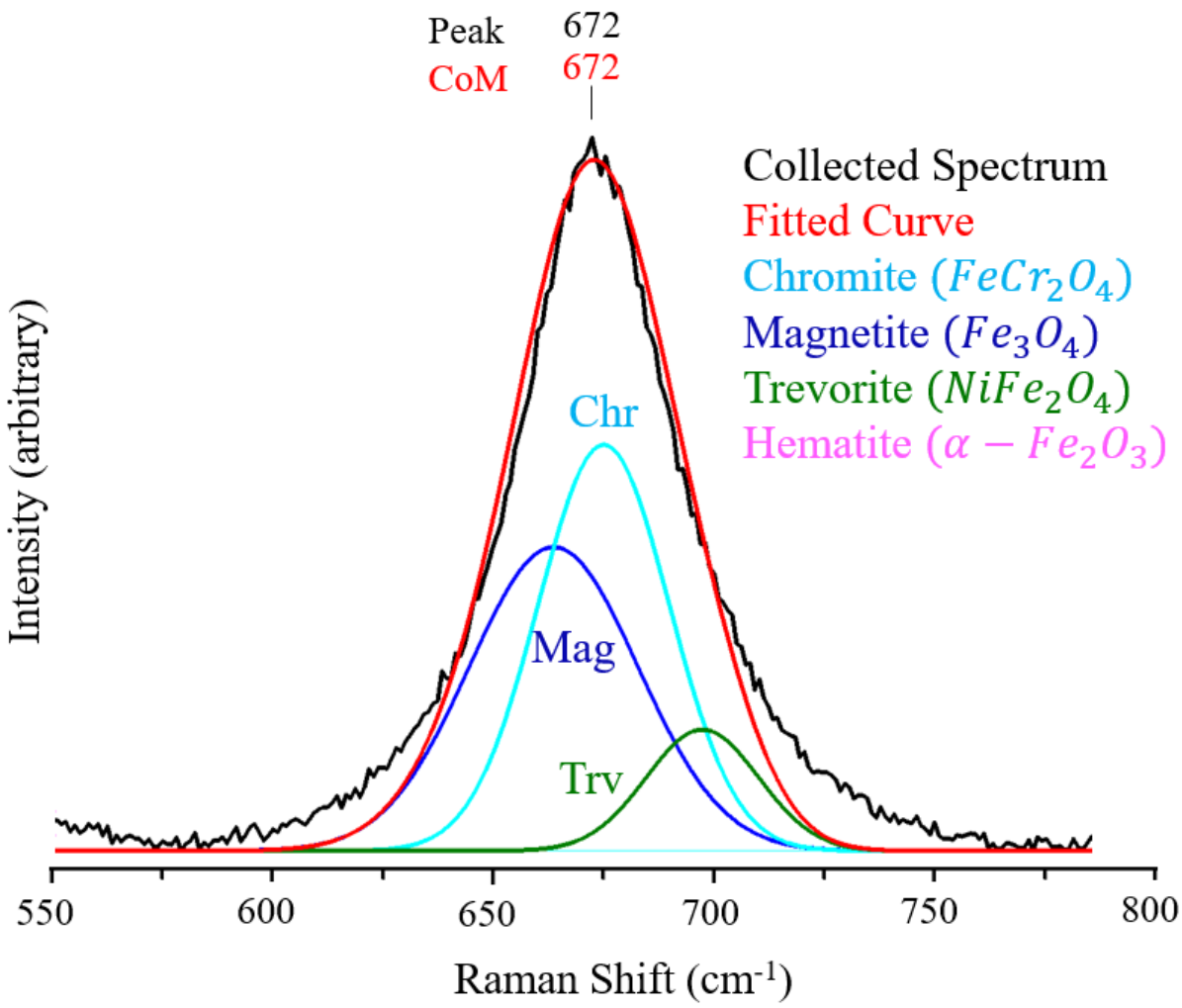

Figure 6.8. Raman spectrum showing the spinel A_{1g} peak on sample Un24, with fitting, representing the *no-effect* regions. The wavenumber of the peak and center-of-mass (CoM) are labeled in black and red respectively.

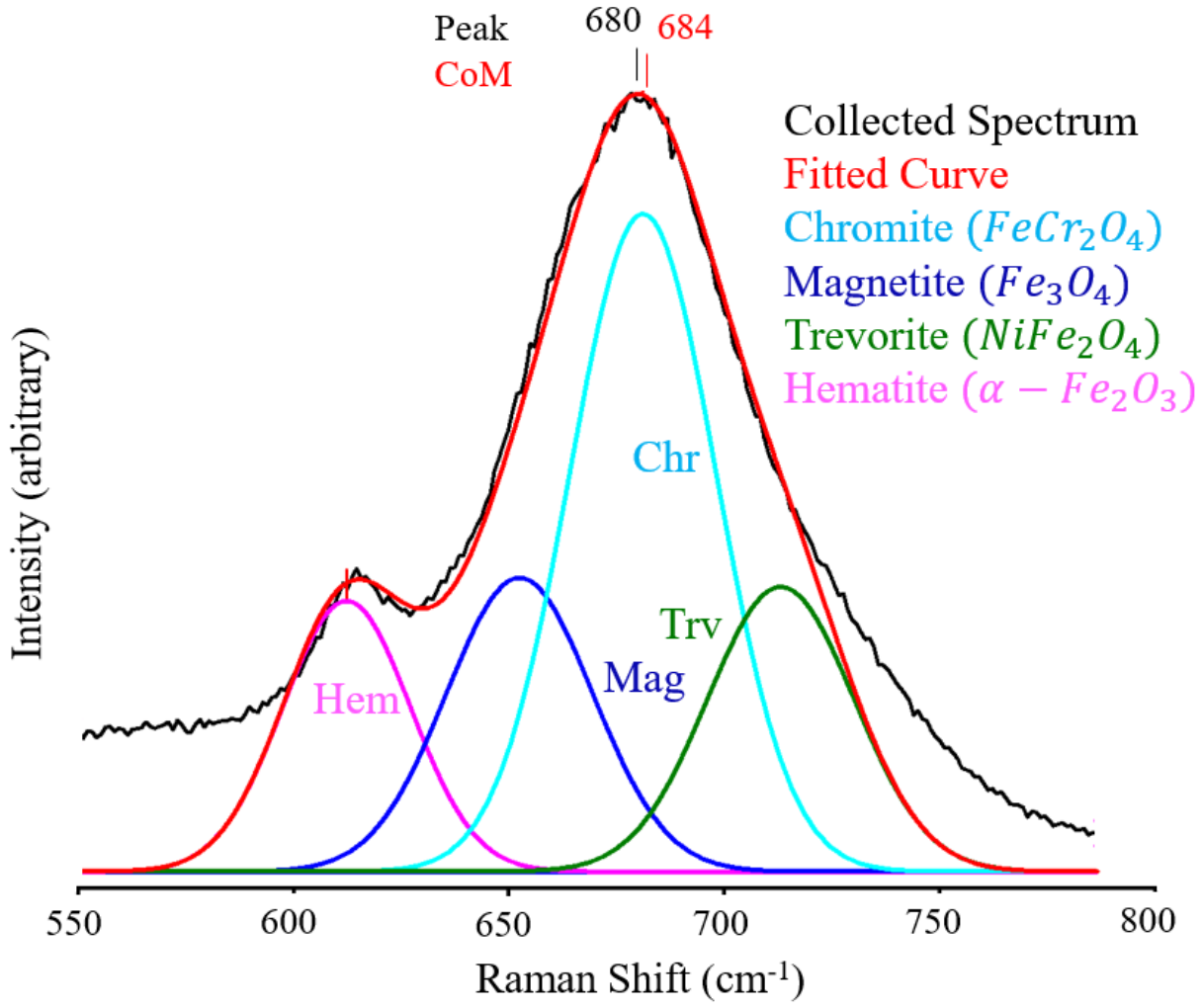

Figure 6.9. Raman spectrum showing the spinel A_{1g} peak from the unirradiated region of sample Hi72 with fitting, representing the *long-low* regions. The wavenumber of the peak and center-of-mass (CoM) are labeled in black and red respectively.

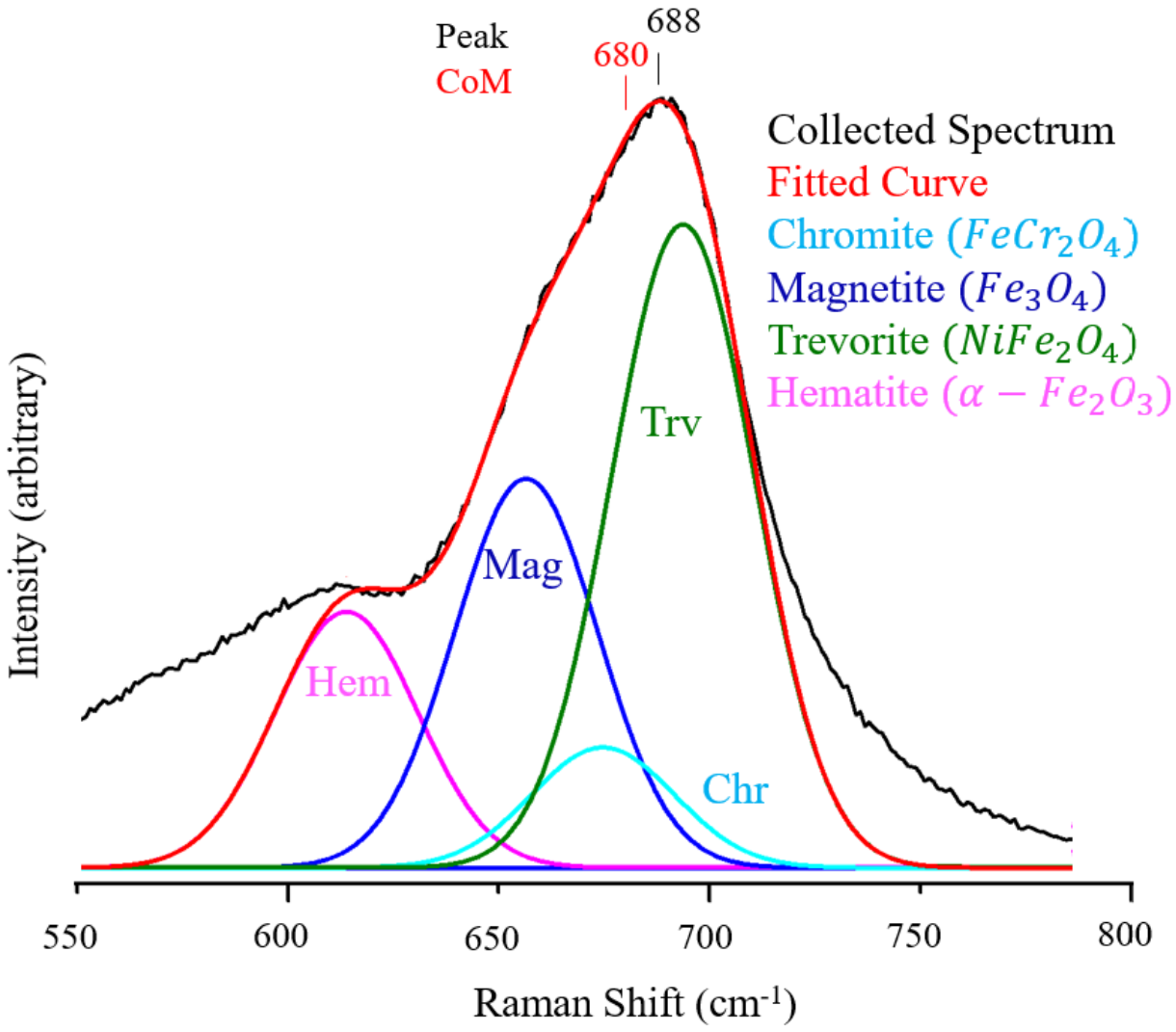

Figure 6.10. Raman spectrum showing the spinel A_{1g} peak from the flow region of sample Hi04 with fitting, representing the *short-high* regions. The wavenumber of the peak and center-of-mass (CoM) are labeled in black and red respectively.

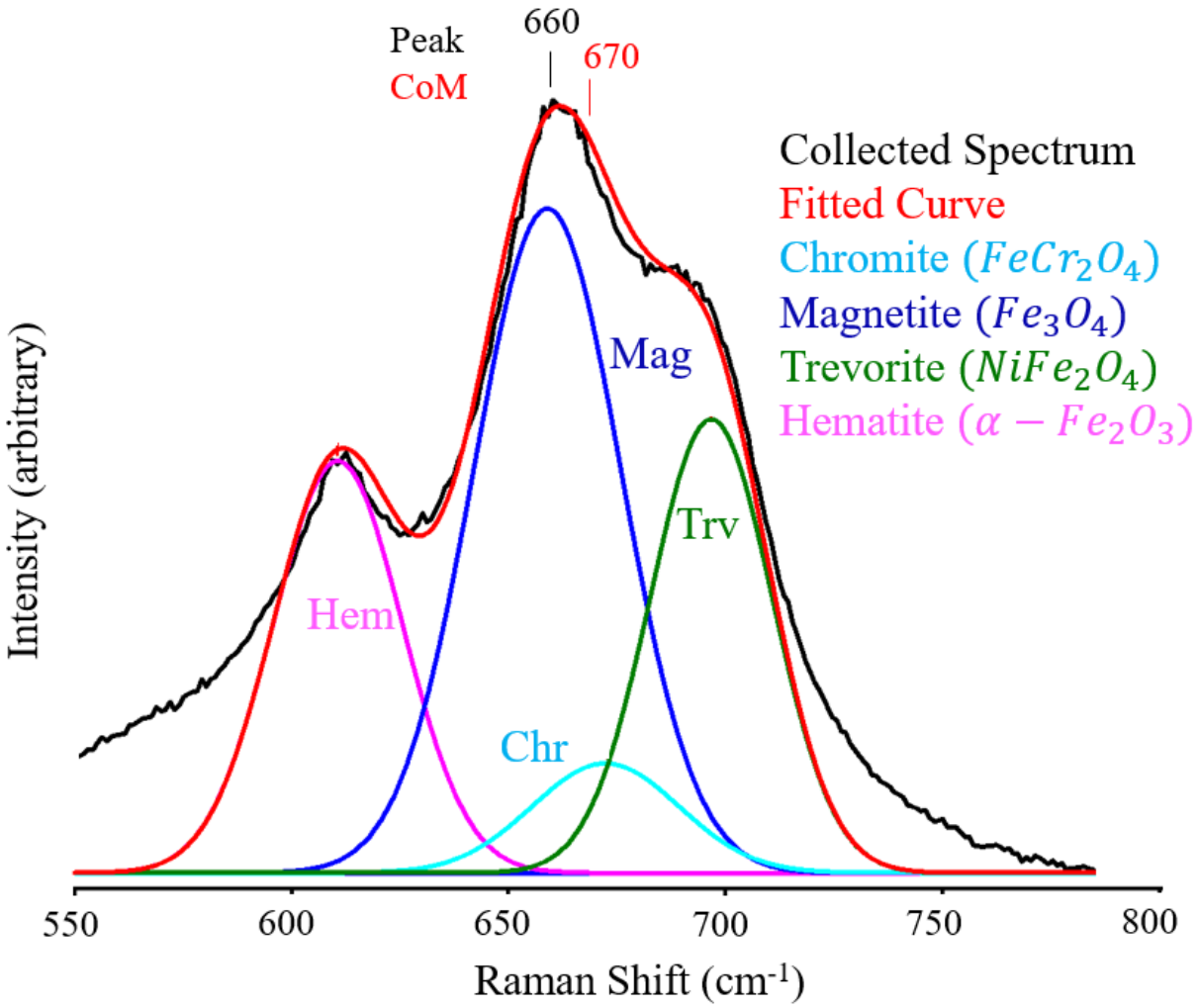

Figure 6.11. Raman spectrum showing the spinel A_{1g} peak from the flow region of sample Hi72 with fitting, representing the *long-high* regions. The wavenumber of the peak and center-of-mass (CoM) are labeled in black and red respectively.

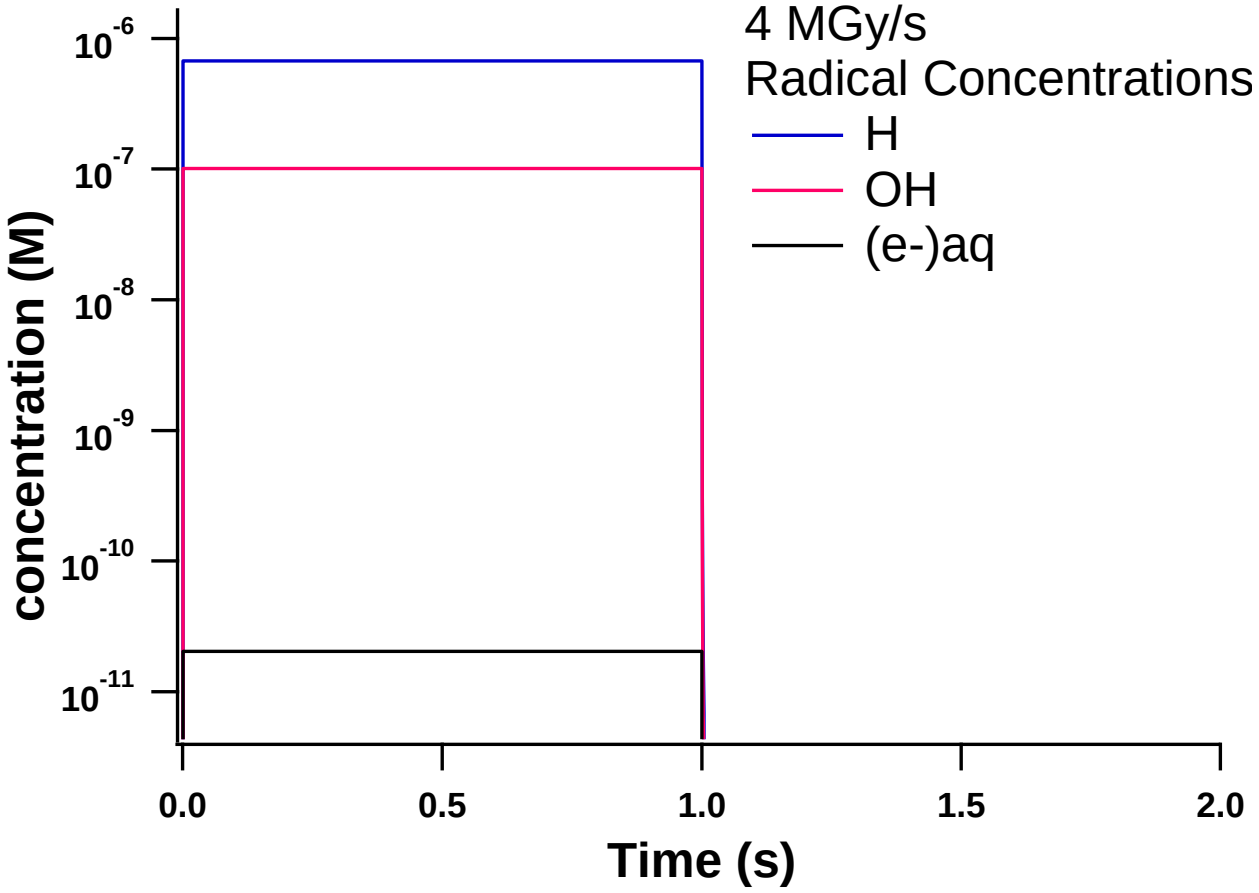

Figure 6.12. Concentration of radical species produced by a 1 second pulse of 1.4 MeV protons in 300˚C water with 3 wppm H_2 (1.6 mM) at a dose rate of 4000 kGy/s.[118]

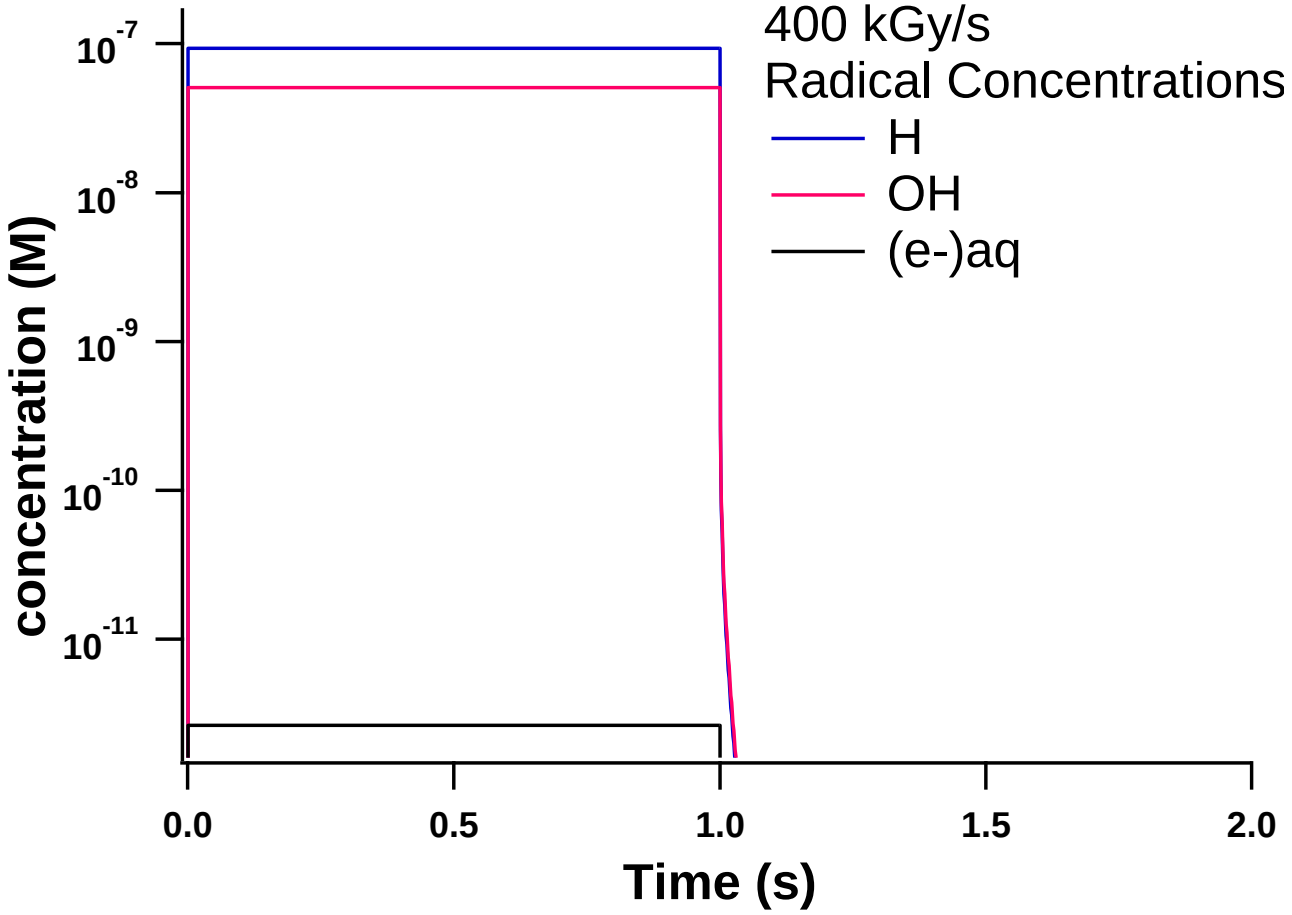

Figure 6.13. Concentration of radical species produced by a 1 second pulse of 1.4 MeV protons in 300˚C water with 3 wppm H_2 (1.6 mM) at a dose rate of 400 kGy/s.[118]

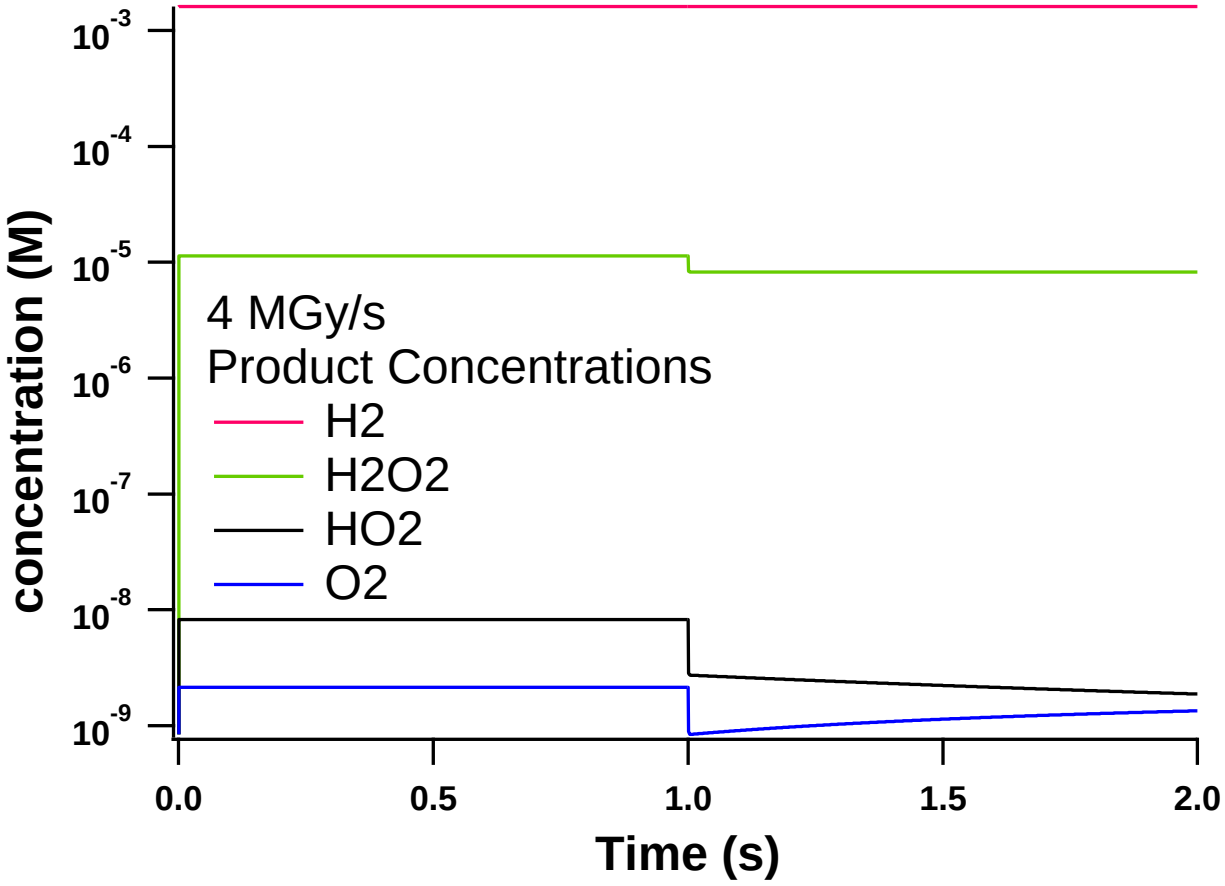

Figure 6.14. Concentration of long-lived species produced by a 1 second pulse of 1.4 MeV protons in 300˚C water with 3 wppm H_2 (1.6 mM) at a dose rate of 4000 kGy/s.[118]

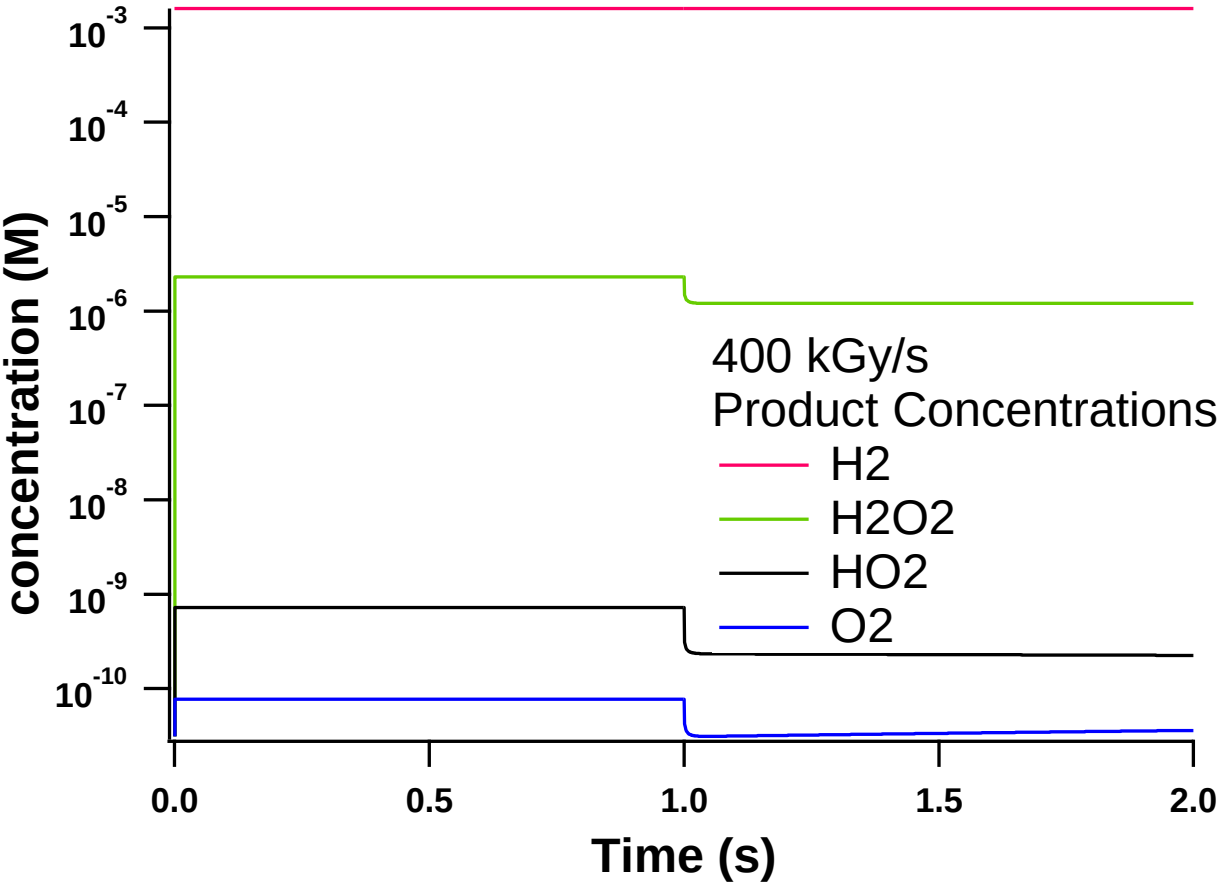

Figure 6.15. Concentration of long-lived species produced by a 1 second pulse of 1.4 MeV protons in 300˚C water with 3 wppm H_2 (1.6 mM) at a dose rate of 400 kGy/s.[118]

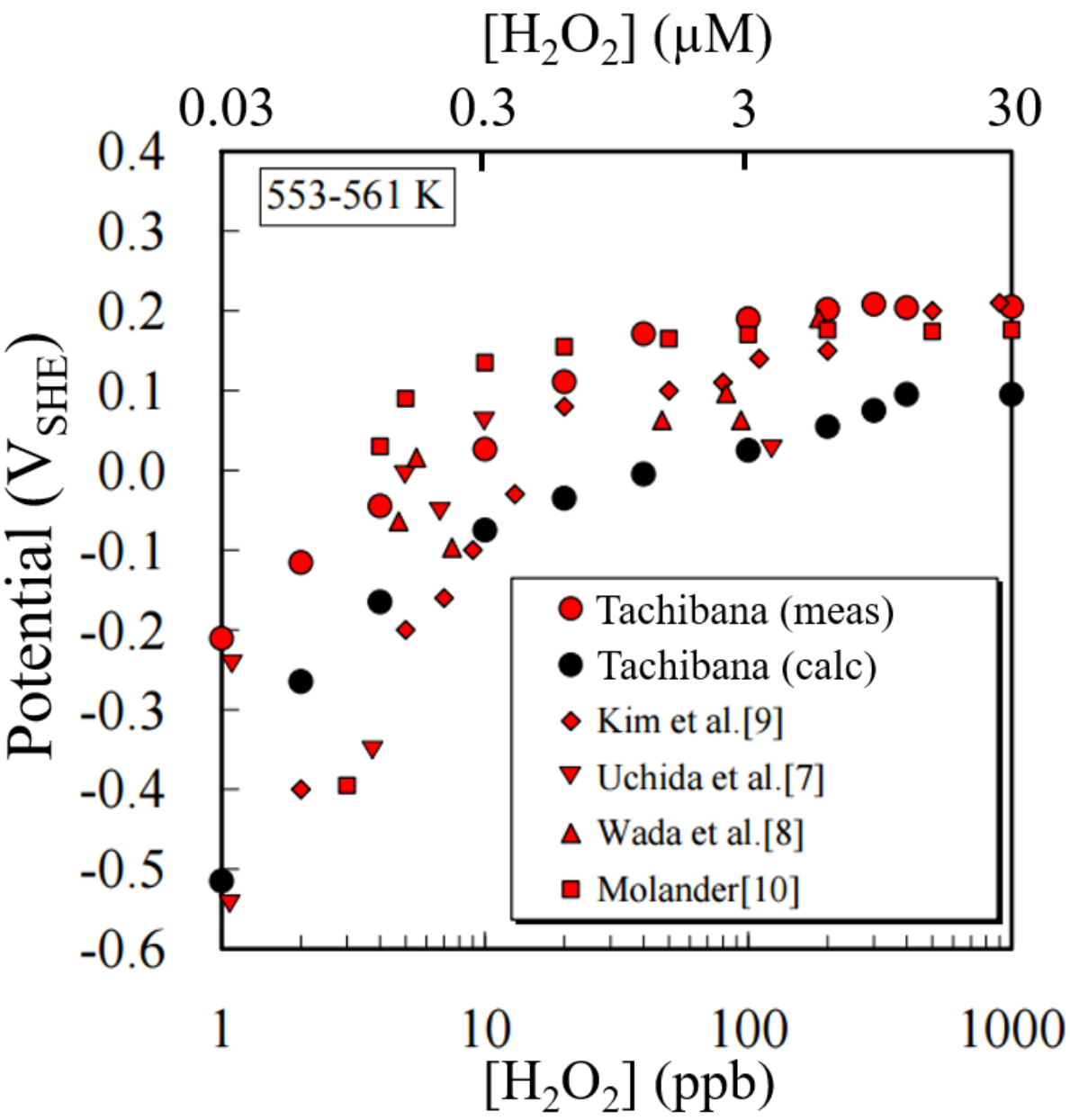

Figure 6.16. ECP as a function of H_2O_2 concentration, as measured in several works. The data labeled "this work" refers to Tachibana, the paper from which the graph was taken.[119]

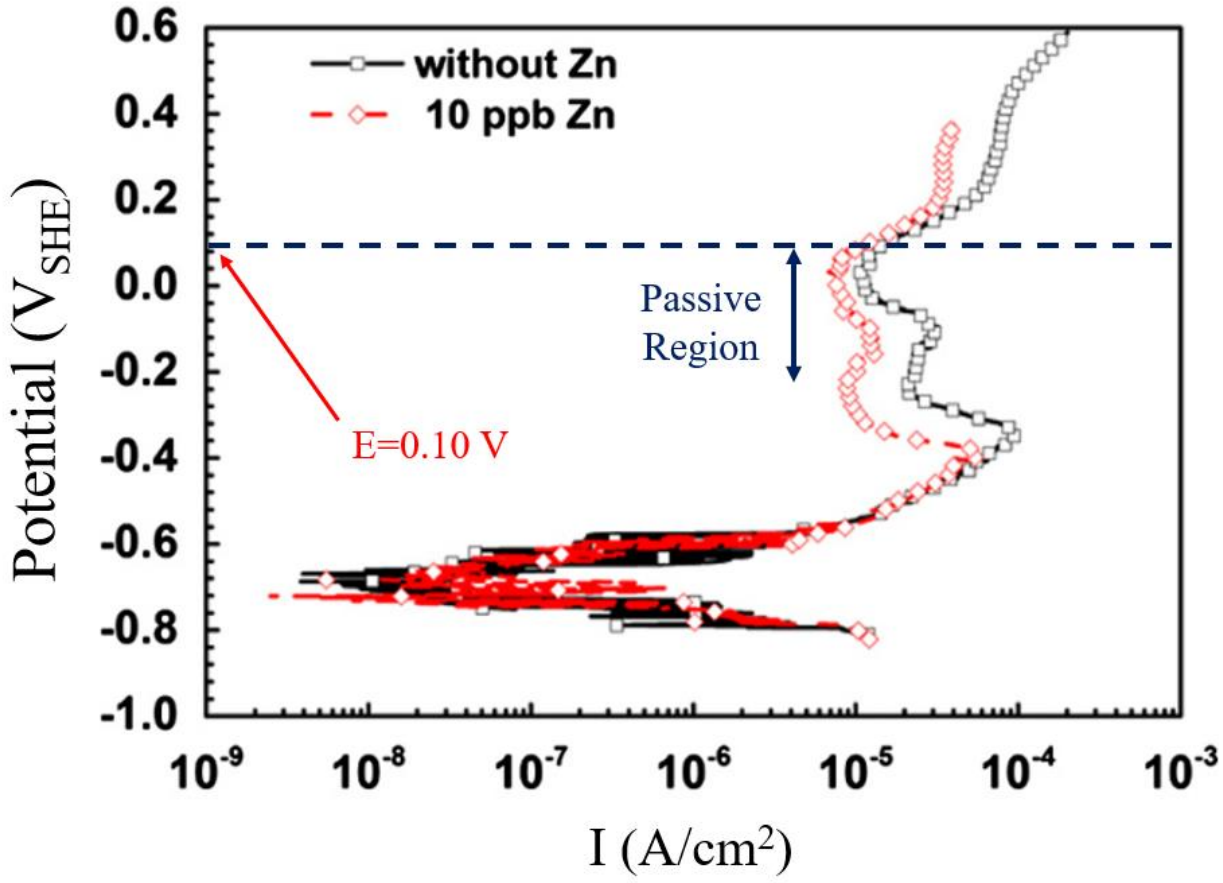

Figure 6.17. Polarization curve of stainless steel in 300˚C water with 1200 wppm B and 3.6 wppm Li at pH=7.1 with and without Zn addition measured by Liu et al.[93].

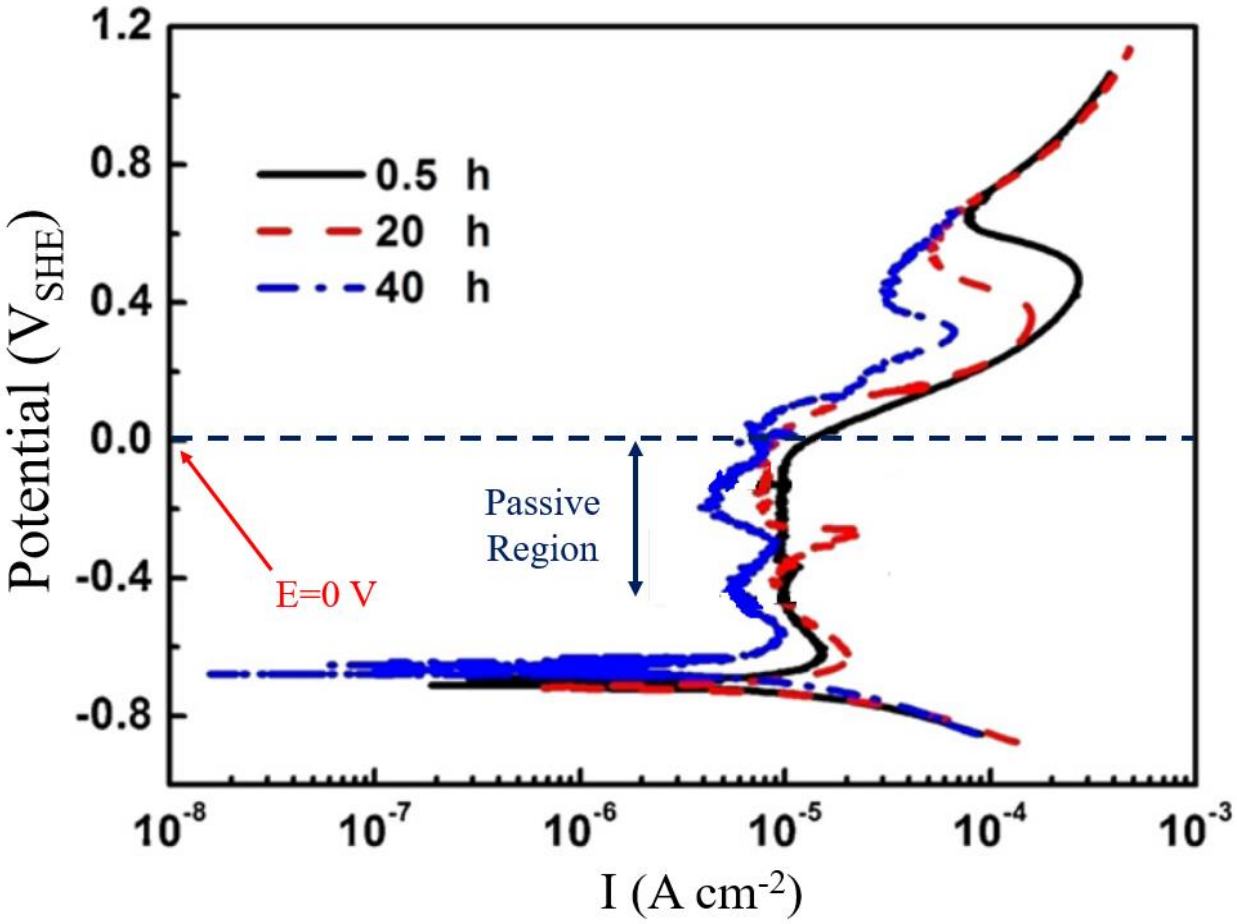

Figure 6.18. Potentiostatic polarization curve of 304 stainless steel in 250˚C water at pH=6.8 after 0.5, 20, and 40 hrs measured by Xu et al.[59] A line showing the calculated $FeCr_2O_4$ / $HCrO_4^-$ phase boundary is added.

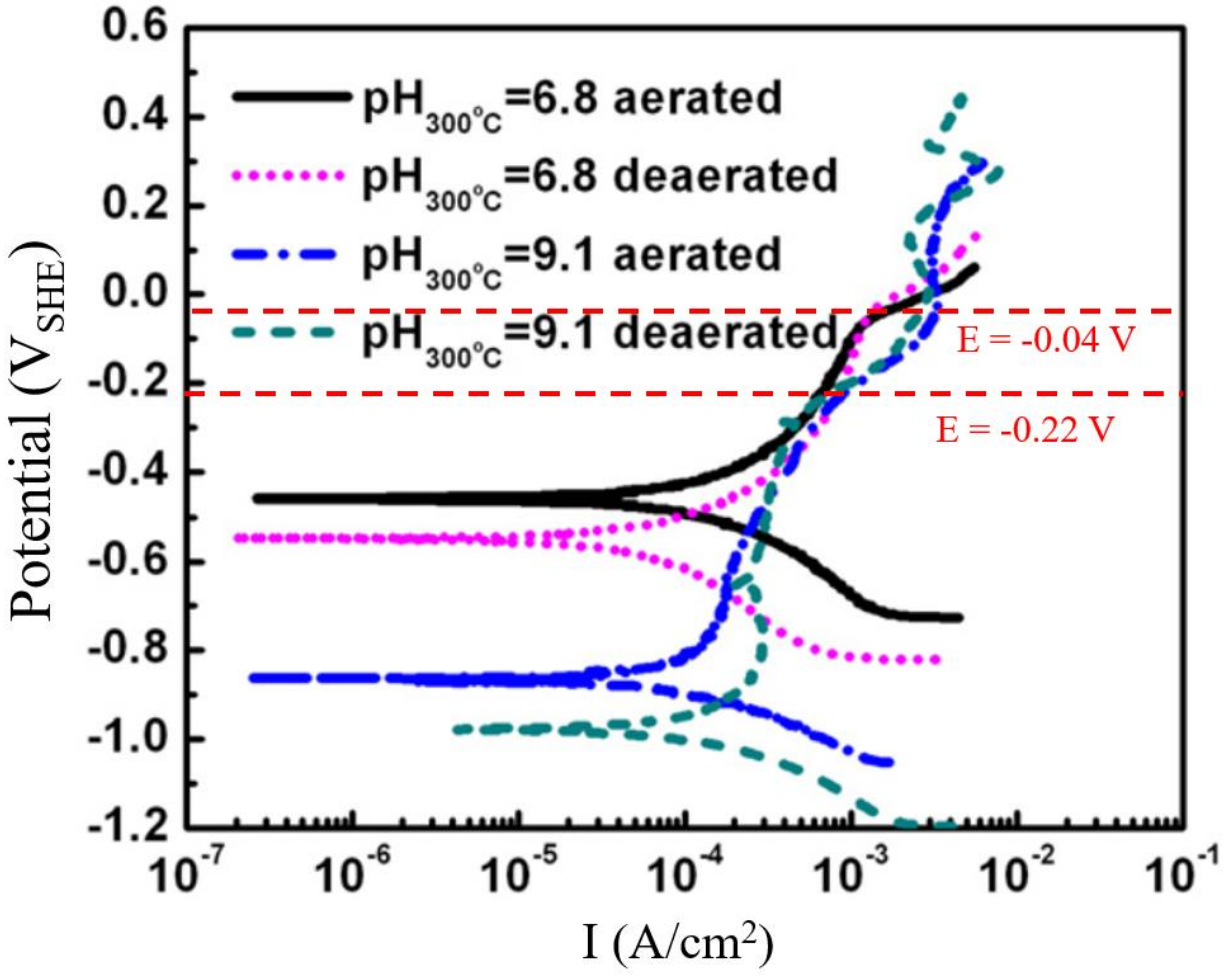

Figure 6.19. Potentiostatic polarization curve of 304 stainless steel in 300˚C water at pH=6.8 and 9.1 after 48 hrs measured by Sun et al.[19] Line showing the calculated $FeCr_2O_4$ / $HCrO_4^-$ phase boundaries at each pH are added.

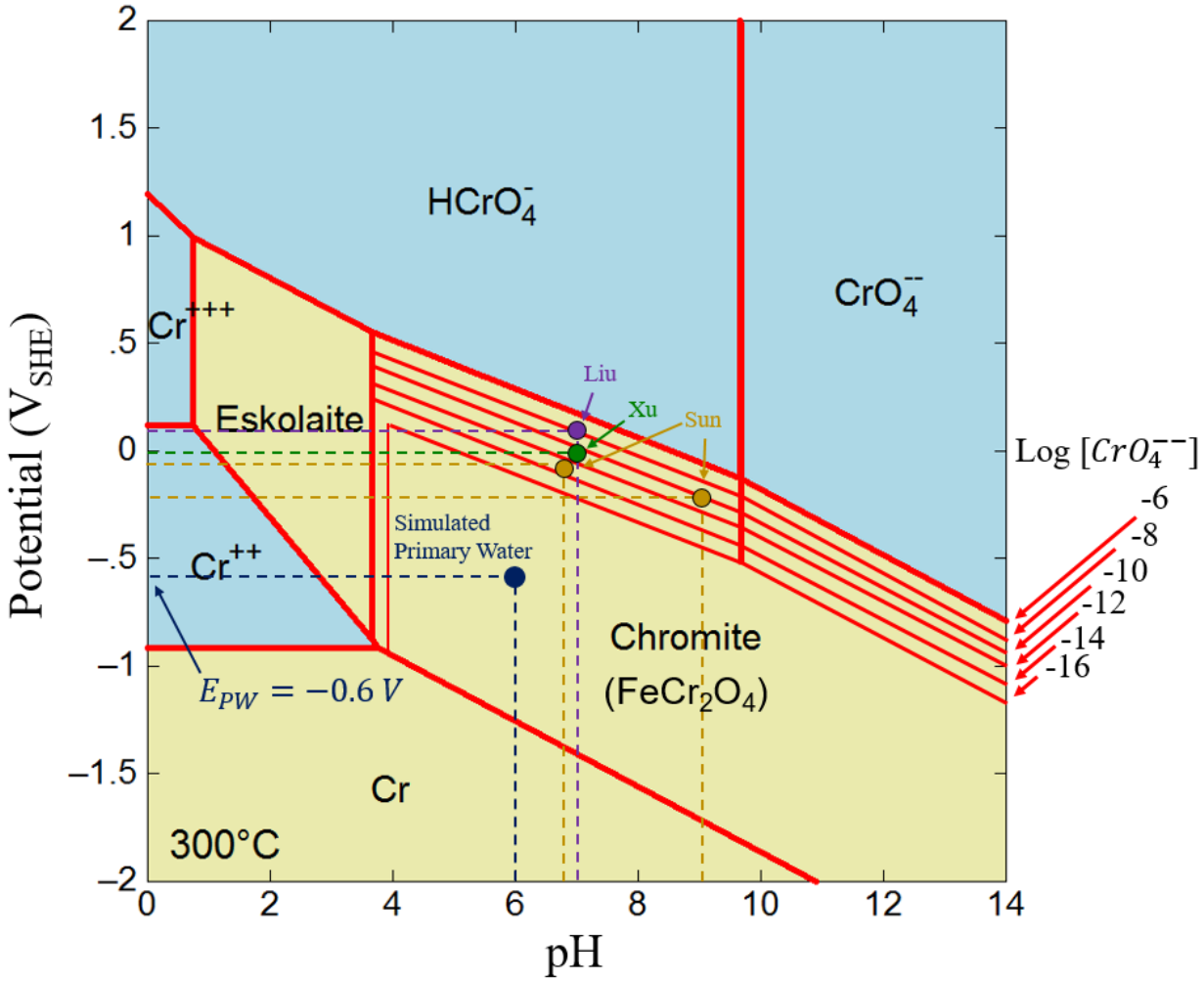

Figure 6.20. Pourbaix diagram of chromium in the Fe-Cr system in 300˚C water, calculated with Geochemists' Workbench 11[110]. Ionic species are set to an activity of 10^{-6}. Additional lines are drawn for the upper phase boundary of chromite at decreasing CrO_4^{2-} activity. Blue guide lines indicate primary water conditions. Literature data showing the potential and pH at which passive regions transitioned to transpassive regions are indicated in purple, green, and brown for Liu[141], Xu[59], and Sun[19], respectively. Note: Sun data was taken at 250˚C.

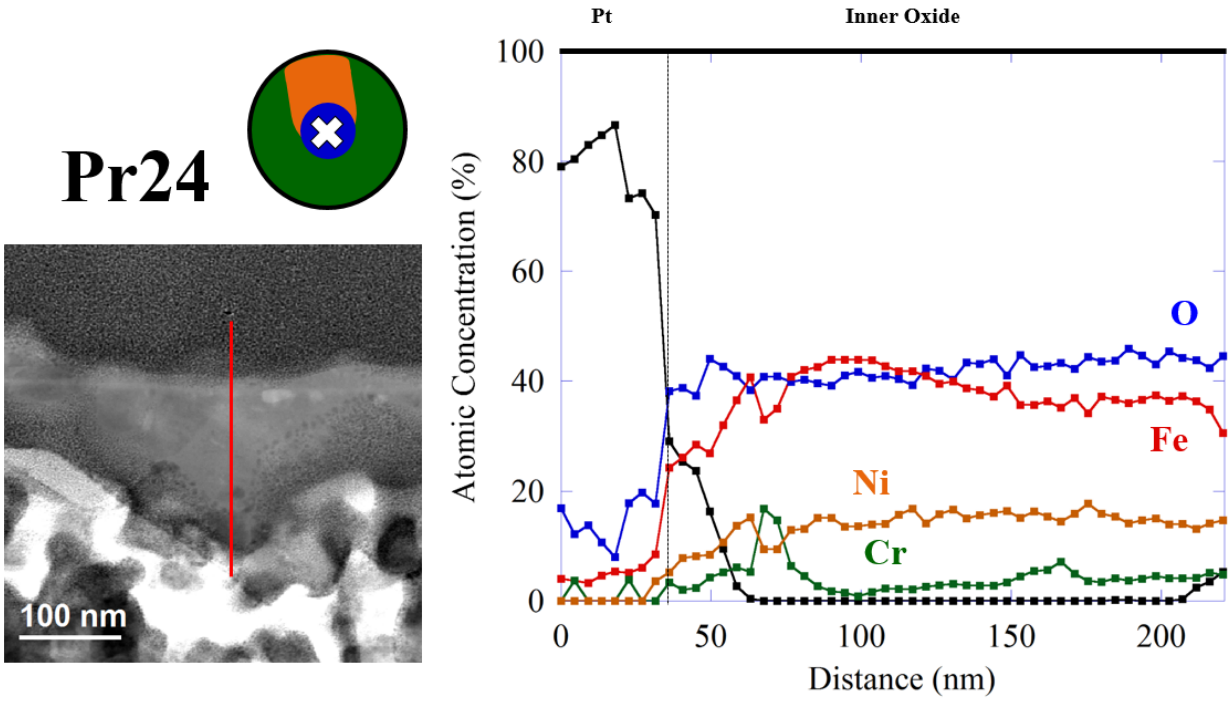

Figure 6.21. Cross sectional atomic composition of a non-porous inner oxide on the irradiated region of sample Pr24, measured by STEM-EDS. Note that the scan ends in the milled-away porous oxide, and does not continue into the metal, as with most STEM-EDS scans in this work.

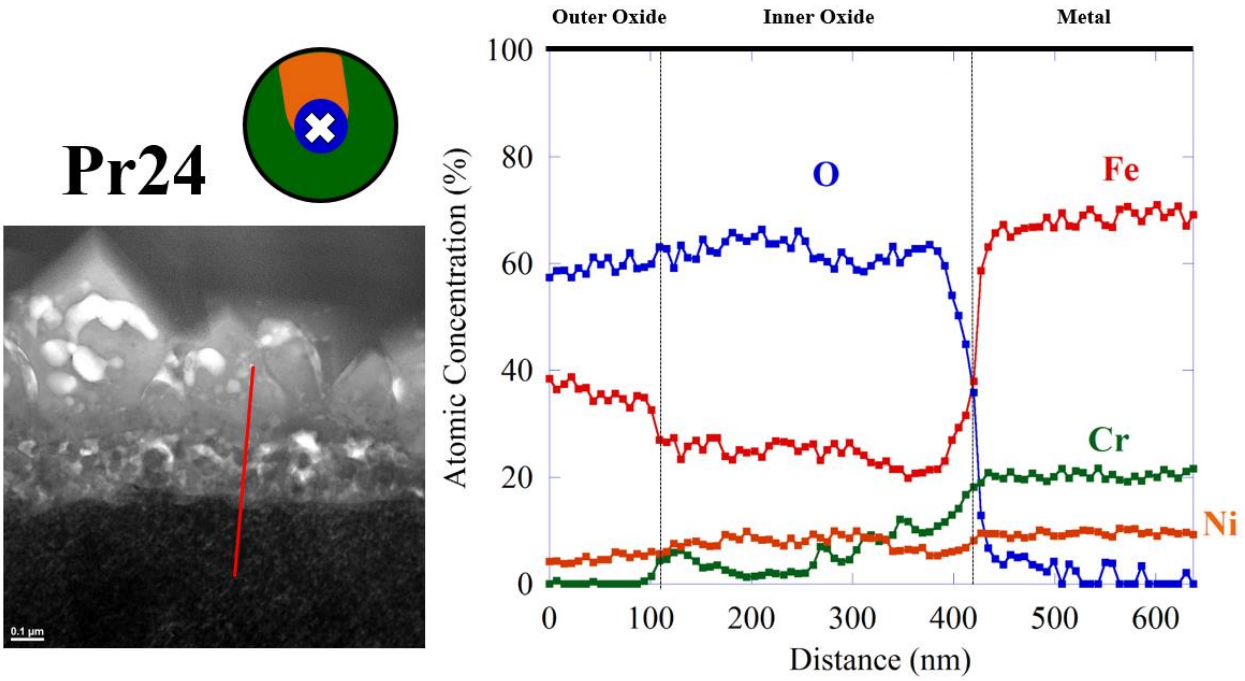

Figure 6.22. Cross sectional atomic composition of a porous inner oxide on the irradiated region of sample Pr24, measured by STEM-EDS.

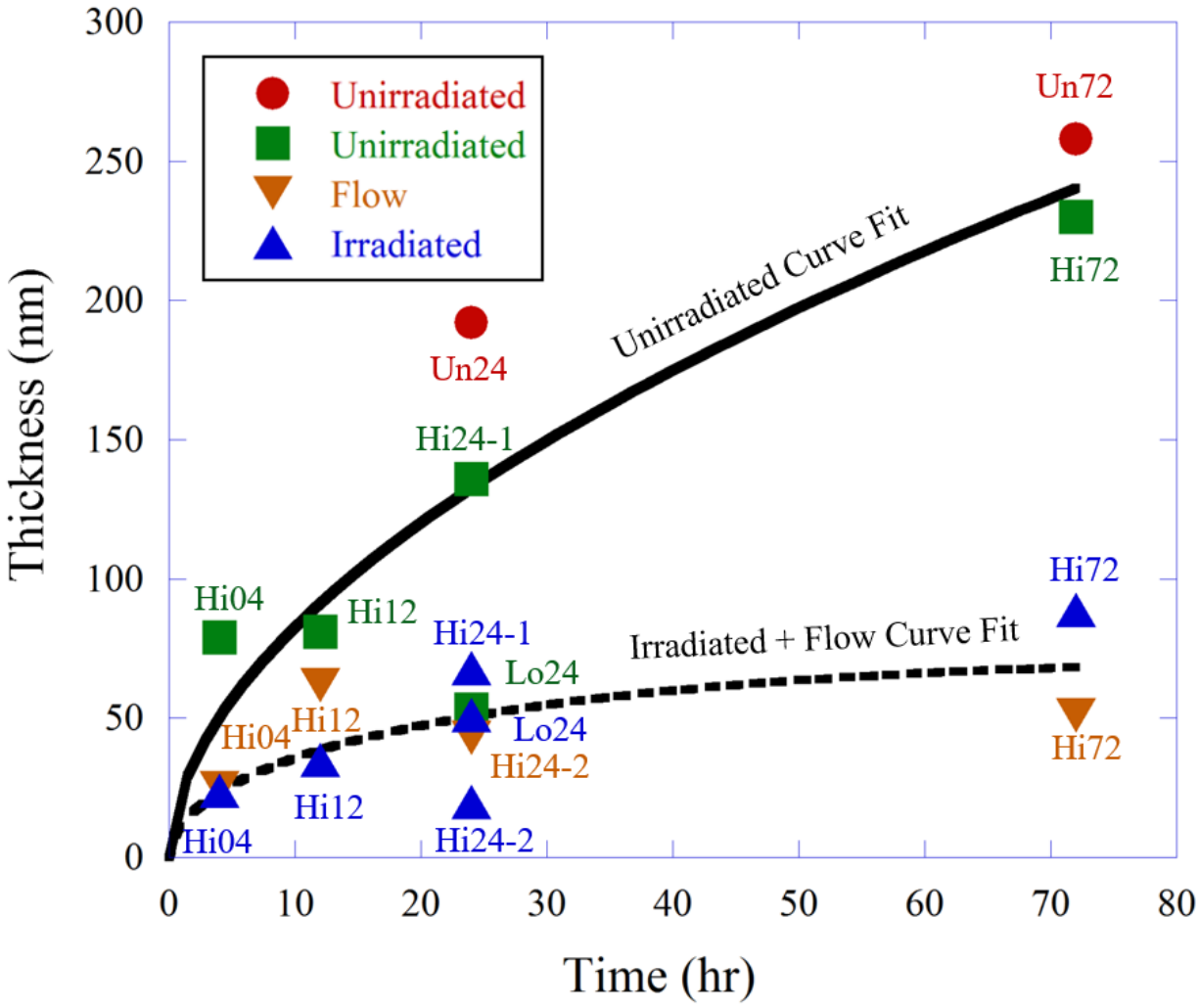

Figure 6.23. Average inner oxide thickness of the irradiated, flow, and unirradiated regions of samples used in this study, with fitted curves. The red circles indicate data points from unirradiated samples, while the green circles are indicate specimens taken from the unirradiated areas of irradiated samples.

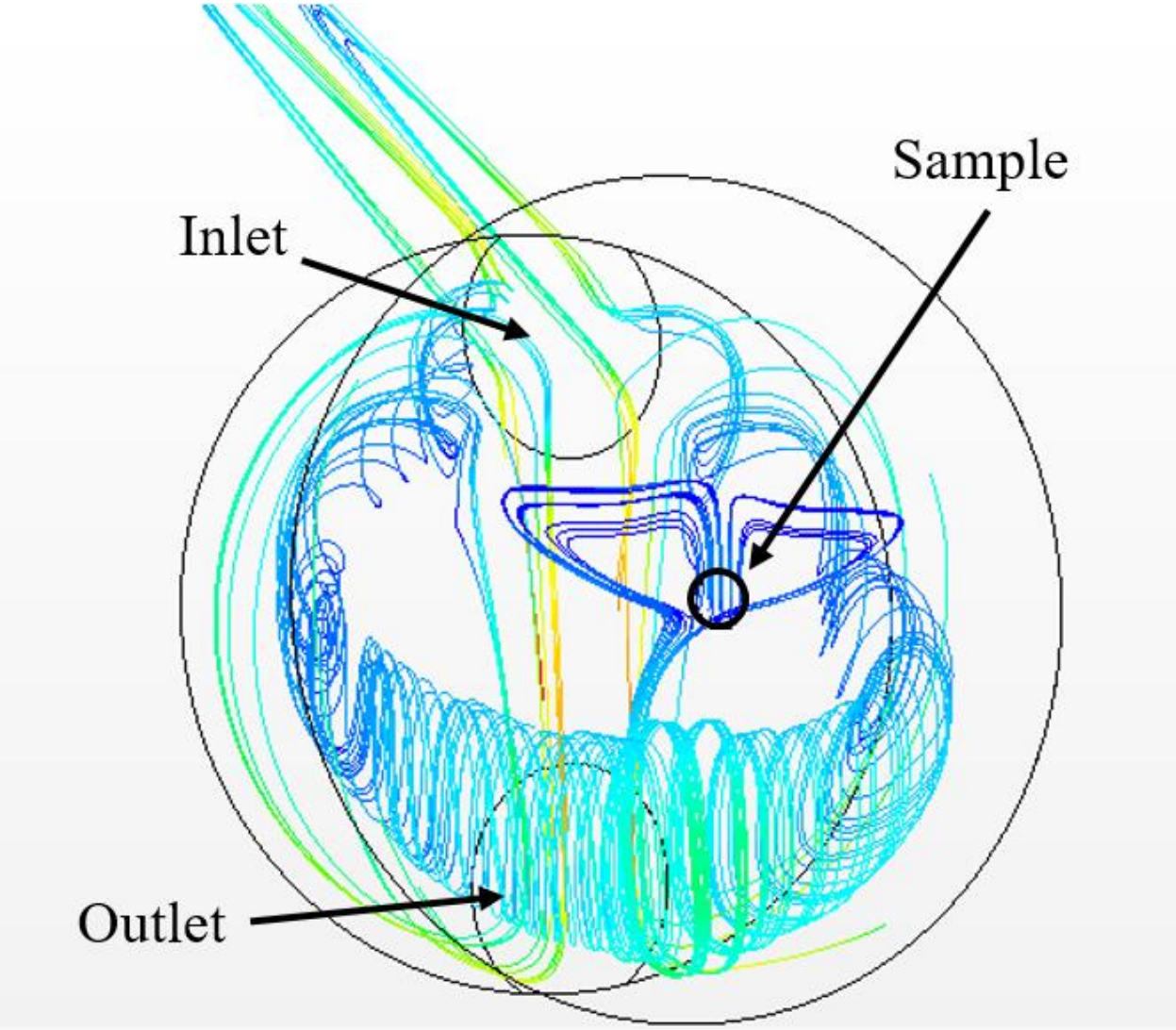

Figure 6.24. Computational fluid dynamics model showing the direction and velocity of fluid flow in the corrosion cell during irradiation at 10 μA/cm^2. Streamlines are color coded blue (fast) through red (slow)[127]

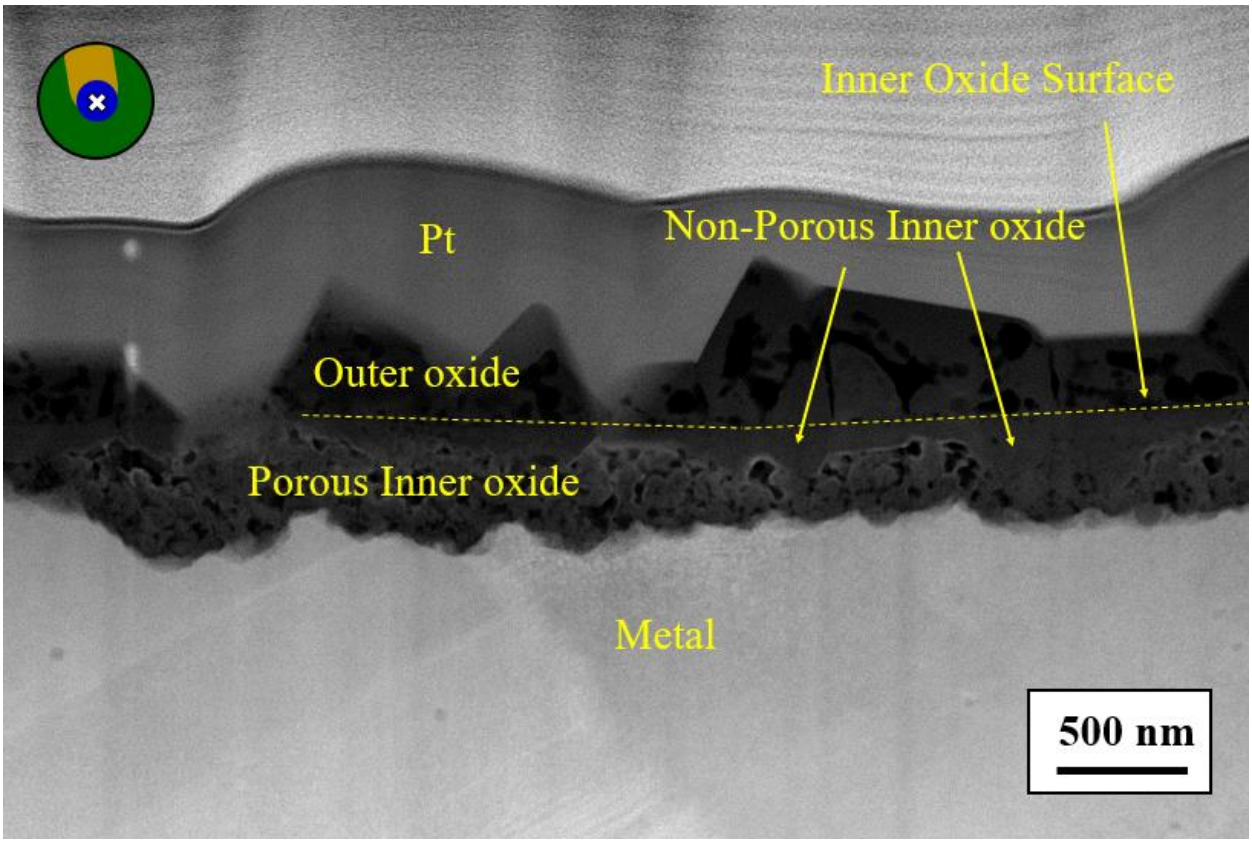

Figure 6.25. HAADF image of the oxide on the irradiated region of sample Pr24, highlighting the porous and non-porous sections of the inner oxide

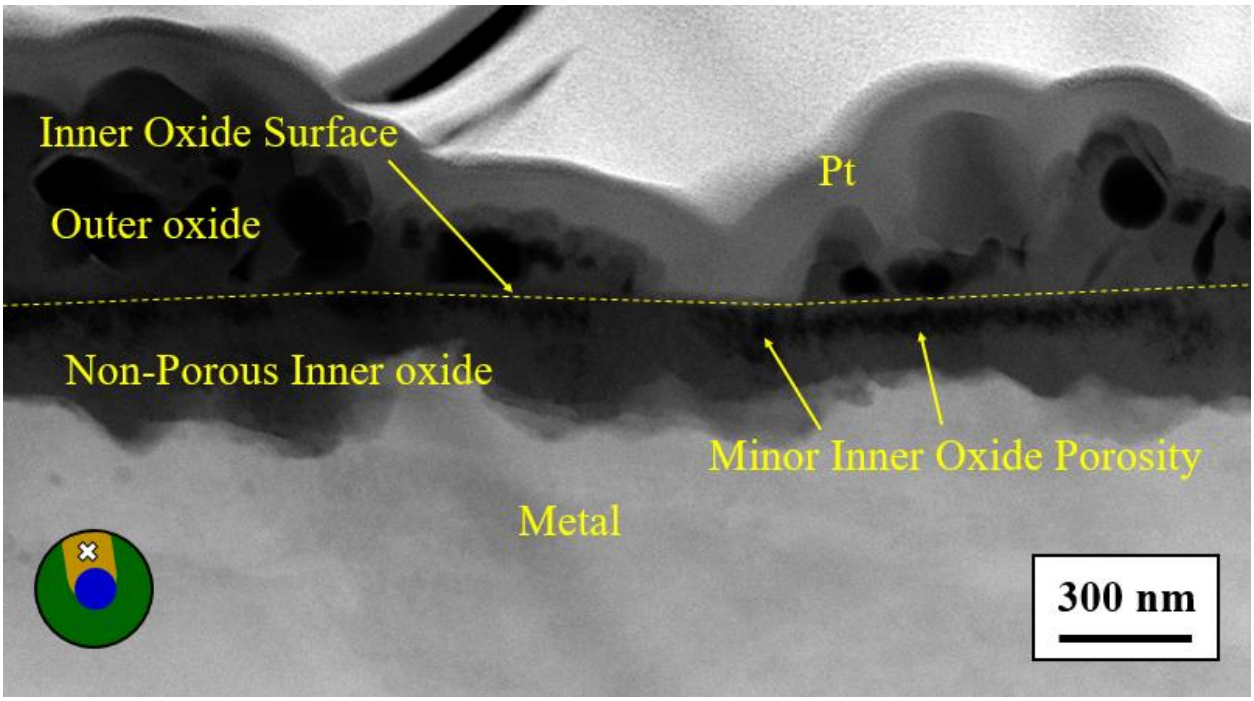

Figure 6.26. HAADF image of the oxide on the flow region of sample Pr24, showing minor inner oxide porosity near the solution interface

CHAPTER 7 - CONCLUSIONS

This work has reached the following conclusions:

1. *Irradiation caused an increase in ECP*. Hematite was observed on the irradiated regions of all irradiated samples except Hi04 (which displayed only early signs of hematite formation), and on the flow regions of all irradiated samples. The presence of hematite indicates elevated corrosion potential at the oxide-solution interface. Reaction modeling, and Pourbaix diagrams predict a phase boundary between magnetite and hematite at approximately -0.3 mV_{SHE}. Outer oxides on areas exposed to radiolyzed water showed an increase in equiaxed crystals, consistent with the formation of hematite. Radiolysis models showed that H_2O_2 production is sufficient to raise ECP past the magnetite-hematite phase boundary.
2. *Elevated corrosion potential due to radiolysis caused changes in spinel oxide stability*. Raman spectroscopy showed shifts in the spinel A_{1g} peak. Unirradiated oxides exhibited a spinel A_{1g} peak between the characteristic modes of magnetite and chromite. The unirradiated regions of samples Hi24 and Hi72 had spinel A_{1g} peaks shifted up toward the characteristic mode of trevorite, attributed to the dissolution of magnetite. The irradiated and flow regions of sample Hi04 also saw a shift up, attributed to the dissolution of magnetite and chromite. The flow and irradiated regions of samples Hi12, Hi24, and Hi72 had spinel A_{1g} peaks shifted down, attributed to the dissolution of chromite, and to

greater outer oxide coverage leading to a stronger magnetite signal. Radiolysis models also showed that the production of oxidizing species is sufficient to cause the necessary dissolution reactions.

3. *Exposure to irradiated water causes a loss of inner oxide chromium, leading to a decrease in passive behavior.* STEM-EDS and Raman data showed chromium was depleted in the inner oxides of the irradiated and flow regions of all samples except Pr24, on which chromium was only depleted on the inner oxide of the irradiated region. Enhanced dissolution of Cr-rich spinel oxides to form aqueous $HCrO_4^-$ is proposed as a mechanism of chromium depletion of the inner oxide. Chromium spinels are thermodynamically and kinetically more stable than iron spinels, and as a result, are responsible for the passive region on stainless steel. The decrease in inner oxide chromium implies a loss of oxide protectiveness and accelerated oxidation kinetics.
4. *The rate of oxide dissolution increases due to irradiation*. Oxides on irradiated and flow regions were more porous than unirradiated oxides. It is hypothesized that enhanced dissolution due to the depletion of inner oxide chromium is responsible for the increased porosity. Oxides were thinner on irradiated and flow regions than on unirradiated regions, which implies heightened rates of oxide dissolution resulting in a thinner scale. The decreased porosity on the irradiated region of sample Pr24, and lack of porosity on the flow region show that a pre-grown oxide scale can lessen oxide dissolution, and suggests that irradiation prevented a protective film from forming on the samples that were not pre-oxidized.
5. *Radiolysis was found to be the main driver of irradiation accelerated corrosion*. Flow regions on all samples except Pr24 were found to be similar to the irradiated regions,

exhibiting outer oxides with significant hematite, and inner oxides that were thinner, more porous, and depleted in chromium when compared to unirradiated oxides. Since the flow regions were not directly irradiated, the presence of these phenomena in the flow regions indicates radiolysis is the cause. A thermodynamic mechanism was identified to explain chromium depletion in the inner oxides, and it was found to be consistent with modeled radiolysis yields for this experiment.

6. *A pre-grown oxide scale is effective at slowing oxide growth and dissolution*. The inner oxides on the irradiated region on sample Pr24 displayed the effects of oxide dissolution, but they were not observed on the inner oxide of the flow region, despite both regions showing signs of increased potential. This showed that a preformed oxide scale can slow chromium depletion and oxide dissolution. The loss of chromium from the preformed film in the irradiated region and not elsewhere may be an indication of the effect of an elevated diffusion coefficient due to athermal displacement mixing.

APPENDIX A - MILL CERTIFICATION

Mill Certification for the sample material used in this work

Zapp Precision Strip, Inc. 12533 Clark Street, Santa Fe Springs, CA 90670

BS&B SAFETY SYSTEMS, INC.
7455 E. 46th Street
TULSA OK 74145

Zapp Precision Strip, Inc.
12533 Clark Street
Santa Fe Springs, California
90670
Phone+1 562-944-5484
Fax+1 562-944-1874
Tollfree 888-236-0004
www.zapp.com

Member of the Zapp Group

March 13, 2012

Inspection certificate Type 3.1 per EN 10204:2004

Certificate No.	**2210032213000030 01**
Your purchase Order	159284 dated March 01, 2012
Sales Order	2302019199 Delivery Note 2210032213
Production Lot	2597751 Inspection Lot 020000229918
Item 30	STAINLESS STEEL
Grade / Alloy	SS316/316L
Dimensions	0.0020 " X 24.0000 "
Thickness tolerance	-0.00010 " / 0.00010 "
Width tolerance	0.00000 " / 0.06250 "
Conditions	ANN
Surface	BA
Edge	slit edges
Techn. Specification	ASTM A240/A240M-11A
Techn. Specification	SA-240/SA-240M
Specifications	ASTM A 240 ASME SA240
Material	8800692
Customer part no	01-092-05H-00
Quantity / Weight	**51.000 LB**

BSB 5

Chemical composition **Heat 7401444**

C (%)	Si (%)	Mn (%)	S (%)	P (%)	Cr (%)
0.019	0.500	1.40	0.0004	0.0290	16.77
Ni (%)	**Mo (%)**	**Cu (%)**	**N (%)**	**Co (%)**	
10.28	2.08	0.300	0.020	0.130	

Melt Source AK Steel - US

Quality inspection results

Tensile Strength	93.0 KSI
.2% Yield Strength	38.0 KSI
Elongation 2"	51.70 %
Grain Size	9.5
Hardness	70.0 HRB

Batch DC13364044

L-576

159284-5

This material is melted and produced in the United States and meets the

APPENDIX B - WATER DATA

Note: Water data was not recorded for unirradiated exposures, so only irradiated experiments are included in this appendix.

Hi04

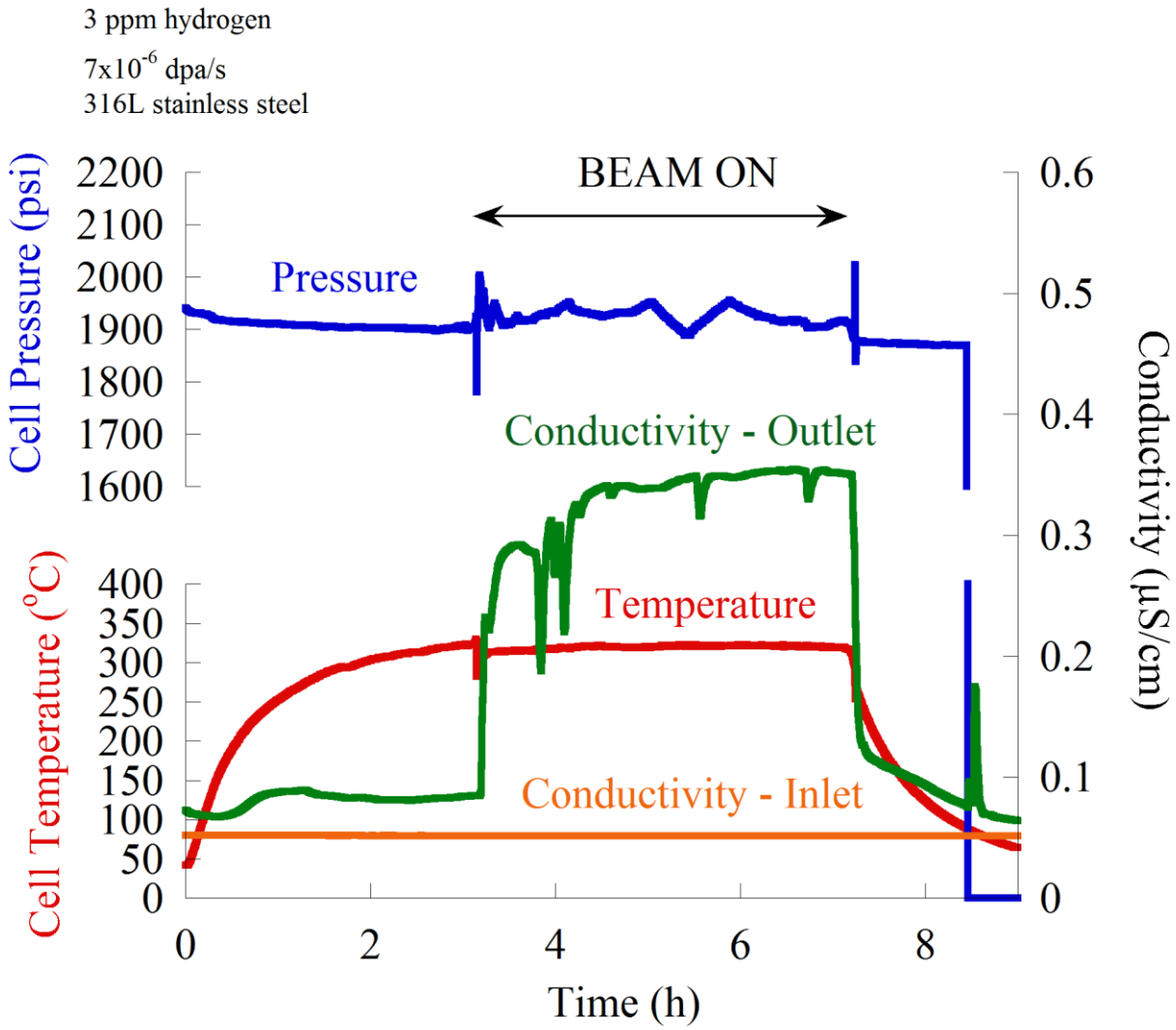

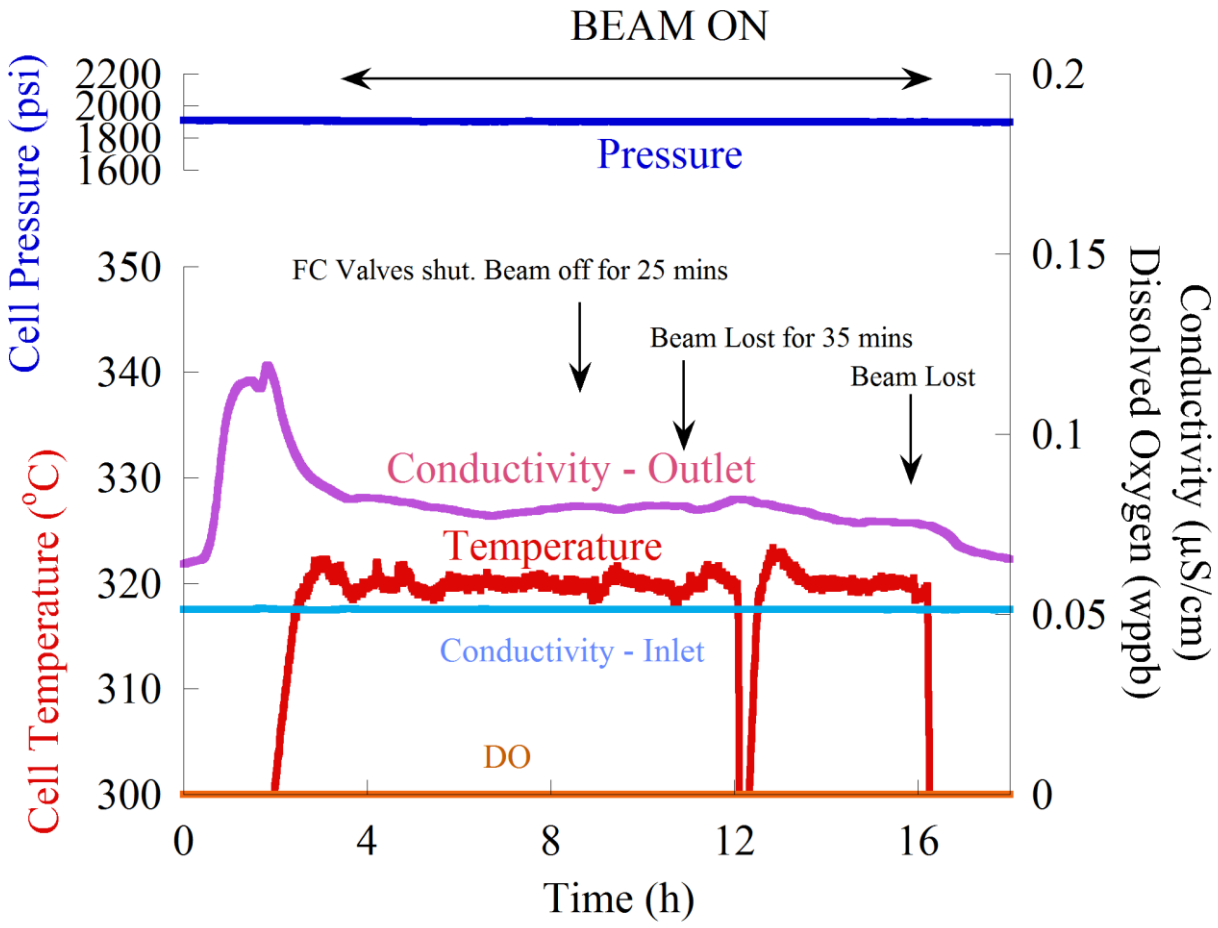
BEAM ON
Cell Pressure (psi)
2200
2000
1800
1600
Pressure
FC Valves shut. Beam off for 25 mins
Beam Lost for 35 mins
Beam Lost
Conductivity - Outlet
Temperature
Conductivity - Inlet
DO
Cell Temperature (°C)
350
340
330
320
310
300
0.2
0.15
0.1
0.05
0
Dissolved Oxygen (wppb)
Conductivity (µS/cm)
0
4
8
12
16
Time (h)

Hi24-1

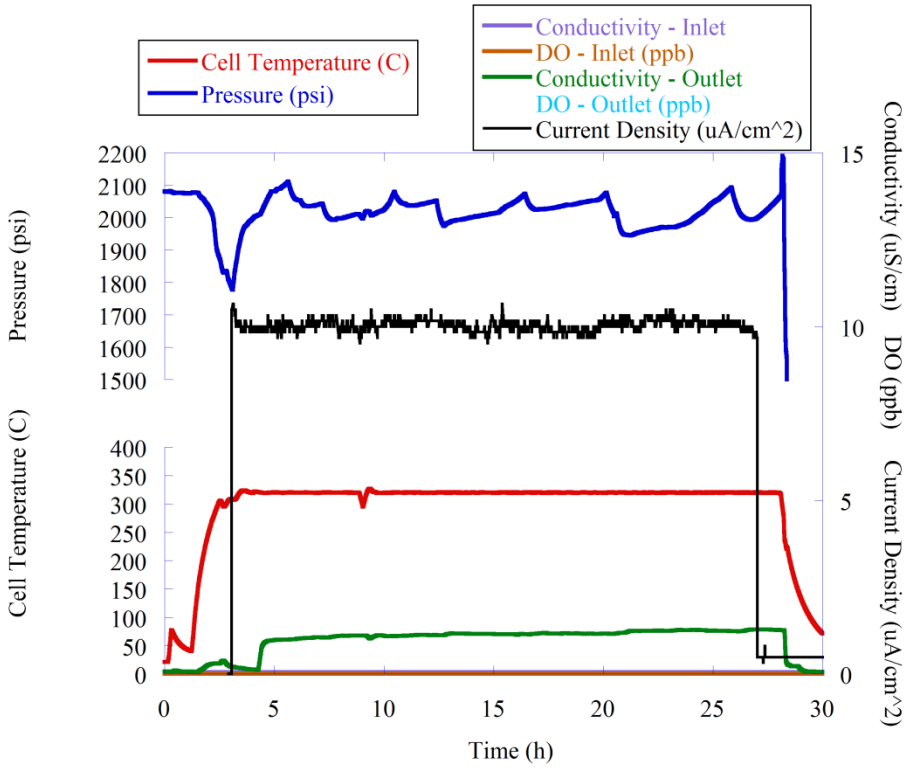
Cell Temperature (C)
Pressure (psi)
Conductivity - Inlet
DO - Inlet (ppb)
Conductivity - Outlet
DO - Outlet (ppb)
Current Density (uA/cm^2)
Pressure (psi)
Cell Temperature (C)
Conductivity (uS/cm)
DO (ppb)
Current Density (uA/cm^2)
Time (h)

Hi24-2

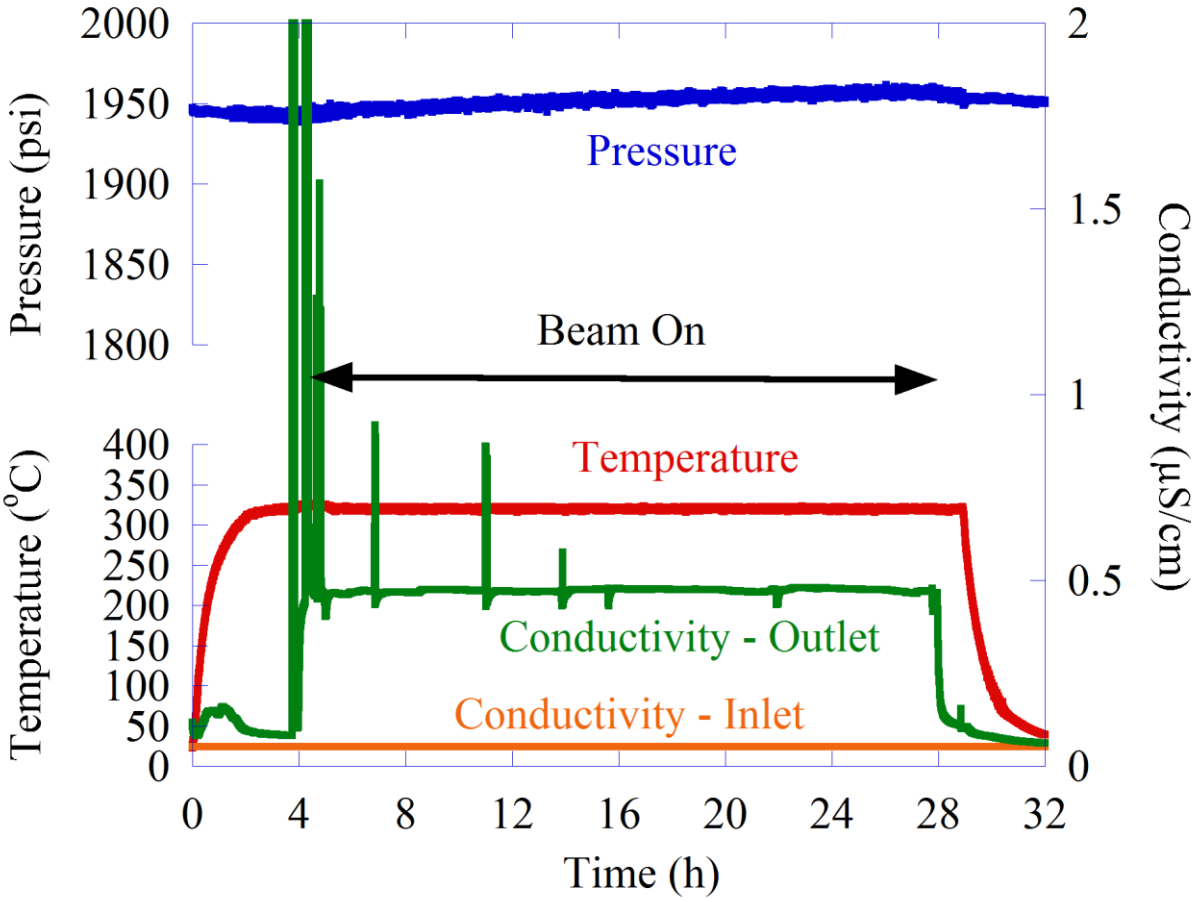
Pressure (psi)
2000
1950
1900
1850
1800
Pressure
Beam On
Temperature (°C)
400
350
300
250
200
150
100
50
0
Temperature
Conductivity - Outlet
Conductivity - Inlet
2
1.5
1
0.5
0
Conductivity (µS/cm)
0
4
8
12
16
20
24
28
32
Time (h)

Lo24

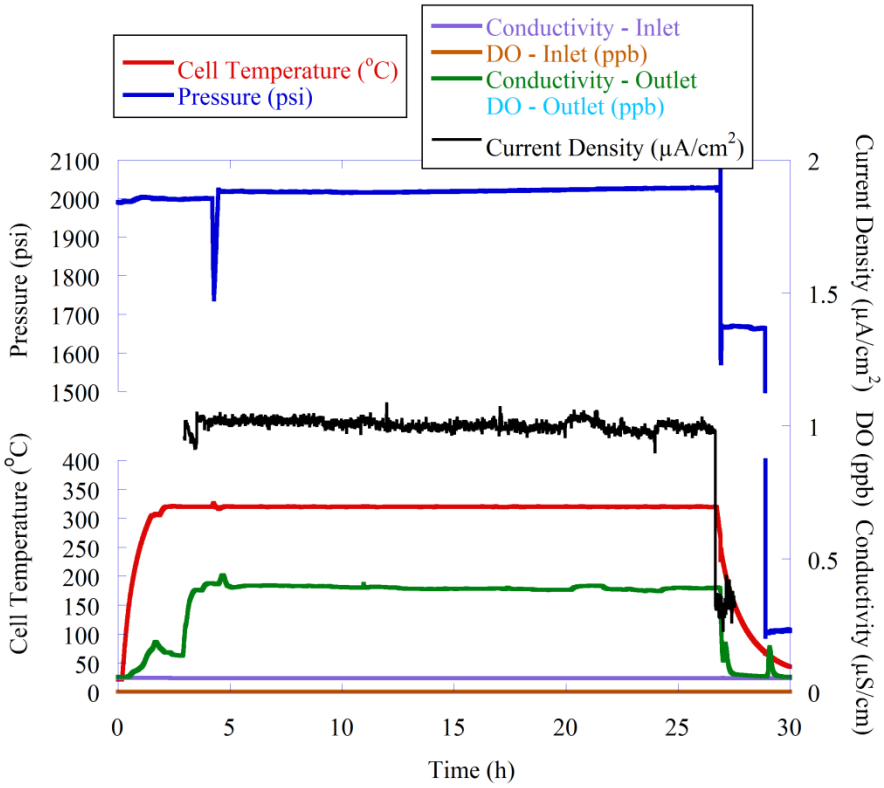
Cell Temperature (°C)
Pressure (psi)
Conductivity - Inlet
DO - Inlet (ppb)
Conductivity - Outlet
DO - Outlet (ppb)
Current Density (µA/cm²)
Pressure (psi)
Cell Temperature (°C)
Current Density (µA/cm²)
DO (ppb)
Conductivity (µS/cm)
Time (h)

Hi72

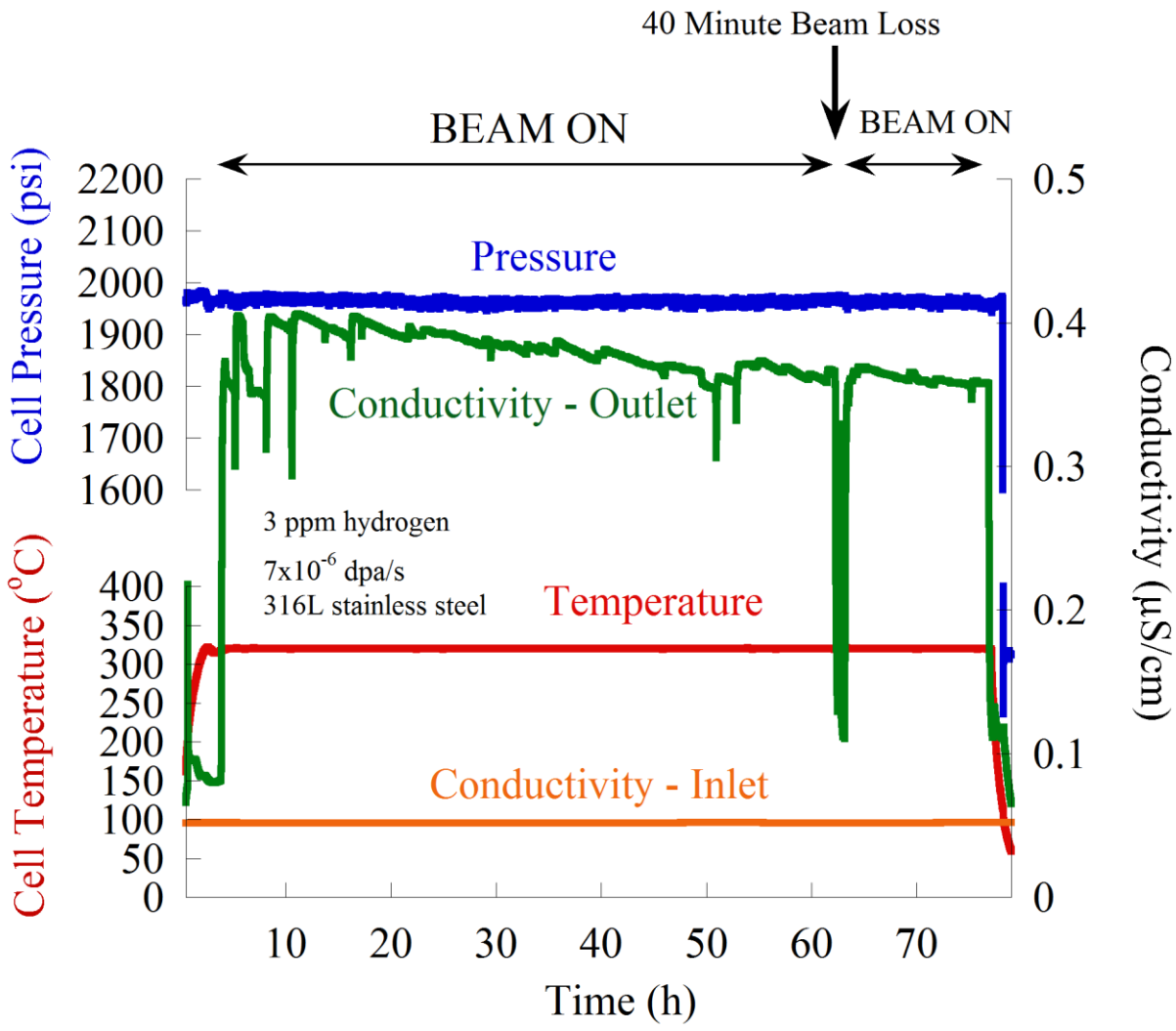
40 Minute Beam Loss
BEAM ON
BEAM ON
Cell Pressure (psi)
Cell Temperature (°C)
Conductivity (µS/cm)
Pressure
Conductivity - Outlet
3 ppm hydrogen
7x10-6 dpa/s
316L stainless steel
Temperature
Conductivity - Inlet
Time (h)
2200
2100
2000
1900
1800
1700
1600
400
350
300
250
200
150
100
50
0
0.5
0.4
0.3
0.2
0.1
0
10
20
30
40
50
60
70

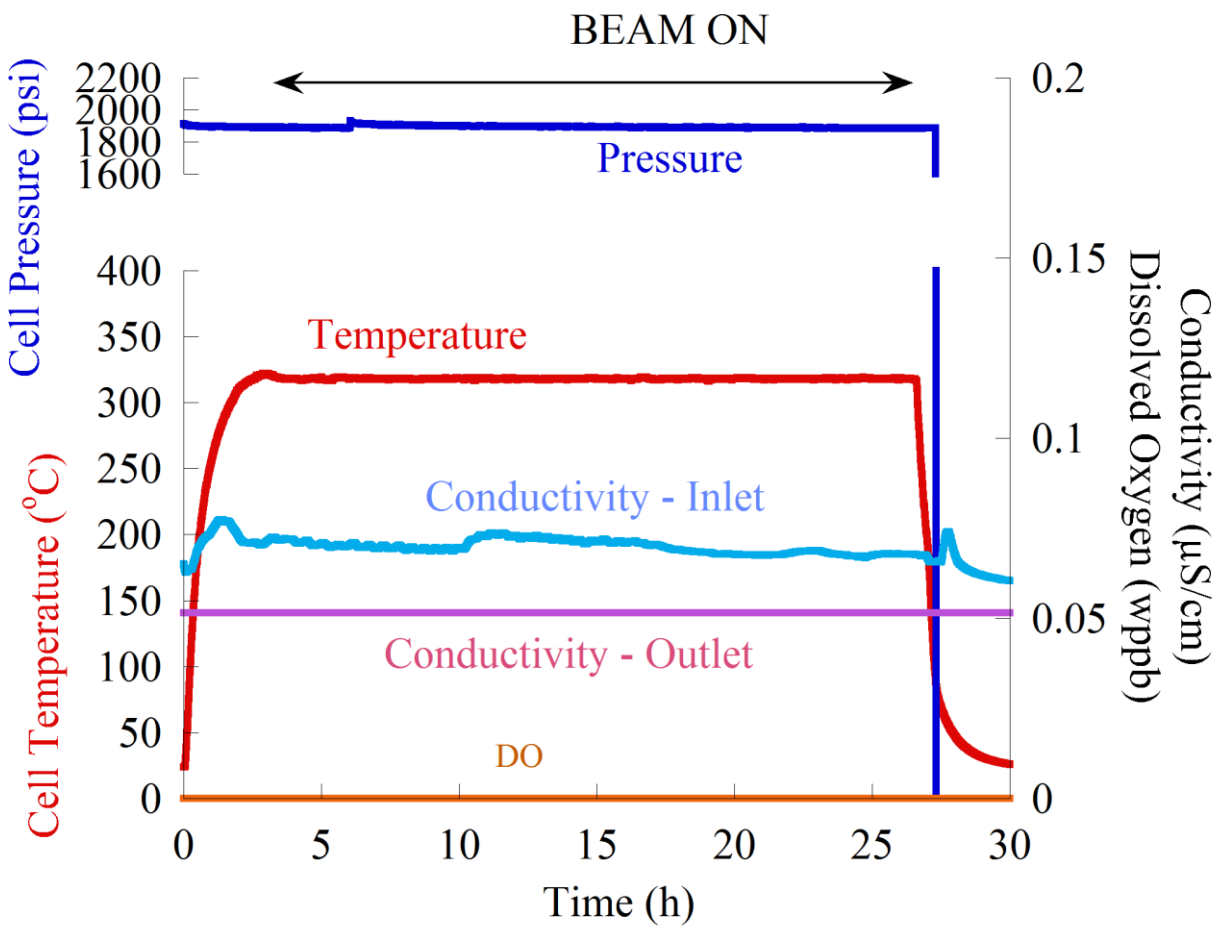
BEAM ON
Cell Pressure (psi)
2200
2000
1800
1600
Pressure
0.2
0.15
0.1
0.05
0
Conductivity (µS/cm)
Dissolved Oxygen (wppb)
400
350
300
250
200
150
100
50
0
Cell Temperature (°C)
Temperature
Conductivity - Inlet
Conductivity - Outlet
DO
0
5
10
15
20
25
30
Time (h)

APPENDIX C - IMAGES USED FOR THICKNESS MEASUREMENT

Hi04 Unirr

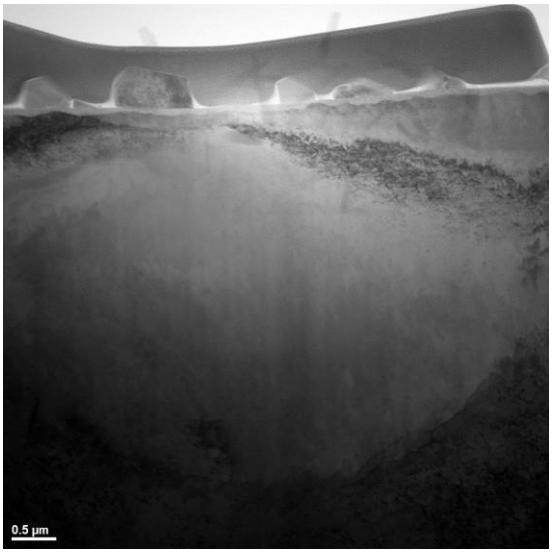

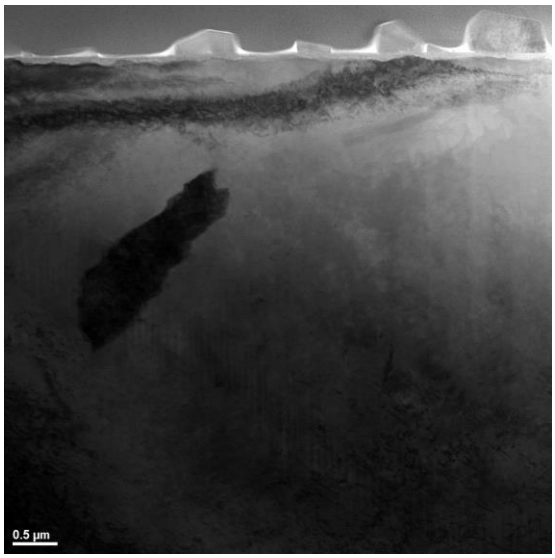

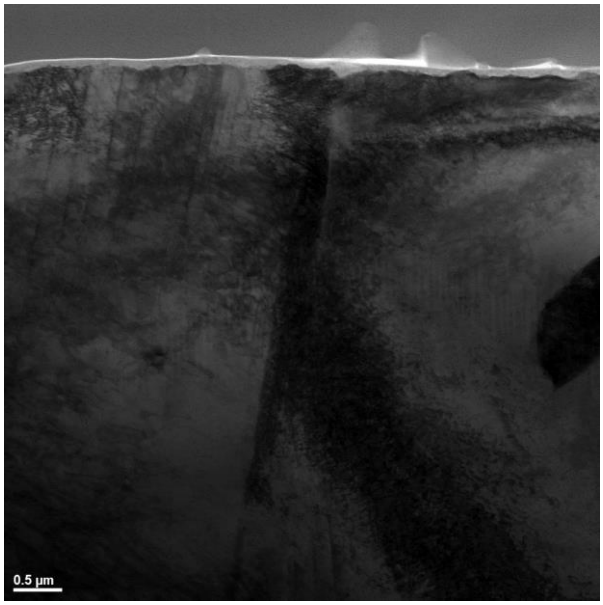
0.5 µm

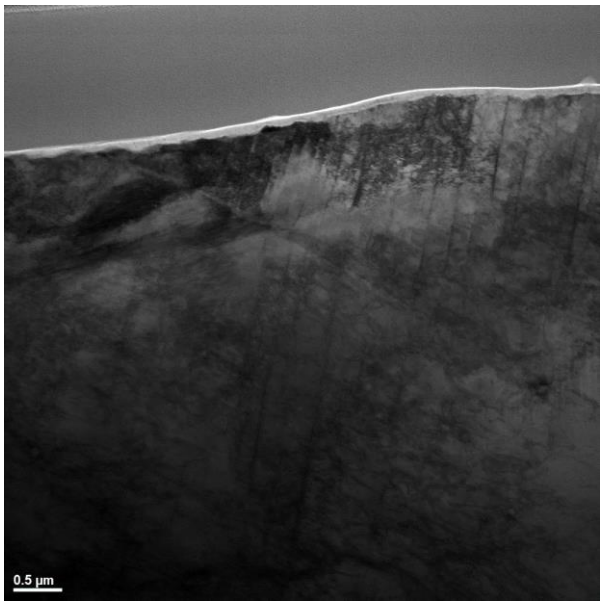
0.5 µm

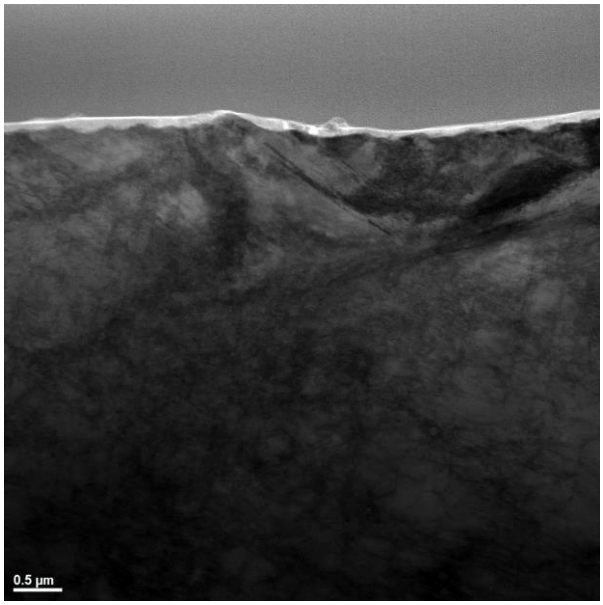
0.5 µm

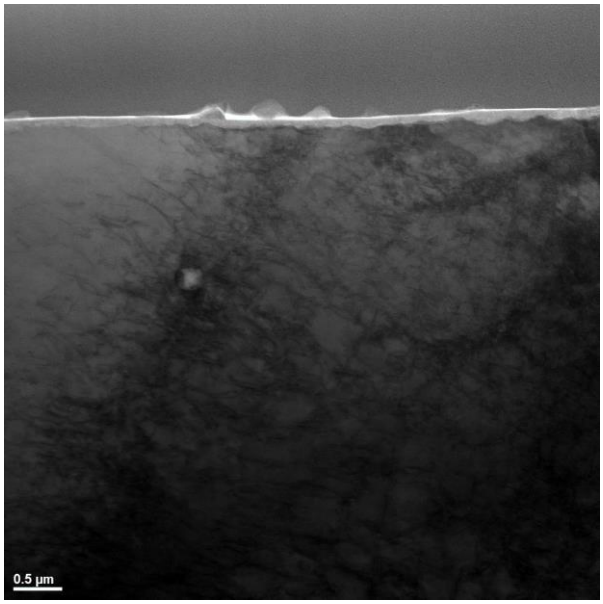
0.5 µm

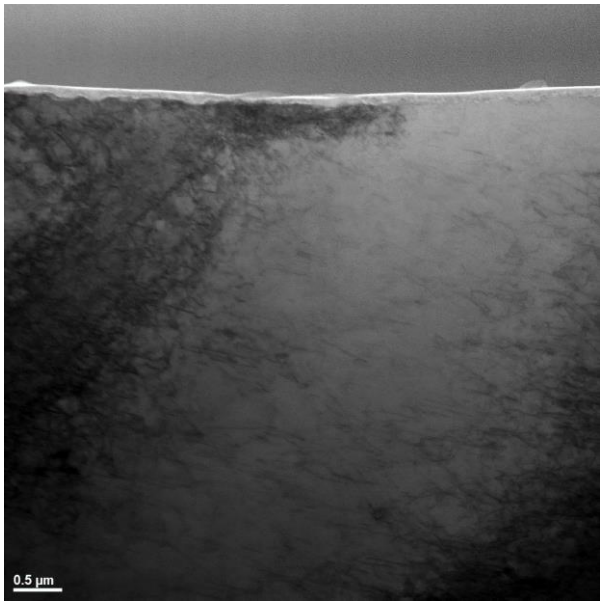
0.5 µm

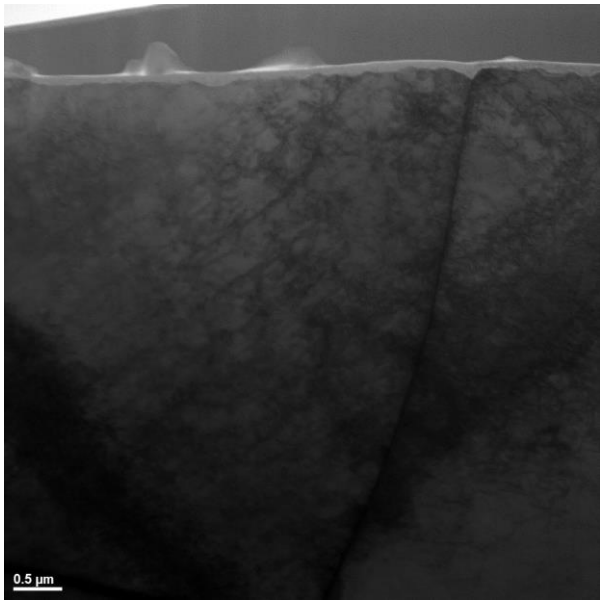
0.5 µm

Hi04 Flow

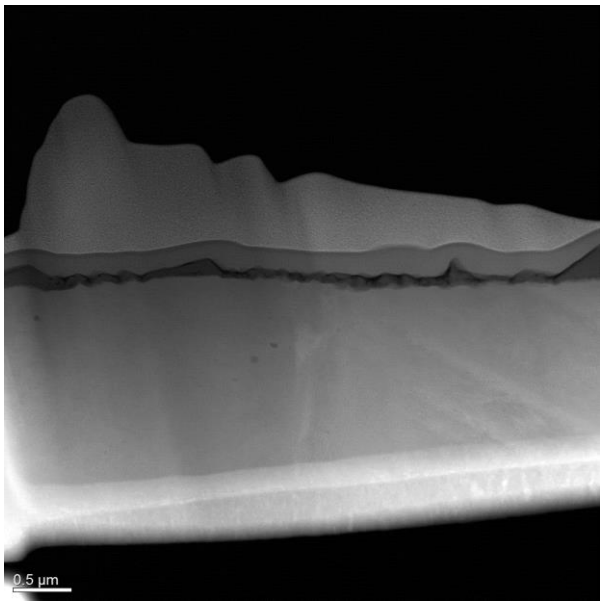

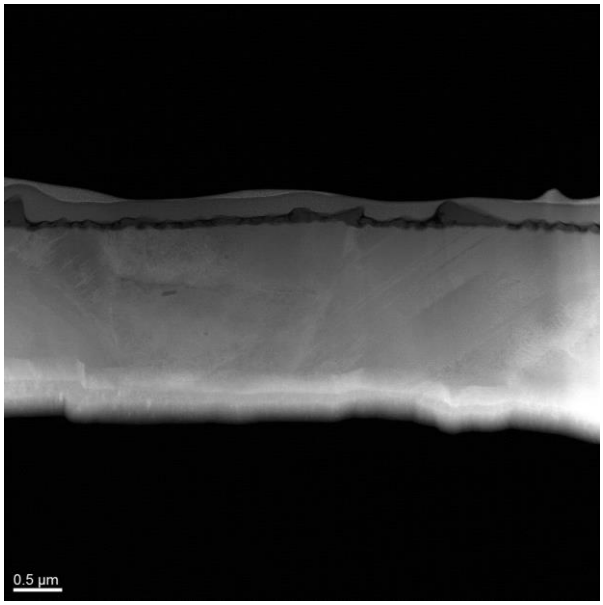

Hi04 Irr

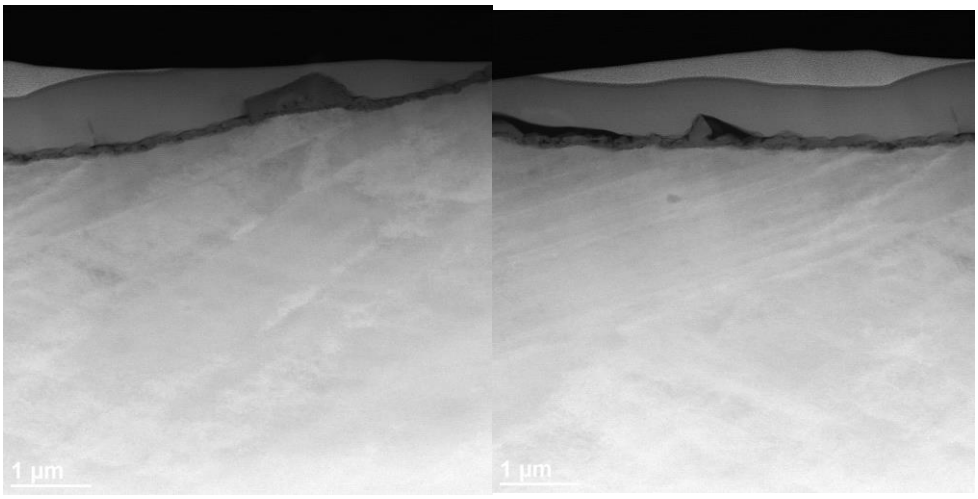

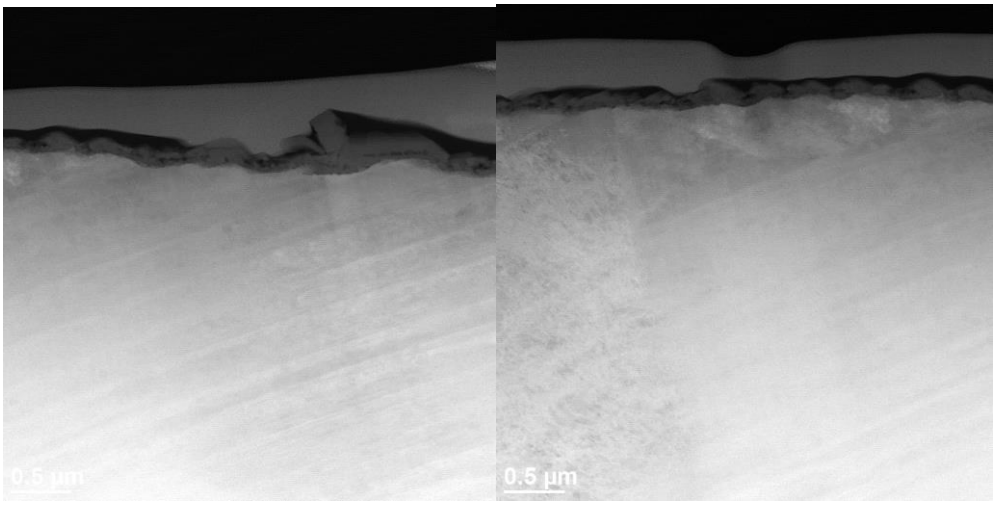

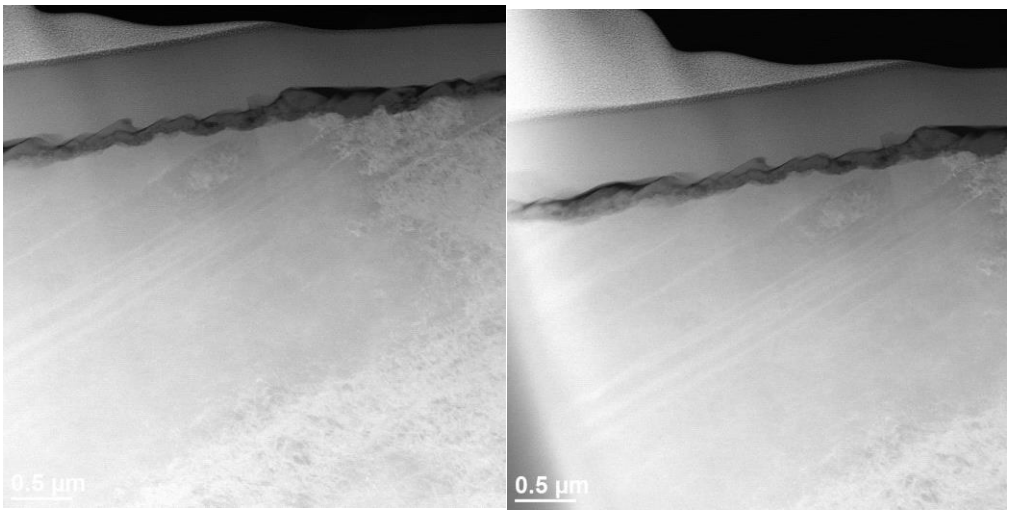

Hi12 Unirr

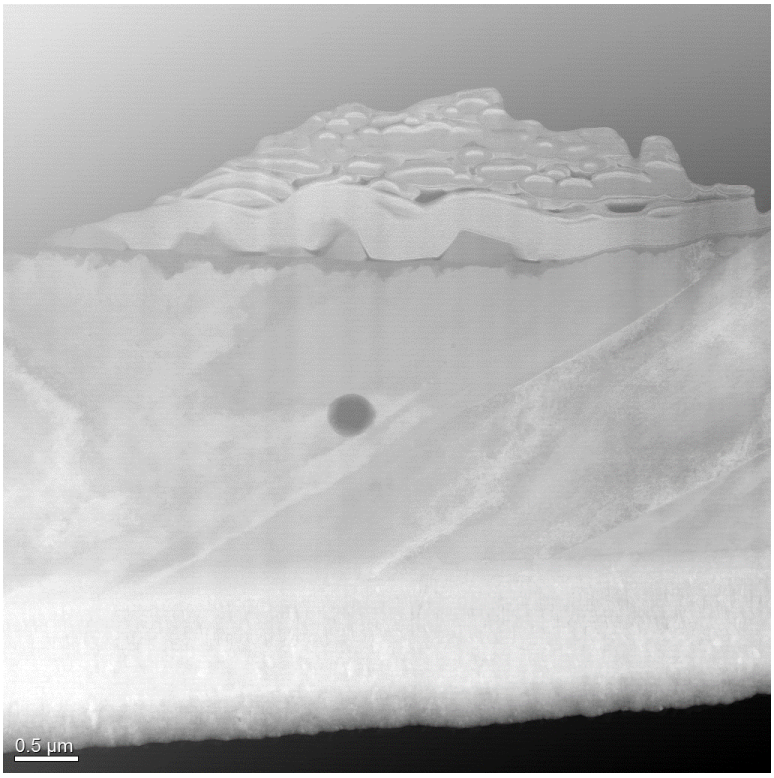

Hi12 Flow

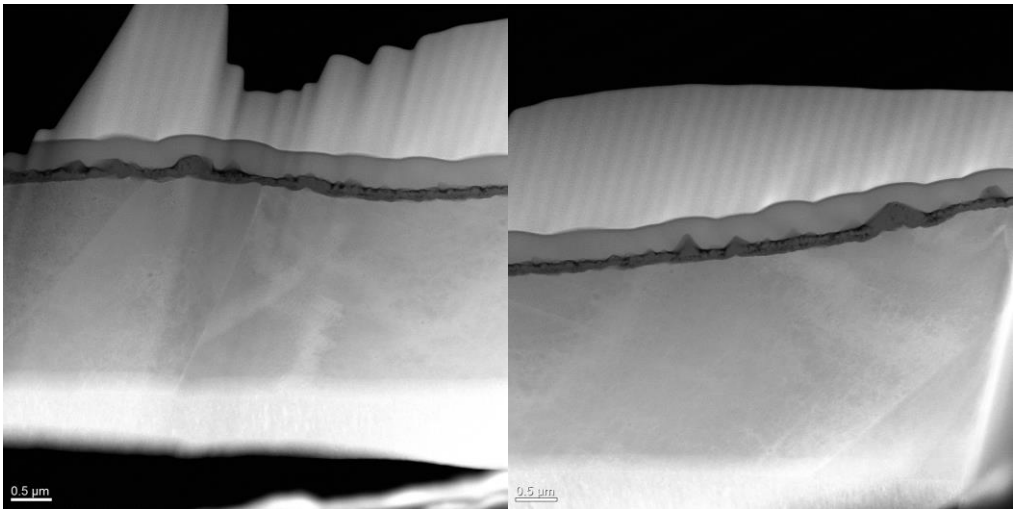

Hi12 Irr

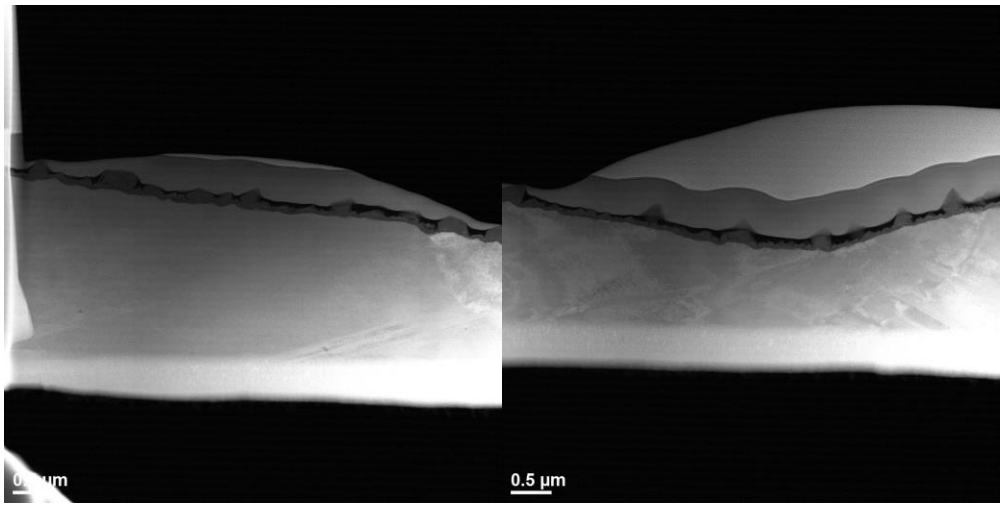

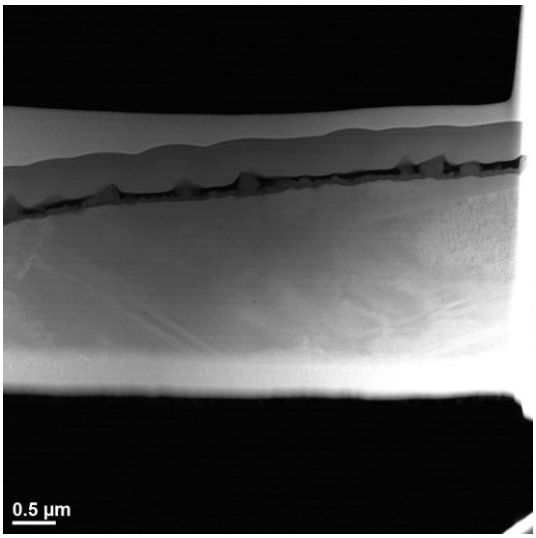

Un24

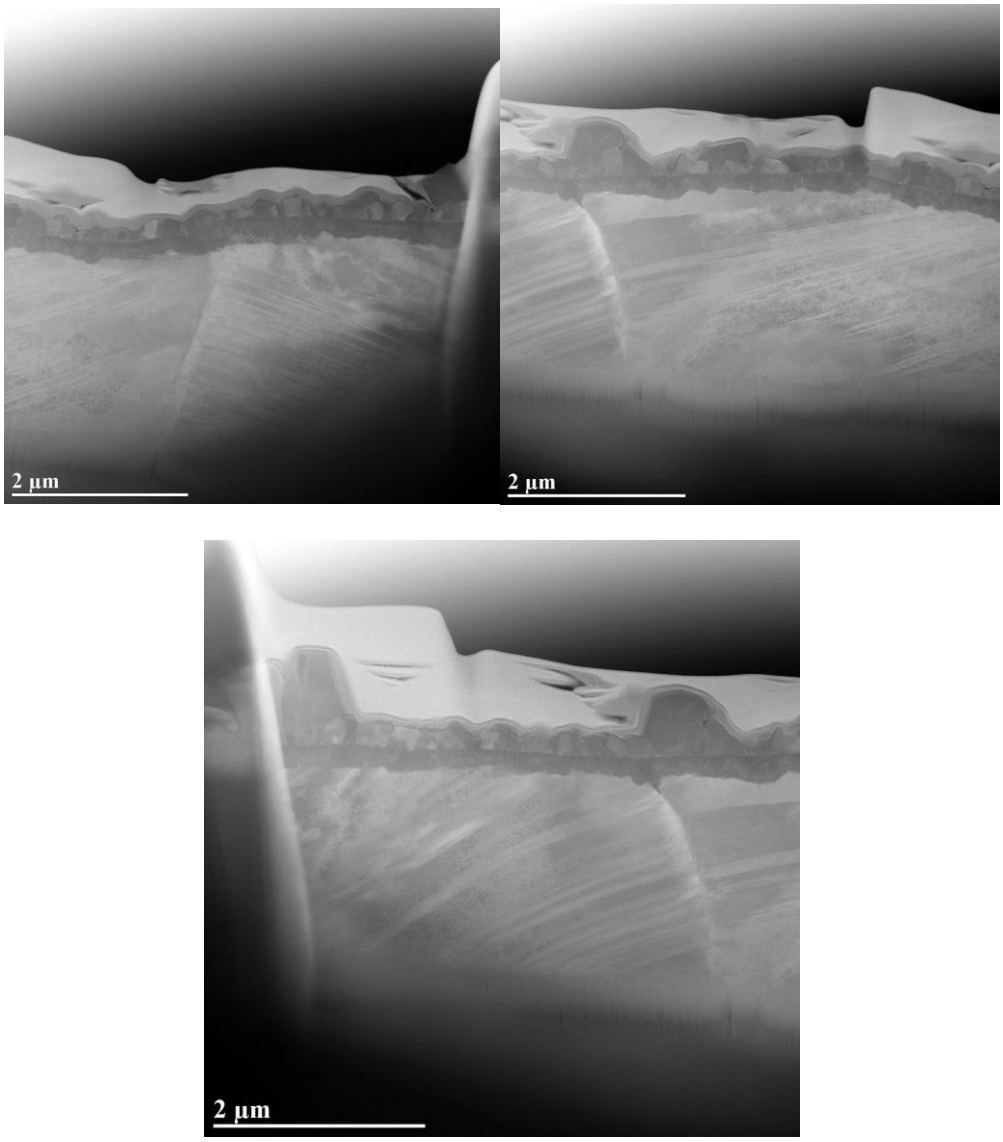

Hi24 Unirr

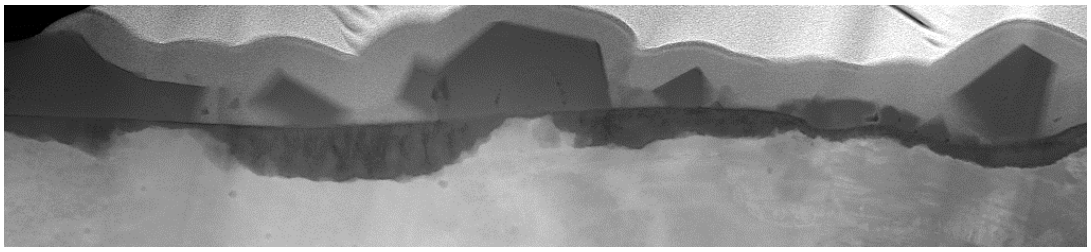

Hi24 Irr

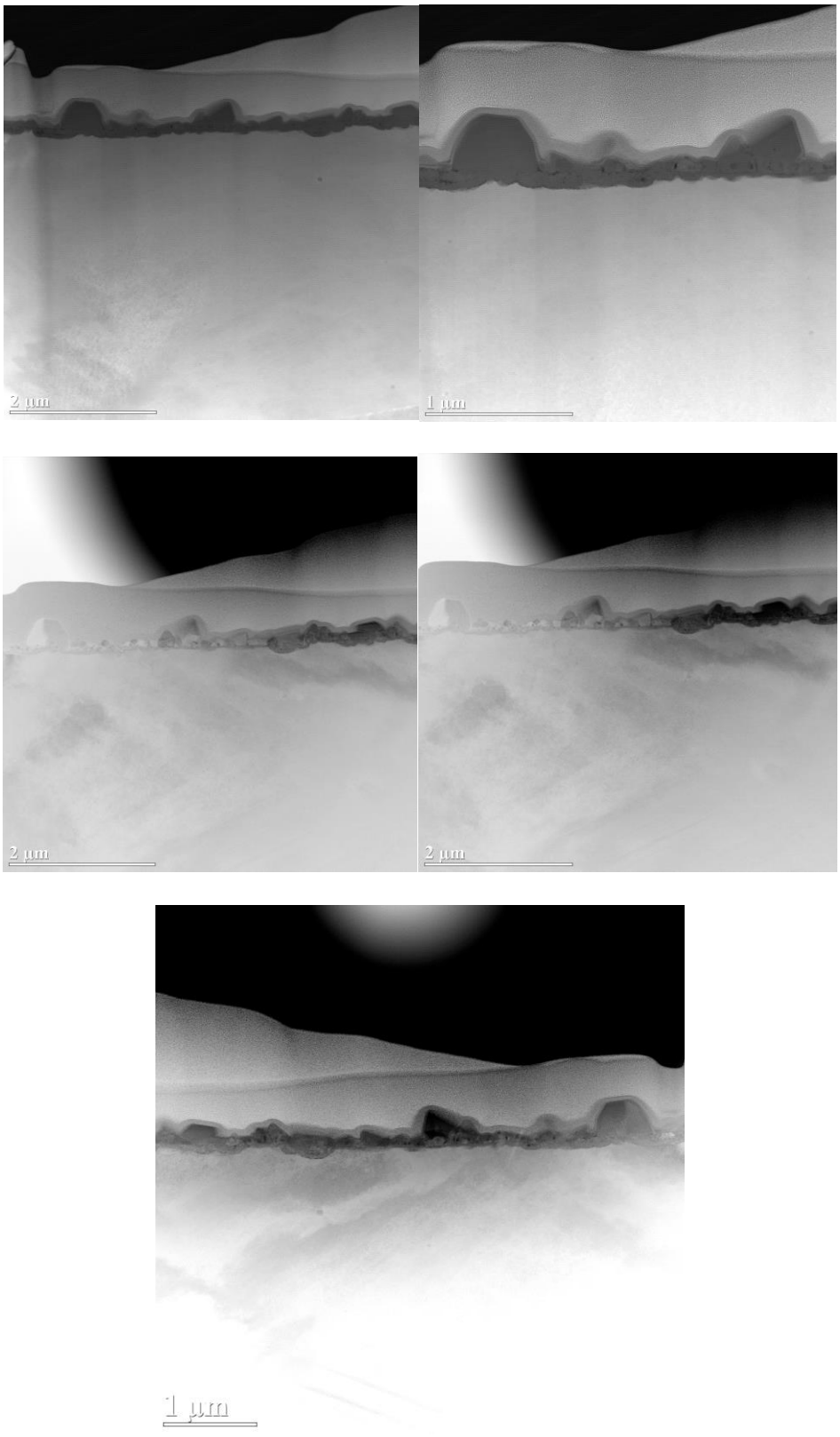

Hi24-2 Flow

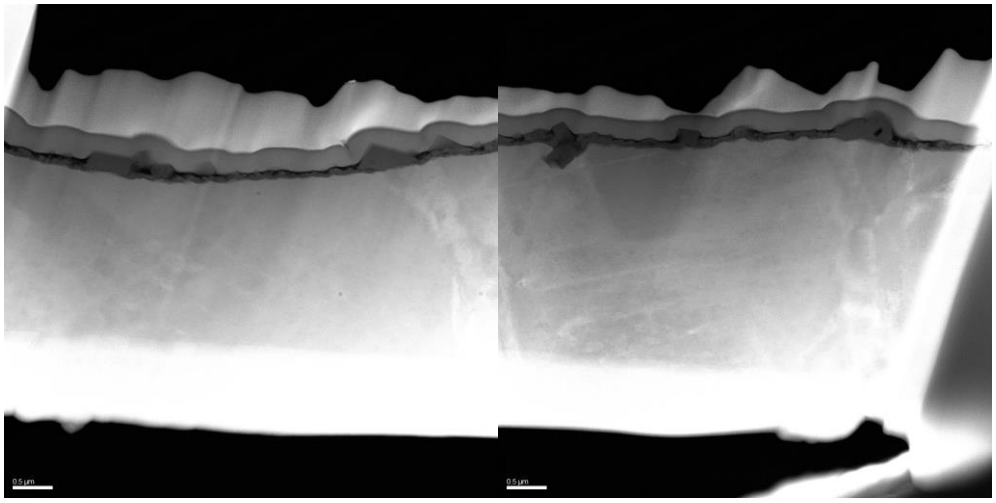

Hi24-2 Irr

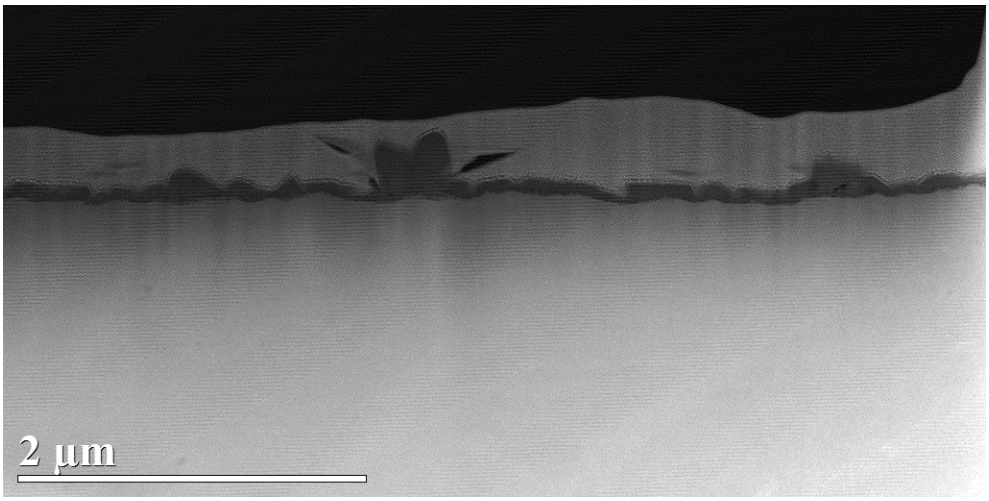

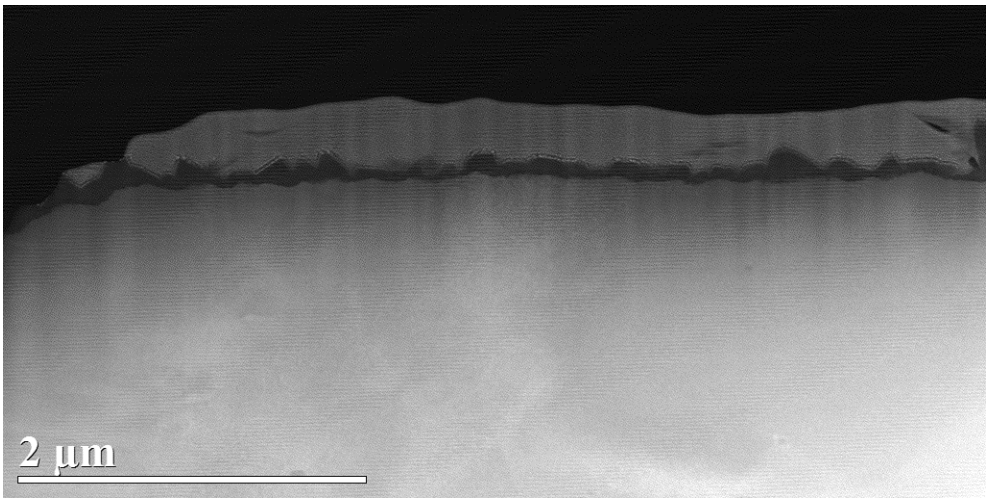

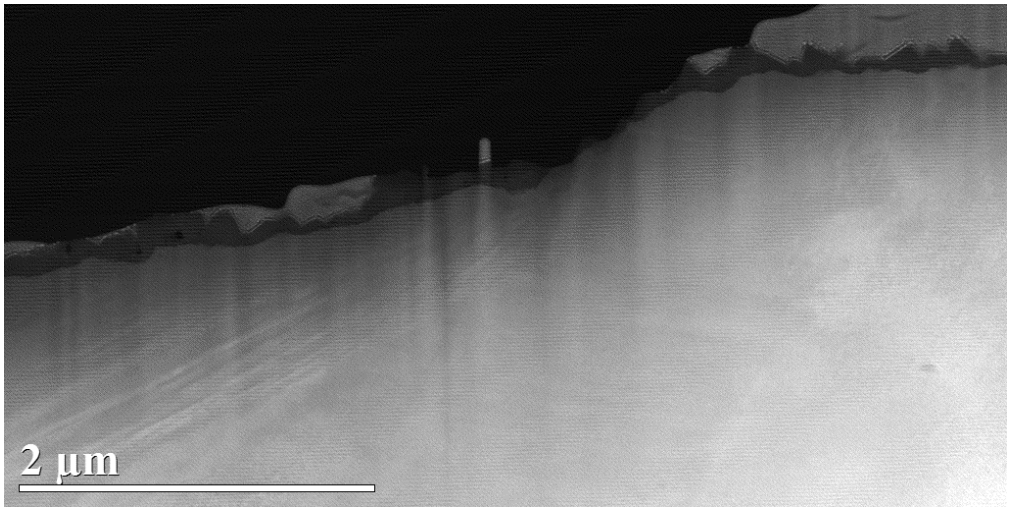
2 µm

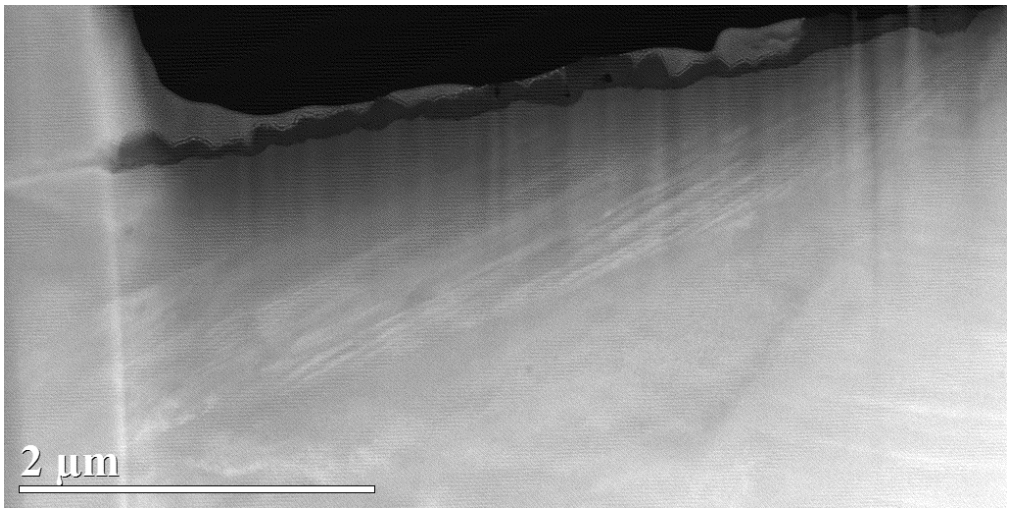
2 µm

Lo24 Unirr

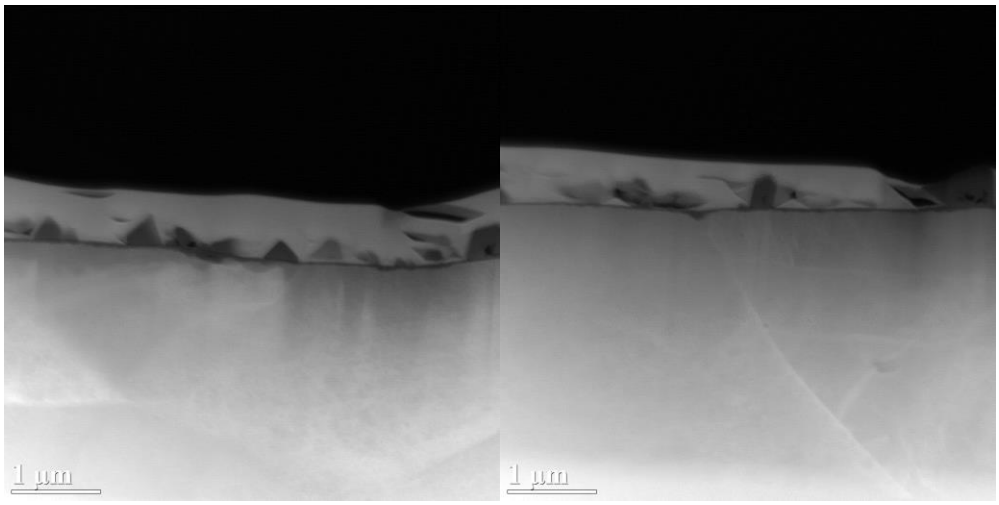

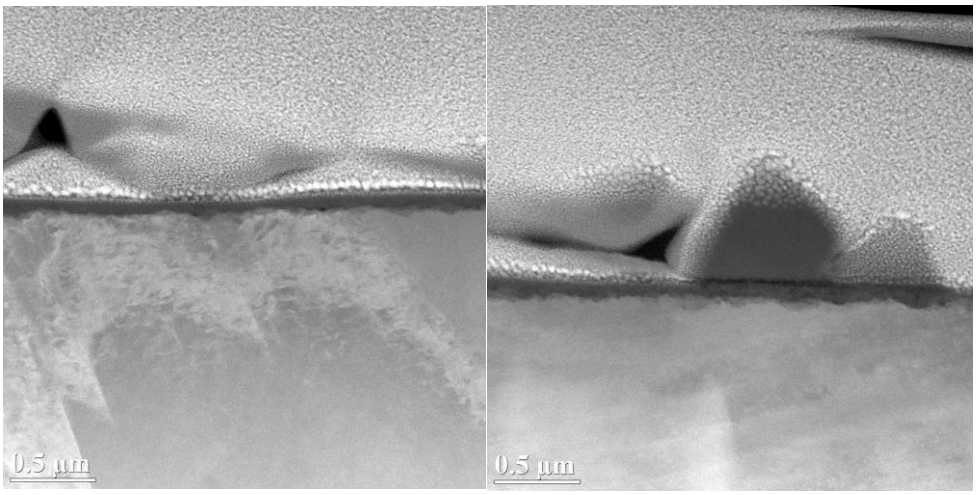

Lo24 Irr

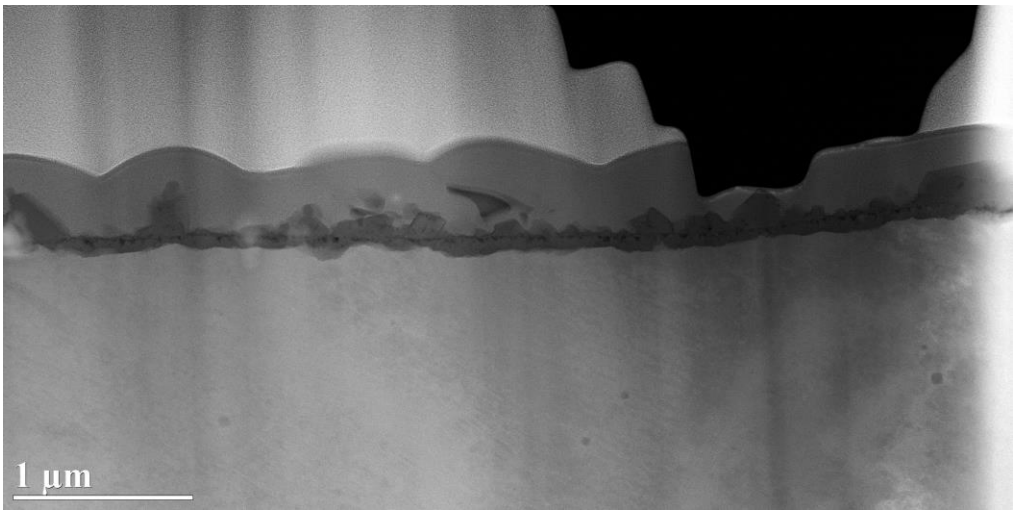

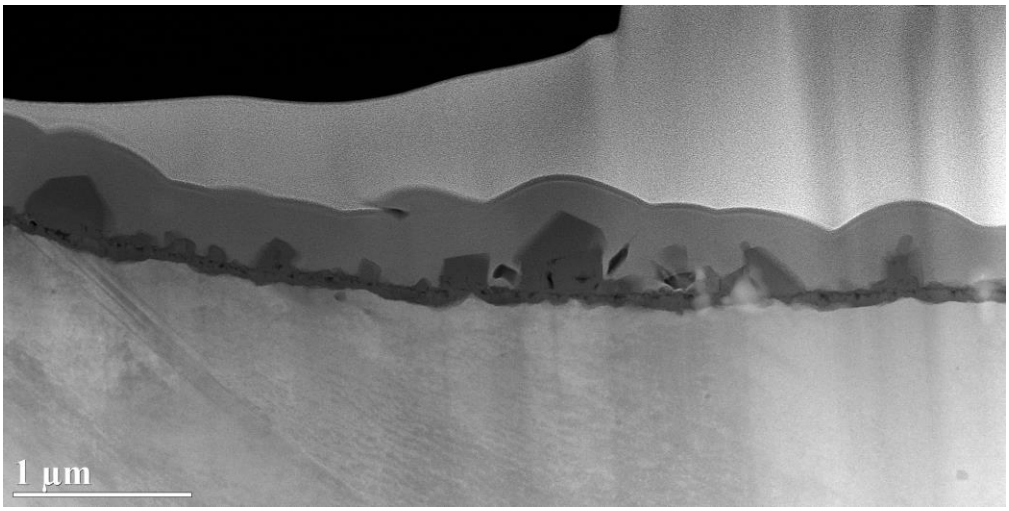

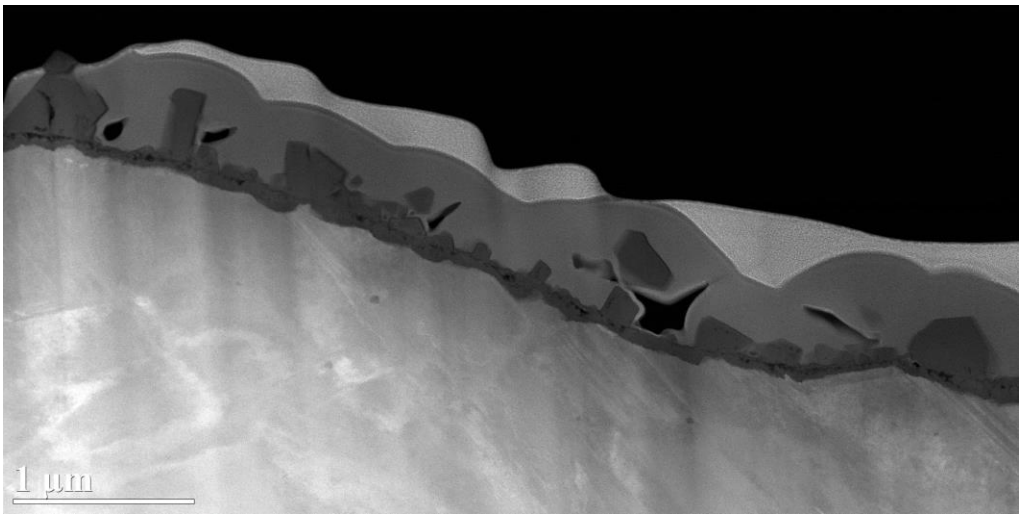

Un72

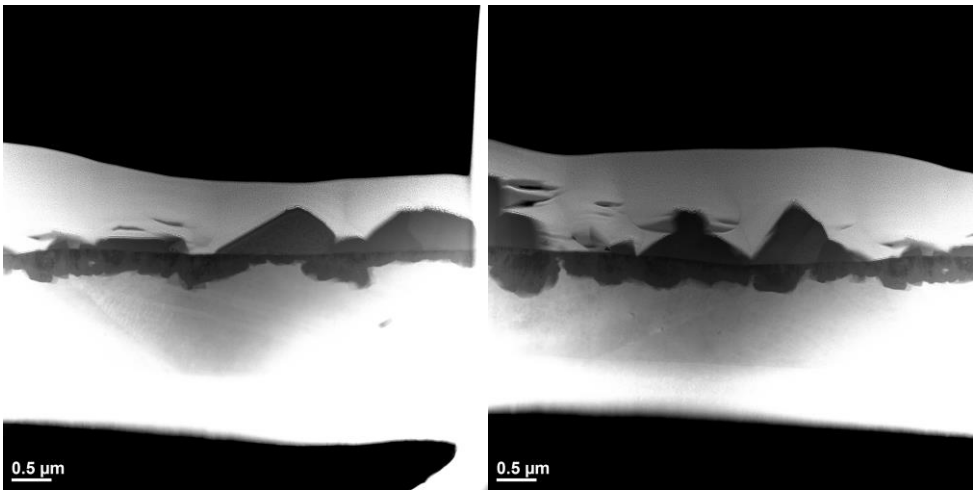

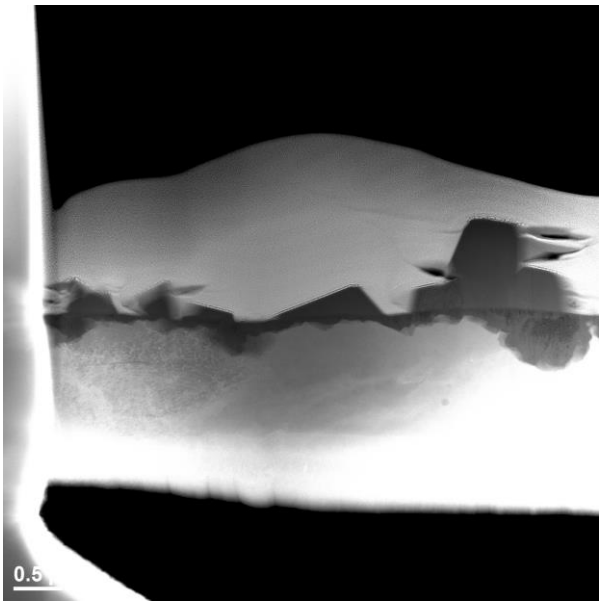

Hi72 Unirr

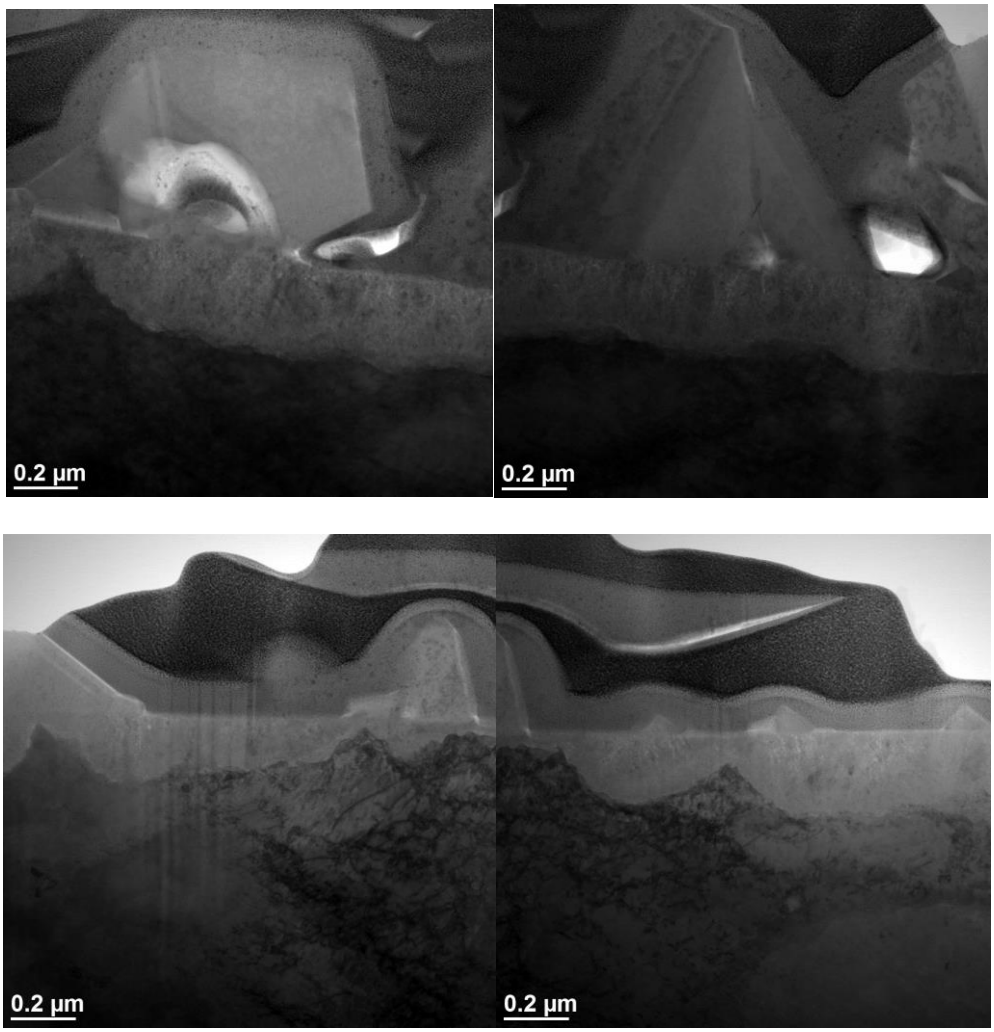

Hi72 Flow

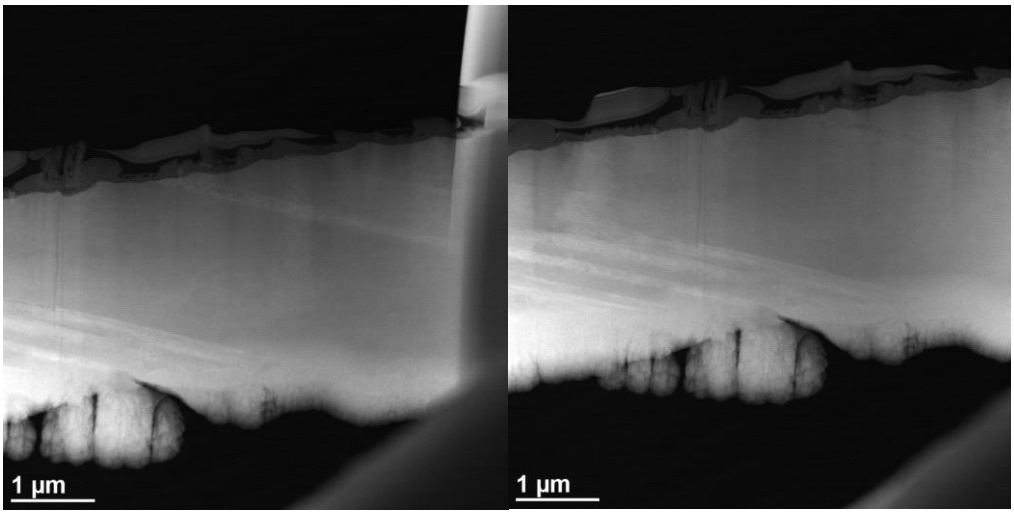

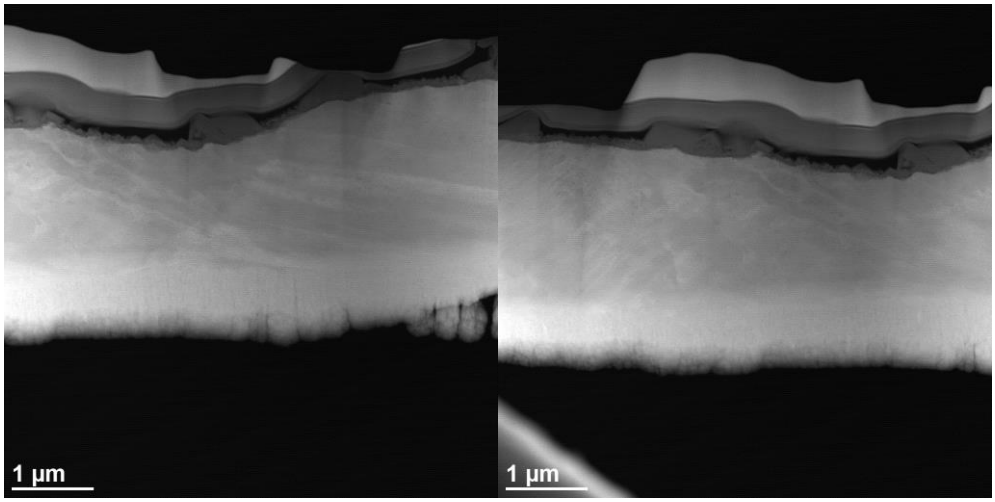

Hi72 Irr

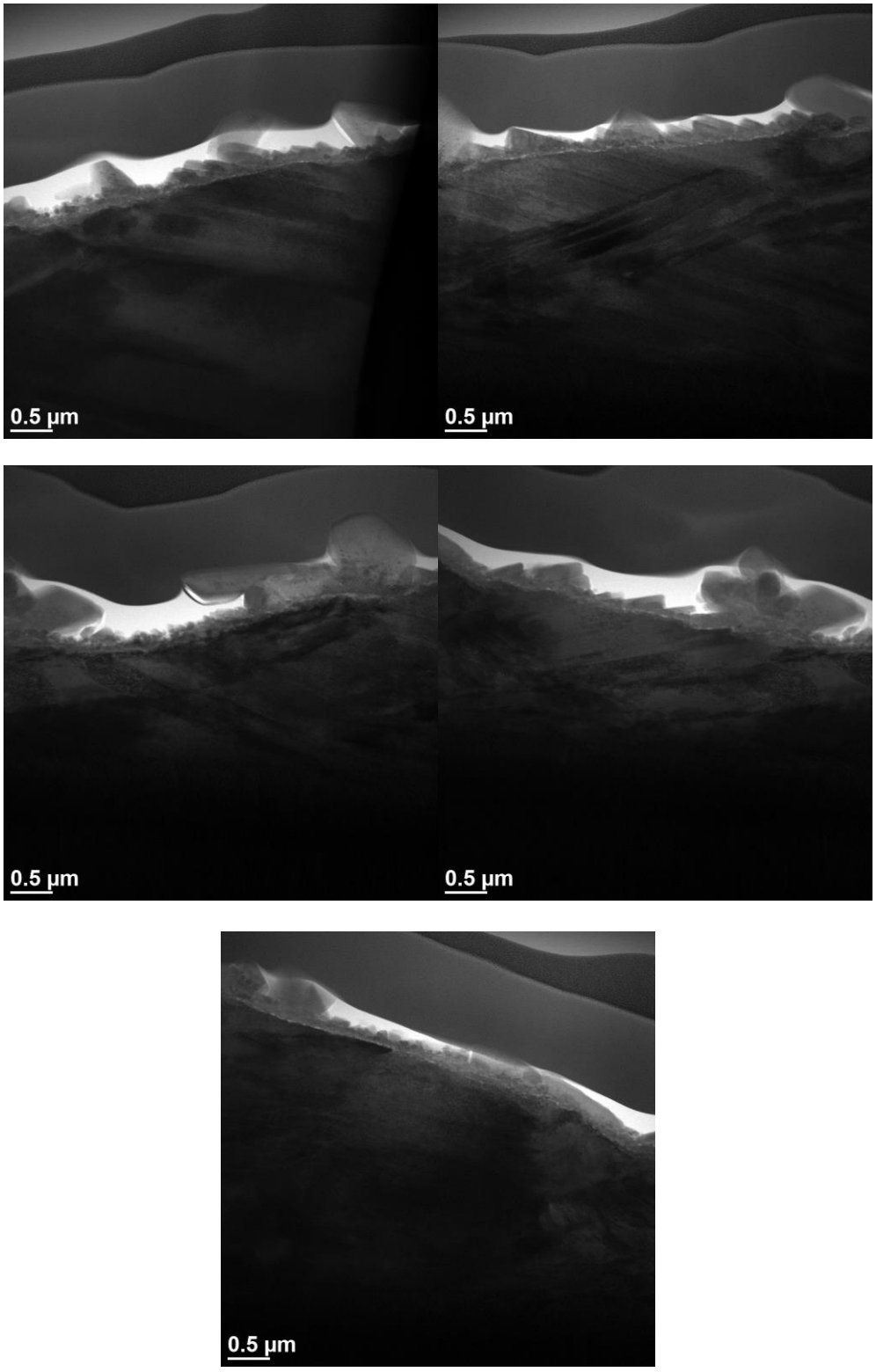
0.5 µm
0.5 µm
0.5 µm
0.5 µm
0.5 µm

APPENDIX D - EDS LINE SCANS

Hi04 Unirr

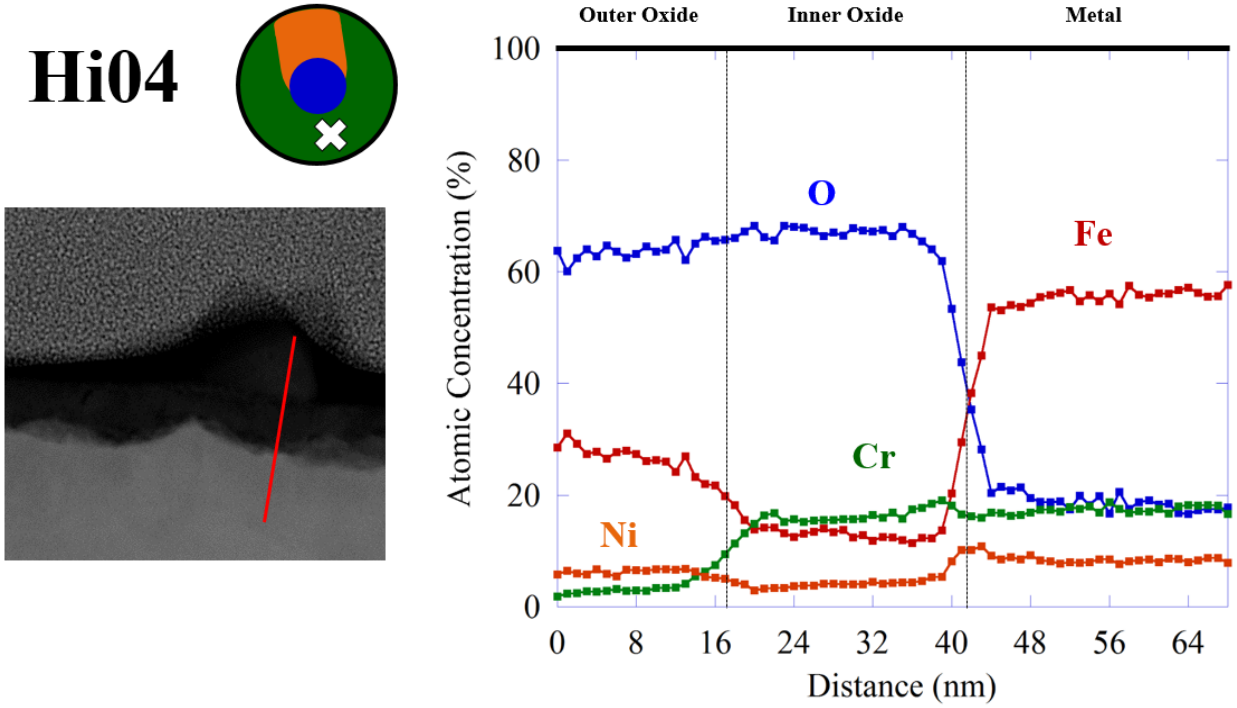

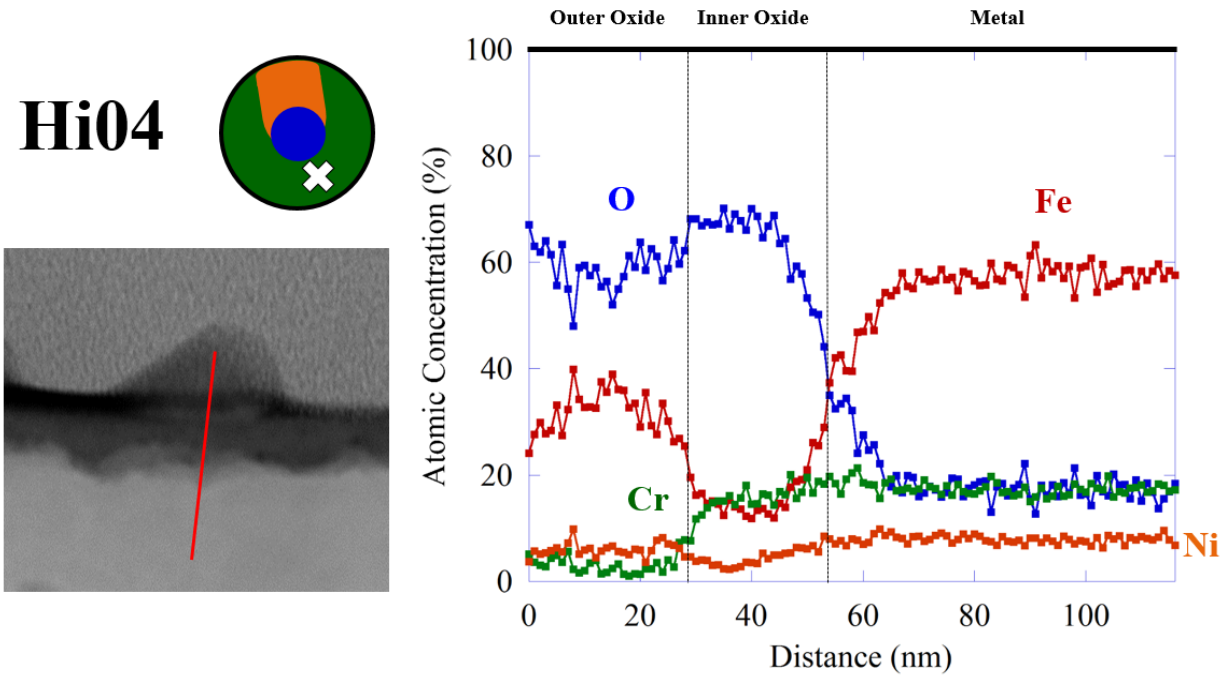
Hi04
Outer Oxide
Inner Oxide
Metal
Atomic Concentration (%)
Distance (nm)
O
Fe
Cr
Ni
0
20
40
60
80
100

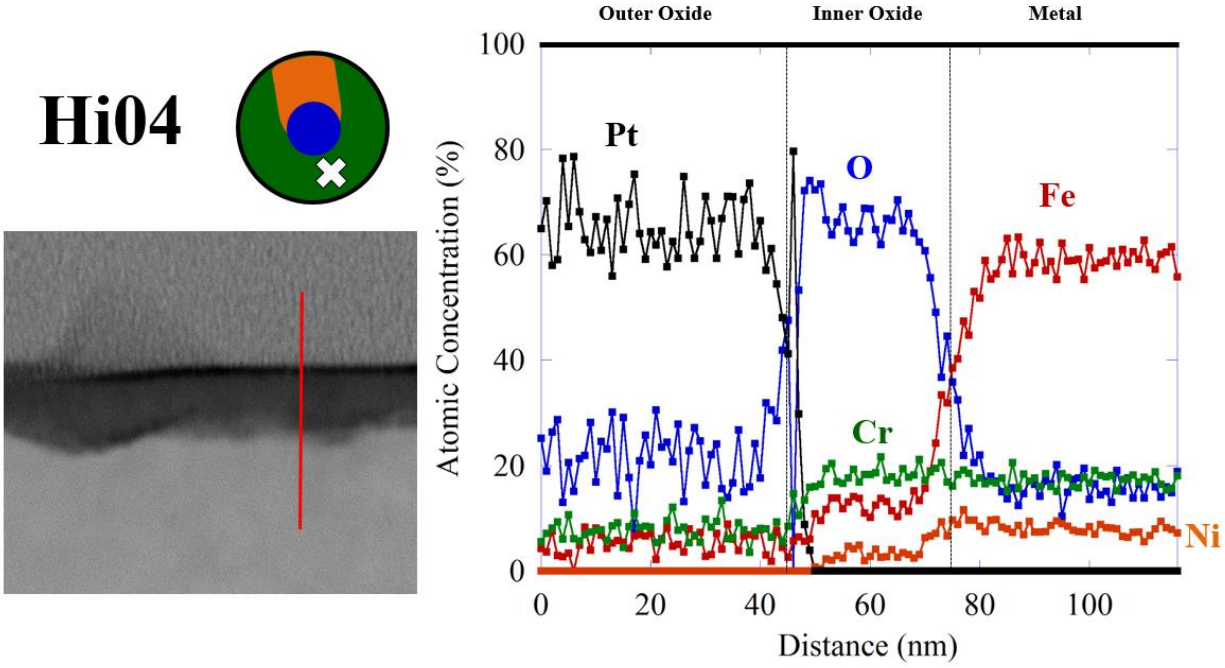
Hi04
Outer Oxide
Inner Oxide
Metal
Atomic Concentration (%)
Distance (nm)
Pt
O
Fe
Cr
Ni
0
20
40
60
80
100

Hi04 Flow

Hi04

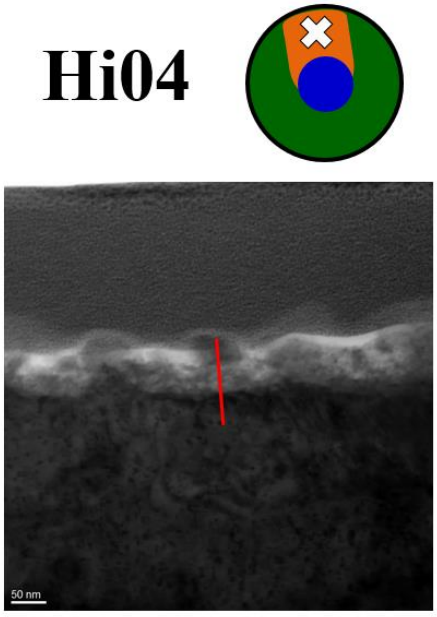
50 nm

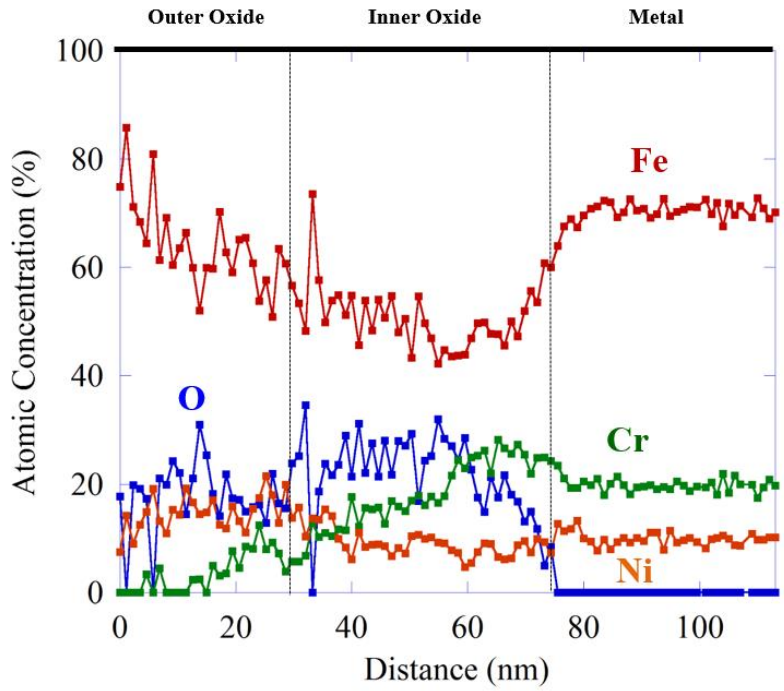
Outer Oxide
Inner Oxide
Metal
Atomic Concentration (%)
Distance (nm)
Fe
O
Cr
Ni
0
20
40
60
80
100
120
140
160

Hi04

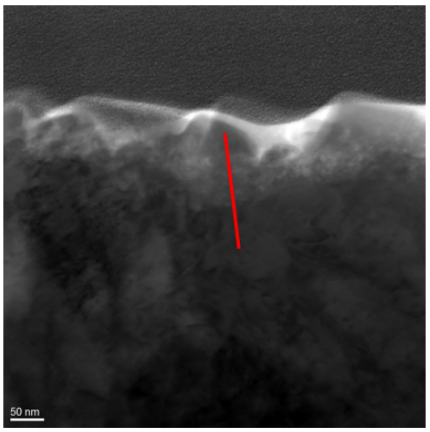
50 nm

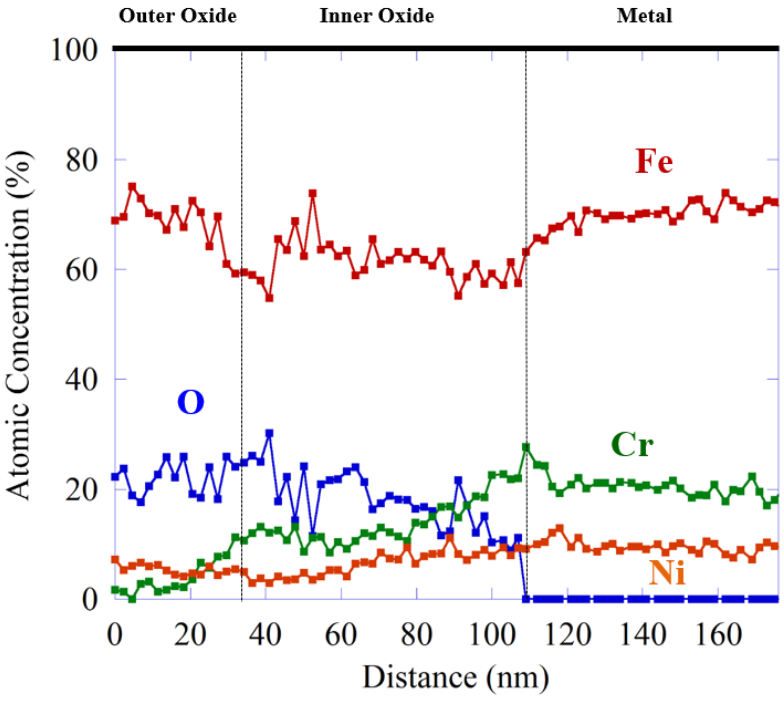
Outer Oxide
Inner Oxide
Metal
Atomic Concentration (%)
Distance (nm)
Fe
O
Cr
Ni
0
20
40
60
80
100
120
140
160

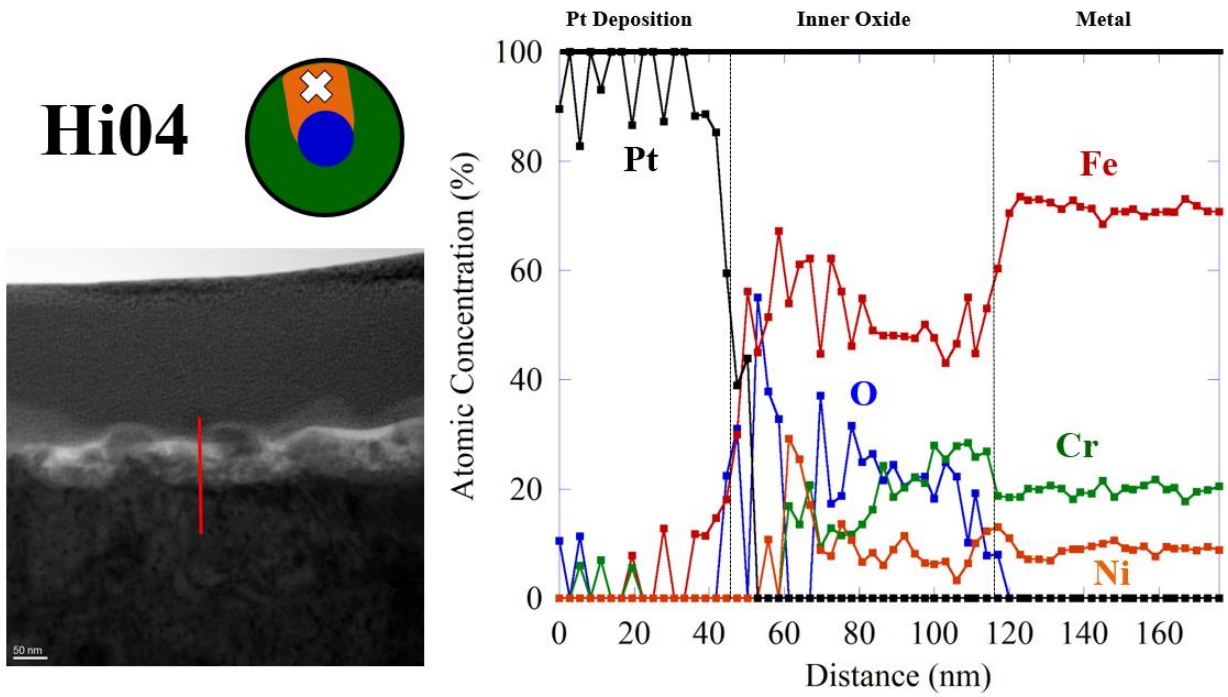

Hi04 Irr

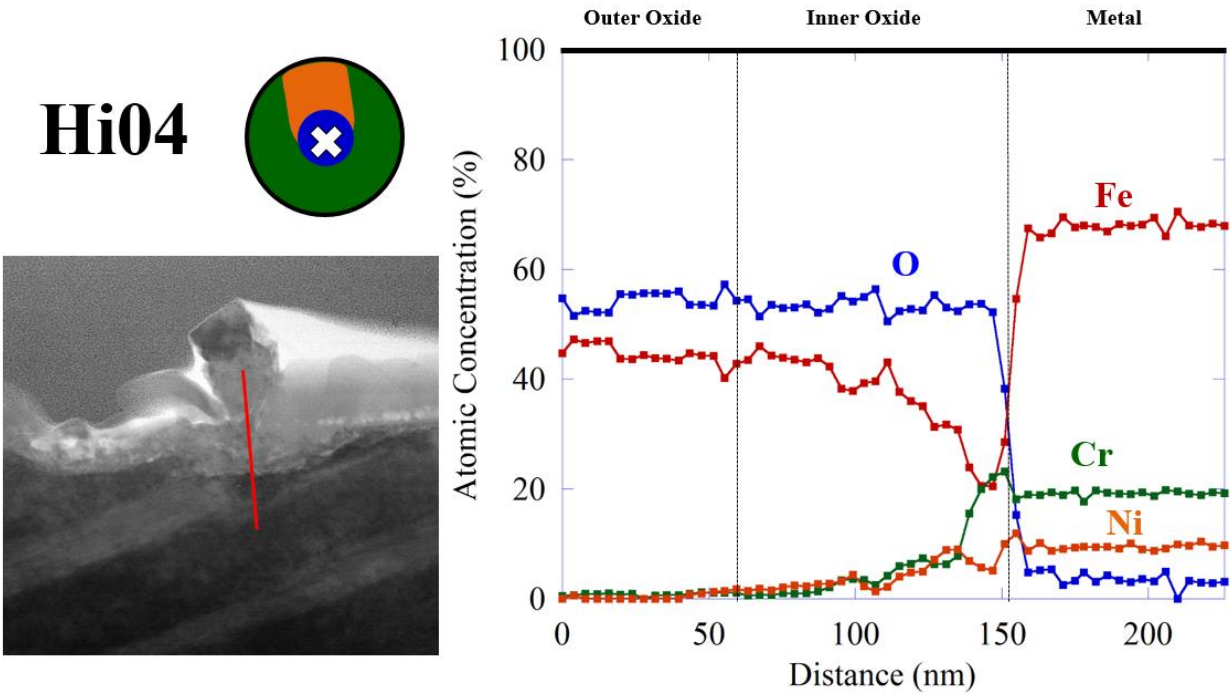

Hi12 Unirr

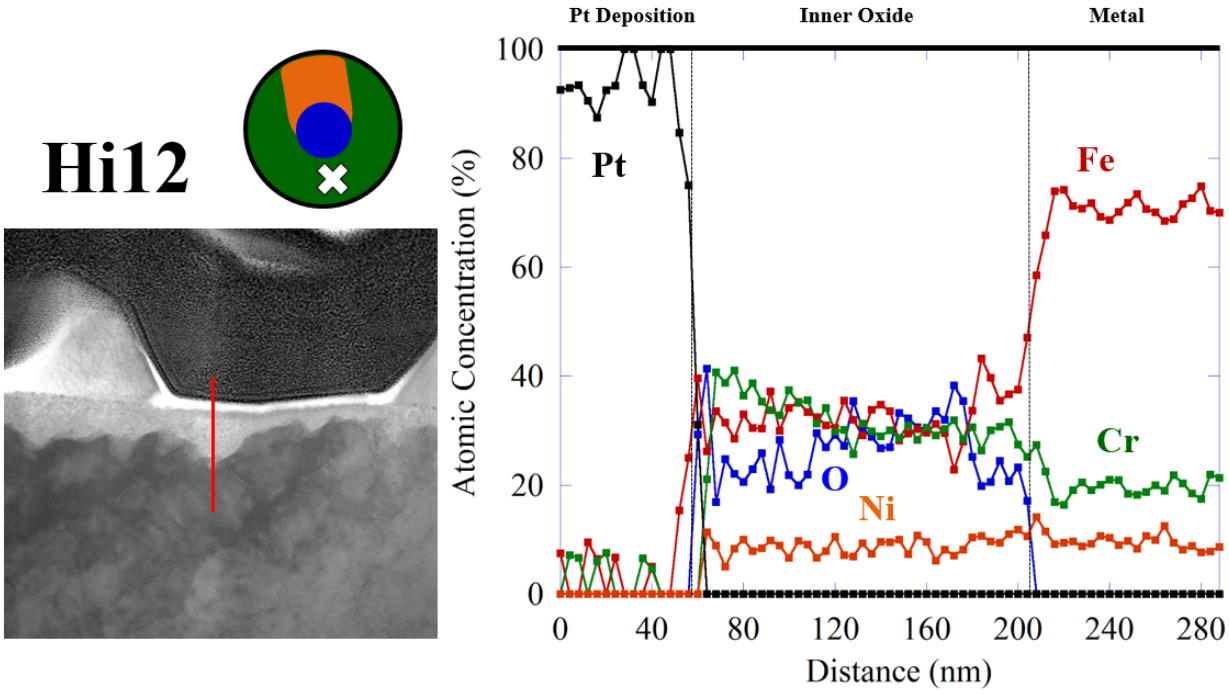
Hi12
Pt Deposition
Inner Oxide
Metal
Pt
Fe
Cr
O
Ni
Atomic Concentration (%)
Distance (nm)
0
20
40
60
80
100
0
40
80
120
160
200
240
280

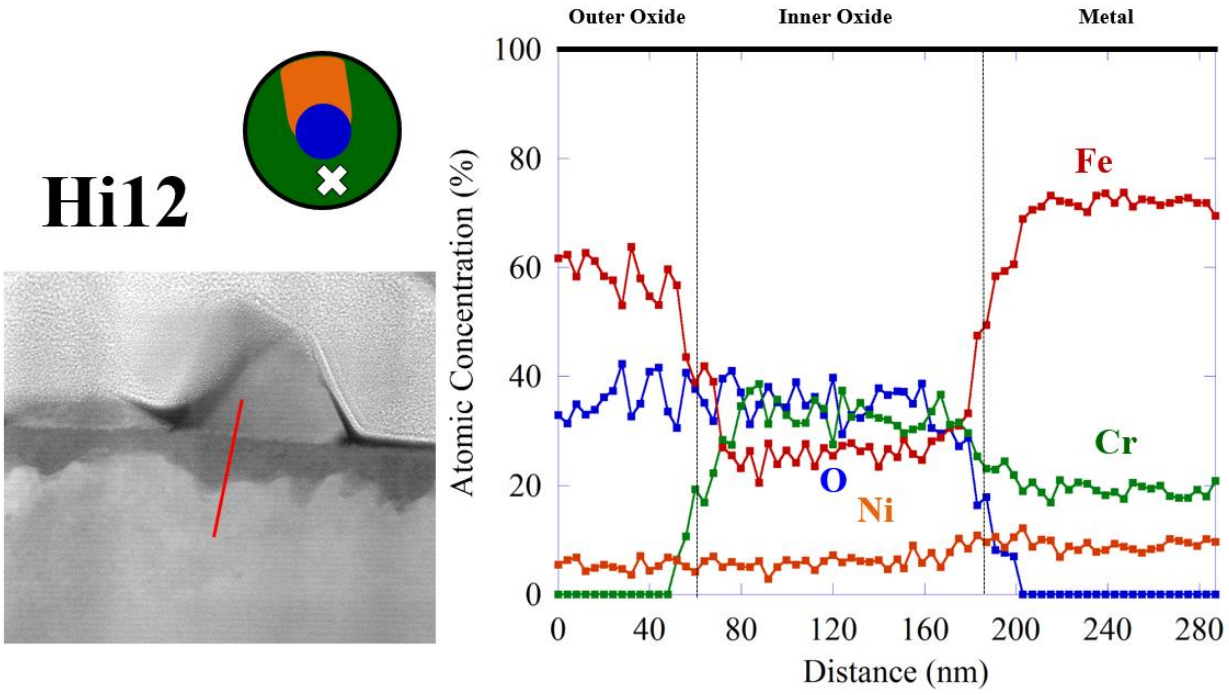
Hi12
Outer Oxide
Inner Oxide
Metal
Fe
Cr
O
Ni
Atomic Concentration (%)
Distance (nm)
0
20
40
60
80
100
0
40
80
120
160
200
240
280

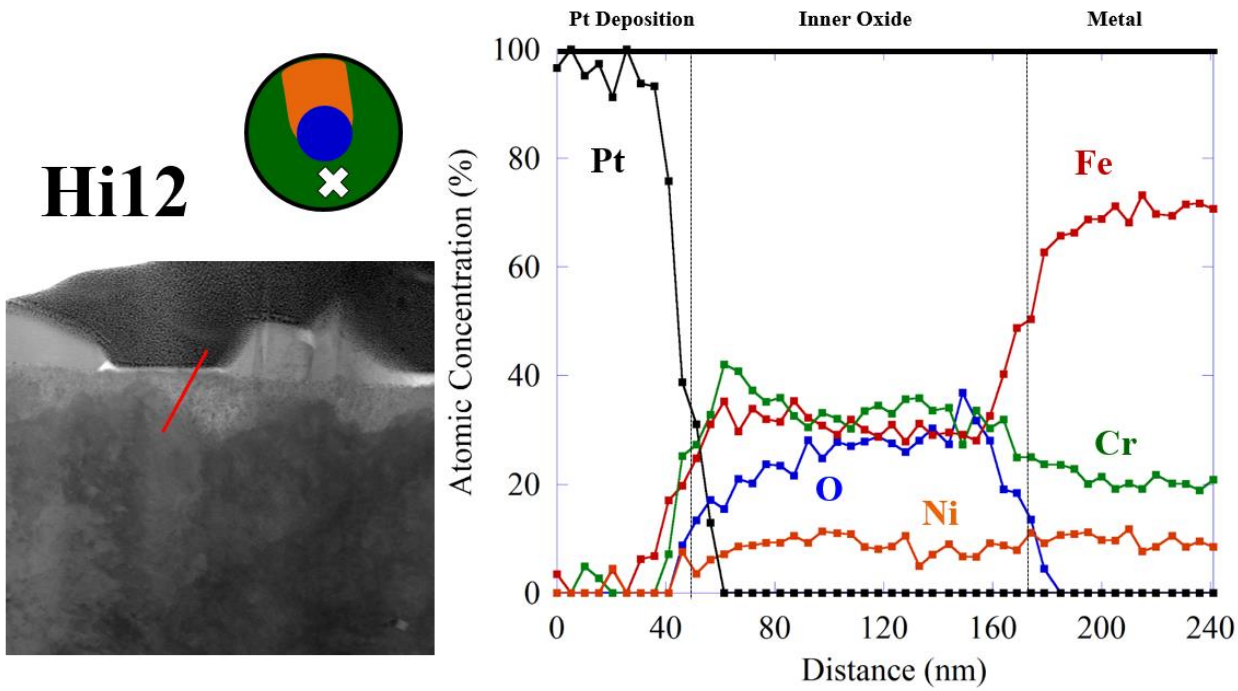
Hi12
Pt Deposition
Inner Oxide
Metal
Pt
Fe
Cr
O
Ni
Atomic Concentration (%)
Distance (nm)
0
20
40
60
80
100
0
40
80
120
160
200
240

Hi12 Flow

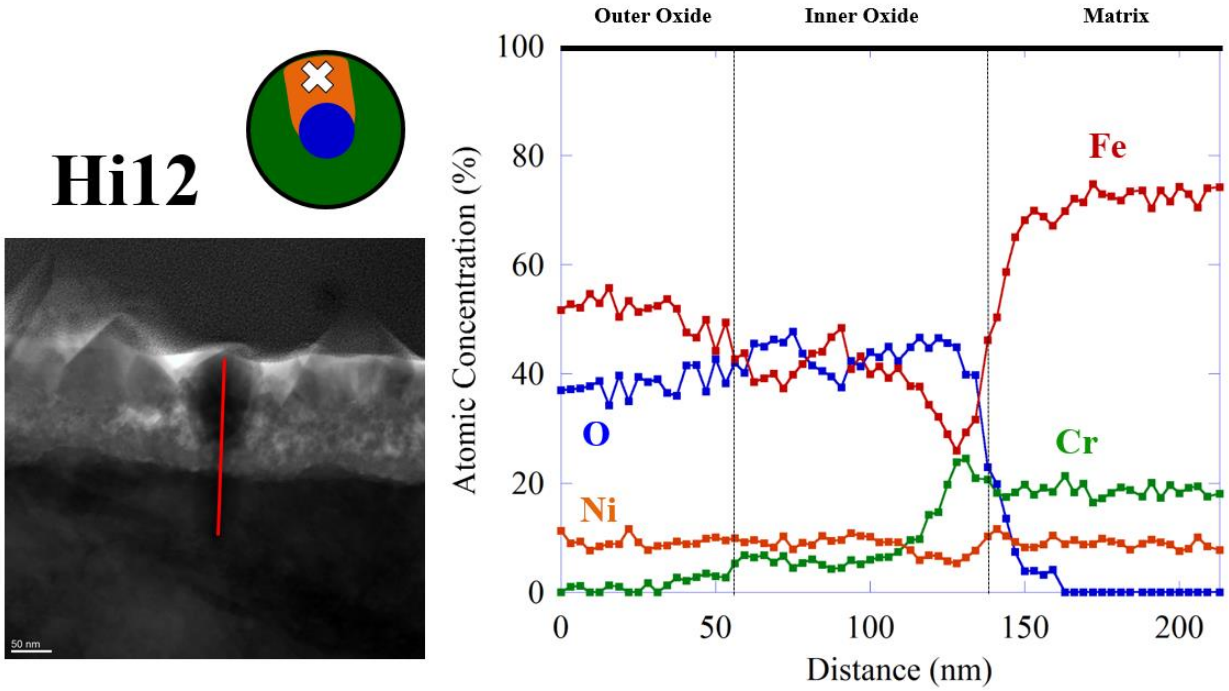
Hi12
Outer Oxide
Inner Oxide
Matrix
Fe
O
Cr
Ni
Atomic Concentration (%)
Distance (nm)
50 nm
0
20
40
60
80
100
0
50
100
150
200

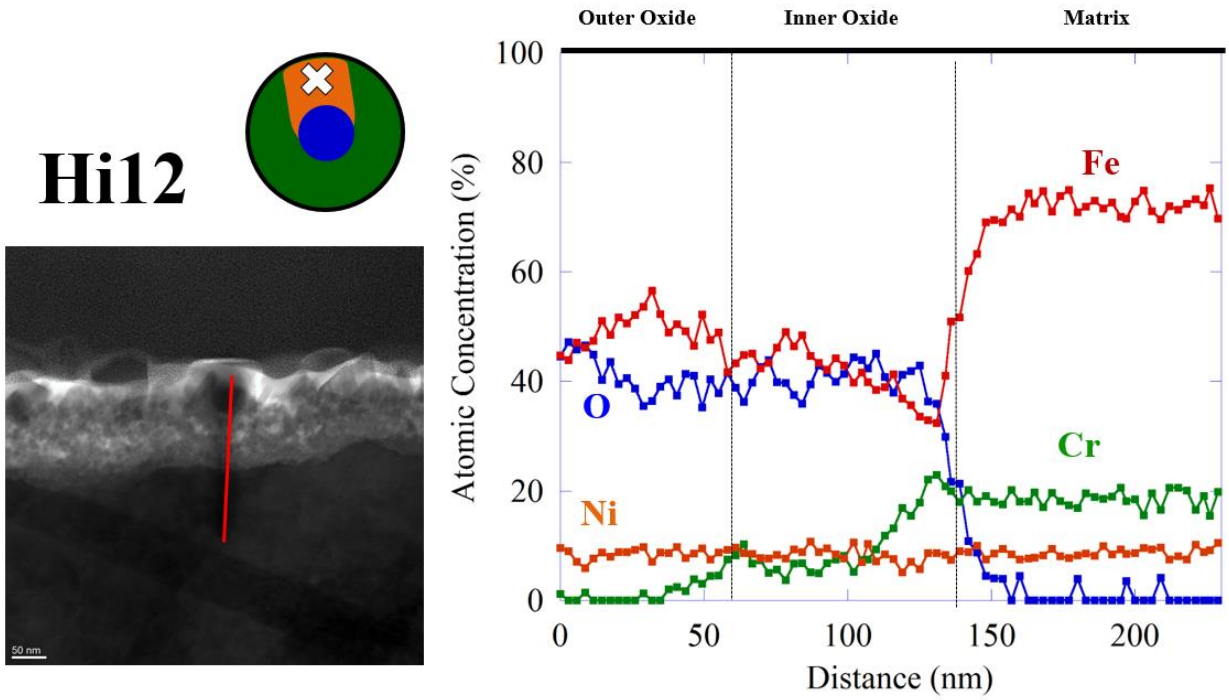
Hi12
50 nm
Outer Oxide
Inner Oxide
Matrix
Atomic Concentration (%)
Distance (nm)
Fe
O
Cr
Ni
0
20
40
60
80
100
0
50
100
150
200

Hi12 Irr

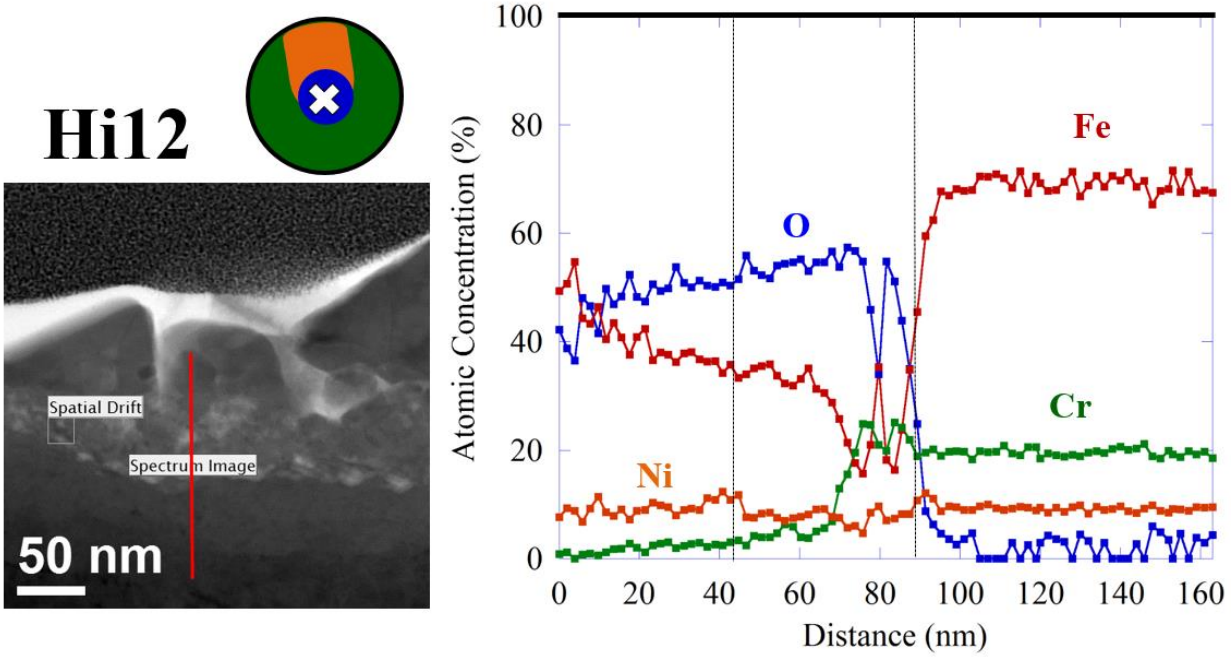
Hi12
Spatial Drift
Spectrum Image
50 nm
Outer Oxide
Inner Oxide
Metal
Atomic Concentration (%)
Distance (nm)
Fe
O
Cr
Ni
0
20
40
60
80
100
0
20
40
60
80
100
120
140
160

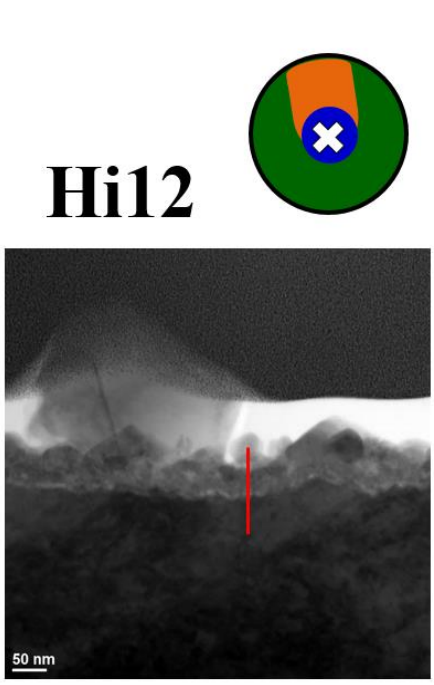

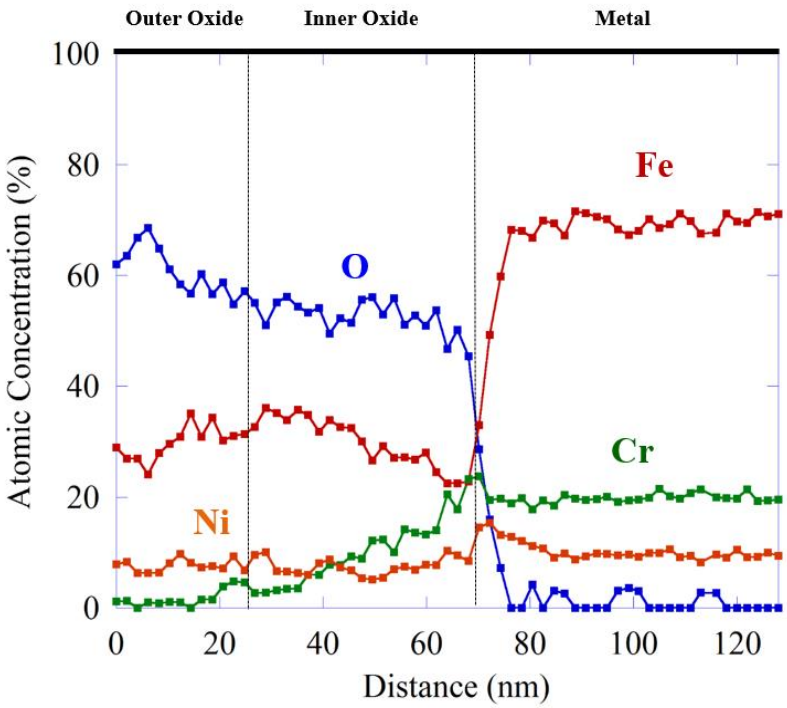

Un24

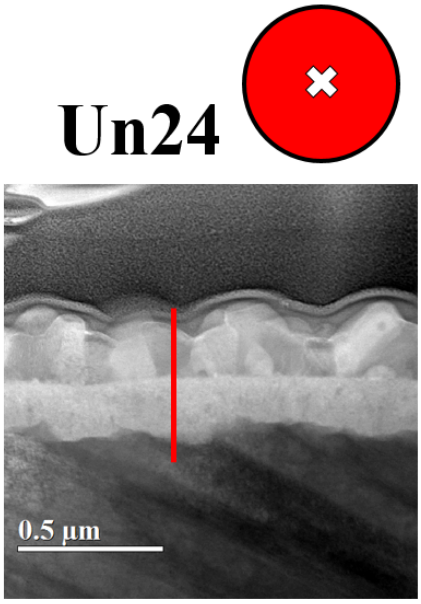

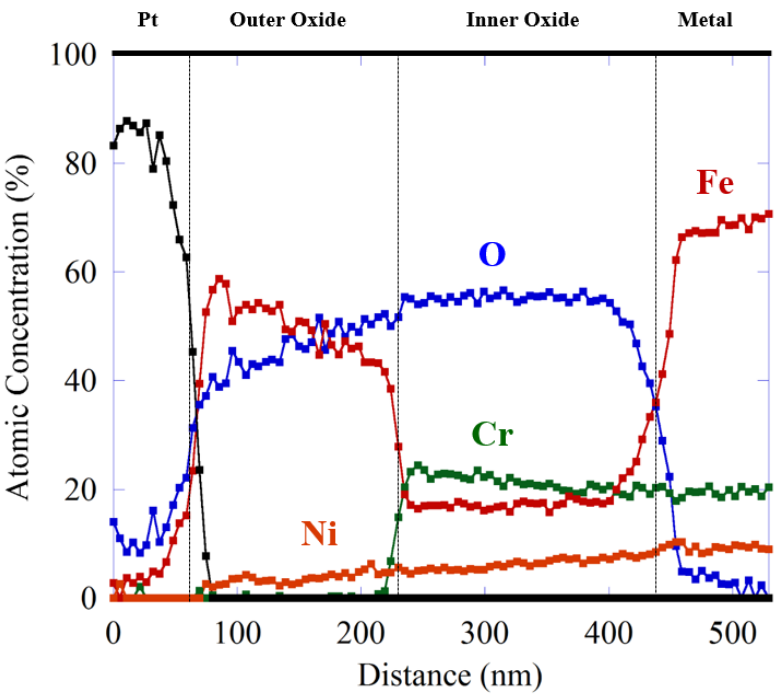

Hi24 Unirr

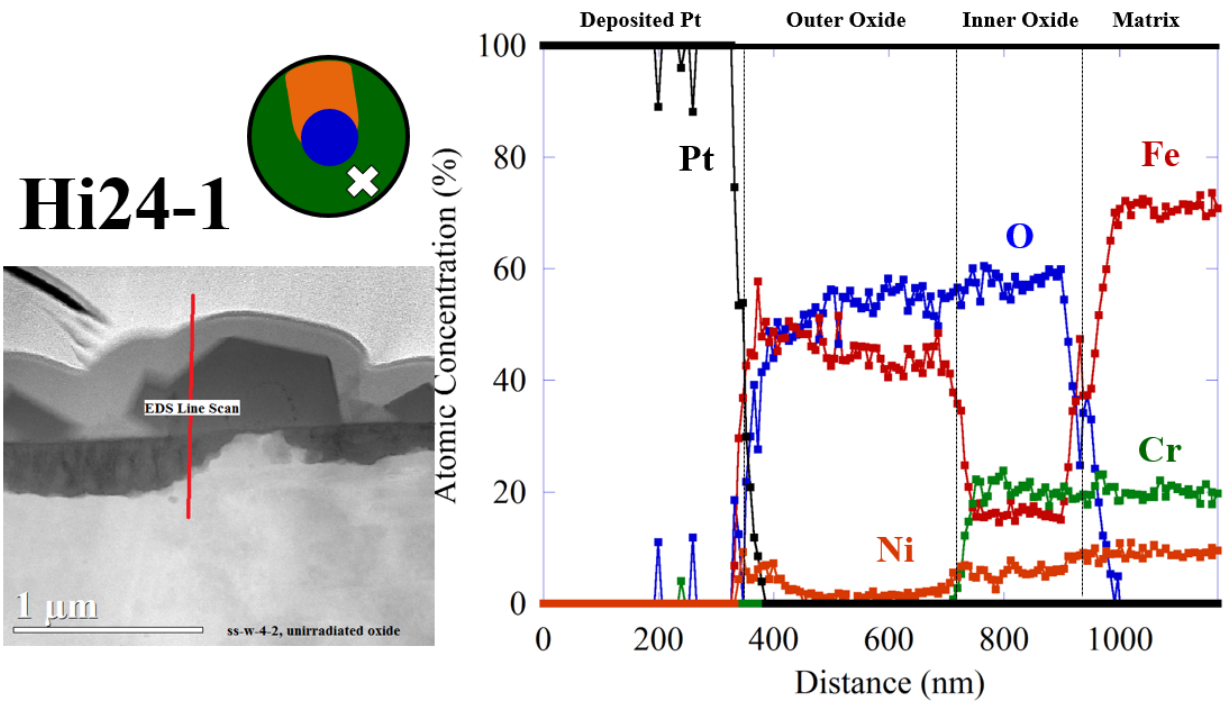
Hi24-1
EDS Line Scan
1 μm
ss-w-4-2, unirradiated oxide
Deposited Pt
Outer Oxide
Inner Oxide
Matrix
Pt
O
Fe
Cr
Ni
Atomic Concentration (%)
Distance (nm)

Hi24 Irr

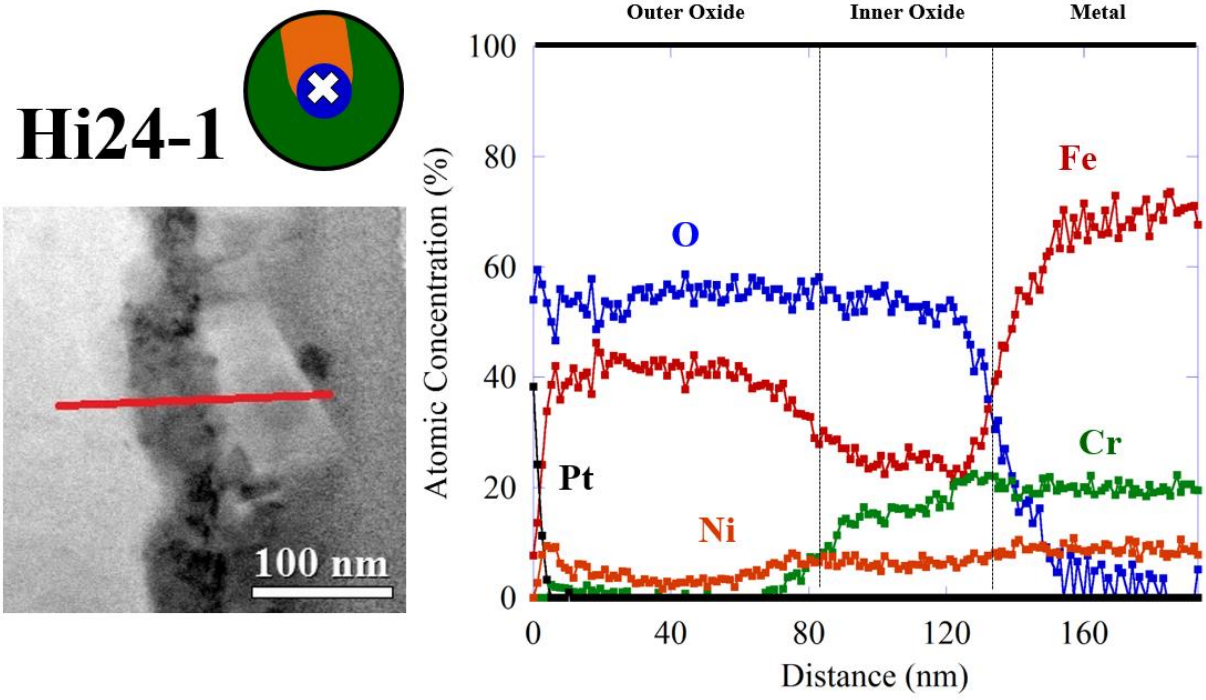
Hi24-1
100 nm
Outer Oxide
Inner Oxide
Metal
O
Fe
Cr
Pt
Ni
Atomic Concentration (%)
Distance (nm)

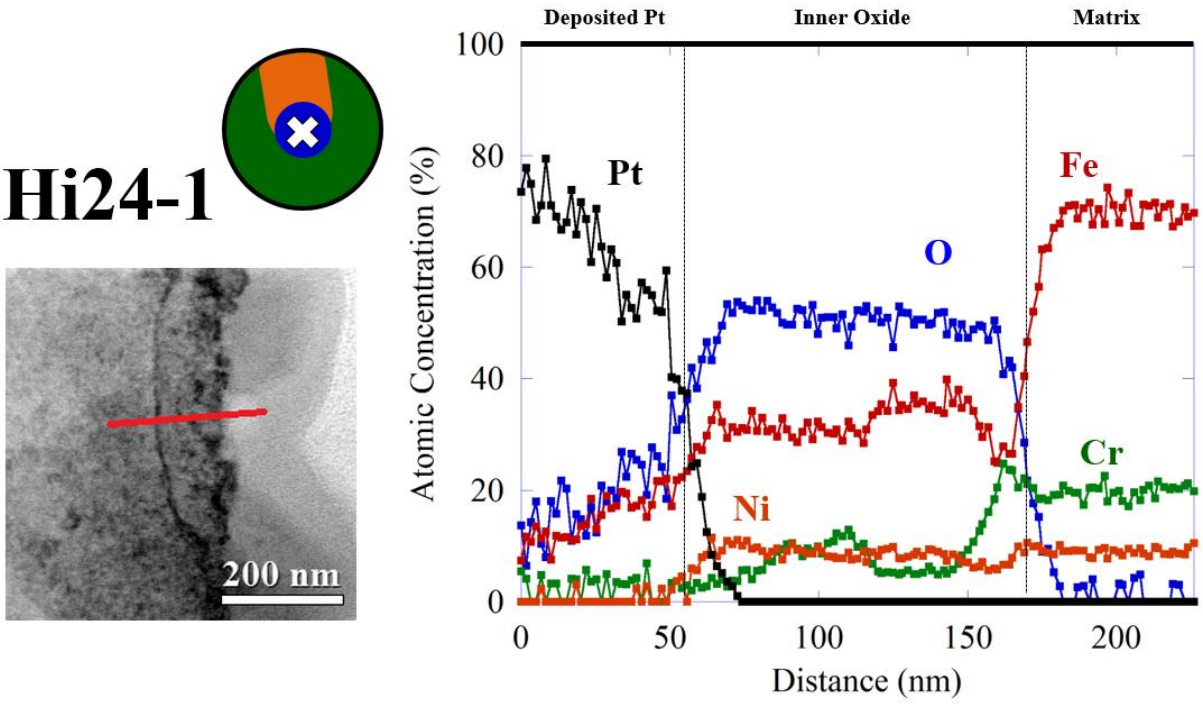
Hi24-1
200 nm
Deposited Pt
Inner Oxide
Matrix
Pt
O
Fe
Cr
Ni
Atomic Concentration (%)
Distance (nm)

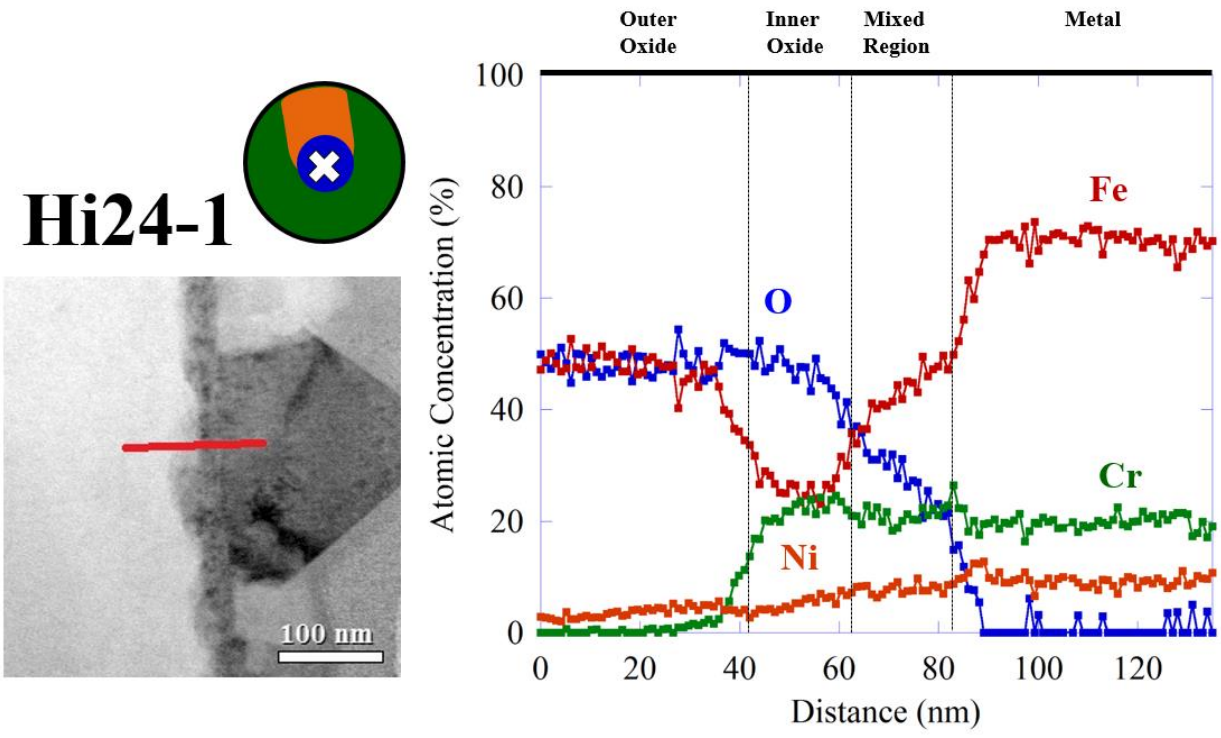
Hi24-1
100 nm
Outer Oxide
Inner Oxide
Mixed Region
Metal
Fe
O
Cr
Ni
Atomic Concentration (%)
Distance (nm)

Hi24-2 Flow

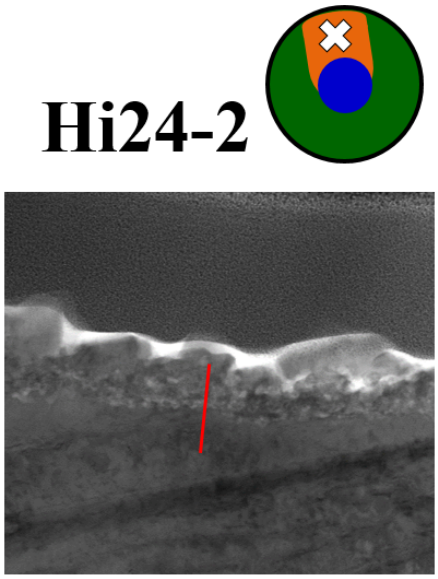
Hi24-2

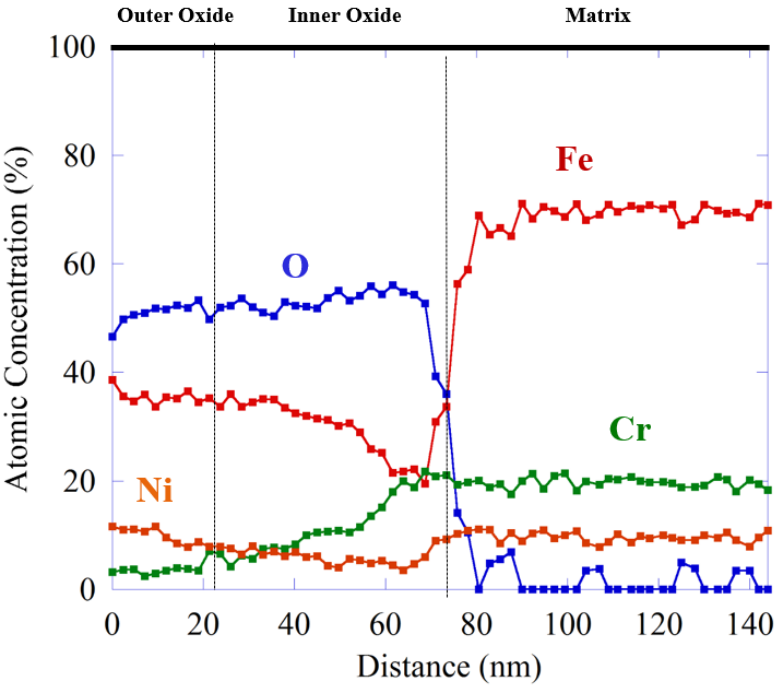
Outer Oxide
Inner Oxide
Matrix
Fe
O
Cr
Ni
Atomic Concentration (%)
Distance (nm)
0
20
40
60
80
100
120
140

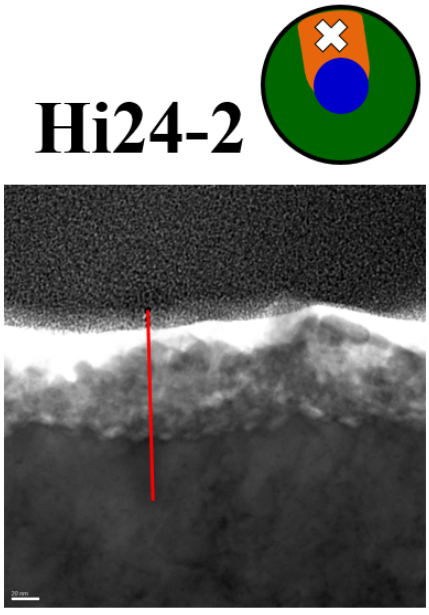
Hi24-2

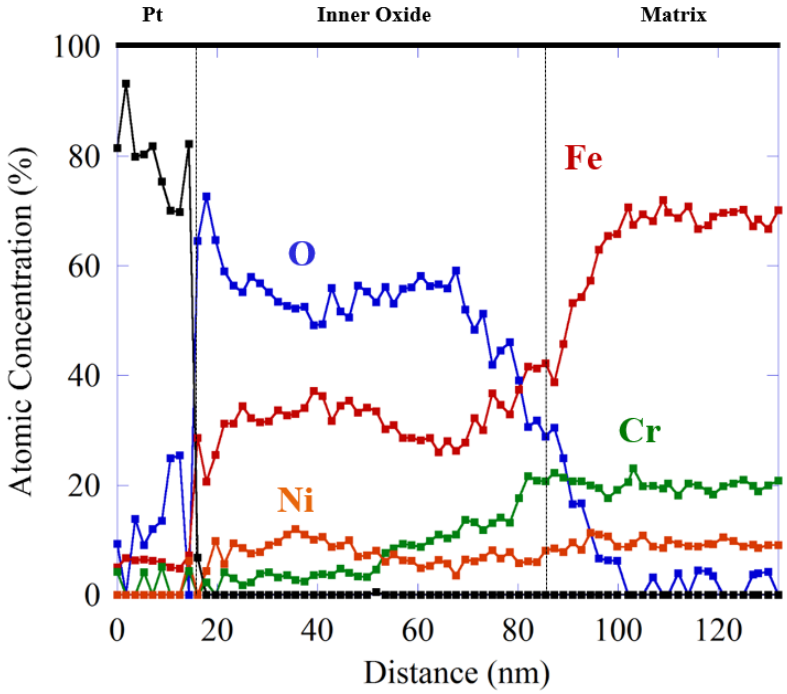
Pt
Inner Oxide
Matrix
Fe
O
Cr
Ni
Atomic Concentration (%)
Distance (nm)
0
20
40
60
80
100
120

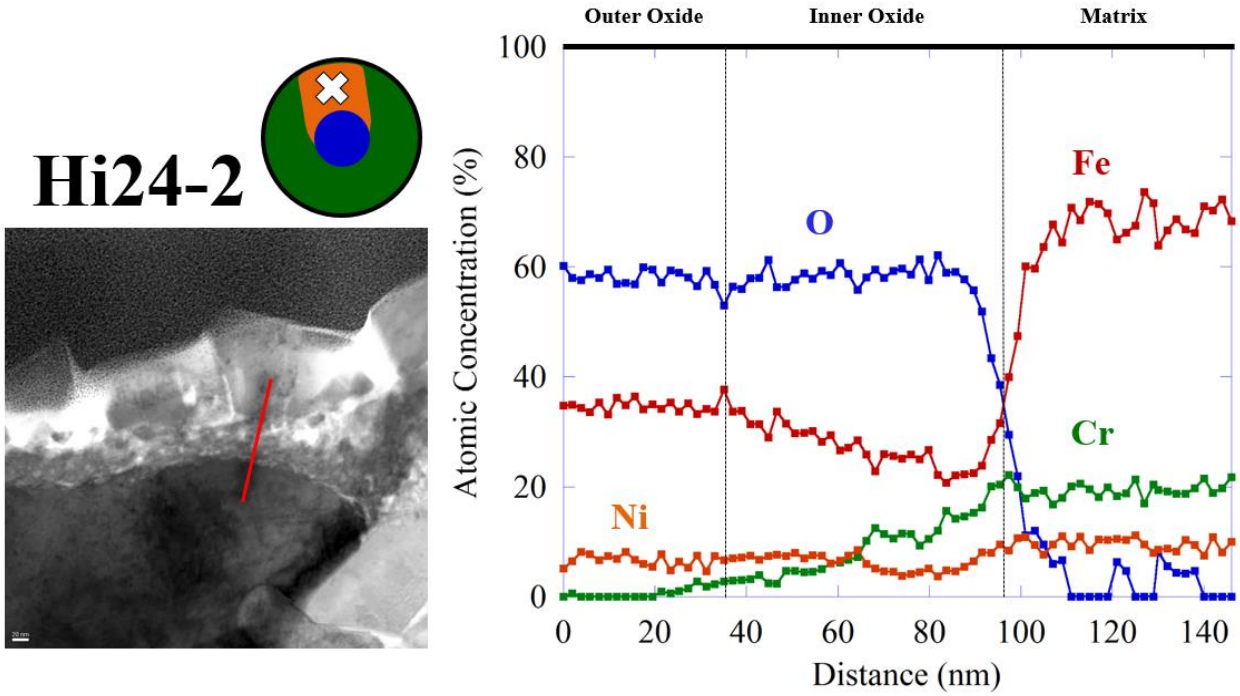
Hi24-2
Outer Oxide
Inner Oxide
Matrix
Atomic Concentration (%)
Distance (nm)
O
Fe
Cr
Ni

Hi24-2 Irr

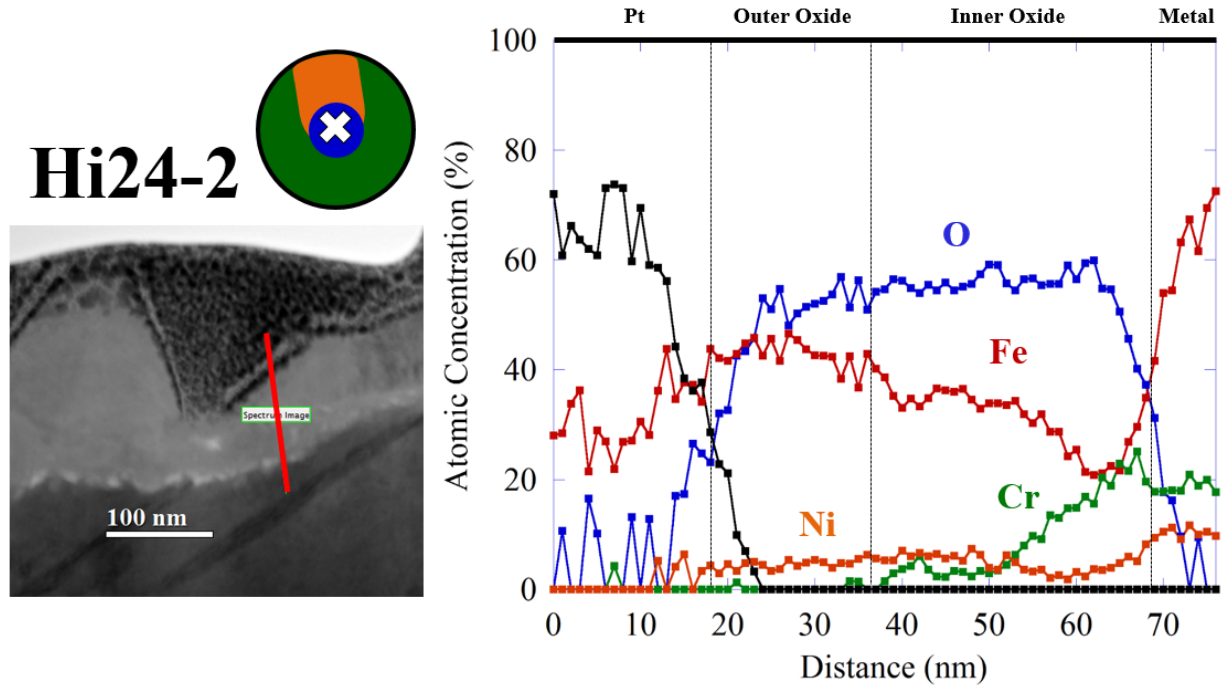
Hi24-2
Pt
Outer Oxide
Inner Oxide
Metal
100 nm
Atomic Concentration (%)
Distance (nm)
O
Fe
Cr
Ni

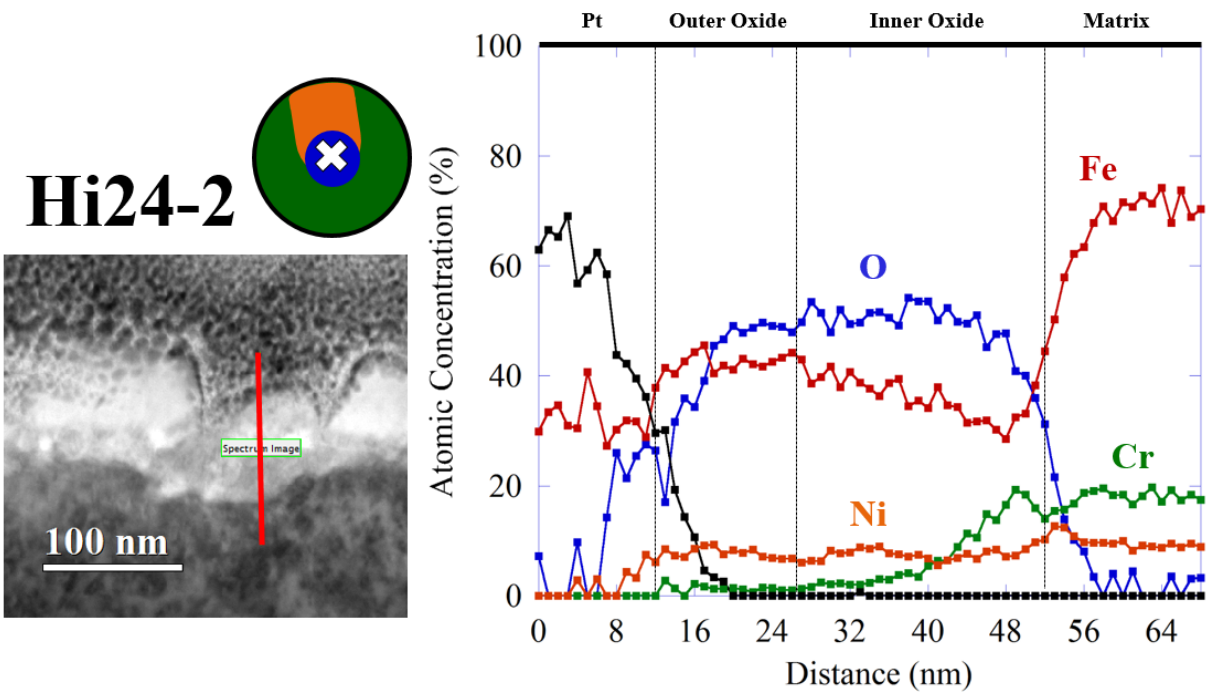

Lo24 Unirr

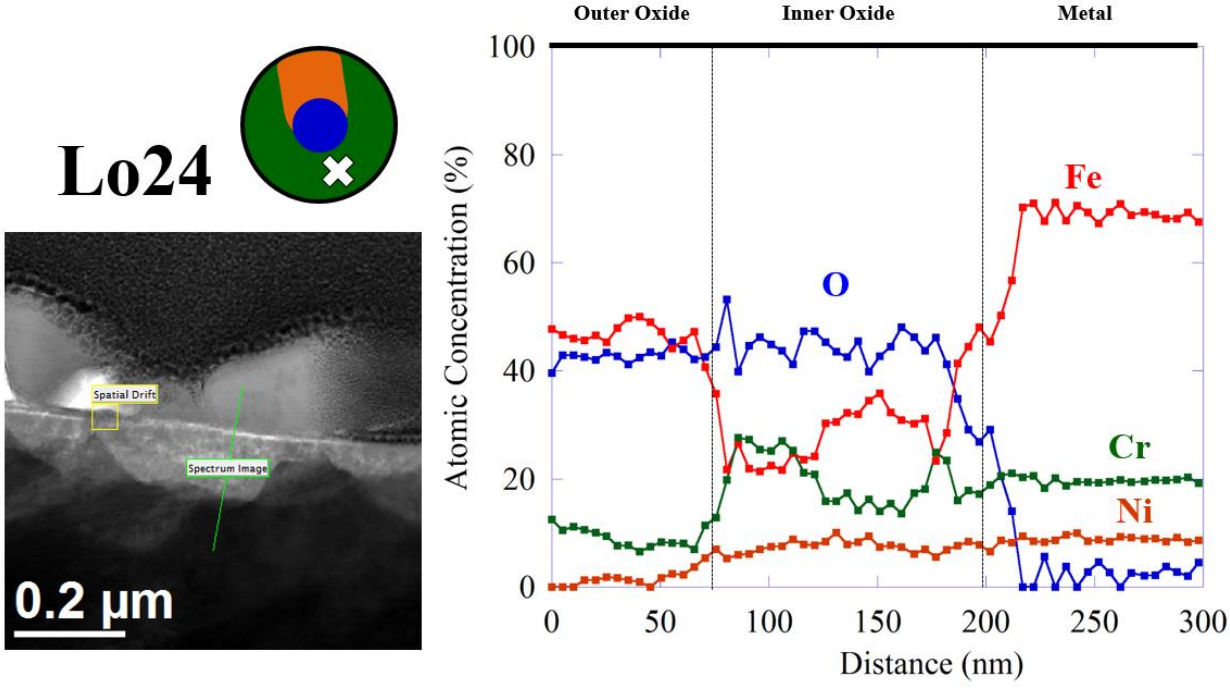

Lo24 Irr

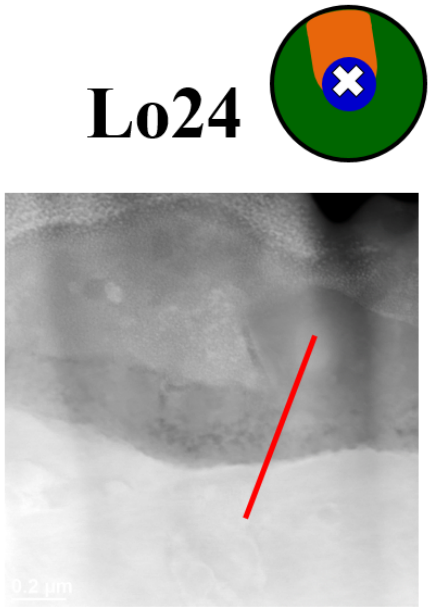
Lo24
0.2 µm

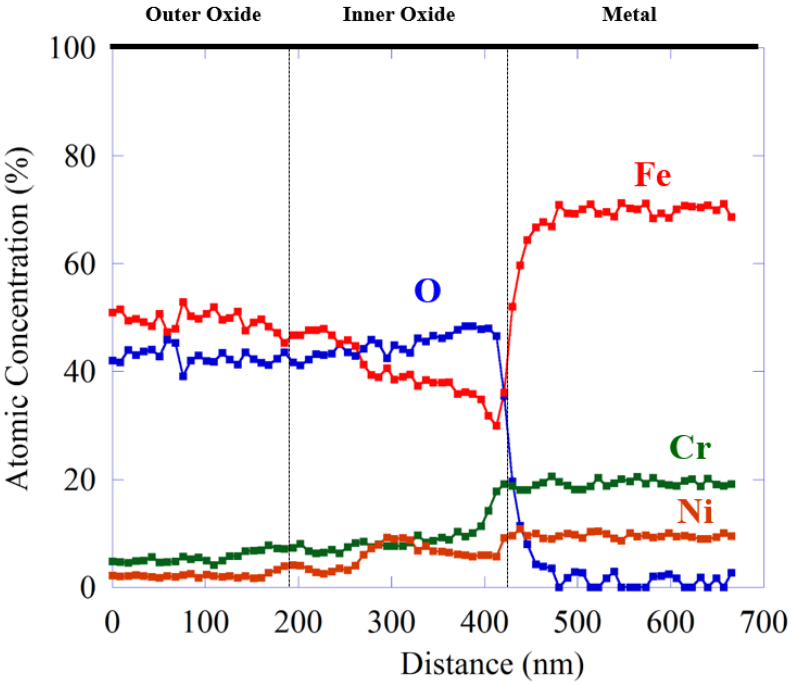
Outer Oxide
Inner Oxide
Metal
Fe
O
Cr
Ni
Atomic Concentration (%)
Distance (nm)
0
20
40
60
80
100
0
100
200
300
400
500
600
700

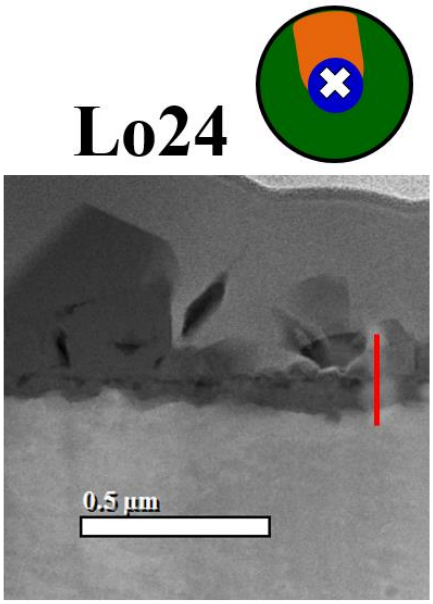
Lo24
0.5 µm

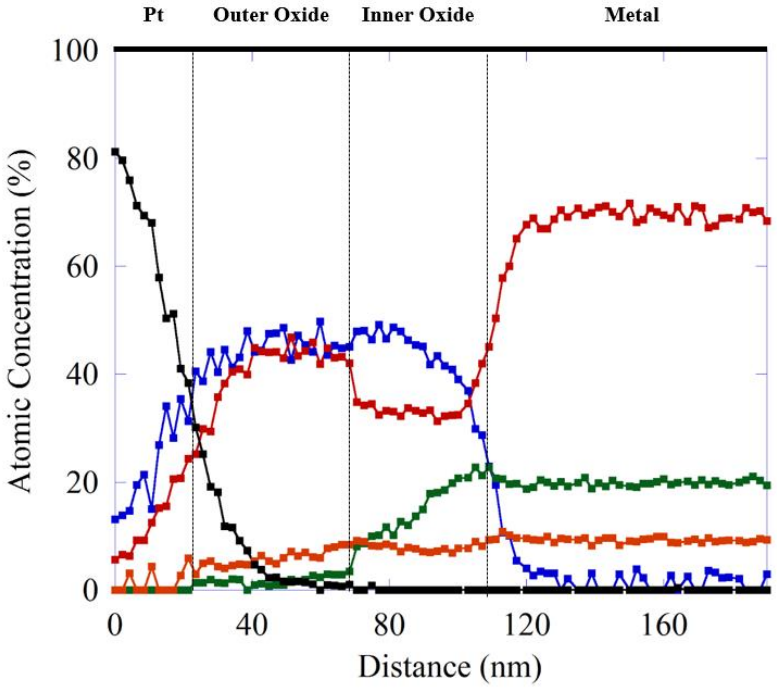
Pt
Outer Oxide
Inner Oxide
Metal
Atomic Concentration (%)
Distance (nm)
0
20
40
60
80
100
0
40
80
120
160

Un72

Un72

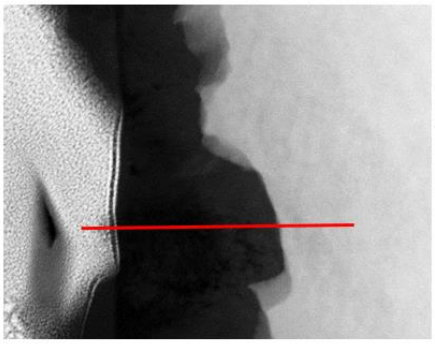

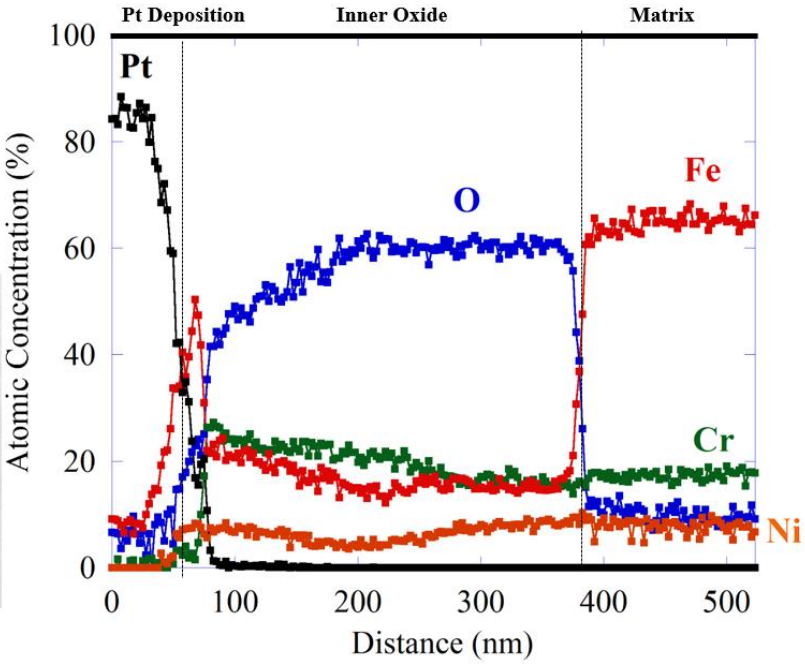
Pt Deposition
Inner Oxide
Matrix
Pt
O
Fe
Cr
Ni
Atomic Concentration (%)
Distance (nm)
0
20
40
60
80
100
0
100
200
300
400
500

Un72

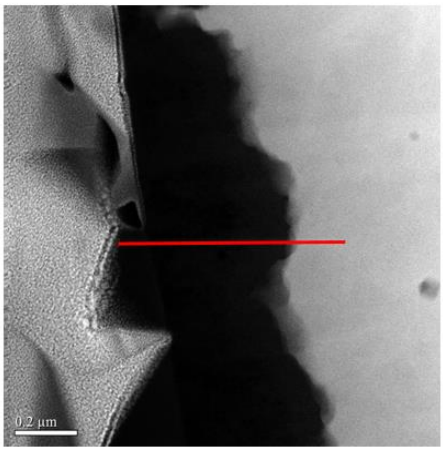
0.2 µm

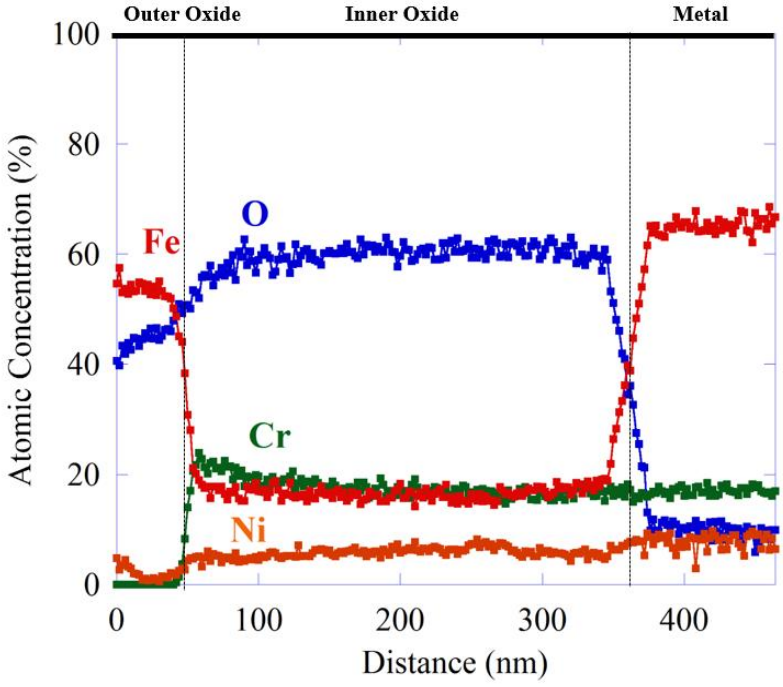
Outer Oxide
Inner Oxide
Metal
O
Fe
Cr
Ni
Atomic Concentration (%)
Distance (nm)
0
20
40
60
80
100
0
100
200
300
400

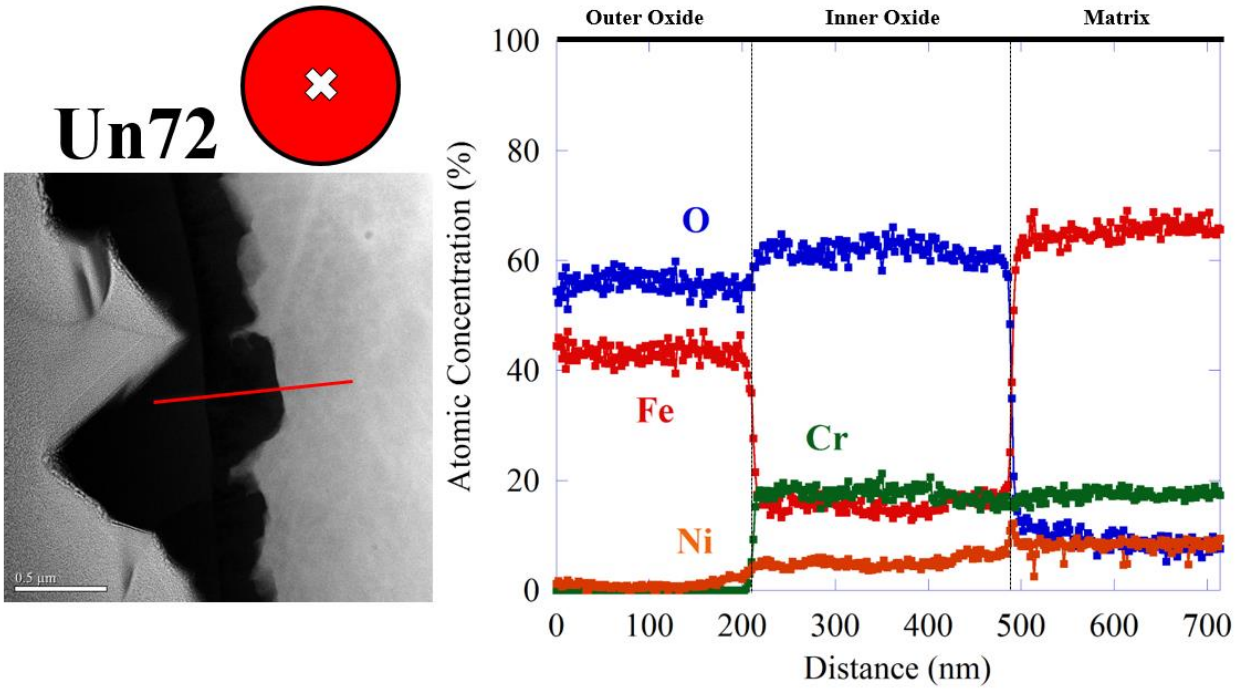
Un72
0.5 µm
Outer Oxide
Inner Oxide
Matrix
Atomic Concentration (%)
Distance (nm)
O
Fe
Cr
Ni
0
20
40
60
80
100
0
100
200
300
400
500
600
700

Pr24 Unirr

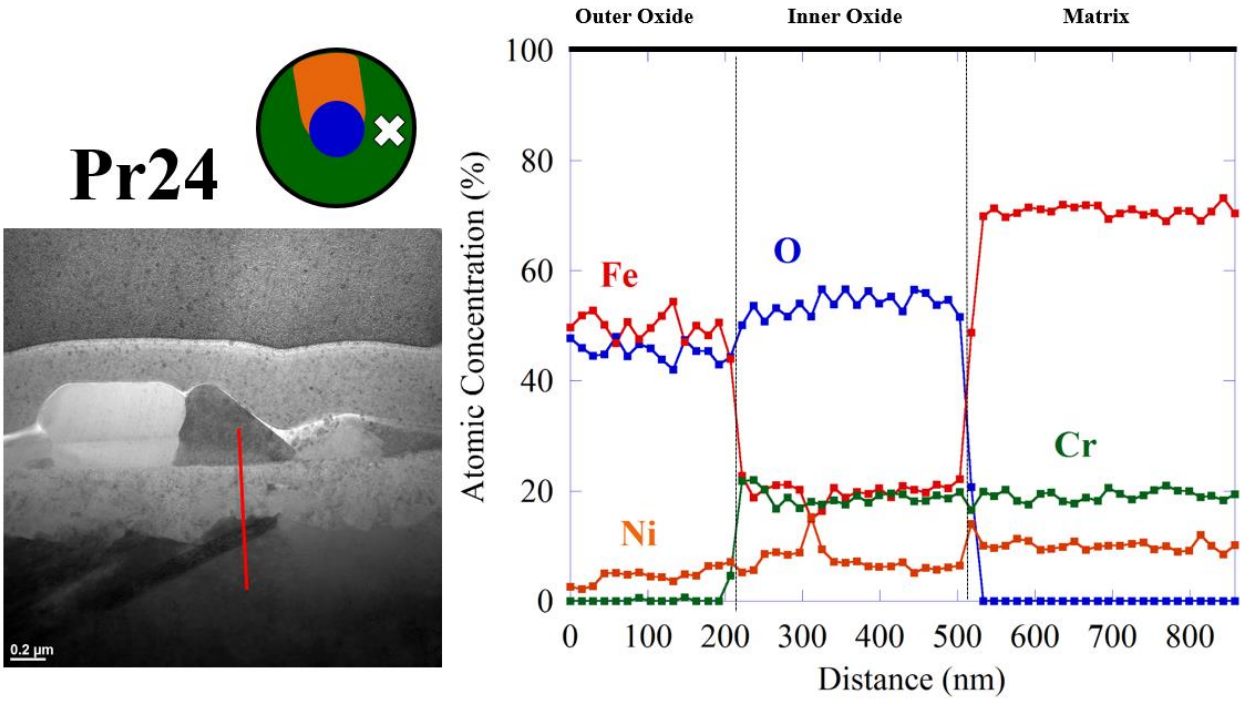
Pr24
0.2 µm
Outer Oxide
Inner Oxide
Matrix
Atomic Concentration (%)
Distance (nm)
O
Fe
Cr
Ni
0
20
40
60
80
100
0
100
200
300
400
500
600
700
800

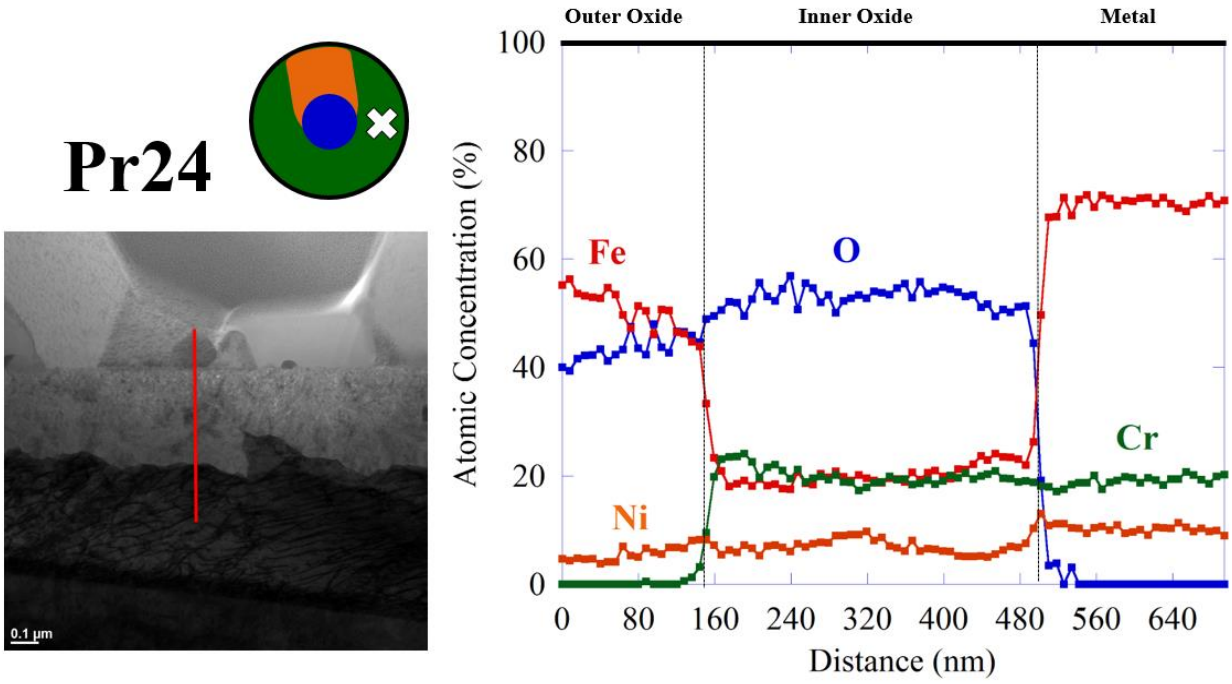
Pr24
0.1 µm
Outer Oxide
Inner Oxide
Metal
Fe
O
Cr
Ni
Atomic Concentration (%)
Distance (nm)

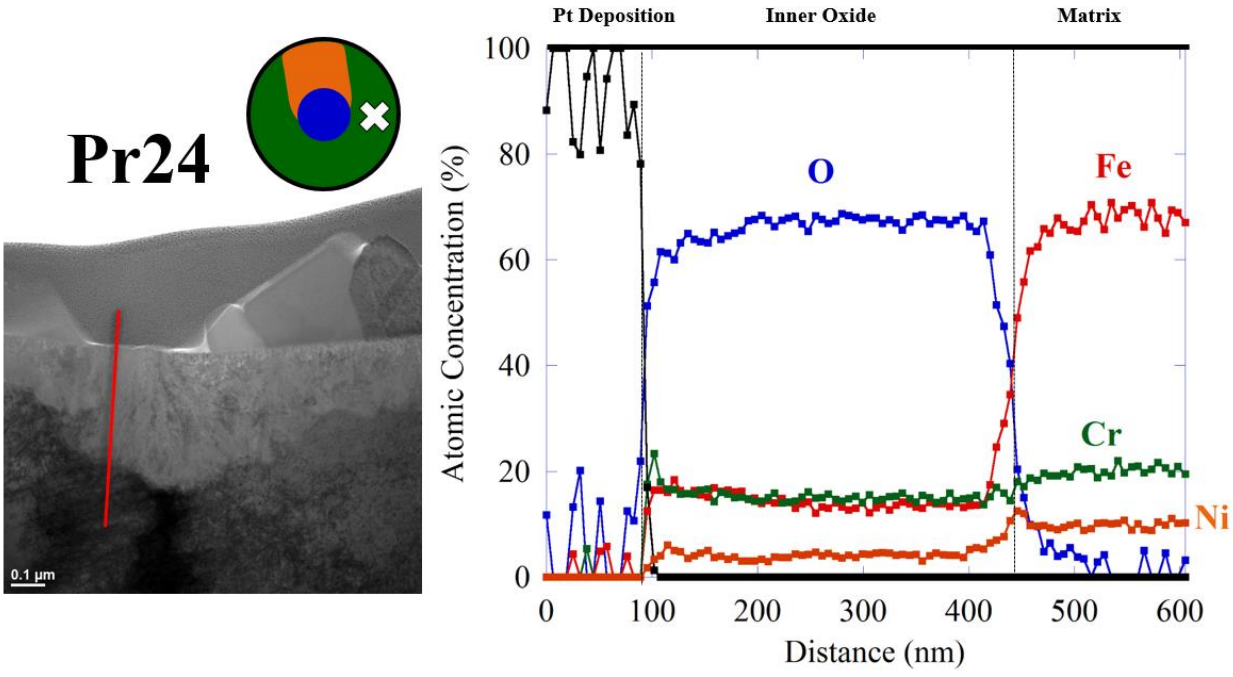
Pr24
0.1 µm
Pt Deposition
Inner Oxide
Matrix
O
Fe
Cr
Ni
Atomic Concentration (%)
Distance (nm)

Pr24 Flow

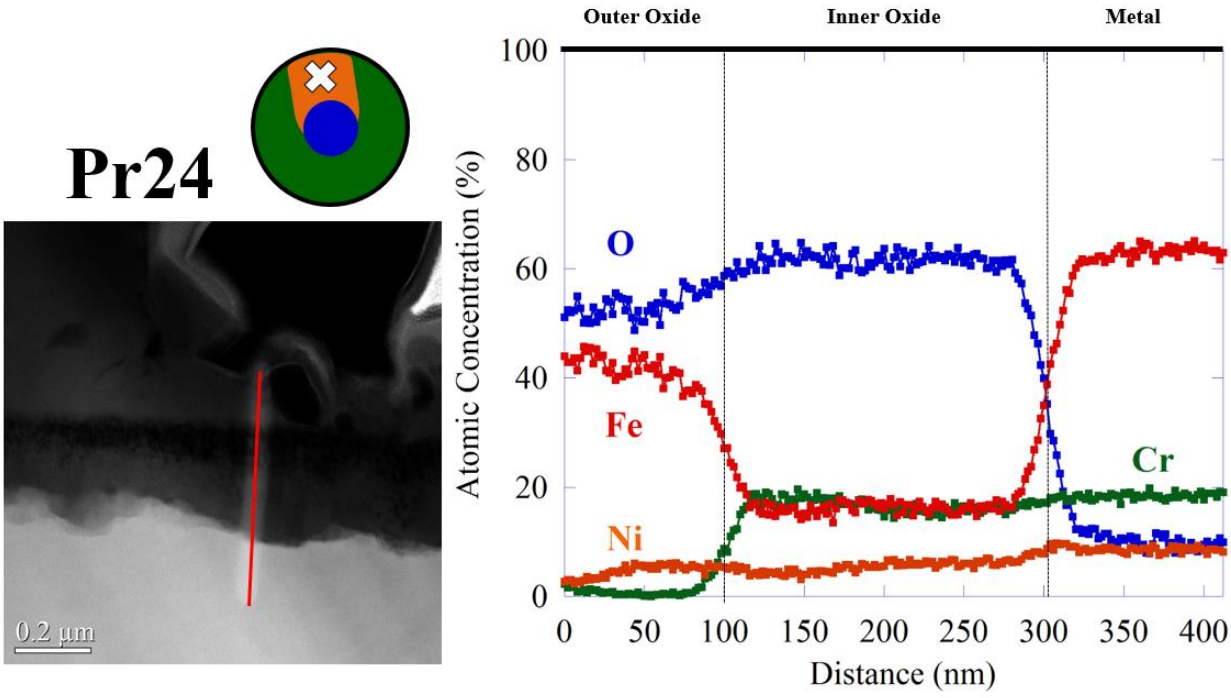
Pr24
0.2 µm
Outer Oxide
Inner Oxide
Metal
Atomic Concentration (%)
Distance (nm)
O
Fe
Cr
Ni

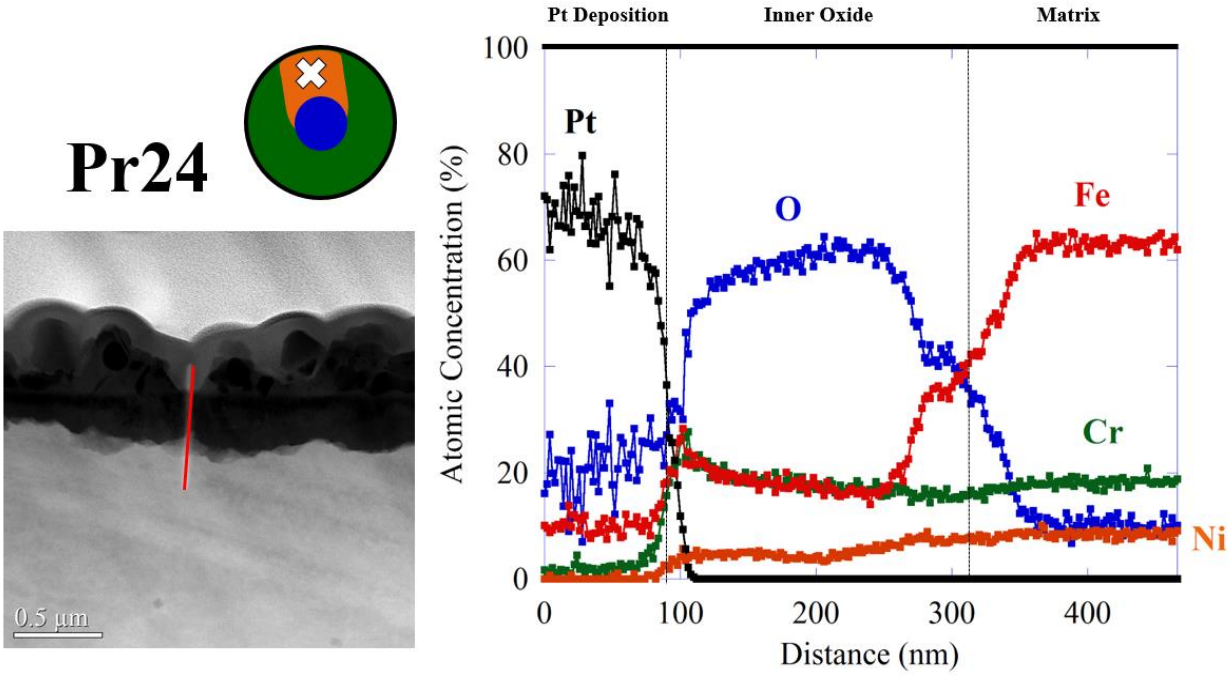
Pr24
0.5 µm
Pt Deposition
Inner Oxide
Matrix
Atomic Concentration (%)
Distance (nm)
Pt
O
Fe
Cr
Ni

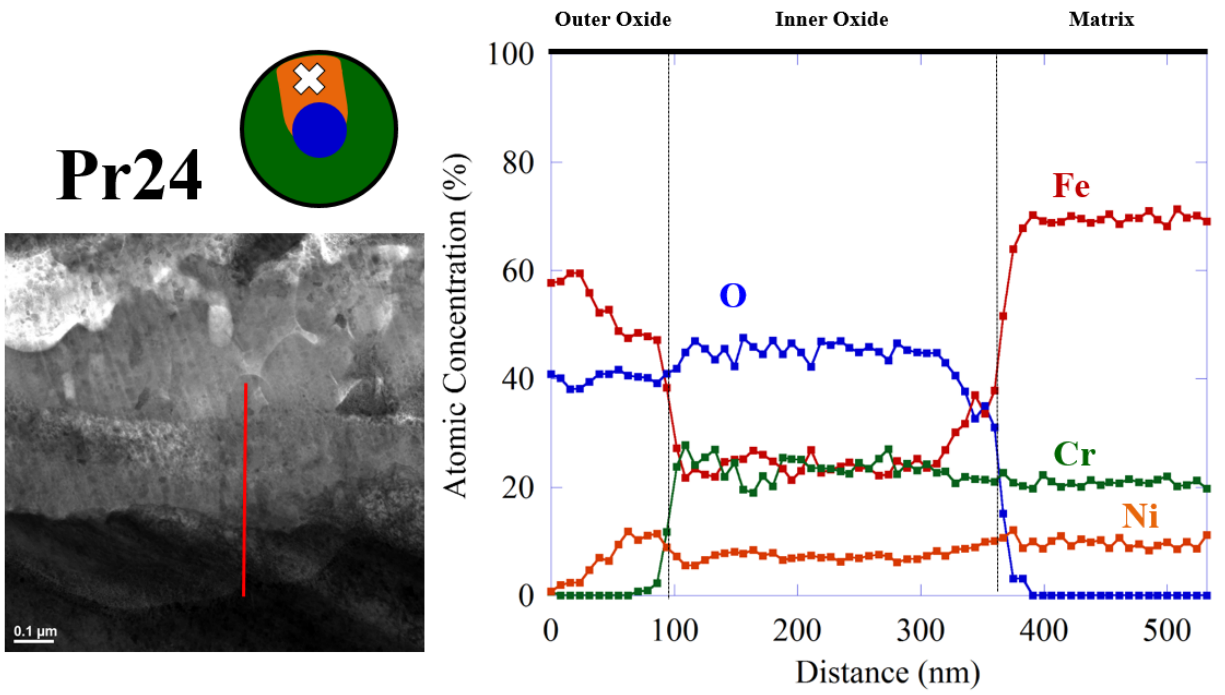
Pr24
0.1 µm
Outer Oxide
Inner Oxide
Matrix
Atomic Concentration (%)
Distance (nm)
O
Fe
Cr
Ni

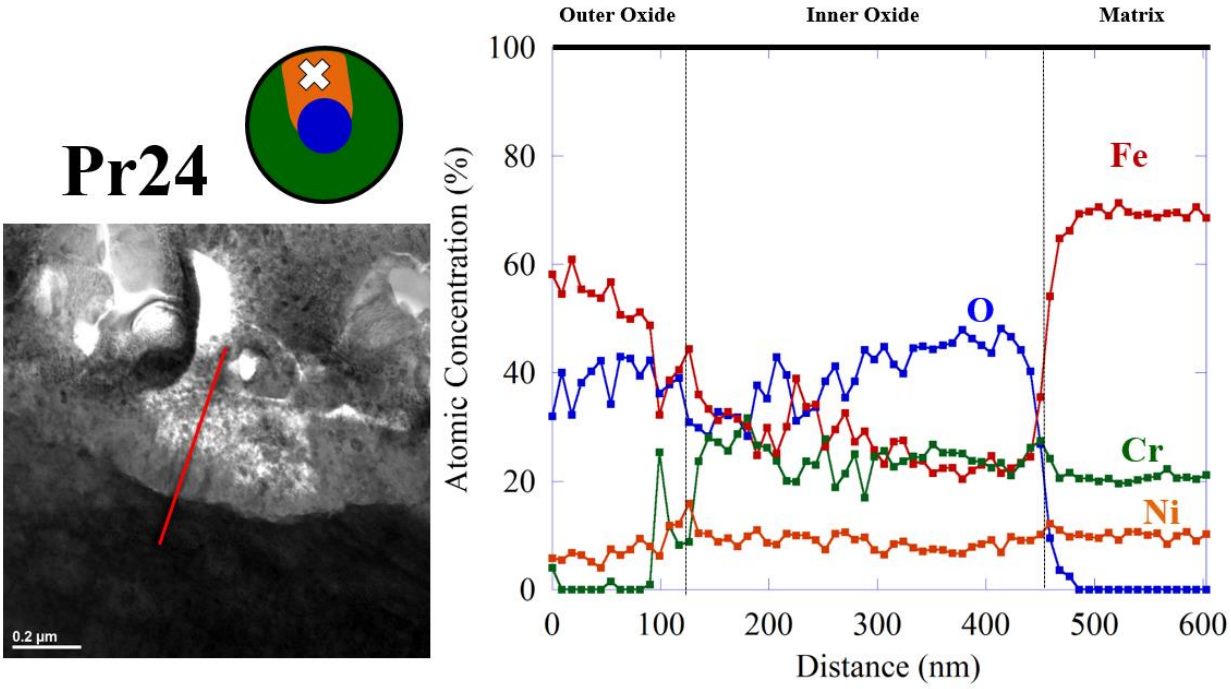
Pr24
0.2 µm
Outer Oxide
Inner Oxide
Matrix
Atomic Concentration (%)
Distance (nm)
O
Fe
Cr
Ni

Pr24 Irr

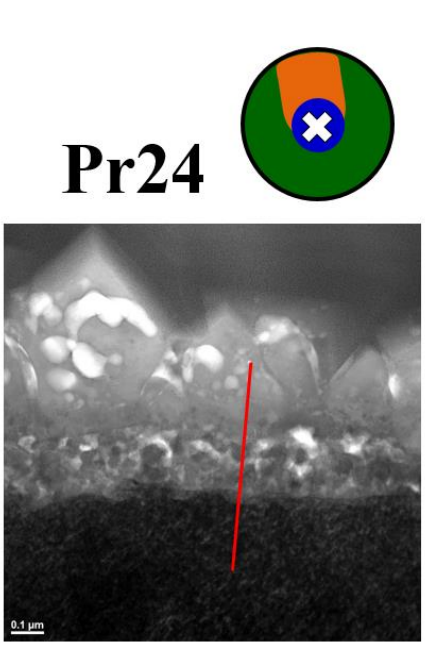
Pr24
0.1 µm

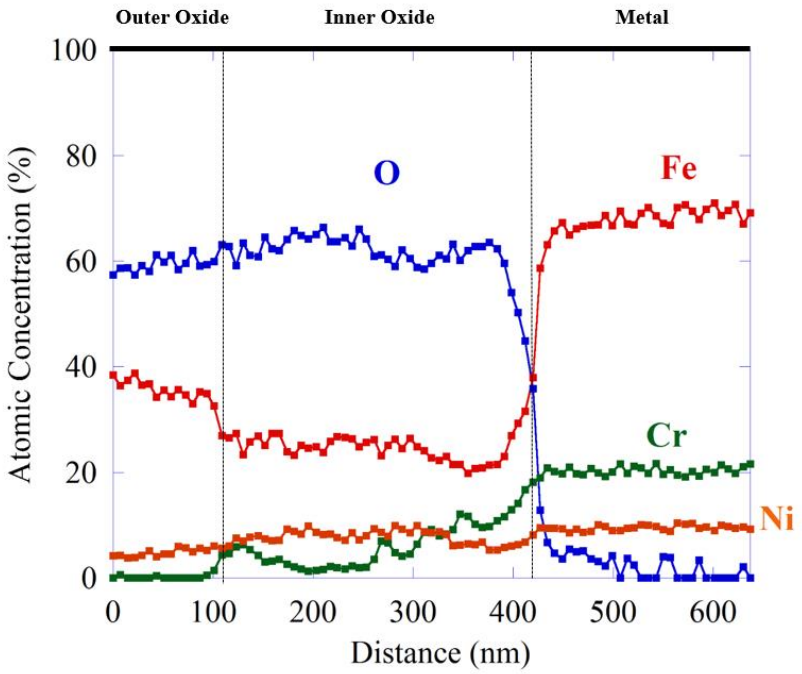
Outer Oxide
Inner Oxide
Metal
O
Fe
Cr
Ni
Atomic Concentration (%)
Distance (nm)
0
20
40
60
80
100
0
100
200
300
400
500
600

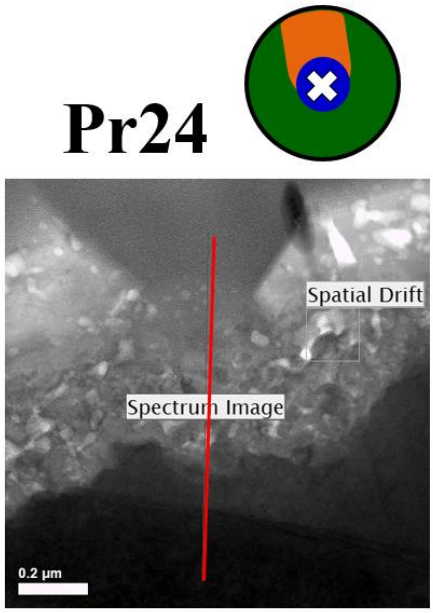
Pr24
Spatial Drift
Spectrum Image
0.2 µm

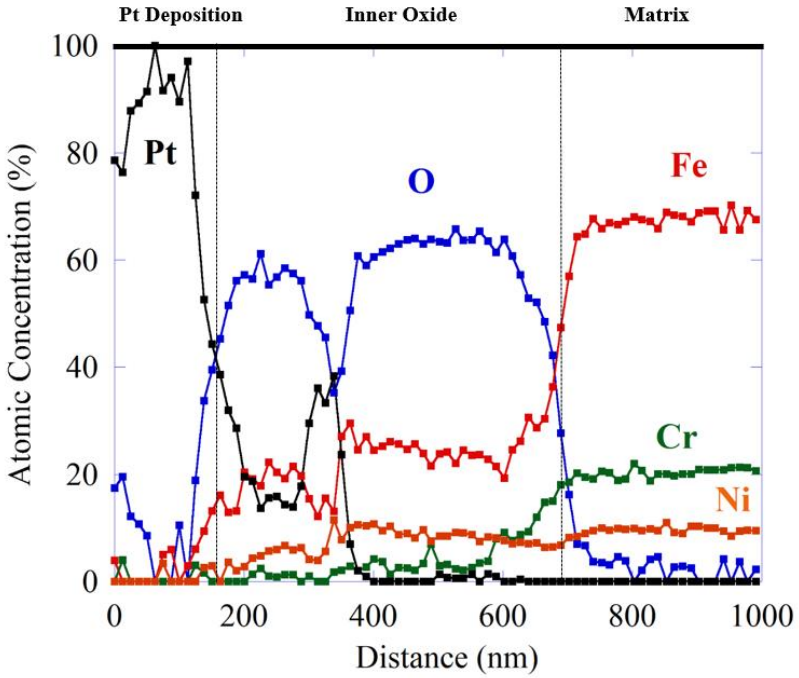
Pt Deposition
Inner Oxide
Matrix
Pt
O
Fe
Cr
Ni
Atomic Concentration (%)
Distance (nm)
0
20
40
60
80
100
0
200
400
600
800
1000

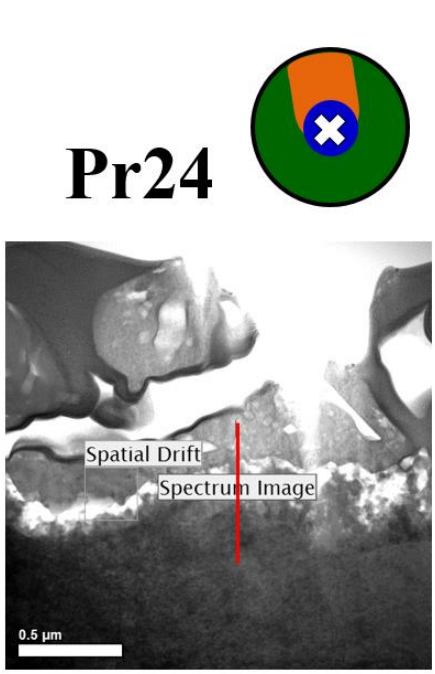
Pr24
Spatial Drift
Spectrum Image
0.5 µm

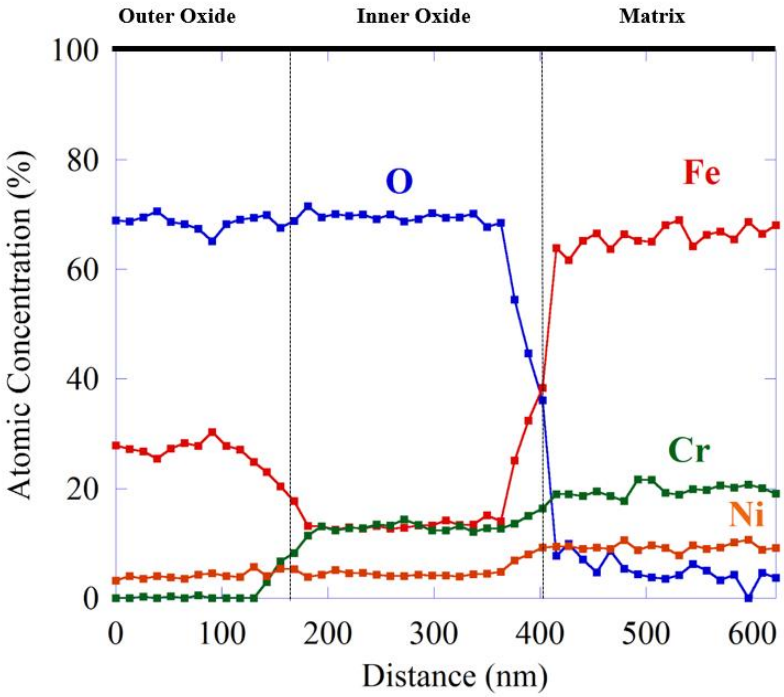
Outer Oxide
Inner Oxide
Matrix
Atomic Concentration (%)
Distance (nm)
O
Fe
Cr
Ni
0
20
40
60
80
100
0
100
200
300
400
500
600

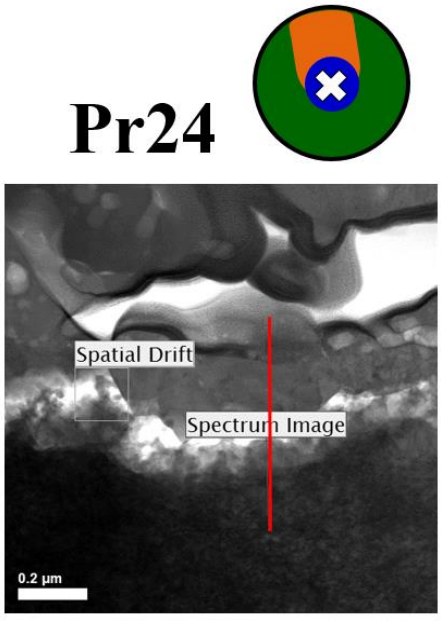
Pr24
Spatial Drift
Spectrum Image
0.2 µm

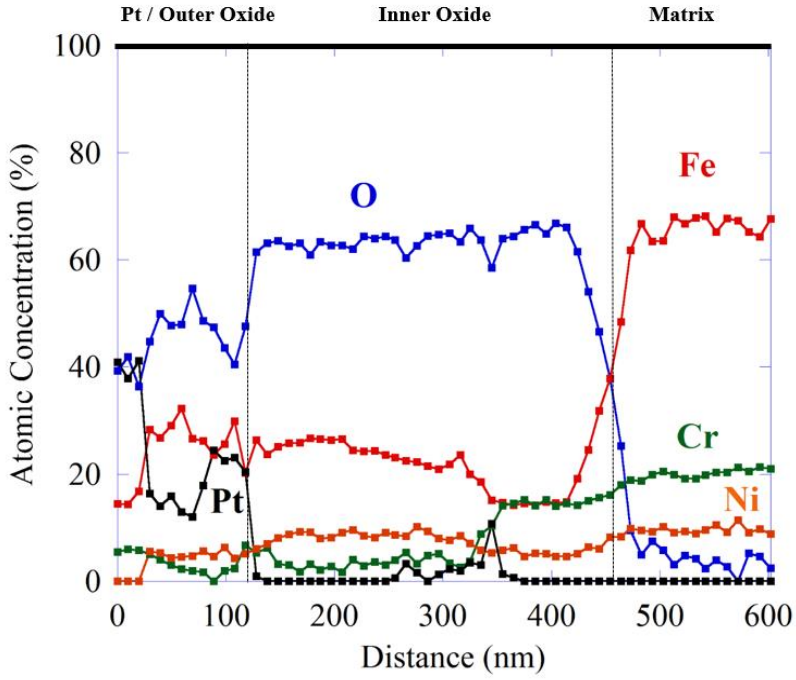
Pt / Outer Oxide
Inner Oxide
Matrix
Atomic Concentration (%)
Distance (nm)
O
Fe
Cr
Ni
Pt
0
20
40
60
80
100
0
100
200
300
400
500
600

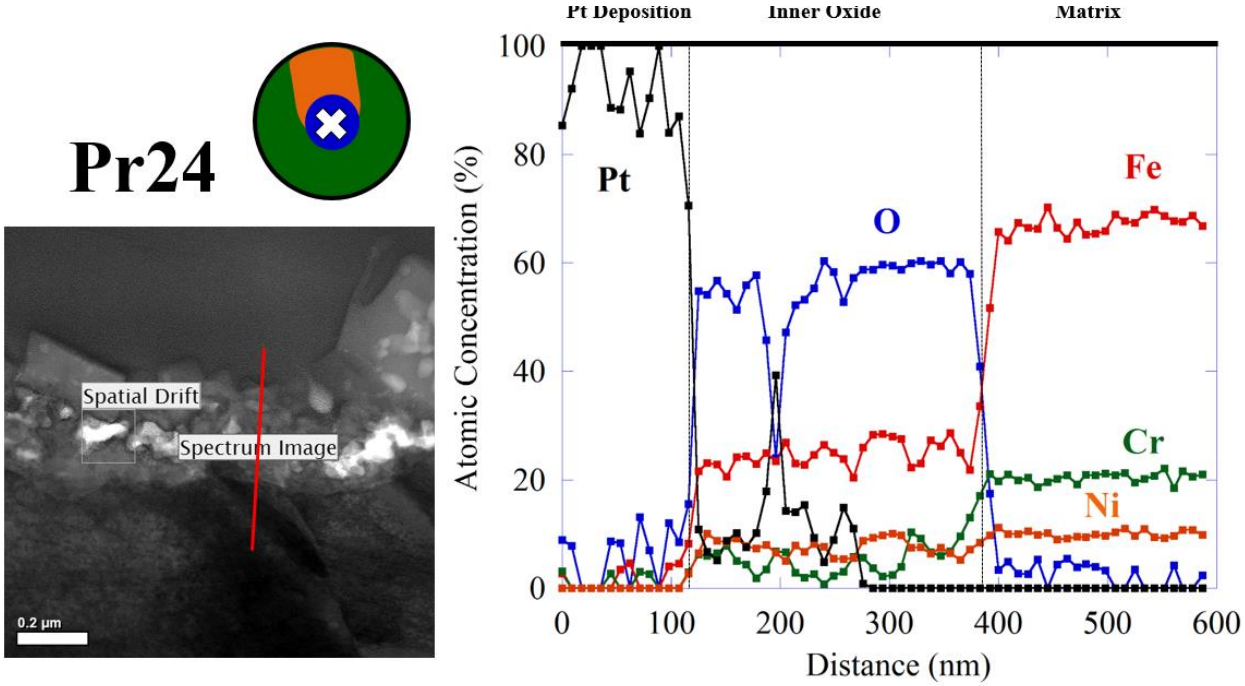
Pr24
Spatial Drift
Spectrum Image
0.2 µm
Pt Deposition
Inner Oxide
Matrix
Pt
O
Fe
Cr
Ni
Atomic Concentration (%)
Distance (nm)

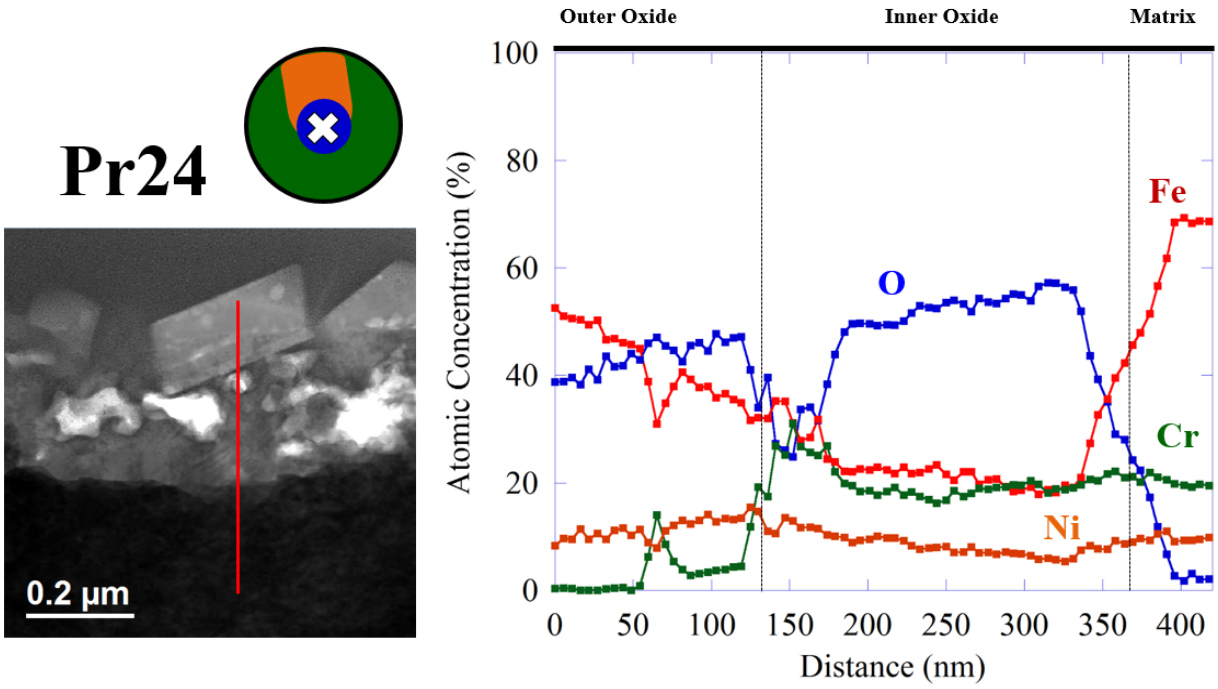
Pr24
0.2 µm
Outer Oxide
Inner Oxide
Matrix
O
Fe
Cr
Ni
Atomic Concentration (%)
Distance (nm)

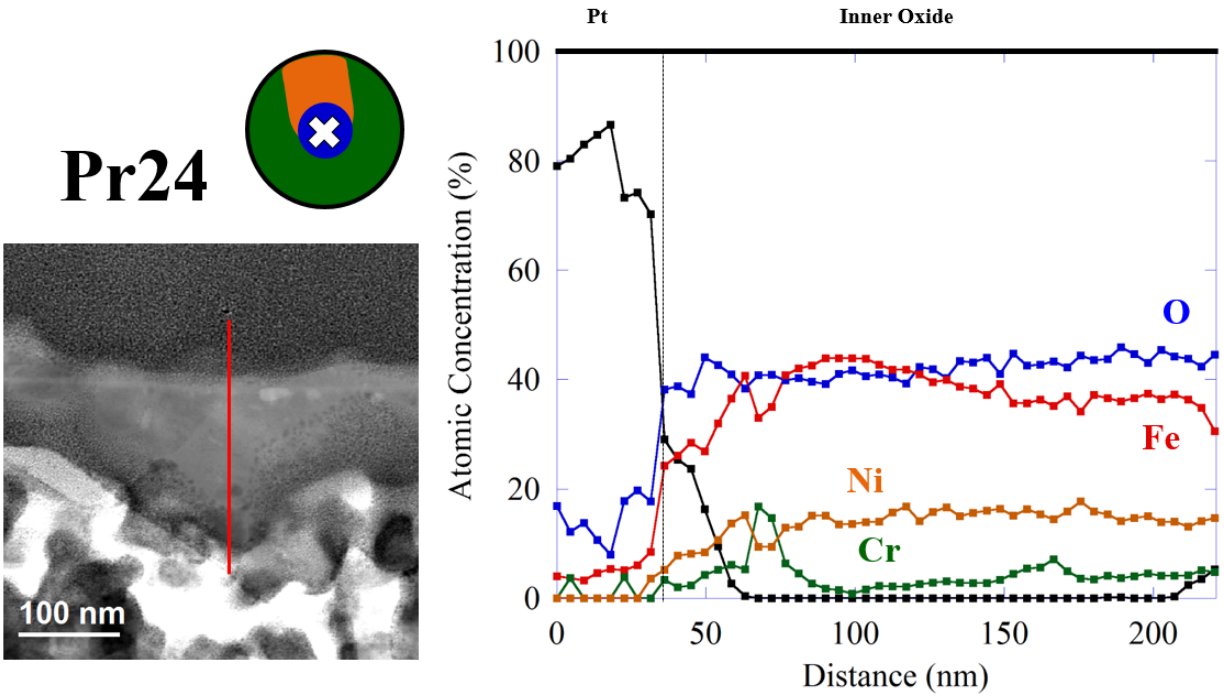
Pr24
100 nm
Pt
Inner Oxide
Atomic Concentration (%)
Distance (nm)
O
Fe
Ni
Cr

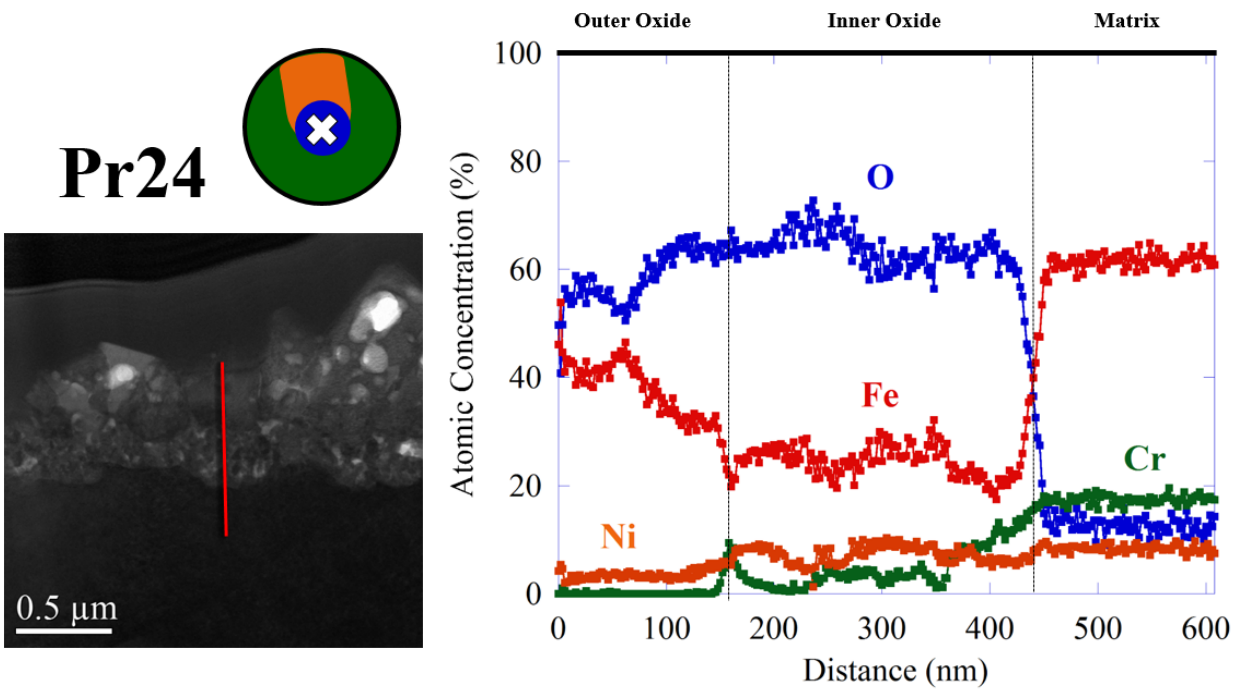
Pr24
0.5 µm
Outer Oxide
Inner Oxide
Matrix
Atomic Concentration (%)
Distance (nm)
O
Fe
Cr
Ni

REFERENCES

[1] U. EIA, “Generation by Utility Scale Facilities.” [Online]. Available: https://www.eia.gov/tools/faqs/faq.cfm?id=427&t=3.

[2] IEA, “Key World Energy Statistics,” 2015.

[3] M. B. Lewis and J. D. Hunn, “Investigations of ion radiation effects at metal/liquid interfaces,” *J. Nucl. Mater.*, vol. 265, no. 3, pp. 325–330, 1999.

[4] S. Lapuerta, N. Moncoffre, N. Millard-Pinard, H. Jaffrézic, N. Bérerd, and D. Crusset, “Role of proton irradiation and relative air humidity on iron corrosion,” *J. Nucl. Mater.*, vol. 352, no. 1–3, pp. 174–181, Jun. 2006.

[5] M. Kawaguchi, K. Ishigure, N. Fujita, and K. Oshima, “Effect of radiation on release of corrosion products in high temperature aqueous system,” *Radiat. Phys. Chem.*, vol. 18, no. 3–4, pp. 733–740, 1981.

[6] U. Kingdom, R. C. Asher, D. Davies, and T. B. A. Kirstein, “The corrosion of some zirconium alloys under radiation in moist carbon dioxide-air mixtures,” *J. Nucl. Mater.*, vol. 49, no. 2, pp. 189–196, 1973.

[7] A. I. A. Almarshad and A. C. Klein, “A model for waterside oxidation of Zircaloy fuel cladding in pressurized water reactors,” *J. Nucl. Mater.*, vol. 183, no. 3, pp. 186–194, 1991.

[8] D. H. Bradhurst, P. J. Shirvington, and P. M. Heuer, “The Effects of Radiation and Oxygen on the Aqueous Oxidation of Zirconium and its Alloys at 290˚C,” *J. Nucl. Mater.*, vol. 46, no. 1, pp. 53–76, 1972.

[9] H. Stehle, F. Garzarollc, A. Garde, P. G. Smerd, and R. Stehle, “Characterization of ZxOi Films Formed In-Reactor and Ex-Reactor to Study the Factors Contributing to the In-Reactor Waterside Corrosion of Zircaloy,” 1984.

[10] S. Lapuerta, N. Moncoffre, H. Jaffrezic, N. Millard-Pinard, N. Bererd, C. Esnouf, and D. Crusset, “Use of the point defect model to interpret the iron oxidation kinetics under proton irradiation,” *J. Appl. Phys.*, vol. 101, no. 6, pp. 64905–64907, 2007.

[11] J. Robertson, “The mechanism of high temperature aqueous corrosion of stainless steels,” *Corros. Sci.*, vol. 32, no. 4, pp. 443–465, 1991.

[12] B. Stellwag, “The mechanism of oxide film formation on austenitic stainless steels in high temperature water,” *Corros. Sci.*, vol. 40, no. 2–3, pp. 337–370, 1998.

[13] G. S. Was, S. Teysseyre, and Z. Jiao, “Corrosion of Austenitic Alloys in Supercritical Water,” *Corros. J. Sci. Eng.*, vol. 62, no. 11, pp. 989–1005, 2006.

[14] S. Lozano-Perez, K. Kruska, I. Iyengar, T. Terachi, and T. Yamada, “The role of cold work and applied stress on surface oxidation of 304 stainless steel,” *Corros. Sci.*, vol. 56, no. 0, pp. 78–85, Mar. 2012.

[15] S. Cissé, L. Laffont, B. Tanguy, M.-C. Lafont, and E. Andrieu, “Effect of surface preparation on the corrosion of austenitic stainless steel 304L in high temperature steam and simulated PWR primary water,” *Corros. Sci.*, vol. 56, pp. 209–216, Mar. 2012.

[16] T. S. Shunsuke Uchida Yusuke Morishima, Tatsuya Hirose, Takahiro Miyazawa, Nagao Kakinuma, Yoshiyuki Satoh, Naoshi Usui, Yoichi Wada, "Effects of Hydrogen Peroxide and Oxygen on Corrosion of Stainelss Steel in High Temperature Water," *Proc. 12th Int. Conf. Environ. Degrad. Mater. Nucl. Power Syst.*, 2005.

[17] X. Gao, X. Wu, Z. Zhang, H. Guan, and E. Han, "Characterization of oxide films grown on 316L stainless steel exposed to H2O2-containing supercritical water," *J. Supercrit. Fluids*, vol. 42, no. 1, pp. 157–163, Aug. 2007.

[18] W. Kuang, X. Wu, and E.-H. Han, "Influence of dissolved oxygen concentration on the oxide film formed on 304 stainless steel in high temperature water," *Corros. Sci.*, vol. 63, no. 0, pp. 259–266, Oct. 2012.

[19] H. Sun, X. Wu, E.-H. Han, and Y. Wei, "Effects of pH and dissolved oxygen on electrochemical behavior and oxide films of 304SS in borated and lithiated high temperature water," *Corros. Sci.*, vol. 59, no. 0, pp. 334–342, Jun. 2012.

[20] Y. J. Kim, "Analysis of oxide film formed on type 304 stainless steel in 288 C water containing oxygen, hydrogen, and hydrogen peroxide," *J. Name Corros. J. Vol. 55; J. Issue 1; Other Inf. DN Pap. Present. Corros. March 1996, Denver, CO (US); PBD Jan 1999*, vol. 55, no. 1, p. Medium: X; Size: pp. 81–88, 1999.

[21] D. M. Bartels and A. J. Elliot, "The Reaction Set, Rate Constants and g-Values for the Simulation of the Radiolysis of Light Water over the Range 20' to 350°C Based on Information Available in 2008," *AECL, Nucl. Platf. Res. Dev.*, no. 153–127160–450–001 Revision 0, 2009.

[22] M. Serrano, “No Title,” Madrid, 2014.

[23] A. International, “ASTM Standard 751-08,” 2007.

[24] F. H. Keating, *Chromium-nickel austenitic steels*. London: Butterworths Scientific Publications, 1956.

[25] A. J. Sedriks and Electrochemical Society., *Corrosion of stainless steels*, 2nd ed. New York: Wiley, 1996.

[26] J. G. Parr and A. Hanson, *Introduction to stainless steel*. Metals Park, Ohio: American Society for Metals, 1965.

[27] D. R. Harries, “Physical metallurgy of Fe-Cr-Ni austenitic steels,” *Proc. Int. Conf. Mech. Behav. Nucl. Appl. Stainl. steel Elev. Temp.*, p. 253, 1982.

[28] R. A. Lula and J. G. Parr, *Stainless steel*. Metals Park, Ohio: American Society for Metals, 1986.

[29] J. Beddoes and J. G. Parr, *Introduction to stainless steels*, 3rd ed. Materials Park, OH: ASM International, 1999.

[30] A. M. Parshin, *Structure, strength, and radiation damage of corrosion-resistant steels and alloys*, no. [1]. La Grange Park, Ill.: American Nuclear Society, 1996.

[31] L. M. Wang, W. L. Gong, N. Bordes, and R. C. Ewing, “A comparative study on ion-beam induced effects in spinel structure types,” in *Ion Beam Modification of Materials*, 1996, pp. 1073–1076.

[32] G. C. Allen, J. A. Jutson, and P. A. Tempest, “Characterization of nickel-chromium-iron

spinel-type oxides," *J. Nucl. Mater.*, vol. 158, no. 0, pp. 96–107, 1988.

[33] O. Kubashewski and B. E. Hopkins, *Oxidation of Metals and Alloys*, 2nd ed. 1962.

[34] N. E. Hakiki, M. F. Montemor, M. G. S. Ferreira, and M. Da Cunha Belo, "Chemical composition and electronic structure of the oxide films formed on 316L stainless steel and nickel based alloys in high temperature aqueous environments," *Corros. Sci.*, vol. 42, no. 9, pp. 1635–1650, 2000.

[35] M. da Cunha Belo, M. Walls, N. E. Hakiki, J. Corset, E. Picquenard, G. Sagonb, and D. Noel, "Composition, structure and properties of the oxide films formed on the stainless steel 316L in a primary type PWR environment," *Corros. Sci.*, vol. 40, no. 2–3, pp. 447–463, Feb. 1998.

[36] N. E. Hakiki, M. F. Montemor, M. G. S. Ferreira, and M. Da Cunha Belo, "Semiconducting properties of thermally grown oxide films on AISI 304 stainless steel," *Corros. Sci.*, vol. 42, no. 4, pp. 687–702, Apr. 2000.

[37] J. Kieffer, "Kinetic Processes in Materials." Unpublished, 2004.

[38] P. Kofstad, *High Temperature Corrosion*. Elsevier, 1988.

[39] D. D. Macdonald, "The Point Defect Model for the Passive State," *J. Electrochem. Soc.*, vol. 139, no. 12, pp. 3434–3449, 1992.

[40] N. Birks and G. H. Meier, *Introduction to the High Temperature Oxidation of Metals*. 1983.

[41] C. Wagner, "The formation of thin oxide films on metals," *Corros. Sci.*, vol. 13, no. 1, pp.

23–52, 1973.

[42] S. Ghosh, M. K. Kumar, and V. Kain, “High temperature oxidation behavior of AISI 304L stainless steel—Effect of surface working operations,” *Appl. Surf. Sci.*, vol. 264, no. 0, pp. 312–319, Jan. 2013.

[43] R. Dieckmann, T. O. Mason, J. D. Hodge, and H. Schmalzried, “Defects and Cation Diffusion in Magnetite (III.) Tracerdiffusion of Foreign Tracer Cations as a Function of Temperature and Oxygen Potential,” *Berichte der Bunsengesellschaft für Phys. Chemie*, vol. 82, no. 8, pp. 778–783, 1978.

[44] A. F. Smith, “The tracer diffusion of transition metals in duplex oxide grown on a T316 stainless steel,” *Corros. Sci.*, vol. 21, no. 7, pp. 517–529, Jan. 1981.

[45] A. . G. Crouch and J. Robertson, “Creep and oxygen diffusion in magnetite,” *Acta Metall. Mater.*, vol. 38, no. 12, pp. 2567–2572, Dec. 1990.

[46] K. Kruska, S. Lozano-Perez, D. W. Saxey, T. Terachi, T. Yamada, and G. D. W. W. Smith, “Nanoscale characterisation of grain boundary oxidation in cold-worked stainless steels,” *Corros. Sci.*, vol. 63, no. 0, pp. 225–233, Oct. 2012.

[47] S. Lozano-Perez, D. W. Saxey, T. Yamada, and T. Terachi, “Atom-probe tomography characterization of the oxidation of stainless steel,” *Scr. Mater.*, vol. 62, no. 11, pp. 855–858, Jun. 2010.

[48] B. Beverskog and I. Puigdomenech, “Pourbaix Diagrams for the Ternary System of Iron-Chromium-Nickel,” *Corrosion*, vol. 55, no. 11, pp. 1077–1087, 1999.

[49] D. Cubicciotti, “Potential-pH diagrams for alloy-water systems under LWR conditions,” *J.*

Nucl. Mater., vol. 201, pp. 176–183, 1993.

[50] J. Nakano, T. Sato, C. Kato, M. Yamamoto, T. Tsukada, and Y. Kaji, "Effects of temperature on stress corrosion cracking behavior of stainless steel and outer oxide distribution in cracks due to exposure to high-temperature water containing hydrogen peroxide," *J. Nucl. Mater.*, vol. 444, no. 1–3, pp. 454–461, Jan. 2014.

[51] V. A. Maroni, C. A. Melendres, T. F. Kassner, R. Kumar, and S. Siegel, "Spectroscopic characterization of oxide films on type 304 SS exposed to water at 289° C: correlation with the Fe-Cr-H2O pourbaix diagram," *J. Nucl. Mater.*, vol. 172, no. 1, pp. 13–18, Jun. 1990.

[52] C. S. Kumai and T. M. Devine, "Influence of Oxygen Concentration of 288°C Water and Alloy Composition on the Films Formed on Fe-Ni-Cr Alloys," *Corrosion*, vol. 63, no. 12, pp. 1101–1113, 2007.

[53] W. Kuang, X. Wu, E.-H. Han, and L. Ruan, "Effect of nickel ion from autoclave material on oxidation behaviour of 304 stainless steel in oxygenated high temperature water," *Corros. Sci.*, vol. 53, no. 3, pp. 1107–1114, Mar. 2011.

[54] J. Robertson, "Corrosion Science," vol. 32, no. 4, pp. 443–465, 1991.

[55] S. E. Ziemniak, L. M. Anovitz, R. A. Castelli, and W. D. Porter, "Thermodynamics of Cr2O3, FeCr2O4, ZnCr2O4, and CoCr2O4," *J. Chem. Thermodyn.*, vol. 39, no. 11, pp. 1474–1492, Nov. 2007.

[56] B. D. Hosterman, "Raman Spectroscopic Study of Solid Solution Spinel Oxides," University of Nevada, Las Vegas, 2011.

[57] V. A. Kurepin, D. A. Kulik, A. Hiltpold, and M. Nicolet, “Thermodynamic modeling of Fe-Cr-Ni spinel formation at the light-water reactor conditions,” 2002.

[58] S. E. Ziemniak and R. A. Castelli, “Immiscibility in the Fe3O4–FeCr2O4 spinel binary,” *J. Phys. Chem. Solids*, vol. 64, no. 11, pp. 2081–2091, Nov. 2003.

[59] J. Xu, X. Wu, and E.-H. Han, “The evolution of electrochemical behaviour and oxide film properties of 304 stainless steel in high temperature aqueous environment,” *Electrochim. Acta*, vol. 71, no. 0, pp. 219–226, Jun. 2012.

[60] Q. W. Knapp and J. C. Wren, “Film formation on type-316L stainless steel as a function of potential: Probing the role of gamma-radiation,” *Electrochim. Acta*, vol. 80, pp. 90–99, Oct. 2012.

[61] * F. Di Quarto, C. Sunseri, S. Piazza, and and M. C. Romano, “Semiempirical Correlation between Optical Band Gap Values of Oxides and the Difference of Electronegativity of the Elements. Its Importance for a Quantitative Use of Photocurrent Spectroscopy in Corrosion Studies,” *J. Phys. Chem. B*, vol. 101, no. 14, pp. 2519–2525, 1997.

[62] I. Balberg and J. I. Pankove, “Optical Measurements on Magnetite Single Crystals,” *Phys. Rev. Lett.*, vol. 27, no. 9, pp. 596–599, Aug. 1971.

[63] K. Kanjana, K. S. Haygarth, W. Wu, and D. M. Bartels, “Laboratory studies in search of the critical hydrogen concentration,” *Radiat. Phys. Chem.*, vol. 82, no. 0, pp. 25–34, Jan. 2013.

[64] S. Sanguanmith, Y. Muroya, J. Meesungnoen, M. Lin, Y. Katsumura, L. Mirsaleh Kohan, D. a. A. Guzonas, C. R. R. Stuart, and J.-P. P. Jay-Gerin, “Low-linear energy transfer

radiolysis of liquid water at elevated temperatures up to 350 °C: Monte-Carlo simulations," *Chem. Phys. Lett.*, vol. 508, no. 4–6, pp. 224–230, May 2011.

[65] J. Meesungnoen, J.-P. Jay-Gerin, A. Filali-Mouhim, and S. Mankhetkorn, "Monte-Carlo calculation of the primary yields of H 2 O 2 in the 1 H + , 2 H + , 4 He 2+ , 7 Li 3+ , and 12 C 6+ radiolysis of liquid water at 25 and 300°C," *Can. J. Chem.*, vol. 80, no. 1, pp. 68–75, Jan. 2002.

[66] H. Stehle, A. M. Garde, P. G. Smerd, and F. Garzaroli, "No Title," *6th Int'l Conf. Zircon. Nucl. Ind.*, vol. Vancouver, 1982.

[67] G. S. Was, *Fundamentals of radiation materials science : metals and alloys*. Berlin: Springer, 2007.

[68] H. Dogo, "POINT DEFECT PROPERTIES IN IRON CHROMIUM ALLOYS," Naval Postgraduate School, 2006.

[69] J. B. Goodenough, "Metallic oxides," *Prog. Solid State Chem.*, vol. 5, pp. 145–399, 1971.

[70] Y. Fukuda and A. Ignatiev, "Characteristic electron energy loss structure for clean and oxidized chromium surfaces," *Solid State Commun.*, vol. 41, no. 8, pp. 597–600, 1982.

[71] R. Nuyts and P. Phariseau, "On the calculation of surface exciton energies in molecular crystals," *Surf. Sci.*, vol. 61, no. 1, pp. 198–206, 1976.

[72] A. L. Shluger, J. L. Gavartin, M. A. Szymanski, A. M. Stoneham, and A. Marshall Stoneham, "Atomistic modelling of radiation effects: Towards dynamics of exciton relaxation," *Nucl. Instruments Methods Phys. Res. Sect. B Beam Interact. with Mater. Atoms*, vol. 166–167, pp. 1–12, 2000.

[73] J. A. Laverne, L. Tandon, V. Uni, and N. Dame, “H 2 Production in the Radiolysis of Water on CeO 2 and ZrO 2,” pp. 380–386, 2002.

[74] L. T. Jay A. LaVerne, “H2 Production in the Radiolysis of Water on UO2 and Other Oxides,” *J. Phys. Chem. B Lett*, vol. 107, pp. 13623–13628, 2003.

[75] J. a LaVerne, “H2 Formation from the Radiolysis of Liquid Water with Zirconia,” *J. Phys. Chem. B Lett.*, vol. 109, no. 12, pp. 5395–5397, 2005.

[76] N. G. Petrik, a B. Alexandrov, and a I. Vall, “Interfacial Energy Transfer during Gamma Radiolysis of Water on the Surface of ZrO2 and Some Other Oxides,” *J. Phys. Chem. B*, vol. 105, no. 25, pp. 5935–5944, 2001.

[77] C. B. Breslin, D. D. Macdonald, J. Sikora, and E. Sikora, “Influence of uv light on the passive behaviour of SS316--effect of prior illumination,” *Electrochim. Acta*, vol. 42, no. 1, pp. 127–136, 1997.

[78] C. B. Breslin and D. D. Macdonald, “The influence of UV light on the dissolution and passive behavior of copper-containing alloys in chloride solutions,” *Electrochim. Acta*, vol. 44, no. 4, pp. 643–651, 1998.

[79] D. D. Lanning Johnson, A.B., Trimble, D.J., Boyd, S.M., “Corrosion and Hydriding of N Reactor Pressure Tubes,” *Zircon. Nucl. Ind.*, vol. 8th Intern, pp. 3–19, 1989.

[80] E. Hillner, J. N. Chirigos, B. A. P. Laboratory, U. S. A. E. Commission, and U. S. D. of C. O. of T. Services, *The effect of lithium hydroxide and related solutions on the corrosion rate of zircalloy in 680F water*. Bettis Atomic Power Laboratory, 1962.

[81] J. a. Davies, B. Domeij, J. P. S. Pringle, and F. Brown, “The Migration of Metal and

Oxygen during Anodic Film Formation," *J. Electrochem. Soc.*, vol. 112, no. 7, pp. 675–680, 1965.

[82] P. Billot, A. Giordand, J. Thomazet, and A. Beslu, "Development of a Mechanistic Model to Assess the External Corrosion of the Zircaloy Claddings in PWRs-," *Proc. 8th Int. Symp. Zircon. Nucl. Ind. ASTM-STP 1023*, p. 165, 1989.

[83] P. Wang and G. S. Was, "Oxidation of Zircaloy-4 during in situ proton irradiation and corrosion in PWR primary water," *J. Mater. Res.*, vol. 30, no. 9, pp. 1335–1348, 2015.

[84] K. Ishigure, H. Ikuse, K. Oshima, N. Fujita, and S. Ono, "The effect of radiation on the release of corrosion products from 304 stainless steel in high temperature water—II: Effects of flow rate and duration of corrosion experiment," *Radiat. Phys. Chem.*, vol. 21, no. 3, pp. 281–287, 1983.

[85] I. Kenkichi, "Radiation chemistry related to nuclear power technology," *Radiat. Phys. Chem.*, vol. 22, no. 1–2, pp. 119–129, 1983.

[86] P. L. Andresen, "Irradiation Assisted Stress Corrosion Cracking," *Stress. Crack. Mater. Perform. Eval. (ASM Int.*, pp. 181–210, 1992.

[87] Y. Wada, A. Watanabe, M. Tachibana, K. Ishida, N. Uetake, S. Uchida, K. Akamine, M. Sambongi, S. Suzuki, and K. Ishigure, "Effects of hydrogen peroxide on intergranular stress corrosion cracking of stainless steel in high temperature water, (IV) effects of oxide film on electrochemical corrosion potential," *J. Nucl. Sci. Technol.*, vol. 38, no. 3, pp. 183–192, Mar. 2001.

[88] D. D. Macdonald, "Viability of Hydrogen Water Chemistry for Protecting In-Vessel

Components of Boiling Water Reactors," *Corrosion*, vol. 48, no. 3, pp. 194–205, 1992.

[89] Y.-J. Kim, "Characterization of he Oxide Film Formed on Type 316 Stainless Steel in 288°C Water in Cyclic Normal and Hydrogen Water Chemistries," *Corros. Sci.*, vol. 51, no. 11, pp. 849–860, 1995.

[90] J. TOPFER, S. AGGARWAL, and R. DIECKMANN, "Point defects and cation tracer diffusion in (CrxFe1 − x)3 − δO4 spinels," *Solid State Ionics*, vol. 81, no. 3–4, pp. 251–266, Nov. 1995.

[91] B. P. Uberuaga, M. Tang, C. Jiang, J. A. Valdez, R. Smith, Y. Wang, and K. E. Sickafus, "Opposite correlations between cation disordering and amorphization resistance in spinels versus pyrochlores," *Nat Commun*, vol. 6, Oct. 2015.

[92] W. G. Cook and R. P. Olive, "Pourbaix diagrams for the iron–water system extended to high-subcritical and low-supercritical conditions," *Corros. Sci.*, vol. 55, pp. 326–331, Feb. 2012.

[93] X. Liu, E.-H. Han, and X. Wu, "Effects of pH value on characteristics of oxide films on 316L stainless steel in Zn-injected borated and lithiated high temperature water," *Corros. Sci.*, vol. 78, pp. 200–207, Jan. 2014.

[94] J. Meesungnoen, J.-P. Jay-gerin, A. Filali-mouhim, and S. Mankhetkorn, "Monte-Carlo calculation of the primary H[radical sign] atom yield in liquid water radiolysis: effects of radiation type and temperature," *Chem. Phys. Lett.*, vol. 335, no. 5–6, pp. 458–464, 2001.

[95] C. B. Breslin, D. D. Macdonald, E. Sikora, and J. Sikora, "Photo-inhibition of pitting corrosion on types 304 and 316 stainless steels in chloride-containing solutions,"

Electrochim. Acta, vol. 42, no. 1, pp. 137–144, 1997.

[96] J. F. Ziegler, "The Stopping and Range of Ions in Matter (SRIM)." 2013.

[97] V. I. Vodyanik, "Design of safety rupture discs," *Chem. Pet. Eng.*, vol. 8, no. 6, pp. 586–588, 1972.

[98] C. Guangnan, S. Huan, H. Shiguang, and B. Baudelet, "Roughening of the free surfaces of metallic sheets during stretch forming," *Mater. Sci. Eng. A*, vol. 128, no. 1, pp. 33–38, 1990.

[99] R. Becker, "Effects of strain localization on surface roughening during sheet forming," *Acta Mater.*, vol. 46, no. 4, pp. 1385–1401, 1998.

[100] D.-K. Leu, S.-H. Sheen, and D.-K. L. and S.-H. Sheen, "Roughening of Free Surface During Sheet Metal Forming," *J. Manuf. Sci. Eng.*, vol. 135, no. 2, p. 24502, Mar. 2013.

[101] A. Parmar, P. B. Mellor, and J. Chakrabarty, "A new model for the prediction of instability and limit strains in thin sheet metal," *Int. J. Mech. Sci.*, vol. 19, no. 7, pp. 389–398, 1977.

[102] M. Baydogan, M. A. Akoy, E. S. Kayali, H. Cimenoglu, and M. A. A. M. BAYDOGAN E. S. KAYALI and H. CIMENOGLU, "Deformation Induced Surface Roughening of Austenitic StainlessSteels," *ISIJ Int.*, vol. 43, no. 11, pp. 1795–1798, 2003.

[103] P. Hosemann, R. R. R. Greco, I. Usov, Y. Wang, S. a. A. Maloy, and N. Li, "The design, setup and operational testing of the irradiation and corrosion experiment (ICE)," *J. Nucl. Mater.*, vol. 376, no. 3, pp. 392–395, Jun. 2008.

[104] M. J. Vasile and C. G. Enke, “The Preparation and Thermodynamic Properties of a Palladium-Hydrogen Electrode,” *J. Electrochem. Soc.*, vol. 112, no. 8, pp. 865–870, 1965.

[105] T. L. Wijesinghe, L. Sudesh, and D. J. Blackwood, “Characterisation of passive films on 300 series stainless steels,” *Appl. Surf. Sci.*, vol. 253, no. 2, pp. 1006–1009, Nov. 2006.

[106] D. Rodriguez and D. Chidambaram, “Oxidation of Stainless Steel 316 and Nitronic 50 in Supercritical and Ultrasupercritical Water,” *Appl. Surf. Sci.*, 2015.

[107] S. Ramya, T. Anita, H. Shaikh, and R. K. Dayal, “Laser Raman microscopic studies of passive films formed on type 316LN stainless steels during pitting in chloride solution,” *Corros. Sci.*, vol. 52, no. 6, pp. 2114–2121, Jun. 2010.

[108] O. N. Shebanova and P. Lazor, “Raman study of magnetite (Fe3O4): laser-induced thermal effects and oxidation,” *J. Raman Spectrosc.*, vol. 34, no. 11, pp. 845–852, Nov. 2003.

[109] B. Beverskog, “Revised Diagrams for Iron At 25-300 ° C,” *Science (80-.).*, vol. 38, no. 12, pp. 2121–2135, 1996.

[110] C. Bethke, “Geochemists’ Workbench.” Aqueous Solutions, LLC.

[111] C. S. Kumai and T. M. Devine, “Oxidation of Iron in 288 ° C , Oxygen-Containing Water,” vol. 61, no. 3, pp. 201–218, 2005.

[112] T. Miyazawa, T. Terachi, S. Uchida, T. Satoh, T. Tsukada, Y. Satoh, Y. Wada, and H. Hosokawa, “Effects of Hydrogen Peroxide on Corrosion of Stainless Steel, (V) Characterization of Oxide Film with Multilateral Surface Analyses,” *J. Nucl. Sci. Technol.*, vol. 43, no. 8, pp. 884–895, Aug. 2006.

[113] S. J. Keny, A. G. Kumbhar, G. Venkateswaran, and K. Kishore, “Radiation effects on the dissolution kinetics of magnetite and hematite in EDTA- and NTA-based dilute chemical decontamination formulations,” *Radiat. Phys. Chem.*, vol. 72, no. 4, pp. 475–482, Mar. 2005.

[114] M. Watanabe, T. Yonezawa, T. Shobu, and T. Shoji, “Measurement methods for surface oxides on SUS 316L in simulated light water reactor coolant environments using synchrotron XRD and XRF,” *J. Nucl. Mater.*, vol. 434, no. 1–3, pp. 189–197, Mar. 2013.

[115] I. Chourpa, L. Douziech-Eyrolles, L. Ngaboni-Okassa, J.-F. Fouquenet, S. Cohen-Jonathan, M. Souce, H. Marchais, and P. Dubois, “Molecular composition of iron oxide nanoparticles{,} precursors for magnetic drug targeting{,} as characterized by confocal Raman microspectroscopy,” *Analyst*, vol. 130, no. 10, pp. 1395–1403, 2005.

[116] M. A. Legodi, D. De Waal, and S. Africa, “The preparation of magnetite , goethite , hematite and maghemite of pigment quality from mill scale iron waste,” no. February, 2007.

[117] C. Guo, Y. Hu, H. Qian, J. Ning, and S. Xu, “Magnetite (Fe3O4) tetrakaidecahedral microcrystals: Synthesis, characterization, and micro-Raman study,” *Mater. Charact.*, vol. 62, no. 1, pp. 148–151, Jan. 2011.

[118] S. S. Raiman, D. M. Bartels, and G. S. Was, “Radiolysis driven changes to oxide stability during irradiation-corrosion of 316L stainless steel in high temperature water” *In press*

[119] M. Tachiban, K. Ishida, and Y. Wada, “Cathodic Polarization Properties of Hydrogen Peroxide and the Effect on Electrochemical Corrosion Potential Calculation under

Simulated BWR Environment.," 2013.

[120] M. Nastasi, J. Mayer, and J. K. Hirvonen, *Ion-Solid Interactions*. Cambridge University Press, 2004.

[121] R. W. Revie, *Uhlig's Corrosion Handbook, 2nd ed.* New York: Wiley, 2000.

[122] J. Erlebacher, M. J. Aziz, A. Karma, N. Dimitrov, and K. Sieradzki, "Evolution of nanoporosity in dealloying," *Nature*, vol. 410, p. 450+, Jul. 2001.

[123] E. Kim, J. Spooren, K. Broos, L. Horckmans, M. Quaghebeur, and K. C. Vrancken, "Selective recovery of Cr from stainless steel slag by alkaline roasting followed by water leaching," *Hydrometallurgy*, vol. 158, pp. 139–148, 2015.

[124] E. Kim, J. Spooren, K. Broos, P. Nielsen, L. Horckmans, K. C. Vrancken, and M. Quaghebeur, "New method for selective Cr recovery from stainless steel slag by NaOCl assisted alkaline leaching and consecutive BaCrO4 precipitation," *Chem. Eng. J.*, vol. 295, pp. 542–551, 2016.

[125] J. E. Castle and H. G. Masterson, "The role of diffusion in the oxidation of mild steel in high temperature aqueous solutions," *Corros. Sci.*, vol. 6, no. 3–4, pp. 93–104, 1966.

[126] R. L. Tapping, R. D. Davidson, E. McAlpine, and D. H. Lister, "The composition and morphology of oxide films formed on type 304 stainless steel in lithiated high temperature water," *Corros. Sci.*, vol. 26, no. 8, pp. 563–576, Jan. 1986.

[127] T. Grunloh, "Unpublished." .

[128] L. M. Wang, S. X. Wang, W. L. Gong, R. C. Ewing, and W. J. Weber, "Amorphization of

ceramic materials by ion beam irradiation," *Mater. Sci. Eng. A*, vol. 253, no. 1–2, pp. 106–113, Sep. 1998.

[129] S. AGGARWAL, J. Töpfer, T.-L. Tsai, and R. Dieckmann, "Point defects and transport in binary and ternary, non-stoichiometric oxides," *Solid State Ionics*, vol. 101–103, pp. 321–331, Nov. 1997.

[130] R. Dieckmann, "Point defects and transport properties of binary and ternary oxides," *Solid State Ionics*, vol. 12, no. 0, pp. 1–22, 1984.

[131] R. Sizmann, "The effect of radiation upon diffusion in metals," *J. Nucl. Mater.*, vol. 69–70, pp. 386–412, 1978.

[132] G. C. Allen, J. A. Jutson, and P. A. Tempest, "Geoffrey C. ALLEN, Josephine A. JUTSON and Paul A. TEMPEST," 1988.

[133] F. W. Clinard, G. F. Hurley, and L. W. Hobbs, "Neutron irradiation damage in MgO, Al2O3 and MgAl2O4 ceramics," *J. Nucl. Mater.*, vol. 108–109, pp. 655–670, Jul. 1982.

[134] R. Dieckmann and H. Schmalzried, "Defects and Cation Diffusion in Magnetite (VI): Point Defect Relaxation and Correlation in Cation Tracer Diffusion," *Berichte der Bunsengesellschaft für Phys. Chemie*, vol. 90, no. 7, pp. 564–575, 1986.

[135] F. W. CLINARD Jr and L. W. HOBBS, "CHAPTER 7 - Radiation Effects in Non-Metals* ," in *Physics of Radiation Effects in Crystals*, vol. Volume 13, R. A. J. and A. N. O. B. T.-M. P. in C. M. Sciences, Ed. Elsevier, 1986, pp. 387–471.

[136] D. J. Bacon and T. Diaz de la Rubia, "Molecular dynamics computer simulations of displacement cascades in metals," *J. Nucl. Mater.*, vol. 216, pp. 275–290, Oct. 1994.

[137] H. . Heinisch, F. Gao, and R. . Kurtz, “The effects of interfaces on radiation damage production in layered metal composites,” *J. Nucl. Mater.*, vol. 329, pp. 924–928, 2004.

[138] B. Pastina, J. Isabey, and B. Hickel, “The influence of water chemistry on the radiolysis of the primary coolant water in pressurized water reactors,” *J. Nucl. Mater.*, vol. 264, no. 3, pp. 309–318, 1999.

[139] M. Wang, S. Perrin, C. Corbel, and D. Féron, “Electrochemical behaviour of 316L stainless steel exposed to representative chemistry in pressurised water reactors under proton radiation,” *J. Electroanal. Chem.*, vol. 737, pp. 141–149, Jan. 2015.

[140] M. Wang, “Electrochemical Behaviour of Stainless Steel under Radiation and Exposed to Representative Chemistry in Pressurised Water Reactor Conditions.,” Ecole Polytechnique X, 2013.

[141] X. Liu, X. Wu, and E.-H. Han, “Electrochemical and surface analytical investigation of the effects of Zn concentrations on characteristics of oxide films on 304 stainless steel in borated and lithiated high temperature water,” *Electrochim. Acta*, vol. 108, pp. 554–565, Oct. 2013.